UNIVERSITY OF LONDON THESIS

Degree PhD Year 2006 Name of Author WHITEWOOD Amic Pierre

Bistatic Radar Using a Spaceborne Illuminator

by

Aric Pierre Whitewood

A thesis submitted for the degree of Doctor of Philosophy of
the University of London

Faculty of Engineering
Department of Electronic & Electrical Engineering
University College London

The United Kingdom

June 2006

ProQuest LLC
789 East Eisenhower Parkway
P.O. Box 1346
Ann Arbor, MI 48106-1346

Abstract

A bistatic radar has a physically separated transmitter and receiver. This research programme investigates a bistatic radar system which uses a spaceborne synthetic aperture radar transmitter on board the European Space Agency's Envisat satellite and a stationary, ground based receiver. The advantages of this variant of the bistatic configuration includes the passive and therefore covert nature of the receiver, its relatively low cost, in addition to the possibility of using a non-cooperative transmitter.

The theory behind bistatic SAR systems is covered, including the specific case investigated. The design, construction and testing of the bistatic receiver, which uses two separate channels, for the direct signal from the satellite (for synchronisation purposes) and the reflected signals from the imaged scene is also described. A SAR processing scheme using an adapted chirp scaling algorithm is presented and demonstrated through simulations to produce focused images for the scenario. The results of several bistatic imaging experiments are analysed through comparisons with theoretical impulse responses, and comparisons with satellite photographs, the corresponding monostatic image produced by Envisat, and the bistatic ambiguity function.

It is demonstrated that focused images may be produced with such a system, although the performance achievable is dependent upon the imaging geometry. Different look directions of the receiver produce widely differing resolution values. The optimum choice of look direction must be weighed against possible direct signal interference in the reflected signal channel. Other effects, such as azimuth ambiguities caused by the sampling of the moving transmitter beam by the pulse repetition frequency may also have an effect, depending upon the combined transmit/receive beam pattern. Aspects of the system that could be investigated in the future are identified, for example the addition of an extra channel to the receiver in order to perform bistatic displaced phase centre antenna or interferometry experiments.

Acknowledgements

This PhD research was funded by the EPSRC, Thales and the Beck Scholarship.

I would like to thank Professor Hugh Griffiths and Professor Chris Baker for their support and direction from undergraduate level through to the end of this PhD programme. Particular thanks also to Professor Simon Watts, Dr. Andy Stove, Andrew Beaney and Paul Montgomery, for their comments and suggestions, and aid in securing an experimental site outside of London. Being in receipt of the Beck Scholarship, I am also grateful to Mrs. Beck, both for her financial assistance with my research degree, and also for the genuine interest she has taken with my studies.

My friends and colleagues in the Department and University as a whole deserve a mention. In particular, Tom Derham, Richard James and Daniel O'Hagan, who have all offered excellent advice and provided much needed moments of humour over the last three years.

Finally, I would like to thank my family for their constant encouragement and support. In particular, the excellent example set for me by my father as a Consultant Engineer, which has had a significant impact on my career choices to date.

Publications

The following paper was published as a result of the PhD research:
Whitewood, A.P., Müller, B.R., Griffiths, H.D., and Baker, C.J., "Bistatic synthetic aperture radar with application to moving target detection", Proceedings of the IEEE International Radar Conference, 3-5 September 2003, Adelaide, pp. 529-534

In addition, the author will be submitting a further paper to IEE Proceedings on Radar, Sonar and Navigation upon submission of the PhD thesis.

Table of Contents

1 Introduction **17**

1.1 Background 17

1.2 Research Aims 18

1.3 Motivation 18

1.4 Layout of the Thesis 19

2 Context of the work **21**

2.1 Fundamentals and history 21

2.2 Literature review 22

2.2.1 Bistatic Radar 22

2.2.2 Ground-Based Non-Cooperative Transmitters 25

2.2.3 Spaceborne Non-Cooperative Transmitters 27

2.2.4 Summary 31

3 Bistatic SAR theory **32**

3.1 Bistatic radar 32

3.1.1 Introduction 32

3.1.2 Geometry and range relationships 32

3.1.3 Bistatic Doppler Shift 34

3.1.4 Target Cross Section 35

3.1.5 Time and Phase Synchronisation 35

3.2 Monostatic SAR 36

3.2.1 Overview 36

3.2.2 Stripmap SAR theory of operation 37

3.2.3 SAR signal processing 43

3.3 Bistatic SAR: the general case 46
3.3.1 Introduction 46
3.3.2 Signal processing options 46
3.3.3 Bistatic SAR performance measures 47
3.4 Bistatic SAR: moving transmitter, stationary receiver 51
3.4.1 Overview and theory of operation 51
3.4.2 Monostatic and bistatic processing parameters comparison 55
3.4.3 Signal processing 55
3.4.4 Ambiguity function 56

4 Experimental system **60**
4.1 Introduction 60
4.2 Illuminator 60
4.2.1 The Envisat Satellite 60
4.2.2 The ASAR Instrument 61
4.2.3 Monostatic data products 65
4.3 Receiver System Overview 65
4.3.1 Two-channel Receiver 65
4.3.2 Three-channel Receiver 66
4.4 Receiver Design Procedure 66
4.4.1 Power Calculations 66
4.4.2 Antenna Design and Construction 69
4.4.3 Receiver design and testing 75
4.4.4 Analog-to-Digital Conversion 85
4.5 Summary 90

5 Predicted system performance **91**
5.1 Synchronisation 91
5.1.1 Time synchronisation 91
5.1.2 Phase synchronisation 92
5.2 Detection 97
5.3 Resolution 102

6 Bistatic SAR signal processing and simulations **103**

6.1 Data Preparation . . . 103

6.1.1 Overview . . . 103

6.1.2 Orbit propagation simulations . . . 106

6.1.3 Baseline compensation in received data . . . 107

6.2 Bistatic SAR Signal Processing . . . 109

6.2.1 Overview . . . 109

6.2.2 Comparison of monostatic and bistatic signal impulse responses . . . 110

6.2.3 Bistatic chirp scaling algorithm phase functions . . . 113

6.3 Conversion to map coordinates . . . 115

6.4 Processing Algorithm Tests . . . 117

6.4.1 Overview . . . 117

6.4.2 Depth of focus . . . 117

6.4.3 Simulation scenario . . . 121

6.4.4 Simulation results . . . 123

7 Bistatic SAR experimental imagery and analysis **127**

7.1 Introduction . . . 127

7.2 Experimental planning and method . . . 128

7.2.1 DSTL Portsdown West site . . . 129

7.2.2 Torrington Place site, experiment 1 . . . 172

7.2.3 Torrington Place site, experiment 2 . . . 197

7.2.4 Torrington Place site, experiment 3 . . . 211

7.2.5 Gower Street site, experiment 1 . . . 226

7.2.6 Gower Street site, experiment 2 . . . 236

7.2.7 Summary . . . 251

8 Conclusions and future work **253**

8.1 Summary of findings . . . 253

8.2 Future work . . . 254

8.2.1 Bistatic SAR imaging . . . 254

8.2.2 Bistatic displaced phase centre antenna technique . . . 256

8.2.3 Bistatic interferometry . . . 257

Appendices 258

A Calculation of effective satellite velocity 259

B Photographs of the receiver hardware 262

C Range-Doppler transform of the bistatic baseband signal impulse response 264

D Airborne trial processing 268

D.1 Introduction 268

D.2 Results and analysis 270

List of Tables

3.1 Comparison between processing parameters for the monostatic and bistatic SAR systems 55

4.1 Envisat orbit details 61
4.2 ASAR antenna and image mode transmitted signal parameters 62
4.3 ASAR image mode swath physical parameters 63
4.4 ASAR image mode antenna and transmit signal parameters for different swaths 64
4.5 Bistatic azimuth processing parameters for the various image swaths of ASAR 64
4.6 Specifications for the ASAR SLC data product 65
4.7 Comparison between theoretical and measured horn antenna 1 parameters . 70
4.8 Comparison between theoretical and measured parabolic antenna 1 parameters 71
4.9 Comparison between theoretical and measured parabolic antenna 2 parameters 73
4.10 Comparison between theoretical and measured horn antenna 2 parameters . 74
4.11 Component details, two-channel receiver 77
4.12 Component parameters for reflected signal channel noise figure calculation . 77
4.13 Direct signal channel bandwidths for RF and IF sections 78
4.14 Reflected signal channel bandwidths for RF and IF sections 81
4.15 Specifications of the Parsec PM480 analogue-to-digital converter board . . . 86
4.16 Allowable sampling rates for bandpass sampling of the Envisat IF chirp . . 87
4.17 Total cost of the bistatic SAR imaging receiver 90

5.1 Phase noise values at different offset frequencies for a carrier of 5.207GHz generated by the Rhode and Schwartz SMP04 96
5.2 Phase noise values at different offset frequencies for a carrier of 5.207GHz generated by the HP83732A 96

5.3 Phase noise values at different offset frequencies for a carrier of 5.331GHz generated by the oscillator within ASAR 96
5.4 Taylor window compared to uniform weighting 99
5.5 Processing gain for range compression of the ASAR chirp pulse with windowing function loss attributed to Taylor weighting ($\overline{n} = 6$) taken into account 99
5.6 Fixed-value parameters used in the range equation calculations 100

6.1 Quadratic phase error for the change in effective velocity across an imaged scene of 10km in ground range relative to satellite nadir 121
6.2 Defocusing due to a slant range error (non-zero range R_R) for the IS1 and IS7 ASAR image mode swaths 123

7.1 Summary of bistatic imaging acquisitions performed 128
7.2 Acquisition details for DSTL Portsdown West experiment 129
7.3 Bistatic azimuth parameters for the 5th December 2005 acquisition 144
7.4 Comparison between ISLR levels for the azimuth cut at the receiver in the direct phase synchronisation and unsynchronised bistatic images 154
7.5 Selected features in 5th December 2005 image 161
7.6 Resolution of responses for selected features in 5th December 2005 image . 162
7.7 Hamming window compared to uniform weighting 169
7.8 Acquisition details for the first Torrington Place experiment 172
7.9 Bistatic azimuth parameters for the 12th November 2004 acquisition 180
7.10 Bistatic prf time for IS1 and IS7 swaths 189
7.11 Selected features in 12th November 2004 image 194
7.12 Acquisition details for the second Torrington Place experiment 197
7.13 Bistatic azimuth parameters for the 1st December 2004 acquisition 201
7.14 Selected features in 1st December 2004 image 206
7.15 Acquisition details for the third Torrington Place experiment 211
7.16 Bistatic azimuth parameters for the 19th August 2005 acquisition 215
7.17 Acquisition details for the first Gower Street experiment 226
7.18 Bistatic azimuth parameters for the 25th July 2005 acquisition 230
7.19 Acquisition details for the second Gower Street experiment 236
7.20 Bistatic azimuth parameters for the 25th October 2005 acquisition 240

D.1 QinetiQ airborne SAR data acquisition parameters 269

List of Figures

2-1 Bistatic radar geometry 22

3-1 Bistatic radar geometry 32
3-2 Isorange contour 33
3-3 Example ovals of Cassini 35
3-4 SAR data acquisition geometry 37
3-5 Illustration of range cell migration 39
3-6 Curved satellite SAR geometry and equivalent rectilinear model 39
3-7 Chirp scaling algorithm flow diagram 45
3-8 General geometry of bistatic SAR 46
3-9 Bistatic SAR geometry showing various terms in the Ambiguity Function . 49
3-10 Data acquisition geometry for the bistatic SAR configuration investigated . 51
3-11 Comparison of monostatic and bistatic range resolution cells 53
3-12 Specific geometry of bistatic SAR with moving transmit platform and stationary receiver 56

4-1 Photograph of Envisat illustrating the ASAR array 61
4-2 Azimuth and elevation radiation patterns of horn antenna 1 70
4-3 Azimuth radiation pattern of parabolic antenna 1 72
4-4 Azimuth and elevation radiation patterns of parabolic antenna 1 72
4-5 Azimuth radiation pattern of parabolic antenna 2 73
4-6 Azimuth and elevation radiation patterns of parabolic antenna 2 74
4-7 Two-channel receiver block diagram 76
4-8 Frequency response of RF section of direct signal channel 78
4-9 Frequency response of IF section of direct signal channel 79

4-10 Power output versus power input for a CW signal applied to the direct signal channel 80
4-11 Noise captured in the direct signal channel, and a comparison between measured and theoretical histograms of the sample amplitudes 81
4-12 Frequency response of RF section of reflected signal channel 82
4-13 Frequency response of IF section of reflected signal channel 82
4-14 Power output versus power input for a CW signal applied to the reflected signal channel, gain control voltage of 2.4V 83
4-15 Power output versus power input for a CW signal applied to the reflected signal channel, gain control voltage of 2.1V 84
4-16 Noise captured in the reflected signal channel, $G_c = 2.1V$ and a comparison between measured and theoretical histograms of the sample amplitudes . . 85
4-17 Three-channel receiver block diagram 86
4-18 Spectrum of the Envisat IF chirp bandpass sampled at 100MHz 88
4-19 Spectrum of two Envisat IF chirp signals at 110MHz and 130MHz bandpass sampled at 100MHz 89

5-1 Single sideband phase noise of the Rhode and Schwartz SMP04 95
5-2 Integrated sidelobe ratio simulation 97
5-3 Signal-to-noise ratio after range compression using parabolic antenna 2 in the receiver and for the IS1 and IS7 swaths 101

6-1 Imaging receiver down-conversion to baseband 104
6-2 Arrangement of raw data pulses/segments in matrix format 105
6-3 Interpolation and phase shifting operations to compensate for the baseline variation, L 109
6-4 Impulse response width broadening, peak-to-sidelobe ratio increase, and integrated sidelobe ratio increase with quadratic phase error for a matched filter with Taylor weighting, $\overline{n} = 6$ 118
6-5 Effective velocity versus slant range across the swath for IS1 and IS7 120
6-6 Geometry for bistatic SAR point target simulations 122
6-7 Responses produced at the receiver for the IS1 and IS7 simulations 124
6-8 Cuts of response produced at receiver, IS1 swath simulation 124

6-9 Cuts of response produced at receiver, IS7 swath simulation 125
6-10 Defocusing of azimuth impulse response due to R_R, IS1 swath simulation . 125
6-11 Defocusing of azimuth impulse response due to R_R, IS7 swath simulation . 126

7-1 Imaging geometry for 5th December 2005 acquisition 129
7-2 Direct signal channel IF pulses captured by the Parsec ADC 130
7-3 Direct signal channel IF pulse in the frequency domain 131
7-4 Direct signal pulse magnitude versus pulse number for the 5th December 2005 acquisition 132
7-5 Real and imaginary parts of a direct signal pulse after down-conversion to baseband within Matlab 133
7-6 Reflected signal channel IF pulses captured by the Parsec ADC 134
7-7 Reflected signal channel IF pulse in the frequency domain 135
7-8 Real and imaginary parts of a direct signal pulse after down-conversion to baseband within Matlab 135
7-9 Direct signal channel baseband pulse before and after pulse compression with an ideal ASAR chirp signal 136
7-10 Measured phase of the direct signal channel pulses 137
7-11 Reflected signal channel array after range compression and phase referencing 138
7-12 Phase measured at peak position in reflected signal channel array 139
7-13 Amplitude measured at peak position in reflected signal channel array . . . 140
7-14 Measured pulse repetition interval for the direct signal data captured for the 5th December 2005 acquisition 141
7-15 Data loss for the direct signal data captured for the 5th December 2005 acquisition 141
7-16 Simulated direct signal path length (baseline) 142
7-17 Power balancing method applied to simulated azimuth signal 143
7-18 Approximate transmit beam variation and simulated baseline variation over the processing interval for the 5th December 2005 bistatic image 146
7-19 Bistatic image for 5th December 2005 acquisition, bistatic range sum versus azimuth 148
7-20 Overall range cut at the receiver azimuth position 149

7-21 Close-in range cut at the receiver azimuth position 149
7-22 Overall azimuth cut at the receiver azimuth position 150
7-23 Close-in azimuth cut at the receiver azimuth position 151
7-24 Overall azimuth cut at the target point position on 5th December 2005 bistatic image 151
7-25 Close-in azimuth cut at the target point position on 5th December 2005 bistatic image 152
7-26 Bistatic image for 5th December 2005 acquisition, bistatic range sum versus azimuth, no phase synchronisation 153
7-27 Close-in range cut at the receiver azimuth position 154
7-28 Overall azimuth cut at the receiver azimuth position 155
7-29 Close-in azimuth cut at the receiver azimuth position 155
7-30 Bistatic image for 5th December 2005 compared to grid coordinates for image transformation 156
7-31 Contours of constant bistatic range and azimuth position on the earth's surface for the coordinate conversion of the 5th December 2005 bistatic image 157
7-32 Map and satellite photograph of the area around the DSTL Portsdown West site 159
7-33 Photographs of the imaged area, taken from the receiver position - left of centre (top) and right of centre (bottom) 160
7-34 Bistatic image from the 5th December 2005 acquisition interpolated onto a grid coordinates plane 161
7-35 Bistatic image overlaid onto a satellite photograph of the area around DSTL Portsdown West 164
7-36 Cuts along Eastings and Northings at DSTL site boundary for 5th December 2005 image 165
7-37 Cuts along Eastings and Northings at Nelson's monument in 5th December 2005 image 165
7-38 Cuts along Eastings and Northings at electricity pylon in 5th December 2005 image 166
7-39 Theoretical resolutions along East and North directions for 5th December 2005 image 167

7-40 Theoretical bistatic angle and ground resolution cell size for 5th December 2005 image 168
7-41 Monostatic image for 5th December 2005 acquisition, full resolution 170
7-42 Monostatic image for 5th December 2005 acquisition, reduced resolution . . 171
7-43 Imaging geometry for 12th November 2004 acquisition 172
7-44 Direct signal channel IF pulses captured by the Parsec ADC 173
7-45 Direct signal channel IF pulse in the frequency domain 174
7-46 Reflected signal channel IF pulses captured by the Parsec ADC 175
7-47 Reflected signal channel IF pulse in the frequency domain 176
7-48 Measured phase of direct signal channel pulses 177
7-49 Reflected signal channel array after range compression and phase referencing 177
7-50 Phase measured at peak position in reflected signal channel array 178
7-51 Magnitude measured at peak position in reflected signal channel array . . . 178
7-52 Simulated direct signal path length 179
7-53 Bistatic image for 12th November 2004 acquisition, bistatic range sum versus azimuth 182
7-54 Overall range cut at the receiver azimuth position 183
7-55 Close-in range cut at the receiver azimuth position 183
7-56 Overall azimuth cut at the receiver azimuth position 184
7-57 Close-in azimuth cut at the receiver azimuth position 184
7-58 Overall azimuth cut at the target position, 12th November 2004 image . . . 185
7-59 Close-in azimuth cut at the target position, 12th November 2004 186
7-60 Contours of constant bistatic range and azimuth position on the earth's surface for the coordinate conversion of the 12th November 2004 bistatic image 187
7-61 Satellite photograph of the area around the Torrington Place site 188
7-62 Photograph of the imaged area, taken from the receiver position and illustrating the imaged scene 189
7-63 Bistatic image from the 12th November 2004 acquisition interpolated onto a grid coordinates plane 190
7-64 Transmit and receive antenna patterns for constant azimuth line, IS1 swath 191
7-65 Transmit and receive antenna patterns for constant azimuth line, IS7 swath 192

7-66 Bistatic image overlaid onto a satellite photograph of the area around Torrington Place, 12th November 2004 193
7-67 Resolutions along East and North directions for 12th November 2004 image 195
7-68 Bistatic angle β and ground resolution cell size 12th November 2004 image 195
7-69 Monostatic image for 12th November 2004 acquisition 196
7-70 Imaging geometry for 1st December 2004 acquisition 197
7-71 Measured phase of direct signal channel pulses 199
7-72 Reflected signal channel array after range compression and phase referencing 199
7-73 Phase measured at peak position in reflected signal channel array 200
7-74 Magnitude measured at peak position in reflected signal channel array . . . 200
7-75 Simulated direct signal path length 201
7-76 Bistatic image for 1st December 2004 acquisition, bistatic range sum versus azimuth 202
7-77 Overall range cut at the receiver azimuth position 203
7-78 Close-in range cut at the receiver azimuth position 203
7-79 Overall azimuth cut at the receiver azimuth position 204
7-80 Close-in azimuth cut at the receiver azimuth position 204
7-81 Contours of constant bistatic range and azimuth position on the target plane for the coordinate conversion of the 1st December 2004 bistatic image . . . 205
7-82 Bistatic image from the 1st December 2004 acquisition interpolated onto a grid coordinates plane 206
7-83 Bistatic image overlaid onto a satellite photograph of the area around Torrington Place, 1st December 2004 207
7-84 East and North directed resolutions for 1st December 2004 acquisition . . . 208
7-85 Bistatic angle and ground resolution cell size for 1st December 2004 acquisition 209
7-86 Monostatic image for 1st December 2004 acquisition 210
7-87 Imaging geometry for 19th August 2005 acquisition 211
7-88 Measured phase of direct signal channel pulses 212
7-89 Reflected signal channel array after range compression and phase referencing 213
7-90 Phase measured at peak position in reflected signal channel array 213
7-91 Magnitude measured at peak position in reflected signal channel array . . . 214
7-92 Simulated direct signal path length 214

7-93 Bistatic image for 19th August 2005 acquisition, bistatic range sum versus azimuth 215
7-94 Overall range cut at the receiver azimuth position 217
7-95 Close-in range cut at the receiver azimuth position 217
7-96 Overall azimuth cut at the receiver azimuth position 218
7-97 Close-in azimuth cut at the receiver azimuth position 218
7-98 Contours of constant bistatic range and azimuth position on the earth's surface for the coordinate conversion of the 19th August 2005 bistatic image . 219
7-99 Photograph of the imaged area, Torrington Place experiment 19th August 2005, taken from the receiver position and illustrating the imaged scene . . 220
7-100Bistatic image from the 19th August 2005 acquisition interpolated onto a grid coordinates plane 221
7-101Bistatic image overlaid onto a satellite photograph of the area around Torrington Place, 19th August 2005 222
7-102Simulation of the bistatic range sum of three points along the BT tower height for the 19th August 2005 acquisition 223
7-103East and North directed resolutions for 19th August 2005 acquisition 223
7-104Bistatic angle and ground resolution cell size for 19th August 2005 acquisition224
7-105Monostatic image for 19th August 2005 acquisition 225
7-106Imaging geometry for 25th July 2005 acquisition 226
7-107Measured phase of direct signal channel pulses 227
7-108Reflected signal channel array after range compression and phase referencing 228
7-109Phase measured at peak position in reflected signal channel array 228
7-110Magnitude measured at peak position in reflected signal channel array . . . 229
7-111Simulated direct signal path length 229
7-112Bistatic image for 25th July 2005 acquisition, bistatic range sum versus azimuth230
7-113Overall range cut at the receiver azimuth position 232
7-114Close-in range cut at the receiver azimuth position 232
7-115Overall azimuth cut at the receiver azimuth position 233
7-116Close-in azimuth cut at the receiver azimuth position 233
7-117Contours of constant bistatic range only on the target plane for the coordinate conversion of the 25th July 2005 bistatic image 234

7-118Photograph of the imaged area, Gower Street experiment 25th July 2005, taken from the receiver position and illustrating the imaged scene 235
7-119Imaging geometry for 25th October 2005 acquisition 236
7-120Measured phase of direct signal channel pulses 237
7-121Reflected signal channel array after range compression and phase referencing 237
7-122Phase measured at peak position in reflected signal channel array 238
7-123Magnitude measured at peak position in reflected signal channel array . . . 239
7-124Simulated direct signal path length 239
7-125Bistatic image for 25th October 2005 acquisition, bistatic range sum versus azimuth 241
7-126Overall range cut at the receiver azimuth position 242
7-127Close-in range cut at the receiver azimuth position 243
7-128Overall azimuth cut at the receiver azimuth position 243
7-129Close-in azimuth cut at the receiver azimuth position 244
7-130Contours of constant bistatic range and azimuth position on the earth's surface for the coordinate conversion of the 25th October 2005 bistatic image . 245
7-131Map and satellite photograph of the area around the Gower Street site for the second experiment 246
7-132Photograph of the imaged area, Gower Street experiment 25th October 2005, taken from the receiver position and illustrating the imaged scene 247
7-133Bistatic image from the 25th October 2005 acquisition interpolated onto a grid coordinates plane 248
7-134Bistatic image overlaid onto a satellite photograph of the area around Gower Street, 25th October 2005 249
7-135East and North directed resolutions for 25th October 2005 acquisition . . . 250
7-136Bistatic angle and ground resolution cell size for 25th October 2005 acquisition250

A-1 Circular orbit, spherical Earth geometry for calculation of effective satellite velocity V_{FM} 260

B-1 Photograph of the imaging receiver 262
B-2 Photographs of the imaging receiver antennas 263
B-3 Photograph of the extra channel for the DPCA receiver 263

D-1 Geometry for QinetiQ airborne SAR data acquisition 268
D-2 Real and imaginary parts of QinetiQ reference chirp 269
D-3 Airborne SAR image processed by QinetiQ 270
D-4 Airborne SAR image processed using the monostatic chirp scaling algorithm 271
D-5 Section of airborne SAR image processed using the monostatic chirp scaling algorithm 271
D-6 Point-like target from airborne SAR image processed using the monostatic chirp scaling algorithm 272

List of Principal Symbols

Nomenclature for all equations is defined in the main body of the document, however a list of some of the more commonly used symbols is given here.

Symbol	Quantity
β	Bistatic angle
γ	Mainlobe broadening factor
δR	Range resolution
δx	Azimuth resolution
$\boldsymbol{\Theta}$	Unit vector along the bisector of the bistatic angle
θ	Angle
λ	Wavelength of carrier signal
$\boldsymbol{\Xi}$	Unit vector along motion direction
σ	Radar cross section
τ	Delay
$\boldsymbol{\Phi}$	Unit vector (from transmitter or receiver to a target point, depending on subscript)
ω	Angular speed
a	Antenna pattern
B	Signal bandwidth
f	Frequency
f_0	Carrier frequency
F	Noise figure (with a subscript this can also denote pattern propagation factor)
f_p	Pulse repetition frequency
G	Gain
k	Boltzmann's constant
L	Baseline length or azimuth dimension of transmit antenna (with a subscript this can also denote a loss term)
m_A	Inverse Fourier transform of the normalised received signal magnitude pattern (combination of transmitter and receiver patterns)
P_T	Transmit power
p	Inverse Fourier transform of the power spectrum of the transmitted signal
R	Range
r	Range
T_s	System noise temperature
t	Time
V	Velocity

Chapter 1

Introduction

1.1 Background

Radar, from RAdio Detection And Ranging, is a system that uses electromagnetic energy transmission for the detection and location of objects. Part of the transmitted signal is reflected by the object and received by the radar system, whereupon it is processed in order to give information on location and relative velocity. A monostatic radar has a transmitter and receiver that are in the same location, whereas in a bistatic radar the two are separated. The concept of a bistatic radar system was first documented in 1917, with an idea by Nikola Tesla to detect submerged enemy submarines and the first recorded evidence of bistatic detection occurred shortly afterwards, in 1922 at the United States Naval Aircraft Laboratory. All such early radar experiments were bistatic in nature, and conducted independently in the United States, United Kingdom, France, the Soviet Union, Japan, Germany and Italy. For example, Japan, France and the Soviet Union investigated bistatic forward scatter fences, while the British Chain Home monostatic radar could be used in a bistatic mode in the case of ECM or transmitter failure. After World War 2, monostatic radar systems dominated all research and development due to the reduced complexity associated with operating a single site system, with the bistatic radar having several periodic resurgences every 15-20 years.

1.2 Research Aims

The principal aim of the research programme is as follows:

1. To demonstrate a bistatic imaging radar using a moving, satellite-borne transmitter and a stationary receiver. This includes:

   (a) Development of signal processing algorithms e.g. synthetic aperture processing.

   (b) Conduct of trials investigating different bistatic geometries.

   (c) Generation and analysis of bistatic synthetic aperture radar images.

In addition, the following secondary aims are applicable to the research, and are detailed further in the Future Work section of the Conclusions Chapter.

1. To gather and analyse bistatic clutter data.

2. To demonstrate airborne moving target detection using the Displaced Phase Centre Antenna (DPCA) technique to cancel unwanted clutter returns.

3. To perform interferometry experiments.

4. Extrapolation of the results to other satellite illuminators and frequencies.

1.3 Motivation

A resurgence of interest in the field of bistatic radar has been apparent over the last five to ten years, and so such systems are currently an active area of research. The physical separation of transmitter and receiver confers certain advantages as a result of the geometry and due to the receiving system being completely passive. This means it is undetectable, immune to the effects of deliberate directional interference, and may in principle be relatively simple and therefore cheap. That such a passive receiver may use radiation from a non-cooperative transmitter is another advantage and of course has military applications. Some of these so-called 'illuminators of opportunity' have been investigated previously and include: ground-based television transmitters [1] and [2], GSM base stations [3], and satellites [4], [5] and [6], transmitting a variety of waveforms, not all of which e.g. communication signals, are optimum for surveillance. It is the satellite-based illuminator that has

been identified by the US Department of Defense as an important component of future Airborne Moving Target Indication (AMTI) and Ground Moving Target Indication systems (GMTI) [7] and [8], and which forms the basis of this particular investigation. The specific bistatic radar system investigated consists of a satellite-borne synthetic aperture radar (the ASAR instrument on the European Space Agency's Envisat satellite) and a stationary ground-based receiver. The choice of this particular illuminator has the advantages of high power density at the Earth's surface, and the transmission of a radar waveform. Most of the previous work on satellite, as well as airborne, bistatic radars has focused on the case of both transmitter and receiver being mounted on moving platforms (see the Literature Review for more details), with very little research having been published on the configuration considered. In addition, there is a relatively small amount of published results on the measurement of bistatic clutter data. The applications of this system are:

1. Imaging, or generation of bistatic synthetic aperture radar images, in addition to GMTI.

2. AMTI using multiple channels in order to perform DPCA processing and suppress clutter returns. Radar Cross Section (RCS) enhancement of targets close to the baseline of the bistatic geometry allows the possibility of detection of stealthy targets.

3. Interferometry, again using multiple channels, may be used for local area monitoring where a high data update rate is required, Cherniakov [9], and for monitoring terrain subsistence effects such as landslides and collapse precursors, see Cazzani [10].

1.4 Layout of the Thesis

The Literature Review discusses research on bistatic radar in general before considering illuminators of opportunity and finally the specific configuration investigated in this thesis. The Bistatic SAR Theory Chapter then follows, including the fundamental relationships and equations governing the operation of bistatic synthetic aperture radar systems (again, both the general and the specific case investigated). A Chapter on the experimental system covers both the ASAR instrument on Envisat and the receiver constructed for the investigation. The predicted system performance in terms of synchronisation, detection and resolution is presented in the next Chapter, and then Chapter six deals with the signal processing

algorithms used for the generation of the bistatic SAR images. The experimental results and analysis are given in Chapter seven, including comparisons of the bistatic images with the bistatic Ambiguity Function, satellite photographs of the imaged scene, and the monostatic images supplied by ESA. The final Chapter summarises the main findings of the research and considers what further investigations may be possible with such a system.

Chapter 2

Context of the work

2.1 Fundamentals and history

A brief decription of a bistatic radar system is given to start with in order to introduce the main operational issues that must be considered. A diagram is given below, which illustrates the bistatic triangle defined by transmitter, target and receiver, as well as the bistatic angle β.

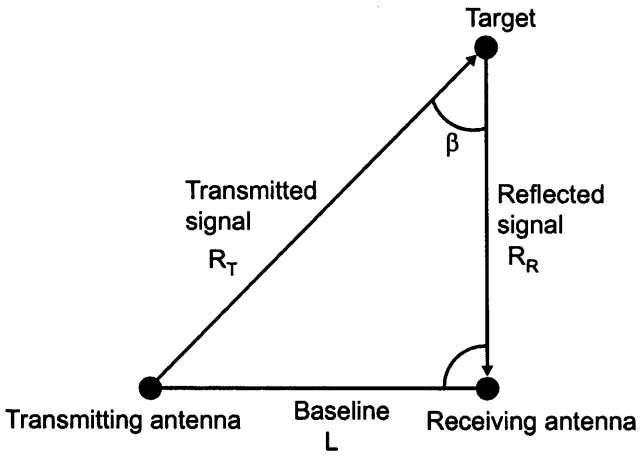

Figure 2-1: Bistatic radar geometry

The physical separation of transmit and receive platforms is key to the definition of such a system, and the resultant, time-varying geometry increases its complexity compared to a monostatic radar. This imposes certain requirements, such as the need to pass information from transmit to receive platform (for example the transmitted waveform, and for time and phase synchronisation) and knowledge of the geometry (in order to solve for the range relationships, and synchronise antenna beams, for example). This information should also allow the system to compensate for adverse geometry-dependent effects or alternatively to draw benefit from any beneficial effects that may arise.

2.2 Literature review

2.2.1 Bistatic Radar

This section is intended to give some idea as to the research undertaken and literature available on bistatic radar in general. As an overview to the subject of bistatic radar, the text book by Willis [11] is an excellent starting point, providing a comprehensive section on the history and applications of such systems. Hanle [12] considers the more general case of multistatic radars, as well as bistatic, defining and comparing the two. It is concluded that both of course require an increase in control and processing, with the important point being made that performance depends significantly on the geometry, described in this case as the positions of targets with respect to transmitter-receiver baselines. Glaser [13] gives some examples of bistatic radars, from the first radar detection in 1922 by Taylor and Young, to

such systems as the AN/FPS-118 over-the-horizon backscatter radar (1970). Non-military applications are also considered, such as lunar surface exploration [14], and observation of long-wavelength directional ocean wave spectra [15]. Hsu [16] examines the specific case of spaceborne bistatic radar - using a spaceborne transmitter and passive airborne or ground based receivers, similar to the system investigated in this thesis. Requirements are examined in terms of illuminator coverage, radar functions, satellite orbit, antenna, waveform, power level, and direct signal prescence. Griffiths [17] gives a description of the history, main concepts and recent developments in the bistatic radar field.

Schoenenberger [18] describes bistatic and multistatic radar configurations with one or more receivers that operate in coordination with a single transmitter. Experiments are detailed on the use of a bistatic receiver with the transmissions from a UHF air traffic control radar. Yang [19] describes tests of a short range bistatic radar used at sea, with emphasis on the resolution obtainable, while Munich [20] deals with the 'airborne bistatic object location system' developed by AIL Systems. Wardrop [21] postulates that a mobile support receiver could be constructed that would integrate into air defence networks, and Yague [22], similarly to Schoenenberger [18], details a ground based bistatic receiver used in experiments with one of Barcelona airport's radar transmitters. The paper by Nordwall [23] considers a bistatic radar system used to evaluate the RCS of low-observable air vehicles, while Gjessing [24] describes a 'radar fence' that uses frequency coding, time coding and spatial diversity. Johnssen [25] reports on experiments into the operation of a CW bistatic radar system used to detect and classify helicopter targets, including extending the system to multiple transmitter-receiver pairs i.e. multistatic operation. Burkholder [26] examines the relationships between monostatic and bistatic radar images using a body-of-revolution Method-of-Moments algorithm, and focusing on two perfectly conducting targets, an ogive and a cone-cylinder. Significant differences are observed in the higher order scattering effects between the monostatic and bistatic systems. This paper highlights the difficulties in predicting bistatic scattering. Weiss [27] reports on the FGAN experimental bistatic radar, which uses both cooperative and non-cooperative illuminators. The important topic of synchronisation is covered by Weib [28], although more details on this subject may of course be found in Willis [11]. Time and frequency synchronisation requirements and methods are described, an important aspect of bistatic systems. The former is needed to establish timing relationships and so measure range, the latter to enable coherent operation

of the system, necessary for such applications as bistatic synthetic aperture radar.

Horne [29] discusses the fundamental problems associated with bistatic SAR, and considers performance, synchronisation (and in particular, phase noise), processing methods and motion compensation, and the characteristics of the resultant imagery. A bistatic SAR has a reduced resolution compared to an equivalent monostatic SAR (with the same bandwidth and synthetic aperture time), as well as a non-orthogonal point-spread function that may affect eventual image interpretability. Care must be taken over the choice of oscillators in both transmitter and receiver as the combined phase noise will affect the coherent integration times of the system. The phase synchronisation requirements are also very demanding. Yates [30], follows on from Horne [29], with an experimental investigation where the transmitter and receiver are mounted on airborne moving platforms, with the SAR transmitter operated in spotlight, as opposed to stripmap mode. The synchronisation problem is solved here with the indirect method - very accurate, independent time and frequency standards in the form of caesium atomic clocks are used on both platforms. The phase noise is measured and compared to that which would be produced by monostatic operation, illustrating the performance degradation in the bistatic case. High resolution images are produced and compared to equivalent monostatic images of the same scene, highlighting the different scattering mechanisms involved and so extra information that is provided, an aspect that is further investigated with scattering simulation programs. Martinsek [4]: here, the illuminator is spaceborne (ERS-1 or SIR-C) and the receiver is airborne. Two antennas are used - one for the direct and one for the reflected signal, in this way direct synchronisation is achieved between the two platforms. A single channel is used as the direct signal always arrives earlier than any reflected echo due to the geometry: the aircraft flew parallel to the satellite path, looking in the same direction, for maximum resolution. Examples of the bistatic images produced are given, with processing simply consisting of matched filtering with the direct reference signal for range compression, and discrete Fourier transformation for azimuth compression. This is in contrast with the typical case of complex signal processing for bistatic image formation, as will be considered now. Some examples of bistatic processing algorithms are given in Ender [31]. Two such algorithms, the bistatic range-Doppler and bistatic backprojection algorithm are applied to data collected during a radar trial with airborne platforms. An $\omega - k$ type algorithm is also examined in conjunction with simulated data. As a result of the complexity of a completely general bistatic

SAR configuration, the algorithms themselves are specific to a particular flight geometry. They are also all based on monostatic processors. Another bistatic SAR processing scheme is described in Rigling [32], based on the Polar Format algorithm. Again, it is specific to a particular flight situation, and while it is computationally efficient, the approximations introduced in the derivation mean that the final bistatic scene size is limited. An alternative to these full processing schemes is the so-called 'Rocca's smile' operator, D'Aria [33] and Loffeld [34], that transforms bistatic data in such a way that a monostatic processor may be used for subsequent image generation.

Bistatic spaceborne radar with GMTI mode is discussed in Czernik [35]. A Matlab model was produced in order to investigate the motion induced clutter spread with a medium earth orbit transmitter and a low earth orbit receiver. The clutter spread for such a spaceborne platform is inherently wider than that for an airborne radar system, as a result of the higher ground speeds involved. The use of clutter-suppression techniques such as DPCA and STAP on space-based radars is necessary for moving target detection, but have more stringent requirements as a result. Finally, Gleason [36] examines a GPS-based bistatic radar system in order to investigate signals reflected by the ocean for determination of surface roughness and wind speed. They conclude that reliable detection is possible despite the low power density on the earth's surface, and identify applications such as global climate weather models and marine ocean safety. Here the disadvantage of low power density affects the detection performance of the system, and is one of the factors that must be taken into account in the choice of illuminator.

2.2.2 Ground-Based Non-Cooperative Transmitters

The radar system considered in this thesis uses a non-cooperative transmitter or "illuminator of opportunity", and so a summary of some of the research on these specific systems with a ground-based illuminator now follows.

Hawkins [37] deals with the general case of a 'non-cooperative bistatic radar', which is basically a passive receiver system. The emphasis is placed on using the enemy's own radars, the motivation behind the research is the desire to operate a radar system in hostile areas with little chance of detection. The paper includes discussions of the principle of operation (e.g. calculation of target azimuth, and target location accuracy) and optimum illuminators, as well as results of trials undertaken using such a receiver and ship-borne

transmitters. In conclusion, the non-cooperative radar is identified as being invaluable for covert activity, although it is of course dependent on illuminators being available. It also needs to be able to make the best use of transmissions from a variety of different sources. Earlier research includes Fawcette [38] (description of a tactical bistatic radar known as the Sanctuary System), Retzer [39] and Thompson [40], the last two of which consider ways of overcoming synchronisation problems. The applications of counter narcotics drug interdiction, as well as covert surveillance are covered in the paper on bistatic laptop radar Ogrodnik [41], while in contrast the celldar system [3], developed by Roke Manor Research in 2001, uses reflections of digital telephone signals for Ground based Air Defense, Passive Airborne Early Warning, and Traffic Monitoring. Zoeller [42] uses FM broadcast signals as the source, while Griffiths [1] and Howland [2] both use TV transmitters - the latter demonstrates target tracking at distances of several hundred kilometres from the receiver, albeit with less accuracy than with a dedicated monostatic radar. A slightly different concept is presented in Hershey [43], where the transmitter is naturally occurring galactic noise. Although altimetric functions are identified as the main application, it is also noted that some low resolution imaging radar may also be possible, for example of ships at sea.

A recent special issue on passive radar systems [44] covers a variety of illuminators of opportunity, with papers on experimental investigations, signal processing, improved computational performance, and optimal deployment of receivers. That the transmitter parameters are not within our control is an important point that is made early in this issue, choice of illuminator therefore involves some level of compromise between different factors, for example transmit power and waveform. Some examples from this collection include Howland [45], using a single commercial FM radio transmitter, together with simple computer hardware and a dipole antenna in order to achieve detection and tracking of air targets 150km away from the receiver. The main challenges faced in this project included direct and surface clutter signal cancellation, in addition to development of a cross-correlation algorithm that can process the data in real time. The direct signal cancellation/mitigation problem is one that is common to many bistatic systems and will be discussed at a later stage in relation to the system investigated in this thesis. Various algorithms are described for removal of interference and clutter, target detection, and target association and the results of the system are compared to air traffic control data. The Saini [46] paper is an investigation into the suitability of terrestrial digital TV broadcast signals for use in a bistatic

radar system. The choice of illuminator does not impact just the received power, as was noted previously for GPS, but also the waveform transmitted, which may not be ideally suited to a surveillance application. The ambiguity function is used to analyse the signal properties with a direct computer model of the transmitted signal (an analytic formulation is given in another paper). It is found that the random nature of the main component of the signal results in no ambiguities in the delay and Doppler plots, although components such as the guard interval and pilot carrier introduce some unwanted peaks. To partially remove these, signal processing at the receiver is employed which introduces a mismatch between the two receiver channels. The resultant improvement is countered by a power loss of approximately 0.6dB. Griffiths part 1 [47] and Baker part 2 [48] examine several illuminators of opportunity. In the first part, a performance analysis based on a tailored version of the bistatic radar range equation is presented. The three example illuminators chosen are analogue FM radio, cellular telephone base stations, and digital audio broadcast. Although the noise and direct signal levels are high, detection ranges of several tens of kilometres are predicted. The second part focuses on resolution and ambiguity. Measurements of FM radio, GSM 1800 and analogue UHF television signals are used to illustrate the respective 'self-ambiguity' in each case (equivalent to a monostatic ambiguity function plot). A bistatic ambiguity function formulation is then used with simulated FM radio data and later extended to a multistatic arrangement. It is found that the measured waveforms are relatively narrow band and time-varying with good Doppler but poor range resolution. From the simulations, it is noted that careful consideration of the geometry and time-varying effects on performance must be taken into account.

2.2.3 Spaceborne Non-Cooperative Transmitters

Considering now the use of spaceborne illuminators of opportunity, and related research. Much of the work undertaken considers the case of a moving receiver, mounted on a satellite or airborne platform. The same factors affecting performance that were noted in the previous sections are applicable here, for example, transmit power and waveform, synchronisation, direct signal interference at the receiver, and geometry. An example of an earlier paper on this topic is that by Braun [49], which investigates different combinations of transmitter and receiver platform orbits, for civil applications. Direct Broadcast by Satellite television (DBS) as the transmitter is investigated by Griffiths [6], which follows on

from previous work contained in Griffiths [1]. The TV waveforms used were found to give acceptable results for a radar application, and a simple model of the system indicated that a large amount of processing gain was required, suggesting that the radar is applicable to detection of large, slowly-moving targets. Soumekh [50] describes a processing technique used for CW bistatic radars. Moccia [51] and Rufino [52] investigate a proposed system that uses an active SAR mounted on a large platform, and a passive SAR on a smaller platform as the receiver. The technology is based on the COSMO/SkyMed X-Band SAR2000 (a constellation of small satellites used for Mediterranean basin observation). Distributed spaceborne radar system design is where a non-cooperative transmitter is combined with several receivers (Haifeng [53]). This paper considers six variations of beam-pointing synchronisation, attitude and antenna pointing, and swath overlap, and provides an overall simulation in order to validate the described design methods.

The specific system considered in this thesis has a spaceborne transmitter and ground based receiver, research on this configuration now follows. Cazzani [10] investigates a system that uses the motion of an almost geostationary TV satellite in order to generate a synthetic aperture relative to a ground based receiver. The direct signal is measured using a dedicated channel (the echo signals are detected in a separate channel), used for synchronisation and range compression. Azimuth compression is achieved with a standard monostatic processing algorithm. The system consists of low-cost consumer components, and an area of 200m by 200m was imaged with a ground resolution cell size of 10m by 10m. McIntosh [54] also considers a ground based receiver, but in a theoretical study into a pre-detection signal processing scheme that adapts to the bistatic signal, so as to increase the possible coherent integration time and therefore integration gain. Cherniakov [55], Cherniakov [5] and Homer [56] all deal with Low Earth Orbit Satellite (LEOS) transmitters such as Iridium and Globalstar which are identified as having certain favourable characteristics, such as a high power density at the Earth's surface. In addition, the high speed means that despite a television or other non-radar transmission, they may still be potentially used as a bistatic synthetic aperture radar. The first paper considers a system design with Iridium and vessel detection at sea. The second applies to air target detection using a communication LEOS, with theoretical and experimental studies showing that detection at ranges of 30km is possible, although highlighting the problems of clutter and direct signal interference. The third paper covers the development of a model to determine the resolution capabilities of

a system using a LEOS transmitter and a stationary, ground-based receiver. Mojarrabi [57] describes a theoretical study into the use of a ground receiver with a GPS satellite in order to detect air targets, which again highlights the problems of low signal power for GPS systems and large clutter returns. The next reference, Griffiths [58], presents the system investigated in this thesis, that of a bistatic radar system with the ASAR instrument on the Envisat satellite as the illuminator of opportunity. This transmitter is chosen because of its high power density, and optimum (radar) waveform. It is also shown that the clutter Doppler spectrum, which affects detection of moving targets in such a space-based system, is half as broad as in an equivalent monostatic SAR. Despite this, a clutter suppression technique such as DPCA is still necessary in order to achieve adequate detection performance of moving targets. In the same Conference, the paper by Cherniakov [59] deals with the general case of such 'Space-Surface Bistatic Radars', considering their feasibility in terms of operation, signal-to-noise ratio, and resolution. Whitewood [60] follows on from Griffiths [58], with further experimental tests of the SAR receiver, a theoretical investigation into the use of DPCA with two stationary receivers for clutter cancellation, and examines the possibility of interferometry with such a system. The subject of bistatic interferometry is covered in more detail in Cherniakov [9]. Bistatic SAR signal processing for this arrangement is presented in three separate papers. Wong [61] applies the non-linear chirp scaling algorithm to monostatic and bistatic systems, the latter of course being the moving transmitter, stationary receiver configuration. Synchronisation and other performance aspects of the bistatic radar are not considered, while the processing method is confirmed with simulations. Sanz-Marcos [62] derives a geometry-dependent scaling factor that may be applied to the azimuth compression function of the chirp scaling algorithm in order to achieve correct image formation. Two processors are compared, a monostatic algorithm adapted for one-way slant range variation (a narrow-focus processor) and the modified chirp scaling algorithm (with the scaling factor). The latter experiences aberrations in the simulated images for target heights approaching that of the receiver (it is narrow-focus with respect to target height) and also for scenes of greater than 1km in dimension. Sanz-Marcos [63] describes a back-propagation method of processing SAR imagery that is computationally intensive, but gives accurate results based on a flat earth assumption or using a digital elevation map of the scene.

Global satellite navigation systems are examined again in He [64], in terms of a power

budget analysis for GPS, GLONASS and Galileo together with an airborne or ground receiver. They conclude that the detection performance is restricted in the airborne receiver case but more favourable for the ground receiver due to the potentially longer integration times. Applications such as UAVs for search and rescue and disaster damage assessment, as well as interferometric radar are identified.

The last part of this review covers some related research on clutter cancellation, the Envisat satellite, and some methods of countering passive radar systems. The topic of clutter cancellation to facilitate moving target detection has been examined for radar systems in other bodies of research, although only for those bistatic arrangements that use a moving transmitter and receiver. Some examples include: Coe [65] (use of DPCA with an airborne radar), Nohara [66] (comparison of DPCA applied to space-based and airborne radars), Klemm [67] (an investigation into the application of STAP to airborne bistatic radar configurations) and Melvin [68] (research on bistatic STAP performance for airborne radars). Research specific to the ASAR instrument on Envisat itself may also be found in the open literature. General information on the instrument and mission may be found on the Envisat website [69], or in Rosich [70]. Much of the research has considered monostatic data for environmental applications. However, multistatic and bistatic radar using the ASAR instrument has also been examined. Moccia [71] considers using the ASAR as a non-cooperative transmitter in conjunction with a passive receiver on another satellite, while Moccia [72] looks at the more specific case of using a BISSAT (see reference [51]) with ASAR. Krieger [73] examines the possibility of multistatic spaceborne interferometry by use of several microsatellites and ASAR. In addition the paper by Olsen [74], despite using the instrument in monostatic operation, is of interest as it considers the possibility of detection of fishing vessels at sea. The last three papers included in this review describe methods of countering such parasitic receivers. Antonik [75] combines an interferometer with the host radar in order to provide 'coherent reference denial', while Ertan [76] evaluates different techniques to achieve the same aim, all based around the concept of radiating a 'masking signal' in addition to the original radar transmission. It is found that Costas codes provide the best performance of all the waveforms investigated. Griffiths [77] presents several techniques to prevent a radar being used as a non-cooperative transmitter. Again, a masking signal is radiated in addition to the radar signal. This is orthogonal in the coding and spatial domain and it is also found that Costas codes offer the best performance and

flexibility.

2.2.4 Summary

From the previous sections, it is noted that the bistatic configuration brings with it an increase in operational complexity and a performance that is dependent on the geometry. Time and phase synchronisation are both important, but the latter is especially so in bistatic SAR image formation. Bistatic SAR processing is inherently complex in the general case, there being a trade-off between approximations and computational burden, although several algorithms have been introduced that produce accurate results, albeit for specific imaging configurations. The use of a non-cooperative illuminator further complicates the situation by removing from our control the choice of transmitter parameters, and so a compromise must be made between such factors as transmit power, waveform, illuminator availability and illumination area. The effect of direct signal interference must also be taken into account as this will impact upon receiver performance. However, the motivation behind the use of such 'illuminators of opportunity' is clear: a low-cost passive receiver system may adequately perform surveillance and remain undetected, and indeed, may give additional information on targets that a conventional monostatic radar cannot as a result of the different scattering processes involved.

Relatively little research has been published on the specific geometry considered in this thesis. The only experimental study is that by Cazzani [10], which uses a TV broadcasting satellite in near-geosynchronous orbit, although this differs from the investigated system in terms of platform orbit, availability, transmit frequency, power density and transmit waveform. Other research is theoretical in nature, and typically concentrates on different illuminators such as the future Galileo navigation system satellites. The signal processing techniques, for example in Sanz-Marcos [63], are of relevance, and confirm the reduced complexity of the situation when compared to the general bistatic SAR geometry. In addition, the application of a clutter suppression technique such as DPCA to this particular bistatic configuration has not previously been considered, although the motion induced clutter Doppler spread makes its use absolutely necessary for moving target detection.

Chapter 3

Bistatic SAR theory

3.1 Bistatic radar

3.1.1 Introduction

3.1.2 Geometry and range relationships

A bistatic radar system uses antennae at different locations for transmission and reception, compared to the monostatic case, where a single antenna is used for transmitting and receiving (Willis [11] p.2). A diagram of the bistatic geometry is given below:

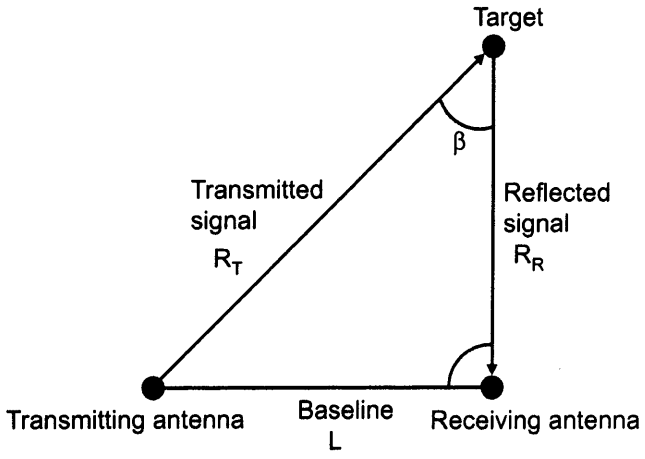

Figure 3-1: Bistatic radar geometry

The geometry defines the bistatic triangle which lies in the bistatic plane, illustrated above. In contrast with a monostatic radar system for which the transmitted signal follows

the same path while travelling to and after being reflected by the target, there are two signal paths; one for the transmitted and one for the reflected signal. The target range is measured by the range sum $R_T + R_R$, and the bistatic angle β is defined at the target. An isorange contour is a contour of constant range sum and is described by an ellipse in the bistatic plane, with the two foci being the transmitter and receiver locations, see Figure 3-2. In order to determine the range sum $R_T + R_R$ and so target location, the direct method

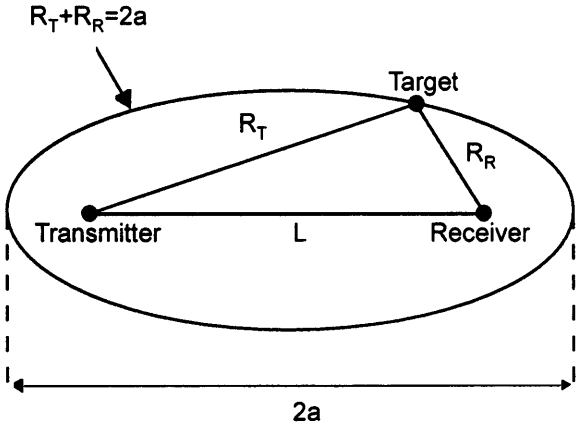

Figure 3-2: Isorange contour

may be used which relies on knowledge of the baseline length L. The relevant equation is:

$$R_T + R_R = c\Delta T_{rt} + L$$

where ΔT_{rt} is the time interval between reception of the transmitted pulse at the receiver (which has travelled along the baseline) and reception of the reflected pulse.

The bistatic radar equation, used for evaluating detection performance is given by:

$$(R_T R_R)_{max} = \left(\frac{P_T G_T G_R \lambda^2 \sigma_B F_T^2 F_R^2}{4\pi^3 k T_s B_n (S/N)_{min} L_T L_R} \right)^{1/2} \tag{3.1}$$

where

R_T = transmitter-to-target range

R_R= receiver-to-target range

P_T = transmitter power output

G_T= transmitting antenna power gain

G_R = receiving antenna power gain

λ = wavelength

σ_B = bistatic radar target cross section

F_T = pattern propagation factor for transmitter-to-target path

F_R = pattern propagation factor for target-to-receiver path

k = Boltzmann's constant

T_s = receiving system noise temperature

B_n= noise bandwidth of receiver predetection filter

$(S/N)_{min}$= signal-to-noise ratio required for detection

L_T= transmitting system losses (not included in any of the other terms)

L_R= receiving system losses (not included in any of the other terms)

κ= bistatic maximum range product

The corresponding monostatic radar equation has the parameters $\sigma_M = \sigma_B$ (monostatic RCS equal to bistatic RCS), $L_M = L_T L_R$ (monostatic system loss), $R_M^4 = R_T^2 R_R^2$ (monostatic maximum range). The range equation as given above applies for all types of waveforms, although a more specific form applicable to synthetic aperture radar processing follows in the next Chapter. It is instructive to use this equation to plot contours of constant signal-to-noise ratio, or ovals of Cassini, in the bistatic plane, as illustrated in Figure 3-3. Here the transmitter is denoted Tx and the receiver Rx. The isorange contours do not follow the same path as the ovals of Cassini, as a result the SNR along an isorange contour will vary. There are three different operating regions for the radar system:

1. Receiver-centred region, $L > 2\sqrt{\kappa}$ and $R_T >> R_R$
2. Transmitter-centred region, $L > 2\sqrt{\kappa}$ and $R_R >> R_T$
3. Cosite region, $L < 2\sqrt{\kappa}$

3.1.3 Bistatic Doppler Shift

Bistatic Doppler shift is proportional to the rate of change of the bistatic range sum:

$$f_B = \frac{1}{\lambda}\left[\frac{d}{dt}(R_T + R_R)\right] = \frac{1}{\lambda}\left[\frac{dR_T}{dt} + \frac{dR_R}{dt}\right]$$

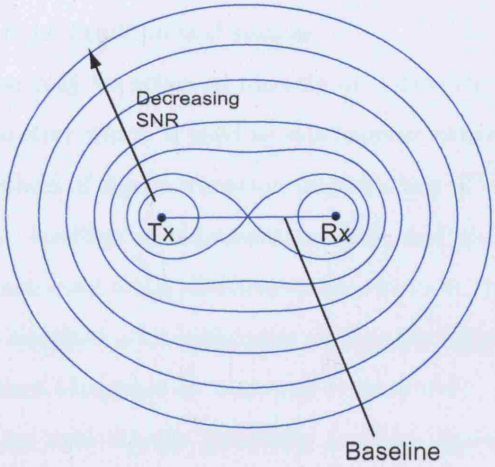

Figure 3-3: Example ovals of Cassini

3.1.4 Target Cross Section

The radar cross section (or RCS) of a target is a measure of the amount of energy it scatters towards the radar receiver. The bistatic RCS is a function of both aspect angle and bistatic angle and so is inherently more complex than the monostatic case. The bistatic angle defines three regions of bistatic RCS, pseudomonostatic, bistatic and forward-scatter. The extent of the bistatic angle for each region is dependent on the type of target illuminated. For a large sphere, the pseudomonostatic region is defined for β up to approximately 100 degrees, while the forward-scatter region starts when β approaches 180 degrees. For complex targets such as the elements within the urban scenes imaged, it is generally found that the bistatic RCS region begins for much smaller bistatic angles, and results in an RCS that differs from the equivalent monostatic value. The scattering cross section per unit area, σ^0, for distributed as opposed to discrete targets, will be defined later in this Chapter, as it is useful in the analysis of SAR images.

3.1.5 Time and Phase Synchronisation

Synchronisation is required between the transmitter and receiver. This is divided into time synchronisation (for range measurements) and phase synchronisation (in order to establish coherency between transmitted and received signals). The general techniques are now

described, the Predicted System Performance Chapter gives more details, including the specific method used for the experimental system.

Time synchronisation may be achieved directly or indirectly. In the former, a signal is received from the transmitter which is used to synchronise either a clock or local oscillator in the receiver. The method of signal reception includes line of sight transmission between transmitter and receiver, landline, communications link, and via a scatterer path. Indirect synchronisation can be achieved using identical stable clocks at the transmitter and receiver (which are periodically matched with each other or another source) as well as with the use of a random code sequence broadcast by a second transmitter.

Phase synchronisation uses similar methods, and can again be separated into direct and indirect. Direct phase synchronisation may be achieved via land line, communications link or at RF. Indirectly this involves using matched local oscillators in transmitter and receiver, and performing a periodic direct synchronisation to counter long-term drift. The phase stability requirements are the same as for a coherent monostatic radar.

3.2 Monostatic SAR

3.2.1 Overview

A Synthetic Aperture Radar (SAR) system generates an image, or more generally a radar backscatter map by scanning the surface of the earth. There are various SAR imaging geometries, including stripmap, spotlight, and scan. Only stripmap SAR will be considered as it is this mode of operation that is used with the bistatic system. The radar is mounted on a moving platform (either airborne or spaceborne) and typically points in a sideways direction relative to the platform motion. Pulses are transmitted at the pulse repetition frequency, each of which illuminates an area of the ground. Echoes are received by the same antenna. As a result of the pulsed transmission and platform motion, the scene is scanned across the swath and in the along-track direction. These two mechanisms can be treated as being mutually independent, with the across-track direction referred to as slant range and the along-track direction as azimuth.

3.2.2 Stripmap SAR theory of operation

The basic theory of stripmap SAR operation for a satellite platform is now given; the notation and analysis used is from Schreier [78] and Cumming [79]. The following diagram, Figure 3-4, shows the SAR data acquisition geometry.

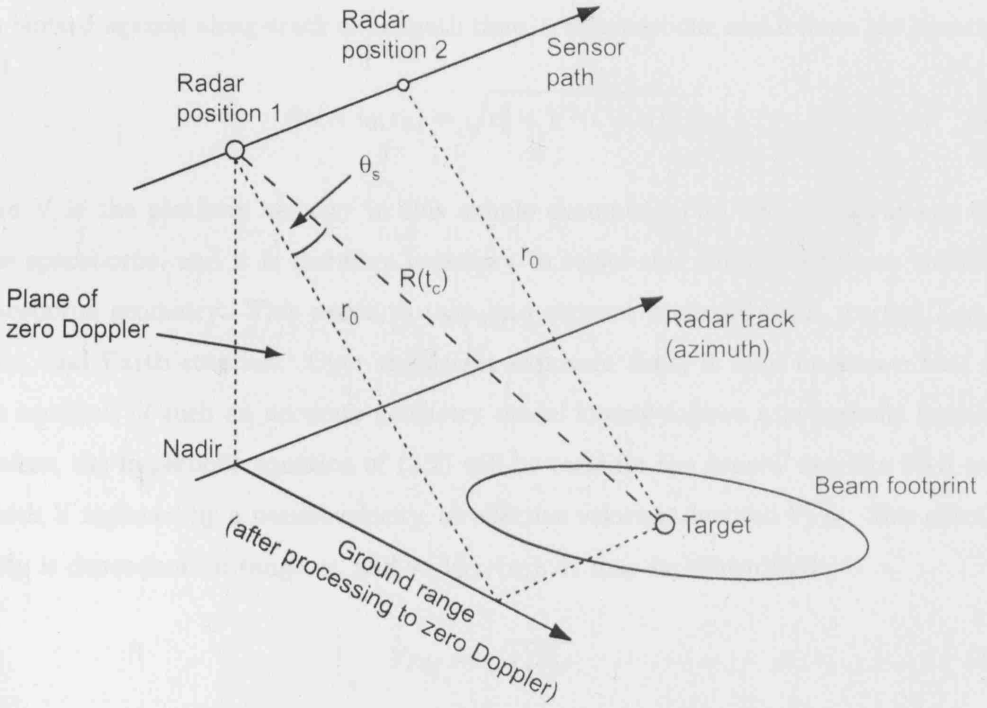

Figure 3-4: SAR data acquisition geometry

Several definitions are now made. The target is a hypothetical point scatterer. The beam footprint is the projection of the antenna beam (within the -3dB limits) onto the ground. The nadir is the point on the Earth's surface that is directly below the sensor, while the radar track is the path of the nadir. The platform velocity is denoted by V_s, and the beam velocity by V_{gr} (the velocity of the zero Doppler line). It is assumed that Earth centred rotating coordinates are used, and so V_s will therefore vary along the platform orbit. The azimuth direction is aligned with the platform velocity vector. The slant range from target to sensor varies with time, with the range of closest approach being r_0, corresponding to zero Doppler time t_0, and the range at which the target is within the antenna beam centre being $R(t_c)$. It follows that the beam centre crossing time is $t_0 + t_c$, defined as the difference

between zero Doppler time and the time when the beam centreline crosses the target. The squint angle θ_s is the angle that the zero Doppler line makes with the slant range vector.

First, a simplified version of the general geometry of Figure 3-4 is considered, where the flight path is assumed straight and level with a flat Earth's surface. As the sensor platform moves along its straight path, the slant range to the point scatterer varies. This variation, when plotted against along-track or azimuth time, t, is hyperbolic and follows the equation,

$$R(t - t_0; r_0) = \sqrt{r_0^2 + V^2(t - t_0)^2} \tag{3.2}$$

Where V is the platform velocity in this simple example. The ASAR instrument is of course spaceborne, and it is therefore necessary to relate this simple rectilinear model to a spaceborne geometry. This needs to take into account a curved orbit, curved Earth's surface, and Earth rotation. Over the target exposure time, it may be shown that the range equation of such an accurate geometry model closely follows a hyperbolic function. Therefore, the hyperbolic equation of (3.2) will be valid for the general satellite SAR case, but with V replaced by a pseudovelocity, or effective velocity, denoted V_{FM}. This effective velocity is dependent on range r_0, and so $V_{FM}(r_0)$. It may be shown that:

$$V_{FM} \approx \sqrt{V_s V_{gr}} \tag{3.3}$$

The derivation of Equation (3.3) may be found in Appendix A.

As the range of the target varies with azimuth time, this leads to a phenomenon known as range cell migration in the received data, which complicates the processing, see Figure 3-5, below. The received pulses from a point target are placed in memory, the arrangement of which may be viewed as a two-dimensional array, with one dimension representing azimuth (or pulse number) and the other range (or delay). If the change in range of the pulses over the total processing time is greater than one sample, then this range cell migration must be accounted for in the SAR processing.

Now consider the diagram given in Figure 3.2.2, which compares the realistic curved earth geometry with the rectilinear approximation. Earth-centred rotating coordinates are assumed. The axes move with the rotation of the earth, and so points on the Earth's surface appear fixed over time. The use of this coordinate system alters the platform velocity, for example a nearly circular orbit will translate to a spiral around the Earth. Earth rotation

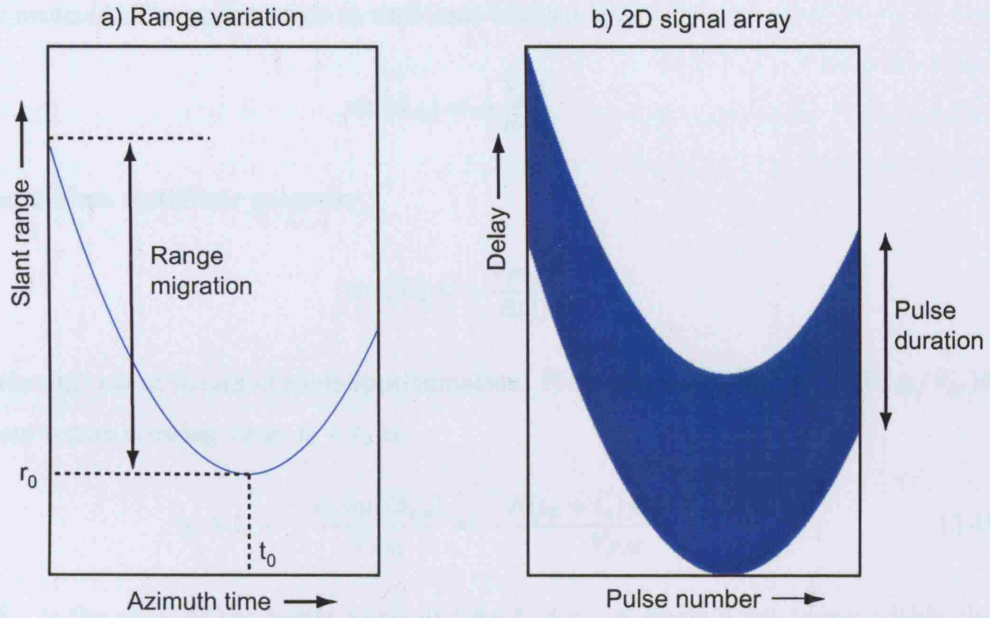

Figure 3-5: Illustration of range cell migration

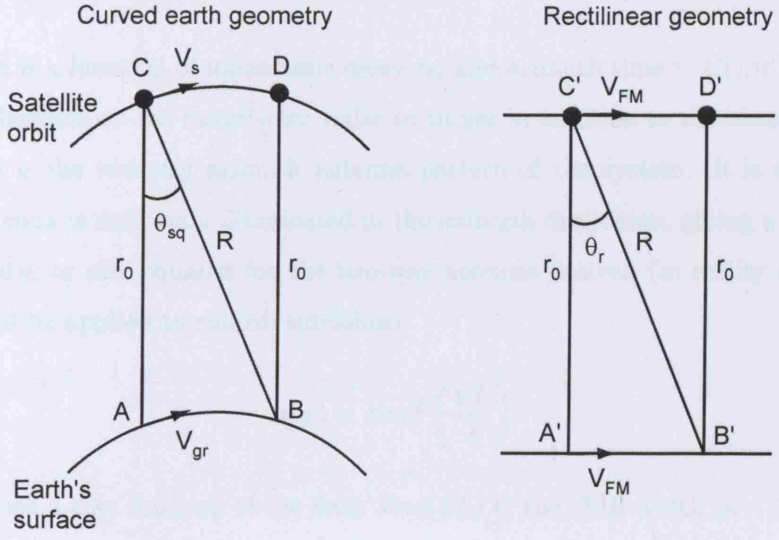

Figure 3-6: Curved satellite SAR geometry and equivalent rectilinear model

has the effect in this coordinate system of producing a squint angle (θ_{sq} or θ_r) or non-zero

Doppler centroid. The squint angle in each case is given by,

$$\sin(\theta_{sq}) = -\frac{V_{gr}t}{R(t)}$$

In the equivalent rectilinear geometry,

$$\sin(\theta_r) = -\frac{V_{FM}t}{R(t)}$$

This is through use of the small angle approximation. From Cumming [79], $\theta_r = (V_{FM}/V_{gr})\theta_{sq}$. The beam centre crossing time, $t_0 + t_c$ is:

$$t_0 + t_c = -\frac{r_0 \tan(\theta_{r,c})}{V_{FM}} = -\frac{R(t_0 + t_c)\sin(\theta_{r,c})}{V_{FM}} \tag{3.4}$$

where $\theta_{r,c}$ is the value of the squint angle at time $t_0 + t_c$. A single point target within the imaged scene produces a point scatterer response,

$$\hat{h}_a(\tau_m, t - t_0; r_0) = C(r_0)a(V(t - t_0 - t_c)/r_0)g(\tau_m - 2R(t - t_0; r_0)/c)\exp(j\phi(t - t_0; r_0)) \tag{3.5}$$

The response is a function of monostatic delay τ_m and azimuth time t. C() is an amplitude factor that depends on the range from radar to target in addition to the antenna elevation pattern. a() is the two-way azimuth antenna pattern of the system. It is assumed that the SAR antenna is uniformly illuminated in the azimuth dimension, giving a sinc function for the pattern, or sinc squared for the two-way antenna pattern (in reality some form of weighting will be applied to control sidelobes).

$$a(\psi) = sinc^2\left(\frac{\psi L}{\lambda}\right)$$

Note that given a sinc function of the form $sinc(\psi L/\lambda)$ the -3dB width is,

$$\psi_{3dB} = 0.886\frac{\lambda}{L}$$

This may be used to calculate the exposure time,

$$T_{3dB} = \psi_{3dB}\frac{R(t_0 + t_c)}{V_{gr}\cos(\theta_{r,c})} = 0.886\frac{\lambda R(t_0 + t_c)}{V_{gr}L\cos(\theta_{r,c})} \tag{3.6}$$

The projection of the azimuth beamwidth onto the ground has been lengthened by the $1/\cos(\theta_{r,c})$ factor. g() gives the echo signal envelope and illustrates the concept of range migration in that the echo arrives back at the radar with a delay dependent upon azimuth time, through the term $2R(t-t_0;r_0)/c$. The final phase term in (3.5) is dependent upon the phase history of the scatterer:

$$\phi = -\frac{4\pi R(t-t_0;r_0)}{\lambda} \tag{3.7}$$

The instantaneous (or Doppler) frequency is,

$$f_D = \frac{1}{2\pi}\frac{d\phi}{dt} = -\frac{2}{\lambda}\frac{V_{FM}^2}{R(t-t_0;r_0)}(t-t_0) \tag{3.8}$$

This Doppler frequency shift is dependent on the target's position within the beam, effectively providing a second coordinate for identifying targets (in addition to slant range r), and is the observation that led to the development of SAR. The time at which the point scatterer passes through the beam centre is $t = t_0 + t_c$, for which the Doppler frequency is equal to the Doppler centroid,

$$f_{DC} = -\frac{2}{\lambda}\frac{V_{FM}^2}{R(t=t_0+t_c)}(t_c) = \frac{2V_{FM}}{\lambda}sin(\theta_{r,c}) = \frac{2V_s\sin(\theta_{sq,c})}{\lambda} \tag{3.9}$$

while the Doppler rate is given by,

$$f_R = \frac{df_D}{dt} = \frac{2V_{FM}^2\cos^3(\theta_{r,c})}{\lambda r_0} \tag{3.10}$$

As before, the extra subscript c for the squint angle indicates its value is that at the beam centre crossing time $t_0 + t_c$.

The frequency change while the target is within the -3dB width of the transmit beam is the azimuth bandwidth,

$$B_a = 0.886\frac{2V_s\cos(\theta_{r,c})}{L} \tag{3.11}$$

The equations for range and azimuth resolution may now be given. Assuming transmission of a linear frequency modulated pulse, the achievable range resolution is:

$$\delta R = 0.886\frac{c\gamma_r}{2B} \tag{3.12}$$

This has assumed a rectangular pulse, which if matched filtered would give a sinc function response. A window may be applied to the matched filter pulse replica during processing, yielding lower sidelobes and a broader mainlobe. The factor γ_r accounts for this mainlobe broadening. For a resolution along the ground δR_g the relationship to use is:

$$\delta R_g = \frac{\delta R}{\sin(\theta_i)}$$

where θ_i is the angle of incidence of the radar beam with the ground.

The azimuth resolution may be taken to be 0.886 times the reciprocal of the azimuth bandwidth. This is assuming that the azimuth antenna pattern is represented by a rectangle function over the -6dB (two-way) bandwidth. The resolution in azimuth time is,

$$\delta t = \frac{0.886}{B_a}$$

The azimuth resolution is therefore:

$$\delta x = 0.886 \frac{V_{gr} \cos(\theta_{r,c}) \gamma_a}{B_a} = \frac{L}{2} \frac{V_{gr}}{V_s} \gamma_a \tag{3.13}$$

Again, it has been assumed that some form of window is applied to the matched filter replica during processing, giving a mainlobe broadening accounted for by γ_a.

The preceding analysis assumed that the full azimuth bandwidth was used for processing, resulting in the theoretical azimuth resolution limit, approximately equal to half the antenna physical size in the azimuth dimension. In reality, a fraction of the full bandwidth is used in order to control azimuth ambiguities in the resultant image and so the achievable resolution will be coarser than this theoretical ideal. In the next section monostatic SAR processing algorithms will be examined, including the chirp scaling algorithm. Bistatic SAR will then be considered, with the analysis presented here adapted to the moving transmitter, stationary receiver configuration in order to illustrate the differences in resolution achievable.

3.2.3 SAR signal processing

Imaging algorithms overview

All SAR image processing algorithms approximate the 2D correlation kernel required for image formation by taking advantage of fast frequency domain correlation techniques. The range-Doppler algorithm, with and without secondary range compression, is widely used and has formed the basis of many precision SAR processors since its introduction over 25 years ago - Wu [80]. It is an efficient technique, although requires interpolation to account for range cell migration correction (RCMC), and with secondary range compression cannot easily incorporate an azimuth frequency dependence. The interpolation is a potentially computationally intensive operation and an accuracy/performance trade-off must be made.

A new class of algorithms introduced in the last 15 years are the wavenumber domain or $\omega - k$ processors. These are based on seismic wave equation formulations and use the full 2D Fourier spectrum of the data. Most operations are achieved with a phase multiply in the 2D frequency domain, although an interpolation is still required for RCMC in the range-Doppler domain or Stolt change of variables in the 2D frequency domain. Examples of algorithms that fall within this class include the wavenumber domain algorithm and the CCRS wavenumber domain algorithm, see Bamler [81], and the range migration algorithm, Cafforio [82].

The Chirp Scaling algorithm was first described in 1992, in Raney [83]. It is an efficient formulation that does not require any interpolation, and in common with the wavenumber domain algorithms is naturally phase preserving (important for such applications as interferometry). It requires only complex multiplies and Fourier transforms to implement, and is suitable for wide-swath, large-beamwidth and large-squint systems. As a result of its accuracy and computational efficiency it was chosen as the basis for the processing used in this investigation. The next section gives a more detailed description of the algorithm itself, with the Signal Processing and Simulations Chapter dealing with extensions to this basic formulation to enable processing of bistatic SAR images.

The chirp scaling algorithm

The description in this section is based on information given in Raney [83]. The following flowchart summarises the operations performed on raw data input to the processor. The

phase functions will be examined in more detail in the Image Processing section later in this thesis.

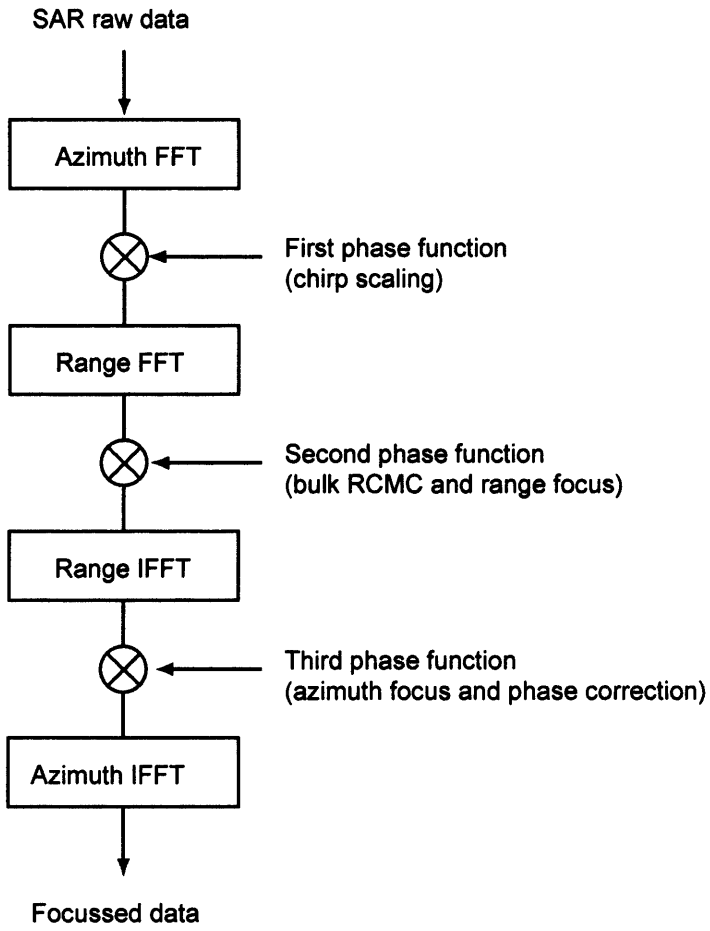

Figure 3-7: Chirp scaling algorithm flow diagram

- **First phase function:** the data array is multiplied by a chirp scaling function whose phase is chosen so that the range migration phase term of each and every scatterer is equalised to that of the reference range
- **Second phase function:** phase multiplication by a second function which has the effect of range cell migration correction and range focus (including secondary range compression)
- **Third phase function:** the third phase function focuses the signal in azimuth and removes a phase residual produced by the original chirp scaling phase multiply

3.3 Bistatic SAR: the general case

3.3.1 Introduction

A general bistatic SAR system is visualised in the next figure, composed of two moving platforms imaging a common area on the ground.

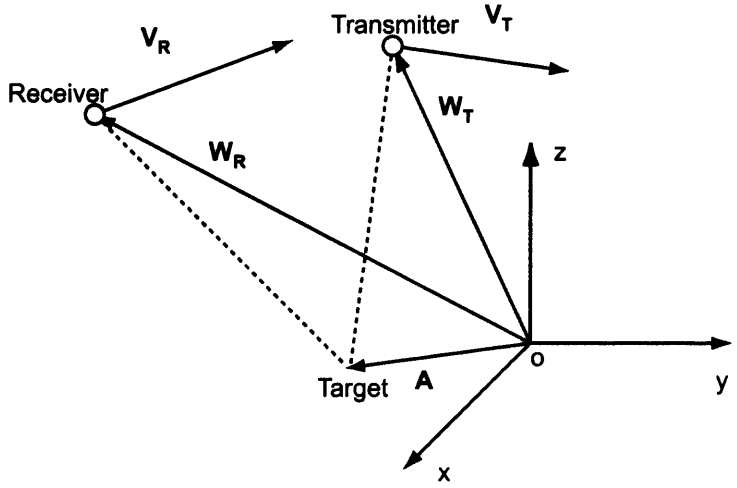

Figure 3-8: General geometry of bistatic SAR

The situation is complicated by the fact that both transmitter and receiver are moving, and with different velocities. The coordinate system used has its origin in the centre of the target area, and x-y plane defining the surface of the earth. The transmitter and receiver have position vectors $\mathbf{W_T}$ and $\mathbf{W_R}$, and velocity vectors $\mathbf{V_T}$ and $\mathbf{V_R}$ respectively, while the target point is defined by the position vector $\mathbf{A}$.

3.3.2 Signal processing options

As mentioned before, the changing geometry complicates matters and as a result it is difficult to derive a general bistatic SAR processor. Those processors discussed in the open literature are typically based on some form of monostatic processing method, and apply to a specific platform flight situation. These flight configurations may be classed, in order of increasing complexity as (based partly on information in Ender [31]):

1. Monostatic configuration: given here as the simplest special case

2. Moving transmitter, stationary receiver configuration: a slightly more complicated special case

3. Tandem configuration: transmitter and receiver travelling with constant and equal velocities along the same path

4. Translationally invariant configuration: transmitter and receiver have the same velocity

5. Constant velocity configuration: both platforms have some constant, but differing, velocity

6. General configuration: as illustrated in figure 3-8

Some examples of bistatic processing algorithms include the bistatic range-Doppler and bistatic back-projection, Ender [31], and the bistatic range migration processor Ender [84], all of which operate with data from a translationally invariant configuration. 'Rocca's smile operator', given in D'Aria [33], is actually a pre-processing technique for bistatic raw data that allows a monostatic SAR processor to be subsequently used, and is used with the tandem arrangement. The special case of stationary receiver, moving transmitter shall be considered in more detail at the end of this Chapter.

3.3.3 Bistatic SAR performance measures

Detection: the range equation for bistatic SAR

The bistatic range equation as described earlier in this Chapter may be applied to a bistatic SAR system. An improvement factor I_{SAR} is included to account for the processing gain due to matched filtering at the receiver:

$$SNR = \left(\frac{P_T G_T G_R \lambda^2 \sigma_B F_T^2 F_R^2}{4\pi^3 k T_s B_n R_T^2 R_R^2 L_T L_R} \right) I_{SAR}$$

With,

$$I_{SAR} = \left(\frac{\tau_i}{\tau_o} \right) N_p$$

Where τ_i is the input pulse length (to the matched filter), τ_o is the output length, after compression, and N_p is the total number of pulses in azimuth that are integrated during

processing. L_p is a processing loss term that accounts for windowing function loss and pattern loss - due to the antenna pattern variation over azimuth time.

Thus far the radar equation has been defined in terms of σ, the radar cross section for a discrete, or point target. It is useful for a SAR system to instead use a scattering cross section per unit area, or scattering coefficient, σ^0. This is because the targets imaged are typically distributed (as opposed to discrete), in other words they extend over some area dA of the ground. Each area dA within the image is assigned a local, or mean value of σ, and σ^0 is then obtained by,

$$\sigma^0 = \frac{\sigma}{dA}$$

As a result σ^0 describes the ratio of the received backscattered energy to that of an isotropic scatterer (one that scatters energy uniformly in all directions). It is a normalised dimensionless number, expressed in decibels, and is a function of incidence angle, polarisation and the properties of the scattering surface. Scene elements have a σ^0 value associated with them (a characteristic of clutter), while the same regions in the radar image have an effective σ^0 value associated with them. For example, the effective σ^0 values observed in a monostatic SAR image vary from the noise level of the data to some maximum value. If the maximum is greater than 0dB, this means that energy for that region has been reflected preferentially back to the radar, for example by specular reflections.

The noise equivalent σ^0, or σ^0_{ne}, can be calculated for a bistatic SAR with,

$$\sigma^0_{ne} = \frac{4\pi^3 k T_s B_n R_T^2 R_R^2 L_T L_R}{P_T G_T G_R \lambda^2 F_T^2 F_R^2 I_{SAR} dA} \tag{3.14}$$

The area dA, assumed to correspond to the resolution cell size, will vary over the image (resolution in such a bistatic SAR system is spatially variant, as shall be discussed in the ambiguity function section). Therefore the noise equivalent σ^0 will also vary. Analysing the bistatic images in terms of σ^0_{ne} would have to consider different regions, each of which would be assumed to have an approximately constant resolution cell size. This would be useful with a calibrated system - one for which the return signal amplitude may be matched to a real value of bistatic radar cross section in the scene.

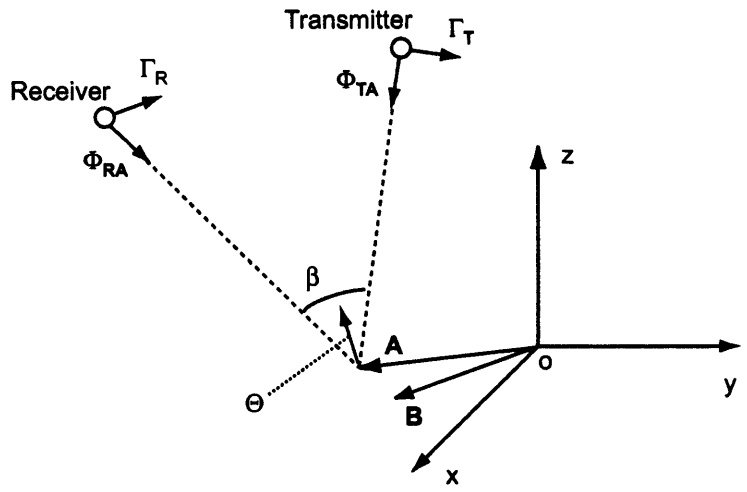

Figure 3-9: Bistatic SAR geometry showing various terms in the Ambiguity Function

Image quality: resolution

The general equation for the bistatic ambiguity function in this situation, and referring to Figure 3-9, is as follows, from Zeng [85]:

$$\chi(\mathbf{A},\mathbf{B}) \approx \exp\left(j2\pi\frac{[\mathbf{\Phi}_{TA}+\mathbf{\Phi}_{RA}]^T(\mathbf{B}-\mathbf{A})}{\lambda}\right) p\left(\frac{2\cos(\beta/2)\mathbf{\Theta}^T(\mathbf{B}-\mathbf{A})}{c}\right) m_A\left(\frac{2\omega_E\mathbf{\Xi}^T(\mathbf{B}-\mathbf{A})}{\lambda}\right) \tag{3.15}$$

A is a vector defining a target point within the target area

B is a point close to **A**

$p(\tau_d)$ is the inverse Fourier transform of P(f), the power spectrum of the transmitted signal

$\mathbf{\Phi}_{TA}$ is a unit vector in the direction transmitter to A

$\mathbf{\Phi}_{RA}$ is a unit vector in the direction receiver to B

β is the bistatic angle, as defined earlier

$\mathbf{\Theta}$ is a unit vector along the bisector of the bistatic angle

$m_A(f_d)$ is the inverse Fourier transform of $\overline{M}_A(u)$, the normalised received signal magnitude pattern, which depends on the antenna radiation patterns and the system geometry.

Finally, ω_E and $\mathbf{\Xi}$ are the modulus and unit vector of

$$\frac{\omega_{TA}\mathbf{\Gamma}_T + \omega_{RA}\mathbf{\Gamma}_R}{2}$$

Where ω_{TA} and ω_{RA} are the angular speeds of transmitter and receiver respectively. $\mathbf{\Gamma}_T$

and Γ_R are unit vectors in the direction of motion of the two platforms. ω_E and Ξ are the equivalent angular speed and motion directions, as a monostatic SAR with these motion parameters will produce an equivalent azimuth resolution.

The bistatic ambiguity function (A.F.) differs from the monostatic equivalent in two important ways. First, the bistatic ambiguity function depends on the transmitted signal, the antenna radiation patterns and the platform trajectories - in the monostatic case the ambiguity function is dependent on the form of the transmitted signal only. Second, the bistatic A.F. is defined in spatial coordinates, compared to the monostatic where it is defined on the delay/Doppler plane. The ambiguity function as described above has two resolution directions, range in the direction of Θ, and azimuth, which is in the Ξ direction. It should be noted that these resolution directions define a resolution plane, which is not necessarily coincident with the surface of the earth and which varies depending on the target position in space. The range and azimuth resolutions, as given in Zeng [85], are:

$$\delta_r = \frac{c\delta_\tau}{\cos(\beta/2)}$$

$$\delta_a = \frac{\lambda\delta_D}{2\omega_E}$$

The system's delay and Doppler resolution cells are given by δ_τ and δ_D, which are the -3dB widths of $p(\tau_d)$ and $m_A(f_d)$ respectively.

Image quality: PSLR and ISLR

The peak sidelobe ratio (PSLR) and integrated sidelobe ratio (ISLR) are both measures of SAR image quality. PSLR is defined as the ratio of the peak value of the highest sidelobe to the mainlobe peak, and gives an indication of the ability of a strong scatterer to mask a weaker scatterer when their physical separation is small. ISLR is the ratio of integrated sidelobe energy to mainlobe energy, and is used as a measure for local image contrast. The calculation of one-dimensional ISLR is found by integrating the power of the impulse response (magnitude squared) over two different regions. The two regions are the mainlobe, and the entire impulse response, with powers P_{main} and P_{total} respectively. The 1D ISLR

is:

$$ISLR = 10\log_{10}\left\{\frac{P_{total} - P_{main}}{P_{main}}\right\} \tag{3.16}$$

3.4 Bistatic SAR: moving transmitter, stationary receiver

3.4.1 Overview and theory of operation

This is the specific case investigated in this thesis, and is substantially simpler in concept and operation than the general case already considered. The geometry is illustrated in Figure 3-10. Given stripmap SAR operation, this is very similar to the monostatic SAR

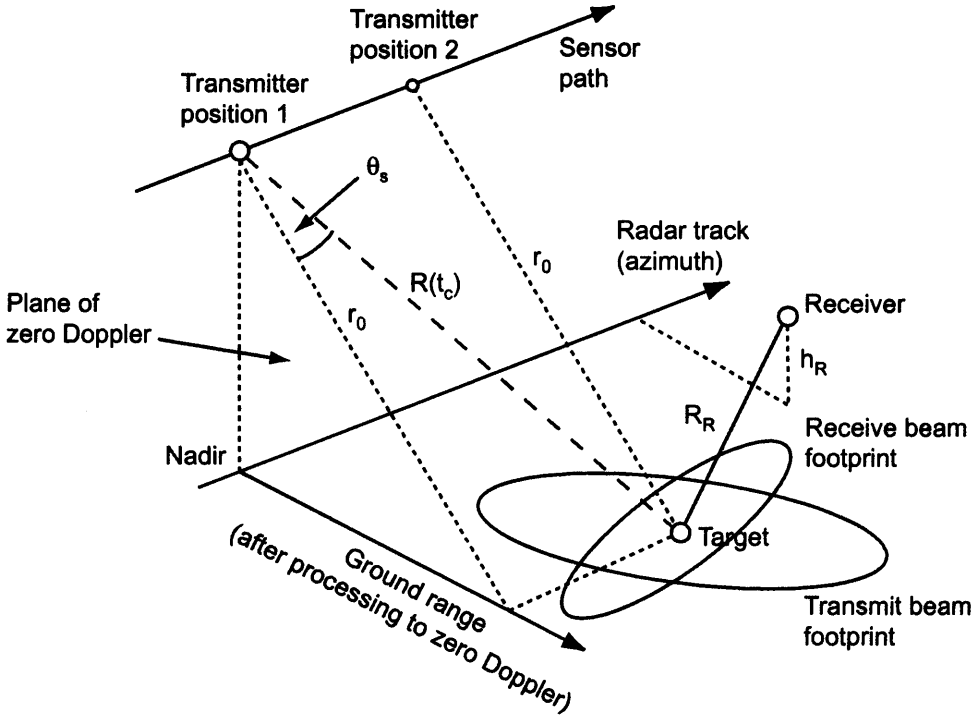

Figure 3-10: Data acquisition geometry for the bistatic SAR configuration investigated

already considered. Indeed, the same assumptions as detailed in the previous stripmap SAR theory of operation section are made for the following analysis, with an equivalent rectilinear geometry for the spaceborne SAR. The receiver is at some location with height h_R above the Earth's surface and slant range R_R from the point target considered. This point scatterer, assumed to be within the overlap of transmit and receive beams, has the

same range variation relative to the transmit platform as given in Equation (3.2), with the addition of a constant R_R to form a bistatic range sum,

$$R_b = R(t - t_0; r_0) + R_R = \sqrt{r_0^2 + V_{FM}(r_0)^2(t - t_0)^2} + R_R \tag{3.17}$$

The point scatterer response is now,

$$h_b(\tau_b, t-t_0; r_0) = C_b(r_0)a_T(V(t-t_0-t_c)/r_0)a_R g(\tau-(R(t-t_0; r_0)+R_R)/c)\exp(j\phi_b(t-t_0; r_0)) \tag{3.18}$$

This is a function of bistatic delay, $\tau_b = R_b/c$, and azimuth time t. The azimuth antenna pattern is now represented by the one-way pattern due to the transmitter, a_T, a function of platform velocity and target range, multiplied by the contribution from the receiver antenna, a_R, which is a constant for a given scatterer. Maintaining consistency with the monostatic discussion, a_T is represented by a sinc function:

$$a_T(\psi_b) = sinc(\frac{\psi_b L}{\lambda})$$

With -3dB width,

$$\psi_{b,3dB} = \frac{0.885\lambda}{L}$$

The exposure time of a target is therefore identical to the monostatic equation of (3.6). The azimuth phase is now:

$$\phi_b = -\frac{2\pi(R(t - t_0; r_0) + R_R)}{\lambda} \tag{3.19}$$

While the corresponding Doppler frequency may be expressed as,

$$f_{D,b} = \frac{1}{2\pi}\frac{d\phi_b}{dt} = -\frac{1}{\lambda}\frac{V_{FM}^2}{R(t - t_0; r_0)}(t - t_0) \tag{3.20}$$

This is half of the monostatic Doppler frequency given in Equation (3.8), as a result of the now one-way instead of two-way varying path length from transmitter to target. The bistatic Doppler centroid and Doppler rate are therefore half as large as their monostatic

counterparts:

$$f_{DC,b} = -\frac{1}{\lambda}\frac{V_{FM}^2}{R(t=t_0+t_c)}t_c = \frac{V_{FM}sin(\theta_{r,c})}{\lambda} = \frac{V_s \sin(\theta_{sq,c})}{\lambda} \tag{3.21}$$

$$f_{R,b} = \frac{df_{D,b}}{dt} = \frac{V_{FM}^2 \cos^3(\theta_{r,c})}{\lambda r_0} \tag{3.22}$$

The bistatic azimuth bandwidth is,

$$B_{a,b} = 0.886\frac{V_s \cos(\theta_{r,c})}{L} \tag{3.23}$$

Again, half as large as the monostatic equivalent, which will give a coarser azimuth resolution performance. The bistatic range resolution is:

$$\delta R_b = 0.886\frac{c\gamma_r}{B\cos(\beta/2)} \tag{3.24}$$

This is a function of bistatic angle β, reaching a minimum value of twice the corresponding monostatic resolution for $\beta = 0^0$. The geometry dependence may be explained with the aid of Figure 3-11. On the left, a monostatic radar system is shown with isorange circles

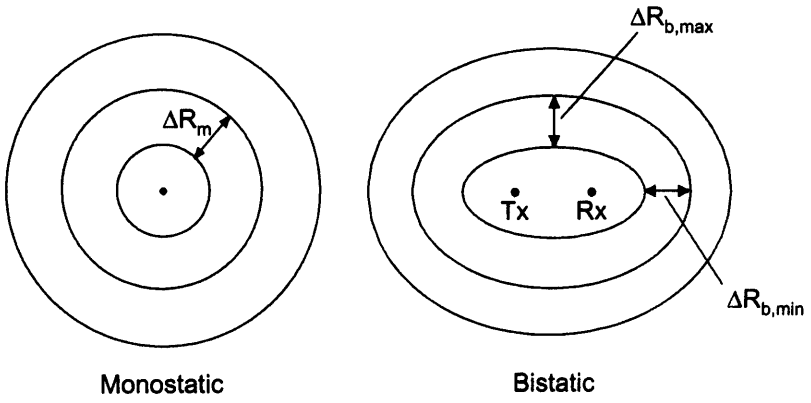

Figure 3-11: Comparison of monostatic and bistatic range resolution cells

(contours of constant monostatic range), all separated by the monostatic range resolution δR_m. On the right is illustrated a bistatic radar and isorange contours, which are separated by the bistatic range resolution δR_b. The bistatic resolution for a given isorange contour depends on the target's position on that contour and is therefore a function of bistatic angle

β, with minimum and maximum values parallel and perpendicular to the baseline, as shown in Figure 3-11.

The azimuth resolution is again taken to be 0.886 times the reciprocal of the azimuth bandwidth:

$$\delta x_b = 0.886 \frac{V_{gr} \cos(\theta_{r,c}) \gamma_a}{B_{a,b}} = L \frac{V_{gr}}{V_s} \gamma_a \tag{3.25}$$

The bistatic azimuth resolution is therefore twice that of the monostatic system (or in other words a factor of two poorer), assuming a rectangular antenna pattern variation over the azimuth bandwidth. As was mentioned in the monostatic SAR section, the actual azimuth bandwidth processed will be less than the full amount given by equations (3.11) and (3.23) in order to control azimuth ambiguities, and so achieve a desired azimuth ambiguity to signal ratio, or AASR. In the general case of using such a processing bandwidth $B_{p,b}$, the azimuth resolution becomes:

$$\delta x_b = 0.886 \frac{V_{gr} \cos(\theta_{r,c}) \gamma_a}{B_{p,b}} \tag{3.26}$$

3.4.2 Monostatic and bistatic processing parameters comparison

Some of the main processing parameters for the monostatic and bistatic SAR systems are summarised in Table 3.1.

Parameter	Monostatic	Bistatic
Slant range resolution	$0.886\frac{c\gamma_r}{2B}$	$0.886\frac{c\gamma_r}{B\cos(\beta/2)}$
Exposure time	$0.886\frac{\lambda R(t_0+t_c)}{V_{gr}L\cos(\theta_{r,c})}$	
Doppler centroid	$\frac{2V_{FM}}{\lambda}\sin(\theta_{r,c})$	$\frac{V_{FM}}{\lambda}\sin(\theta_{r,c})$
Doppler rate	$\frac{2V_{FM}^2\cos^3(\theta_{r,c})}{\lambda r_0}$	$\frac{V_{FM}^2\cos^3(\theta_{r,c})}{\lambda r_0}$
Azimuth bandwidth	$0.886\frac{2V_s\cos(\theta_{r,c})}{L}$	$0.886\frac{V_s\cos(\theta_{r,c})}{L}$
Azimuth resolution	$\frac{L}{2}\frac{V_{gr}}{V_s}\gamma_a$	$L\frac{V_{gr}}{V_s}\gamma_a$

Table 3.1: Comparison between processing parameters for the monostatic and bistatic SAR systems

3.4.3 Signal processing

As has been already mentioned in the literature review, four processing methods have been introduced for this bistatic arrangement, non-linear chirp scaling from Wong [61], narrow-focus and modified chirp scaling from Sanz-Marcos [62], and the bistatic back-propagation algorithm given in Sanz-Marcos [62]. Of all four, the narrow focus algorithm is the simplest to implement, although the least able to compensate for the bistatic geometry. A reference point will be perfectly focussed, although defocussing in the azimuth (or along-track with respect to the transmitter) direction will occur for targets displaced in azimuth

from the reference position. The factor of two change in the varying path length between the equivalent monostatic and bistatic systems may be used to alter the CSA phase functions. The exact details of the processor implementation may be found in Chapter Seven.

3.4.4 Ambiguity function

The generalised ambiguity function presented earlier is applied to this specific geometry. It is assumed that the receiver is stationary and situated at some point on the z axis, with the x-y plane defining the locally flat surface of the earth. The origin of this coordinate system is directly below the receiver. The transmitter is moving with a constant velocity in the x direction. The expressions for range and azimuth resolution given in Zeng [85] are:

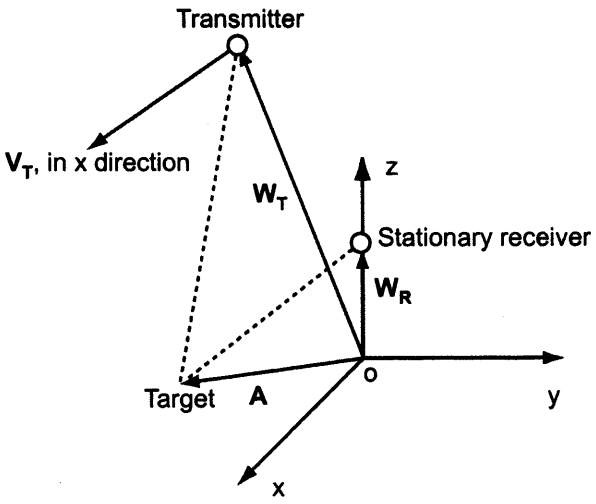

Figure 3-12: Specific geometry of bistatic SAR with moving transmit platform and stationary receiver

$$\delta_r = \frac{c\delta_\tau}{\cos(\beta/2)} \tag{3.27}$$

$$\delta_a = \frac{\lambda\delta_D}{\omega_{TA}} \tag{3.28}$$

Starting with range, the δ_τ term is the system's delay resolution, for a rectangular transmitted pulse of bandwidth B this equates to:

$$\delta_\tau = \frac{0.886}{B}$$

The range resolution is therefore the same as δR_b from (3.24). In the subsequent sections of this document the resolution given in (3.24) shall be used.

Azimuth resolution is now considered. The normalised received signal magnitude pattern, used in the derivation of this resolution in Zeng [85], is given by:

$$\overline{M}_A(t) = \frac{G_T(\mathbf{A},t)G_R(\mathbf{A})}{\int G_T(\mathbf{A},t)G_R(\mathbf{A})dt}$$

For a given target point **A**, the receiver antenna pattern G_R does not vary with azimuth time t, it is simply a constant in the above equation. $\overline{M}_A(t)$ is therefore represented by the normalised transmitter antenna pattern, which is assumed to have a sinc response. The actual antenna pattern over the full azimuth bandwidth may again be represented by a rectangle function. As a result, δ_D, the half-power width of $m_A(f_D)$ is related to δ_t, the half-power width of the normalised antenna pattern, $\overline{M}_A(t)$, by the following:

$$\delta_D = 0.886\frac{\gamma_a}{\delta_t}$$

The angular speed of the transmitter $\omega_{TA} = \frac{V_s}{r_0}$, while δ_t is the same as the exposure time.

$$\delta_a = 0.886\frac{\lambda r_0}{V_s T_{3dB}}$$

Compared to the azimuth resolution δx_b of (3.25), this formulation assumes the squint angle is zero and does not take into account the mainlobe broadening factor γ_a. In order to maintain accuracy of the results, the Equations (3.25) and (3.26) shall be used for the azimuth resolution calculations.

To be able to compare resolutions achieved in the experimental bistatic images and those given by this theory, it is necessary to know the resolutions on the ground plane, but in the East and North directions, instead of x and y. In order to calculate resolution δ_Ω along some direction Ω, the following equation must be solved,

$$p\left(\frac{\delta_\Omega cos(\theta_\tau)cos(\beta/2)}{c}\right) m_A\left(\frac{\delta_\Omega cos(\theta_a)\omega_E}{\lambda}\right) = \frac{1}{\sqrt{2}} \tag{3.29}$$

θ_τ is the angle between the Ω direction and Θ, while θ_a is the angle between the Ω direction and Ξ. The functions $p(\tau_d)$ and $m_A(f_D)$ are assumed to be sinc in shape. The solution to

the previous equation (3.29) is found numerically, using the method outlined in Zeng [85]. A variable change is made from δ_Ω to x.

$$x = \delta_\Omega B \cos(\beta/2) \cos(\theta_\tau)/c$$

The equation to be solved is therefore simplified, giving,

$$sinc(\pi x) sinc(h\pi x) = \frac{1}{\sqrt{2}}$$

Where,

$$h = \frac{cT_a\omega_E \cos(\theta_a)}{\lambda B \cos(\beta/2) \cos(\theta_\tau)}$$

The term T_a in the numerator represents the azimuth time over which the data is processed in order to give a bandwidth B_p and generate the azimuth resolution of δx_b. The relationship between these terms is based upon the approximate relationship:

$$B_p = |f_{R,b}|T_a$$

This is assuming that the Doppler frequency variation is linear with azimuth time, an acceptable approximation for the short time durations and small amounts of squint (Cumming [79]). The Doppler rate $f_{R,b}$ is calculated for zero squint and so,

$$f_{R,b} = \frac{V_{FM}^2}{\lambda r_0}$$

The range and azimuth resolutions δR_b and δx_b used in the solution of Equation (3.29) will include the effect of any amplitude weighting applied. The position and velocity of the satellite will be obtained from orbit simulations, which are described in more detail in the Signal Processing and Simulations Chapter. A simple transformation will be used to convert the Earth-centred rotating Cartesian coordinate system to that shown in Figure 3-12.

In addition to the resolution values thus calculated, the ground resolution cell size will also be given. This is calculated with the following equation, from Zeng [85].

$$S_g = 0.794 \frac{\delta x_b \delta R_b}{\sin\alpha \cos\eta_g} \tag{3.30}$$

The sinc function assumption results in the 0.794 factor. Angle α is between the bistatic bisector vector and the azimuth direction vector. The angle η_g is between the basic plane (containing the bistatic bisector vector and azimuth direction vector) and the ground plane.

Chapter 4

Experimental system

4.1 Introduction

This Chapter describes the bistatic radar system, beginning with the 'illuminator of opportunity', ASAR, and then describing the receiver in terms of the design procedure and hardware configuration. There is the potential for using the system to perform (in addition to SAR imaging) bistatic displaced phase centre antenna experiments (although these experiments were not performed as part of the research programme) - these are covered in more detail in the Future Work section of the final Chapter. An extra channel would be required in this case. A distinction is therefore made throughout the rest of this text between the receiver channel configurations for imaging and that for DPCA, as the antennas and IF subsystems are different for each. Details of the characterisation of the SAR imaging receiver, including antenna radiation patterns and receiver channel frequency responses are given in this Chapter.

4.2 Illuminator

4.2.1 The Envisat Satellite

Envisat is a polar orbiting earth observation satellite, launched by the European Space Agency in March 2002 for the purpose of earth science research and the monitoring of environmental and climate changes. The spacecraft flies in a sun-synchronous polar orbit with an altitude of 800km and a repeat cycle of 35 days. The main orbital parameters are given in the table below.

Orbits per Day	14 11/35
Repeat Cycle (days)	35
Orbits in Cycle	501
Orbit Period (min)	100.59
MLST at descending node	10:00
Inclination (deg)	98.55
Semi-Major Axis [Orbit Radius] (km)	7159.5
Orbit Velocity (km/s)	7.45
Mean Altitude (km)	799.8
Orbital Altitude Range (km)	780 - 820

Table 4.1: Envisat orbit details

4.2.2 The ASAR Instrument

Overview

The satellite has on board nine different instruments to perform such tasks as: sea state forecasting, monitoring of atmospheric variables (temperature, pressure, cloud top height etc), monitoring of ocean colour, ice sheet characteristics and large-scale vegetation processes. Only one instrument is of relevance, the Advanced Synthetic Aperture Radar (ASAR), a C-band high resolution wide swath imaging radar which has five distinct modes of operation: image, alternating polarisation, wide swath, global monitoring and wave mode.

Figure 4-1: Photograph of Envisat illustrating the ASAR array

Image mode is chosen for the experimental investigation as this corresponds to high resolution stripmap SAR data acquisition with VV (vertical transmit and vertical receive) or HH polarisation and seven different swaths. Stripmap SAR imaging has been discussed in the previous Chapter on SAR theory, where a diagram of the imaging geometry may be found.

Image mode parameters

Some details of the ASAR antenna and image mode transmitted signal parameters are shown in Table 4.2. The image mode physical swath parameters now follow. This includes

Antenna	1.3m × 10m phased array
Transmitted signal	Linear frequency modulated pulse
Centre frequency/GHz	5.331
Pulse length/μs	21.3 - 27.2 (dependent on swath)
Bandwidth/MHz	16
Pulse repetition frequency/Hz	1652-2081 (dependent on swath)
Transmit power (peak)/W	1365

Table 4.2: ASAR antenna and image mode transmitted signal parameters

the calculation of ground or beam velocity V_{gr}, which is produced with the method presented in Appendix A. V_{gr}, the ground velocity of the radar beam, may be calculated assuming a locally spherical Earth and a circular orbit. This approximation applies to beam zero Doppler pointing. In summary, the beam incidence angles at scene centre for the various swaths, from the Envisat website [69], are used to calculate angles of depression of the antenna beam. Given knowledge of the satellite height above the Earth's surface and the local Earth radius enables calculation of the slant range for each depression angle. This information is then used to produce ground ranges and the angles subtended at the spherical earth centre, denoted by β_e. The ground velocity is calculated with:

$$V_{gr} = \frac{R_e V_s}{R_e + h} \cos(\beta_e)$$

Where R_e is the Earth radius, assumed to be equal to 6364.550km. This value was calculated for a central London position on the Earth's surface using the coordinate conversion equations detailed in the National GPS Network website [86]. V_s is the satellite velocity, given a value of 7450m/s, and h is the satellite altitude, assumed to be equal to 800km, both values are taken from Table 4.1. The Envisat website [69] contains information on

Image swath	Swath width/km	Incidence angle range/degrees	Slant range to scene centre/km	Ground velocity/m/s
IS1	105	15.0 - 22.9	838	6610
IS2	105	19.2 - 26.7	859	6610
IS3	82	26.0 - 31.4	896	6610
IS4	88	31.0 - 36.3	937	6600
IS5	64	35.8 - 39.4	975	6600
IS6	70	39.1 - 42.8	1010	6590
IS7	56	42.5 - 45.2	1050	6580

Table 4.3: ASAR image mode swath physical parameters

the directivities, pulse lengths, and pulse repetition frequencies for each of the swaths. It is useful to calculate from the directivity and physical dimensions some values for the half-power beamwidths (HPBW) in the slant range and azimuth directions. From Kraus [87], the directivity of a rectangular array is:

$$D_{ra} \simeq \frac{41000\epsilon_M}{B_b\phi_{r,3dB}\phi_{az,3dB}}$$

Where ϵ_M is the beam efficiency (typically 0.7), B_b is the pattern factor (equal to 1 for uniform field distribution over the aperture), $\phi_{r,3dB}$ is the slant range half-power beamwidth and $\phi_{az,3dB}$ is the azimuth half-power beamwidth, both in degrees. The equation for the beamwidths is given in Mailloux [88]:

$$HPBW = \frac{0.886B_b\lambda}{L}$$

Where L is the dimension of the array in the plane considered. The beamwidth equation may be substituted into the equation for directivity in order to calculate B_b for each swath. From this and the values for directivity, the respective beamwidths can be produced, given in Table 4.4.

Bistatic SAR processing parameters: example values

Referring to the Theory Chapter and the summary table of SAR processing parameters 3.1, it is possible to calculate some representative values for the bistatic case based on the information already given in this section. This includes the exposure time, and range cell migration over this time duration, given in Table 6.1. The range cell migration values are

Image swath	Directivity/dBi	Slant range HPBW/degrees	Azimuth HPBW/degrees	Transmit signal pulse length/μs	Transmit signal prf/Hz
IS1	42.97	2.90	0.377	26.6560	1709.48
IS2	41.42	3.27	0.425	27.1776	1652.42
IS3	42.34	3.05	0.396	21.3456	2112.59
IS4	43.21	2.85	0.371	26.6039	1694.99
IS5	44.08	2.67	0.347	21.4498	2080.55
IS6	43.45	2.80	0.364	26.3436	1705.23
IS7	46.22	2.26	0.294	21.6059	2067.12

Table 4.4: ASAR image mode antenna and transmit signal parameters for different swaths

Image swath	Range cell migration/m	Exposure time/s	Doppler rate/Hz/s	Azimuth resolution/m
IS1	11.7	0.632	1040	8.88
IS2	12.0	0.648	1020	8.87
IS3	12.6	0.676	976	8.87
IS4	13.1	0.708	933	8.86
IS5	13.7	0.737	896	8.85
IS6	14.2	0.767	861	8.85
IS7	14.8	0.800	828	8.84

Table 4.5: Bistatic azimuth processing parameters for the various image swaths of ASAR

all above 11m. The signal is sampled at 100MHz in the receiver, and so this range migration represents 3.7 samples. The SAR processor will therefore have to compensate for range cell migration. As can be seen from the exposure time values calculated, the ASAR beam will sweep over a potential bistatic imaging area in a very small amount of time. Given the orbit repeat cycle of 35 days, this transmitter is obviously not ideal for constant or frequent imaging, and this also highlights the need for accurate timing information with regard to a satellite pass. A non-cooperative receiver would require some reliable means of detecting when the illumination of the local area by ASAR has started.

Azimuth resolution is calculated assuming the full azimuth bandwidth of $B_{a,b} = 0.886\frac{V_s}{L} = 660Hz$ is used.

In addition, the Envisat satellite uses yaw steering for the ASAR beam. The satellite attitude is controlled to make the Doppler centroid lie within the range $+/-f_p/2$, where f_p is the pulse repetition frequency. The generation of typical values for the system assuming zero Doppler pointing of the beam will be reasonably accurate as a result. The advantages of using yaw steering include simpler processing, as a result of less range cell migration.

4.2.3 Monostatic data products

Several data products are available for image mode acquisitions, organised into a hierarchal product scheme depending on the level of processing and corrections applied,

Raw data: Data as received directly from the satellite

Level 0: The lowest level product that may be ordered, reformatted and time ordered data.

Level 1B: The most common data product, data has been converted to engineering units, auxiliary data has been separated from the measurements and some calibrations have been applied.

Level 2: Higher level processing on the level 1B product has been applied that converts engineering units into geophysical quantities.

The product used in this investigation is the Level 1B Single Look Complex Image, which is a phase-preserved image generated using the range-Doppler algorithm and to which only a small number of corrections and interpolations have been applied.

Product name	Nominal resolution/m (range × azimuth)	Nominal pixel spacing	Equivalent number of looks
Image Mode Single-Look Complex	9 × 6	natural	1

Table 4.6: Specifications for the ASAR SLC data product

4.3 Receiver System Overview

The receiver has multiple channels, each of which includes an antenna and a single conversion superheterodyne receiver. The outputs of these channels are digitised using an analog-to-digital conversion (ADC) board in a desktop PC. The conversion board chosen for this task is a Parsec PM480 [89], which has two inputs each sampling at a maximum frequency of 100MHz and with a resolution of 14 bits.

4.3.1 Two-channel Receiver

The minimum number of channels used is two, one for the direct or along the baseline signal from the satellite, used for synchronisation purposes, and another for the reflected signal

from the imaged scene or targets.

4.3.2 Three-channel Receiver

There is one synchronisation signal channel and two reflected signal channels in the proposed design. The two reflected signal channels have intermediate frequencies displaced by 20MHz through the use of different local oscillator frequencies. They are then sampled together and separated by filtering in Matlab at a later stage. The use of a single ADC card for the sampling of all three channels avoids the complication of triggering and synchronising two separate cards, perhaps from different manufacturers, and is of course less expensive. Note that the proposed three channel receiver design is given in this document for reference - an experimental investigation with this receiver configuration was not carried out due to time constraints.

4.4 Receiver Design Procedure

4.4.1 Power Calculations

There now follows some basic power calculations, which are meant to illustrate some of the approximate predicted signal levels in the system and the design process adopted in the early stages of the research programme. A more detailed examination of the system loss budget may be found in the Predicted System Performance Chapter. It is useful to calculate a likely value for the thermal noise in the receiver before considering the signal levels. The thermal noise power is,

$$P_n = kT_sB_nF = 1.19 \times 10^{-13}W \equiv -130dBW = -100dBm$$

T_s, the system noise temperature is taken to be 290K, B_n is the noise bandwidth (16MHz) and F is the overall noise figure, taken to be 2dB, a fairly typical value.

Direct signal level

The power density on the Earth's surface for the IS1 and IS7 swaths will be calculated. From Table 4.3, the slant range to swath centre is 838km and 1050km for IS1 and IS7. A transmit power of 1365W and a directivity of 42.97dBi and 46.22dBi, from Table 4.4 (taken

to be equal to the gain of the antenna) means the power density on the earth's surface is for IS1,

$$P_{de,dir} = \frac{P_T G_T}{4\pi R^2} = \frac{1365 \times 19820}{4\pi 838000^2} = 3.07 \times 10^{-6} W/m^2$$

While for IS7,

$$P_{de,dir} = \frac{P_T G_T}{4\pi R^2} = \frac{1365 \times 41880}{4\pi 1050000^2} = 4.13 \times 10^{-6} W/m^2$$

It shall be assumed that the power density for these calculations is equal to the lower value, $3.07 \times 10^{-6} W/m^2$. The direct or synchronisation signal is received in a separate channel as described previously. Assuming a simple rectangular horn antenna is used with an effective aperture of $2.52 \times 10^{-3} m^2$ (or a gain, assuming no loss of 10dBi), the power received will be:

$$P_{r,dir} = 3.07 \times 10^{-6} \times 2.52 \times 10^{-3} = 7.74 \times 10^{-9} W \equiv -81.1 dBW = -51.1 dBm$$

This is well above the likely noise floor, and is therefore an acceptable signal level for detection. The overall gain of the channel used will need to be approximately 50dB.

Reflected signal level

The extent of the earth's surface intercepted by the transmitted signal from ASAR is defined, from Skolnik [90] by the pulse length and the azimuth beamwidth. A fraction of this area is intercepted by the receiver antenna. Assuming that the centre of the target area is 500m from the receiver, which is at a height of 15m above the ground, and given a receiver azimuth and elevation beamwidth of 3^0 (a typical value for the first parabolic antenna used, as will be demonstrated later in this Chapter), the area illuminated by the receiver is calculated as $A_c = 95700 m^2$. The power returned from this section of the ground is $P_c = \sigma^0 A_c P_{de,dir}$, where σ^0 is the radar reflectivity of the surface. From Nathanson [91], a monostatic value for σ^0 of an urban area imaged at C-band is $5 dBm^2$. As the system is bistatic, a more conservative estimate of $\sigma^0 = -10 dBm^2$ shall be assumed. As a result, $P_c = 9570 \times 3.07 \times 10^{-6} = 2.94 \times 10^{-2} W$.

The power density at the receiver due to this reflected signal return is,

$$P_{de,ref} = \frac{P_c}{4\pi 500^2} = 9.35 \times 10^{-9} W/m^2$$

Assuming this signal is received by a parabolic reflector antenna of effective aperture $2.52 \times 10^{-1} m^2$ (equivalent to a gain of 30dBi), the power received is:

$$P_{r,ref} = 9.35 \times 10^{-9} \times 2.52 \times 10^{-1} = 2.36 \times 10^{-9} W = -86.3 dBW = -56.3 dBm$$

This should be detectable using a similar gain to the direct signal channel.
The reflected signal could also result from an air target (for the DPCA experiments). The power reflected in this case would be:

$$P_{air} = 3.07 \times 10^{-6} \times \sigma_{air} = 3.07 \times 10^{-4} W$$

σ_{air} is the aircraft RCS, taken to be $100m^2$, commensurate with a Boeing 747. Assuming the target-receiver separation is 10km, the power density at the receiver is,

$$P_{den} = \frac{3.07 \times 10^{-4}}{4\pi(10000^2)} = 2.44 \times 10^{-13} W/m^2$$

With the parabolic antenna the power received will be:

$$P_r = 2.44 \times 10^{-13} \times 2.52 \times 10^{-1} = 6.16 \times 10^{-14} W \equiv -132 dBW = -102 dBm$$

This is at the noise floor and should be detectable after amplification, matched filtering and coherent integration of pulses.

Direct signal interference

As was discussed in the Literature Review, the presence of the direct signal in the reflected signal channel can be a significant problem in multiple channel bistatic receivers such as the one considered here, as a result of its (potentially) much larger signal power. The method used to reduce the direct signal power received in the reflected channel is the simplest - to point the reflected channel antenna away from the transmitter so that the direct signal is received in the backlobe, or, due to satellite motion, sidelobe of the antenna. In addition,

some anechoic chamber cladding material is also attached to the back of the antenna to provide some further attenuation.

For the simple example considered already, if the direct signal is received in the parabolic antenna mainlobe, the received power will be

$$P_{r,dir} = 3.07 \times 10^{-6} \times 2.52 \times 10^{-1} = 7.74 \times 10^{-7} W \equiv -61.1 dBW = -31.1 dBm$$

Compared to the reflected signal level of -56.2dBm, the direct signal will be 25.1dB greater. The front-to-back ratio (ratio of mainlobe to backlobe) of the parabolic antenna used will need to be at least 25dB, but ideally greater than this. Combined with the anechoic chamber cladding, sufficient direct signal level suppression should be achievable.

4.4.2 Antenna Design and Construction

Two-channel receiver, synchronisation channel

A rectangular horn antenna, constructed in the Department before the start of the PhD programme, was used for the synchronisation channel when conducting SAR imaging experiments. From Balanis [92], the directivity of a horn antenna may be expressed by:

$$D_h = \frac{4\pi A_e}{\lambda} = \frac{4\pi \epsilon_{ap} A_p}{\lambda^2}$$

Where A_e is the effective aperture, A_p is the physical aperture and ϵ_{ap} is the aperture efficiency (equal to A_e/A_p).

The horn antenna used has aperture dimensions 0.049m by 0.095m and so a physical aperture $A_p = 0.049 \times 0.095 = 4.66 \times 10^{-3} m^2$. The aperture efficiency is typically equal to 0.6, and so the directivity is,

$$D_h = \frac{4 \times \pi \times 0.6 \times 4.66 \times 10^{-3}}{\lambda^2} = 11.1 \equiv 10.4 dBi$$

Assuming no loss this value can be taken as the gain of the horn.

The half-power beamwidths in the E and H planes may be calculated with:

$$\theta_{BE} = \frac{56}{a_{E\lambda}}$$

$$\theta_{BH} = \frac{67}{a_{H\lambda}}$$

Where $a_{E\lambda}$ is the E-plane dimension in free space wavelengths, and $a_{H\lambda}$ is the H-plane dimension, similarly normalised. Therefore,

$$\theta_{BE} = \frac{56}{0.049/\lambda} = 64.3^0$$

$$\theta_{BH} = \frac{67}{0.095/\lambda} = 40.0^0$$

The above antenna will be called horn antenna 1. The measured radiation patterns of this antenna follow in Figure 4-2. The measured and theoretical parameters may then be found in Table 4.7.

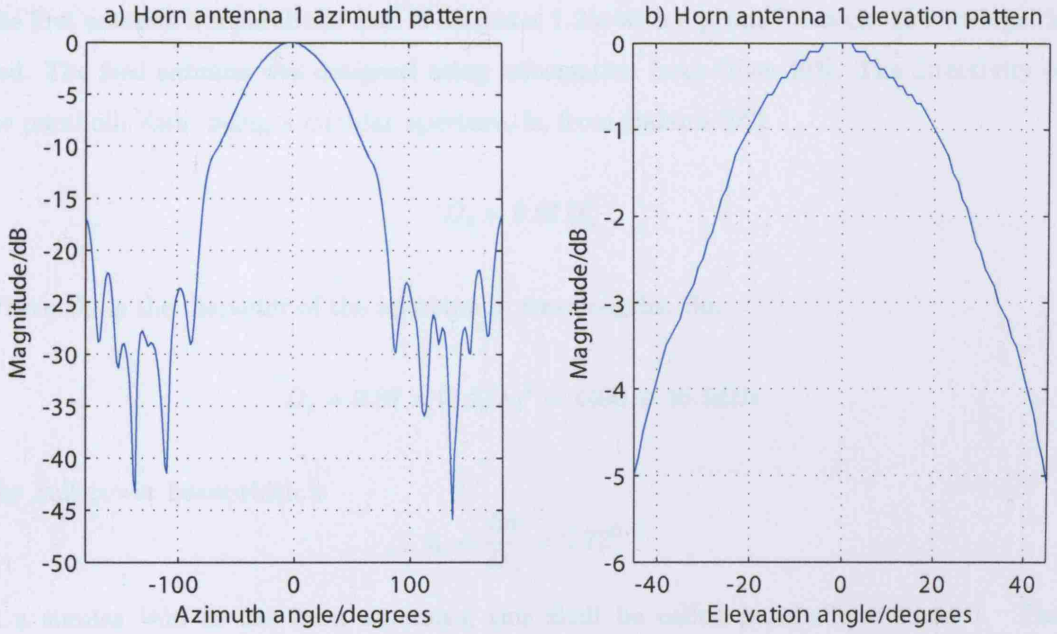

Figure 4-2: Azimuth and elevation radiation patterns of horn antenna 1

Parameter	Theoretical value	Measured value
Gain/dBi	10.4	11.4
Azimuth beamwidth/degrees	40.0	65.9
Elevation beamwidth/degrees	64.3	68.0

Table 4.7: Comparison between theoretical and measured horn antenna 1 parameters

The exposure time of the ASAR beam lasts for less than a second. Over a second the satellite will have travelled 7.45km, which at a range of 800km is equivalent to an angular distance of 0.534^0 (assuming a spherical orbit over that time). The beamwidth of the horn antenna as measured in Table 4.7 means very little attenuation of the direct signal will occur over the exposure time. Coupled with the measured gain (1dB larger than theory predicts), the antenna should be suitable for direct signal detection.

Two-channel receiver, reflected signal channel

A parabolic reflector is used for this channel. Two were constructed, the first is relatively large and bulky and was used solely at a single site in the University. The second, smaller antenna was used when the receiver was transported to alternative sites.
The first antenna is a parabolic dish of diameter 1.2m with a prime focus circular waveguide feed. The feed antenna was designed using information from Olver [93]. The directivity of the parabolic dish, being a circular aperture, is, from Balanis [92]:

$$D_c = 9.87 D_\lambda^2$$

Where D_λ is the diameter of the aperture in wavelengths. So,

$$D_c = 9.87 \times (1.2/\lambda)^2 = 4490 \equiv 36.5 dBi$$

The half-power beamwidth is

$$\theta_c = \frac{58}{D_\lambda} = 2.72^0$$

In a similar vein to the horn antennas, this shall be called parabolic antenna 1. The radiation patterns are shown in Figures 4-3 and 4-4, and a table of compared measured and theoretical parameters in 4.8.

Parameter	Theoretical value	Measured value
Gain/dBi	36.5	35.0
Azimuth beamwidth/degrees	2.72	3.15
Elevation beamwidth/degrees	2.72	3.00

Table 4.8: Comparison between theoretical and measured parabolic antenna 1 parameters

The azimuth radiation pattern is fairly symmetrical, with sidelobes less than -25dB with

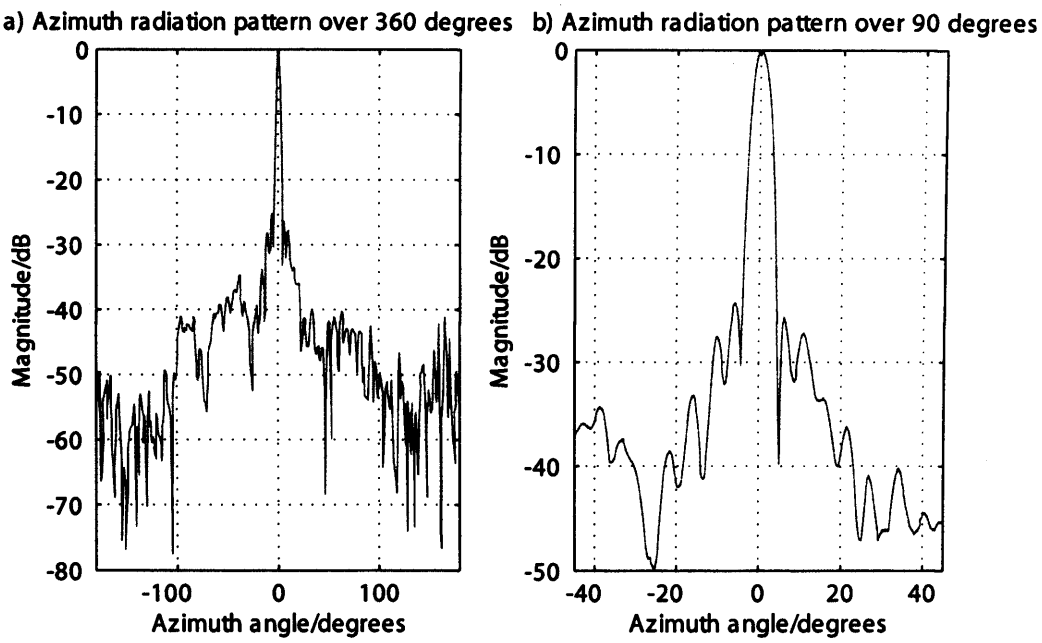

Figure 4-3: Azimuth radiation pattern of parabolic antenna 1

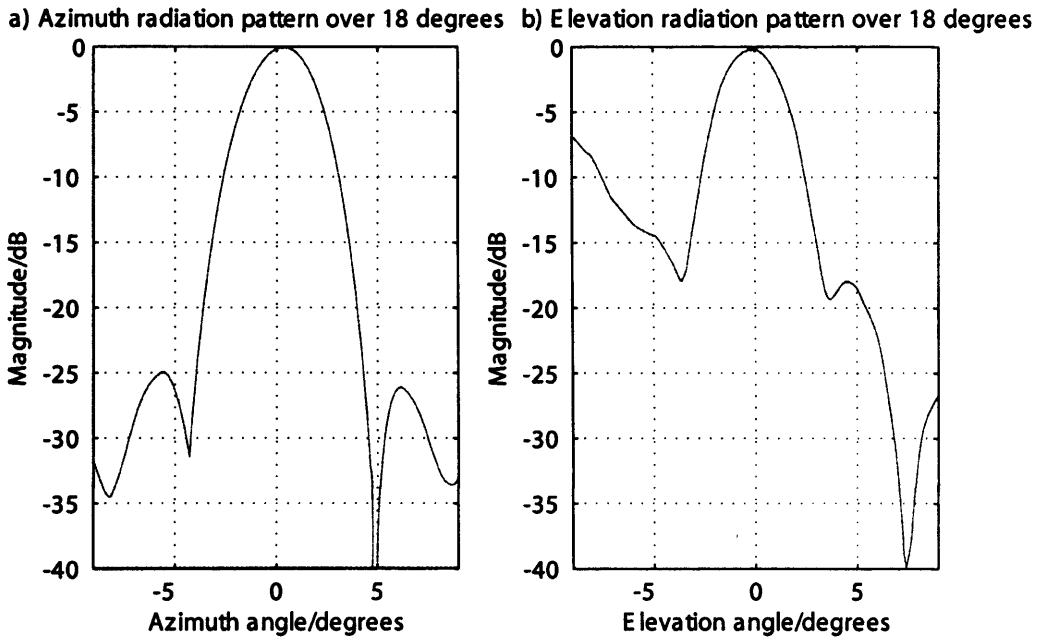

Figure 4-4: Azimuth and elevation radiation patterns of parabolic antenna 1

respect to the mainlobe. The back radiation, as measured in this plane, is more than 40dB down from the mainlobe, which should give adequate direct signal suppression. The mainlobe of the elevation pattern is also quite symmetrical, the distortion for negative elevation angles is due to the field interacting with the mounting structure for the measurements. The measured beamwidths are similar to theory.

The second antenna (parabolic antenna 2) is an offset-fed parabolic reflector, with a long axis length of 0.635m and a short axis length of 0.585m. The computer program, "hdl_ant.exe" from Wade [94] was used to design a feed horn for this reflector. As before, radiation patterns are given, in Figures 4-5 and 4-6, as well as the beamwidths and gain in Table 4.9.

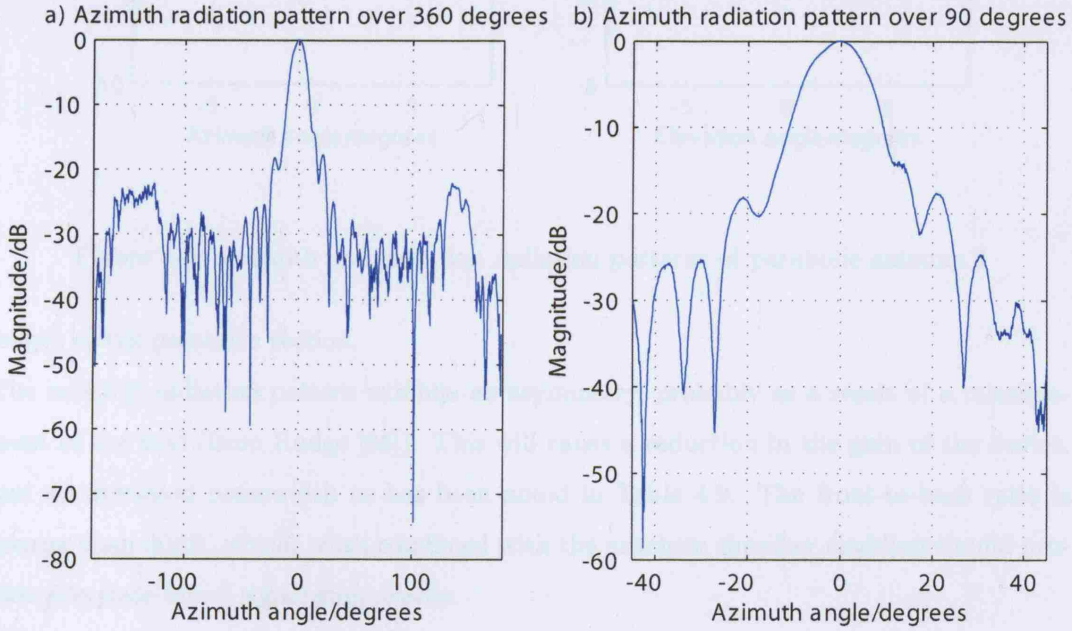

Figure 4-5: Azimuth radiation pattern of parabolic antenna 2

Parameter	Theoretical value	Measured value
Gain/dBi	28.1	23.3
Azimuth beamwidth/degrees	5.58	11.8
Elevation beamwidth/degrees	5.58	13.3

Table 4.9: Comparison between theoretical and measured parabolic antenna 2 parameters

The theoretical gain in Table 4.9 has been calculated given a radiation efficiency of 60%. The theoretical beamwidths assume a circular aperture of diameter 0.585m, the small axis

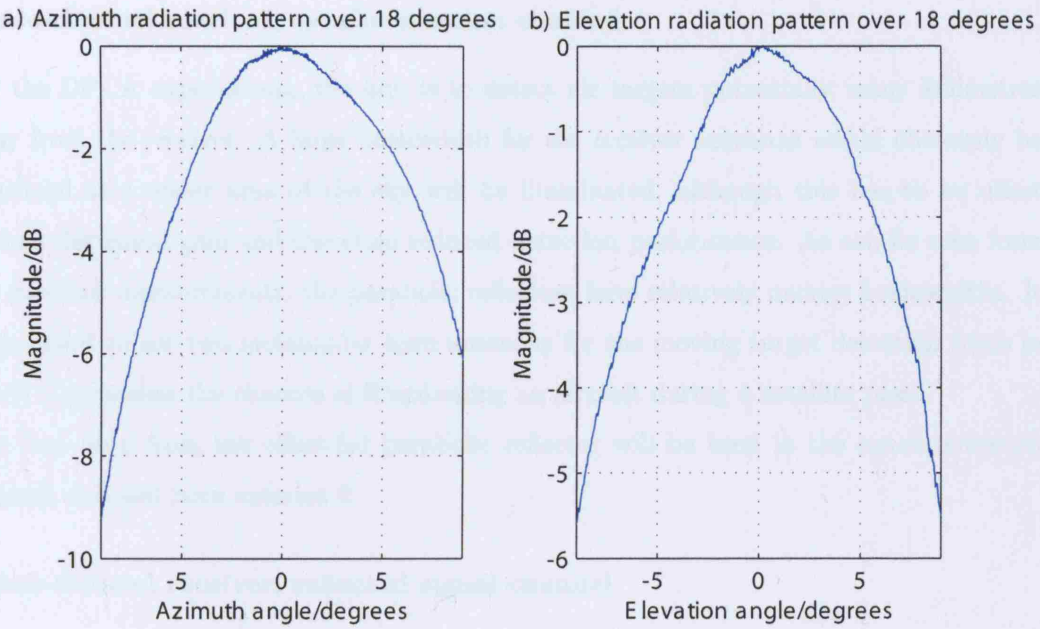

Figure 4-6: Azimuth and elevation radiation patterns of parabolic antenna 2

length of the parabolic section.

The azimuth radiation pattern exhibits an asymmetry, probably as a result of a misalignment of the feed (from Rudge [95]). This will cause a reduction in the gain of the device, and an increased beamwidth as has been noted in Table 4.9. The front-to-back ratio is greater than 30dB, which, when combined with the anechoic chamber cladding should provide adequate direct signal suppression.

Table 4.10 gives the details for the feed horn for parabolic antenna 2, denoted horn antenna 2.

Parameter	Theoretical value	Measured value
Gain/dBi	11.5	12.2
Azimuth beamwidth/degrees	47.7	50.2
Elevation beamwidth/degrees	52.5	77.7

Table 4.10: Comparison between theoretical and measured horn antenna 2 parameters

Photographs of all of the imaging receiver antennas may be found in Appendix B.

Three-channel receiver, synchronisation channel

For the DPCA experiments, the aim is to detect air targets potentially many kilometres away from the receiver. A large beamwidth for the receiver antennas would obviously be beneficial as a wider area of the sky will be illuminated, although this has to be offset against decreased gain and therefore reduced detection performance. As can be seen from the previous measurements, the parabolic reflectors have relatively narrow beamwidths. It is proposed to use two rectangular horn antennas for the moving target detection trials in order to maximise the chances of illuminating an aircraft during a satellite pass.
The feed horn from the offset-fed parabolic reflector will be used in the synchronisation channel, denoted horn antenna 2.

Three-channel receiver, reflected signal channel

Two versions of horn antenna 1 are used in the reflected signal channels.
The reflected signal (from an air or ground target) has a low power density upon reaching the receiver and so the slightly higher gain of horn antenna 1 aids detection. The lower gain of horn antenna 2 will not make a great deal of difference for the direct signal detection, hence its use now in the synchronisation channel.

4.4.3 Receiver design and testing

Each receiver channel consists of a single conversion superheterodyne receiver. From the basic power calculations performed earlier in this Chapter, different levels of gain will need to be used depending upon which signal is to be detected, but apart from this the basic design of each channel remains the same. The sampling frequency (100MHz) and maximum signal level (+/-1.2V pk-pk) of the ADC board are important parameters to consider in the design procedure.

Two-channel receiver design

The receiver is as shown in the Figure 4-7.
The ASAR signal is at a centre frequency of 5.331GHz with a bandwidth of 16MHz. This first passes through a low noise amplifier (marked LNA) and a waveguide filter (identical in both channels) before being mixed down to an intermediate frequency (IF) of 124MHz.

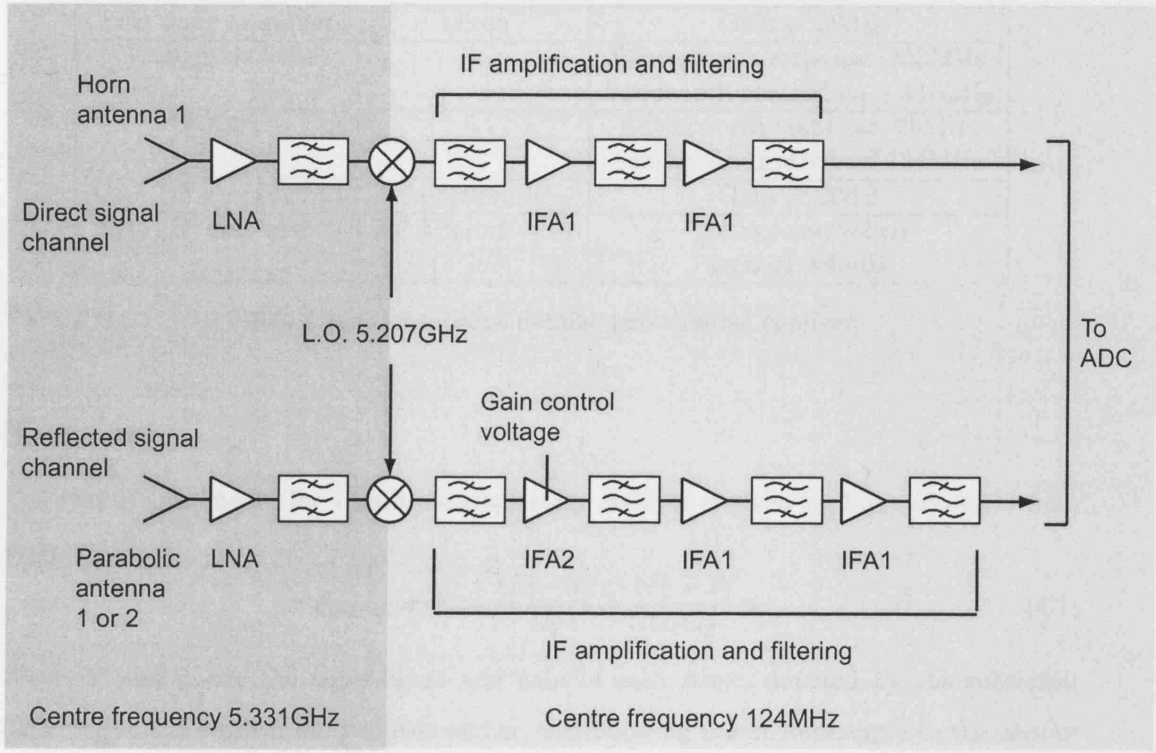

Figure 4-7: Two-channel receiver block diagram

The local oscillator is a Rhode and Schwartz SMP-04, the output of which passes through a power splitter. The subsequent levels of IF amplification are different for each channel, with two different IF amplifiers used, labelled in the previous figure IFA1 and IFA2. The IF bandpass filters are the same in each channel, details of all components are given in Table 4.11. The filters were all constructed in the Department, hence the omission of manufacturer details in Table 4.11. In addition, the IF filters are cascaded in the receiver, giving an overall frequency response with a narrower bandwidth than the 25MHz value for an individual filter.

Component	Manufacturer	Details
Low noise amplifier	Miteq	Gain of 30dB
Waveguide filter	-	Butterworth response, 200MHz bandwidth centred on 5.331GHz
IF filter	-	Butterworth response, 25MHz bandwidth centred on 124MHz
IFA1 (IF amplifier 1)	Minicircuits	Gain of 20dB
IFA2 (IF amplifier 2)	RF Microdevices	Voltage-controlled gain of 0-45dB

Table 4.11: Component details, two-channel receiver

Noise figure

The overall noise figure for a multiple stage stage receiver is given by Equation (4.1) from Skolnik [90].

$$NF_{overall} = F_1 + \frac{(F_2 - 1)}{G_1} + \frac{(F_3 - 1)}{G_1 G_2} + ... \tag{4.1}$$

Where F and G are the noise figure and gain of each stage, denoted by the subscript. Referring to the receiver design given earlier, the following parameters apply to the various components (see Table 4.12).

Component	Noise figure/dB	Gain/dB
Low noise amplifier	1.5	30
Mixer	7	-7
Variable gain IF amplifier	5	20 (typical)
Fixed gain IF amplifier	3.8	20

Table 4.12: Component parameters for reflected signal channel noise figure calculation

For the reflected signal channel used in the imaging receiver, there are five stages, after converting decibel to absolute values this gives an overall noise figure of:

$$NF_{overall} = 1.4125 + \frac{(5.0119 - 1)}{1000} + \frac{(3.1623 - 1)}{1000 \times 0.1995} + \frac{(2.3988 - 1)}{1000 \times 0.1995 \times 100} + \frac{(2.3988 - 1)}{1000 \times 0.1995 \times 100 \times 100}$$

$$NF_{overall} = 1.43 \equiv 1.53dB$$

The value produced for the direct channel, and indeed any of the channel arrangements used for DPCA is 1.42, very similar to the above due to the high gain of the first stage. As a result, the noise figure value calculated above, 1.53dB, shall be taken to apply to all

channel arrangements, and used for all subsequent calculations.

Two-channel receiver tests: direct channel

Starting with the direct signal channel, and referring to the diagram of Figure 4-7, this has been split into two sections either side of the mixer, corresponding to the RF and IF signals. Figure 4-8 gives the frequency response in terms of magnitude and phase for the RF section (low-noise amplifier and waveguide filter), while Figure 4-9 gives the equivalent plots for the IF section (IF bandpass filters and amplifiers). The measured bandwidths of each

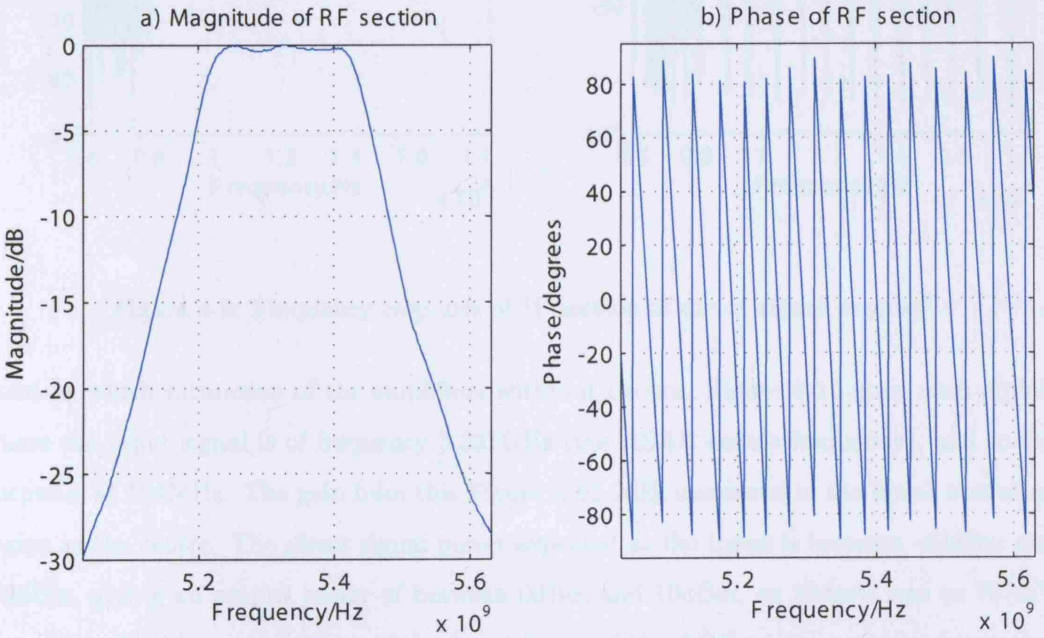

Figure 4-8: Frequency response of RF section of direct signal channel

section are shown in Table 4.13. The theoretical bandwidth is 200MHz for the RF section.

Section	Measured -3dB bandwidth/MHz
RF	235
IF	21.3

Table 4.13: Direct signal channel bandwidths for RF and IF sections

In addition, it is also useful to examine the variation in output power of this channel given a continuous-wave input of varying power. This indicates the gain of the channel and the

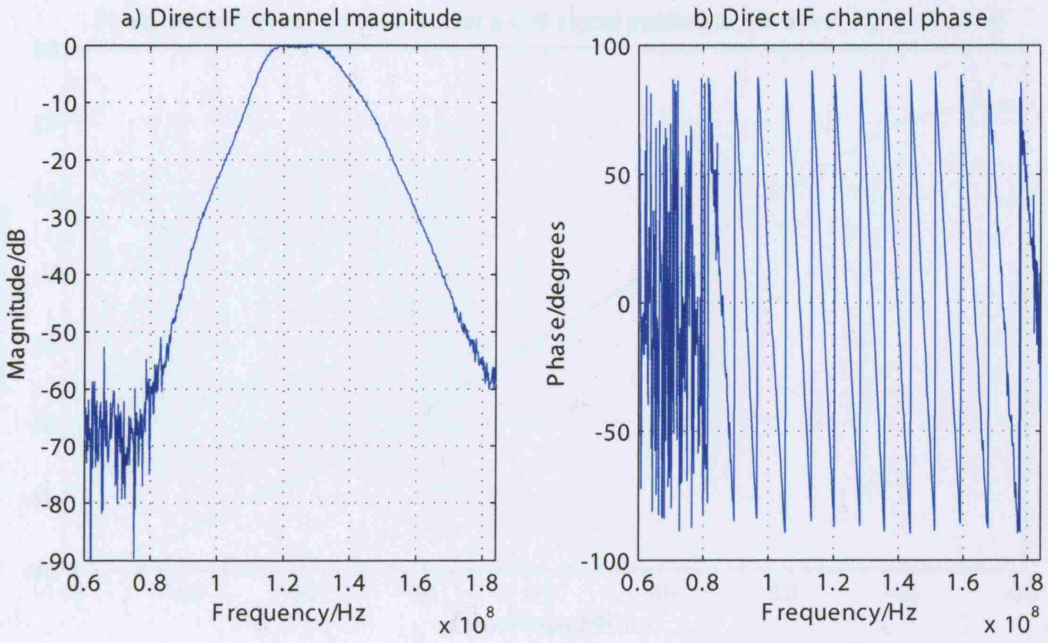

Figure 4-9: Frequency response of IF section of direct signal channel

point at which saturation of the amplifiers within it occurs. Figure 4-10 gives such a plot, where the input signal is of frequency 5.331GHz (the ASAR centre frequency), and so the output is at 124MHz. The gain from this Figure is 61.2dB, measured in the linear operating region in the centre. The direct signal power expected at the input is between -60dBm and -50dBm, giving an output power of between 0dBm and 10dBm, or 224mV rms to 707mV rms. This should enable full use of the input range of the ADC whilst avoiding saturation at the ADC input. The plot of Figure 4-10 becomes non-linear above an input power of -40dBm, indicating saturation of one or more of the amplifiers within the channel. The next Figure, 4-11, in this section shows the noise captured in the channel by the ADC with a matched load applied to the input, together with a histogram of the measured sample amplitudes compared to theory (red).

The captured noise signal has a peak amplitude of 0.0891V. If the noise sources are predominantly thermal in nature, as would be expected, the histogram should follow a Gaussian distribution. It is assumed that the crest factor for the (Gaussian) noise in the channel is equal to 5, and so the rms noise voltage is 1/5 of the peak amplitude. The theoretical plot was generated using the Matlab 'randn' function, with an rms noise voltage of 0.0178V.

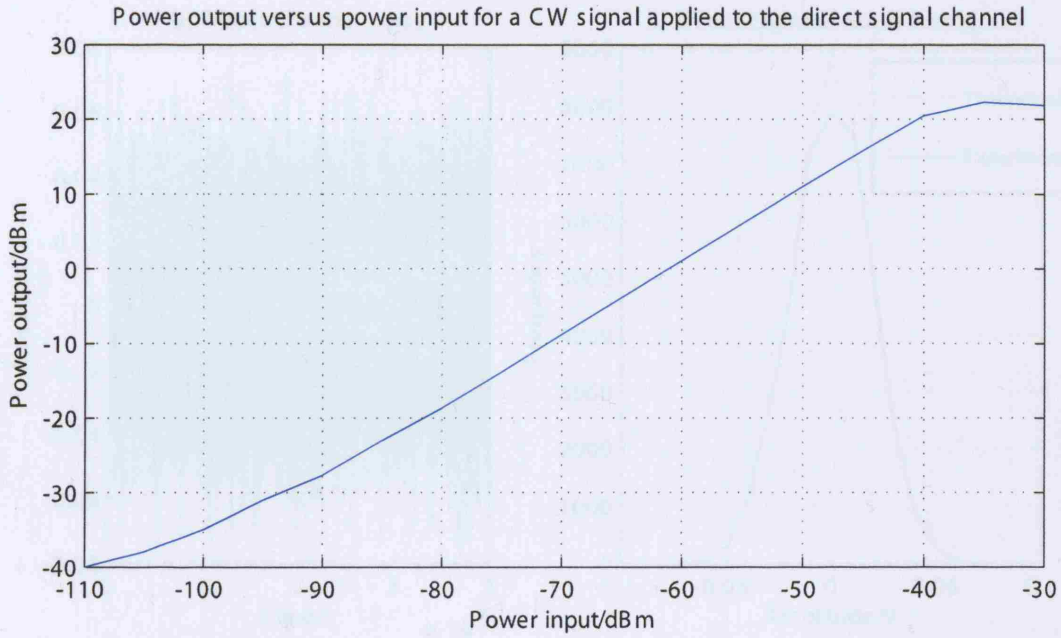

Figure 4-10: Power output versus power input for a CW signal applied to the direct signal channel

The measured noise signal has a histogram that closely follows the theoretical Gaussian distribution. The measured distribution is slightly broader than the theoretical, with a lower peak value as a result.

Such a test is typically performed to test ADC linearity, but would ideally involve applying an input signal that takes the full input voltage range of the ADC and capturing it for a large number of samples (several million for instance).

Given the measured bandwidth of the IF filters in Table 4.13 of 21.3MHz, measured channel gain G_d of 61.2dB, and the noise figure of 1.53dB, the theoretical noise power in this channel after amplification is:

$$P_{n,direct} = kT_sB_nG_dF = -38.0dBm$$

The noise power measured is calculated as $10\log_{10}((0.0178)^2/50) + 30 = -22.0dBm$. The discrepancy may partially be explained through errors in the parameters used in the theoretical noise power equation. An additional explanation will be covered in the section on the analog-to-digital converter.

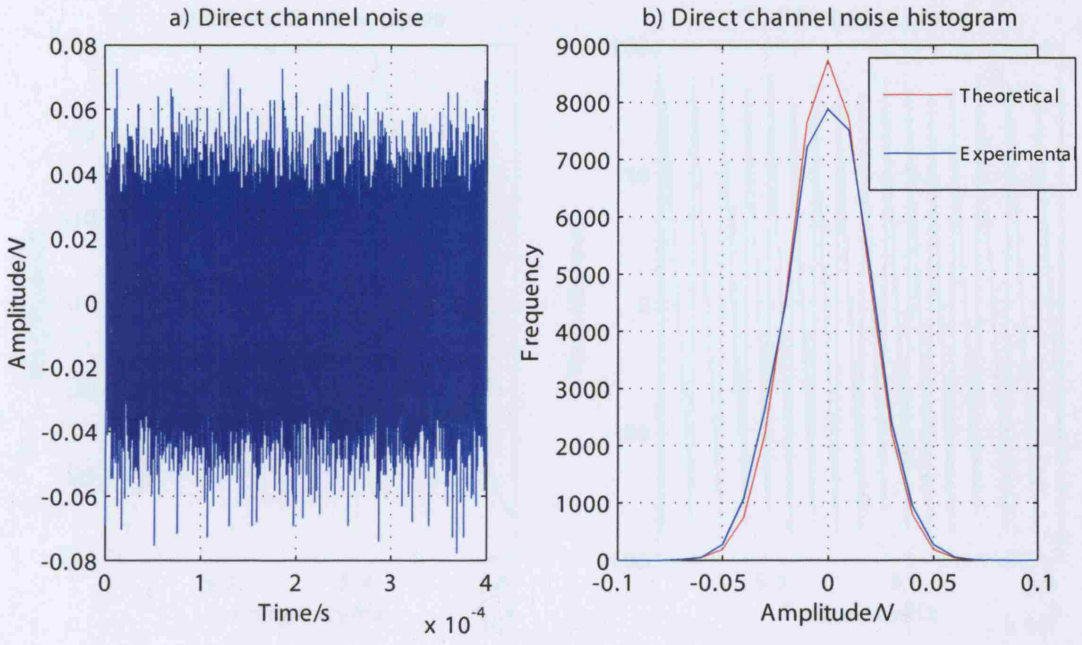

Figure 4-11: Noise captured in the direct signal channel, and a comparison between measured and theoretical histograms of the sample amplitudes

Two-channel receiver tests: reflected channel

The reflected signal channel results are presented in the same way. The frequency responses are reproduced in Figures 4-12 and 4-13, for the RF and IF sections respectively. The measured bandwidths may be found in Table 4.14.

Section	Measured -3dB bandwidth/MHz
RF	236
IF	15.9

Table 4.14: Reflected signal channel bandwidths for RF and IF sections

This channel has a gain control voltage (G_c) that may be applied to the first IF amplifier. This was set to 2.4V for the experiments using parabolic antenna 1, and 2.1V for those employing parabolic antenna 2. The decision as to which particular voltage to use was based on trial and error with several experiments. The reflected signal power expected at the input to the channel is no more than -95dBm, based on this trial and error procedure. The plot of output versus input power for this channel is shown in Figure 4-14, for a gain

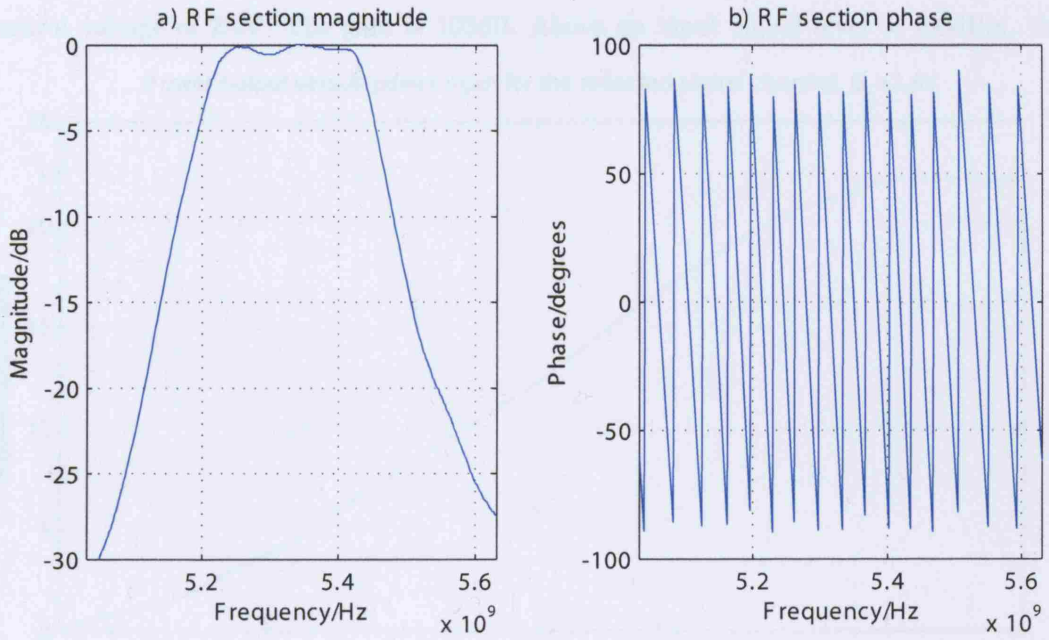

Figure 4-12: Frequency response of RF section of reflected signal channel

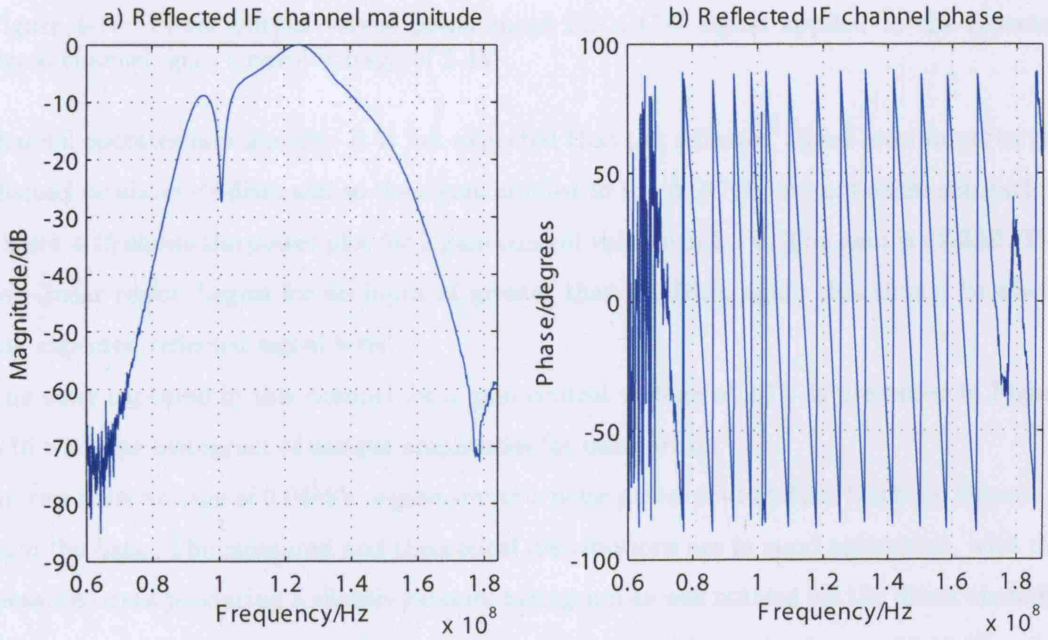

Figure 4-13: Frequency response of IF section of reflected signal channel

control voltage of 2.4V. The gain is 103dB. Above an input signal level of -80dBm, the

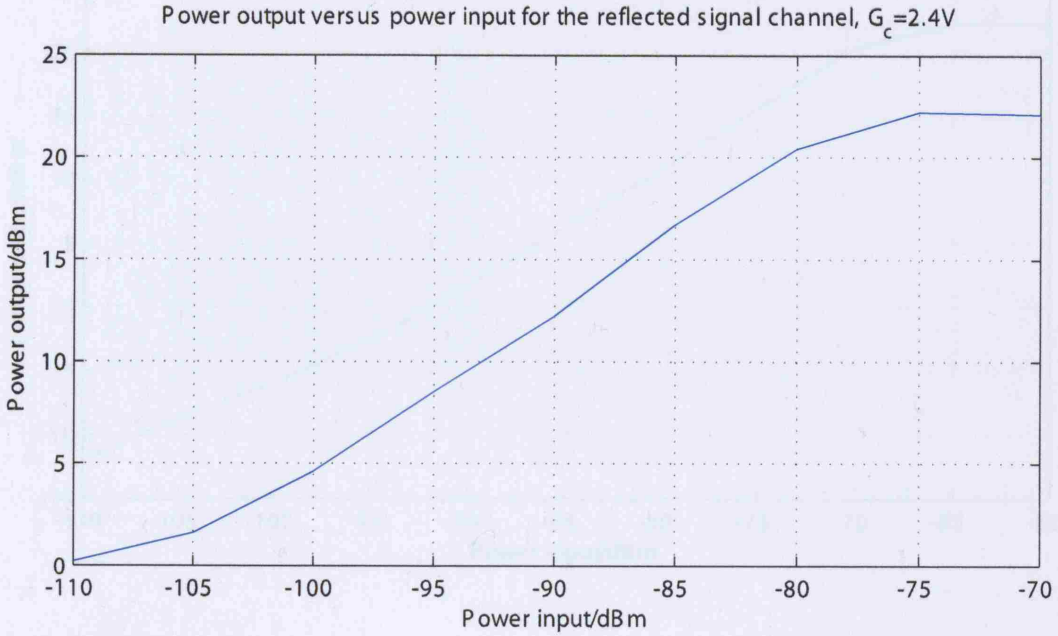

Figure 4-14: Power output versus power input for a CW signal applied to the reflected signal channel, gain control voltage of 2.4V

channel operates non-linearly. It is not expected that the reflected signal level input to the channel be above -95dBm and so the signal applied to the ADC should not cause saturation. Figure 4-15 shows the power plot for a gain control voltage of 2.1V. The gain is 92.2dB. The non-linear region begins for an input of greater than -70dBm, again this should be above any expected reflected signal level.

The noise captured in this channel for a gain control voltage of 2.1V is presented in Figure 4-16 with the histogram of sample amplitudes for comparison.

An rms noise voltage of 0.0448V, equivalent to a noise power of -14.0dBm has been measured from the data. The measured and theoretical distributions are in good agreement, with the measured data producing a slightly broader histogram as was noticed for the direct channel. The theoretical noise power in the channel is calculated with a noise figure of 1.53dB, noise bandwidth of 15.9MHz, and gain of 92.2dB, giving

$$P_{n,reflected,2.1V} = -8.23dBm$$

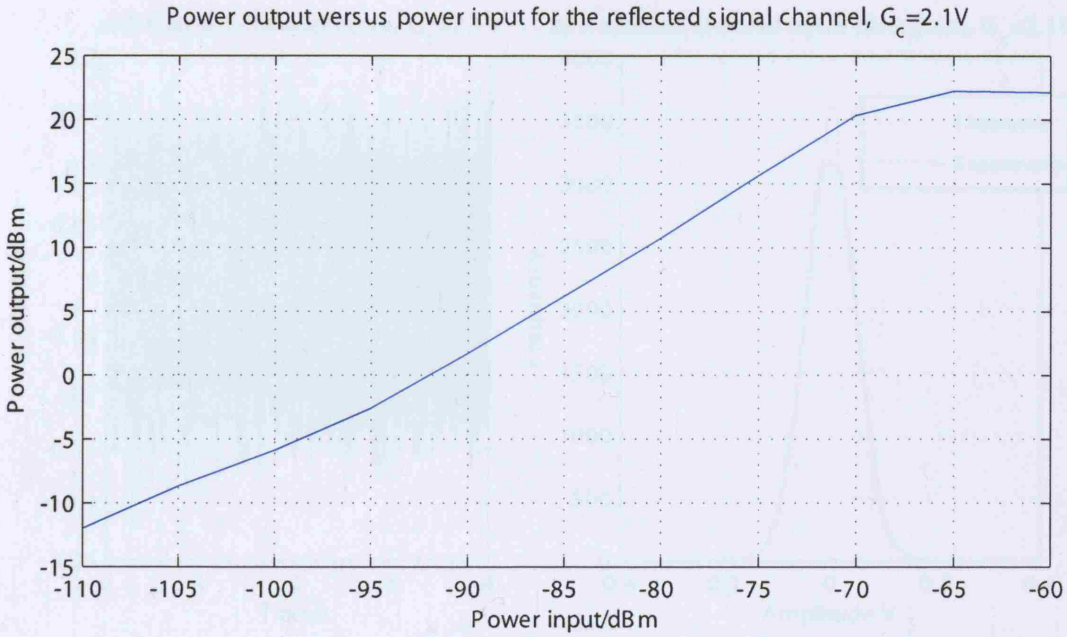

Figure 4-15: Power output versus power input for a CW signal applied to the reflected signal channel, gain control voltage of 2.1V

The measured noise level in the channel for $G_c = 2.4V$ is 0.145V rms, equivalent to a noise power of -3.68dBm. Theory predicts a noise power of,

$$P_{n,reflected,2.4V} = 2.57dBm$$

which has been calculated assuming a channel gain of 103dB.

The difference between measured and theoretical values is possibly due to the gain control voltage being slightly above 2.1V or 2.4V in each case.

The variation in G_c and resultant change in gain of the first IF amplifier will not have a significant effect on the noise figure and so it has been taken as constant for the previous calculations.

Three-channel receiver

The proposed three-channel receiver arrangement is given in Figure 4-17.

The basic design of each channel is as before, although there are two local oscillator frequencies, 5.221GHz and 5.201GHz. The first, generated by the Rhode and Schwartz instrument

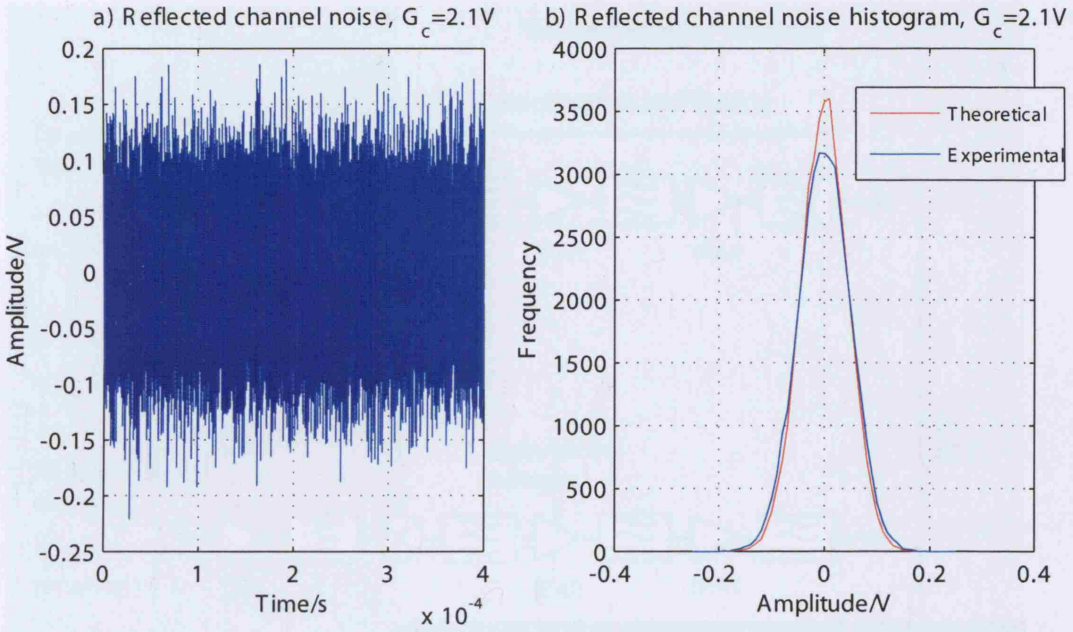

Figure 4-16: Noise captured in the reflected signal channel, $G_c = 2.1V$ and a comparison between measured and theoretical histograms of the sample amplitudes

with a power splitter on the output is applied to the mixers in the synchronisation channel and reflected signal channel 1. The second, applied to reflected signal channel 2, is generated by an HP 8672A which has been set to use an external frequency reference provided by the Rhode and Schwartz signal generator. The two signal generators will be phase locked as a result, although their respective outputs will have some constant phase difference. The intermediate frequencies are different from the value of 124MHz used previously, being 110MHz and 130MHz. The reason behind this is as a result of bandpass sampling theory, discussed in the next section. The frequency separation of the reflected signal IF signals is 20MHz, and they are combined (with a power combiner) before being digitised by a single channel of the Parsec ADC board. A photograph of the third receiver channel built for potential DPCA experiments is given in Appendix B.

4.4.4 Analog-to-Digital Conversion

As mentioned earlier in this Chapter, the analog-to-digital converter used is a Parsec PM480 mounted inside a desktop PC. The specifications of the sampling board are given in the

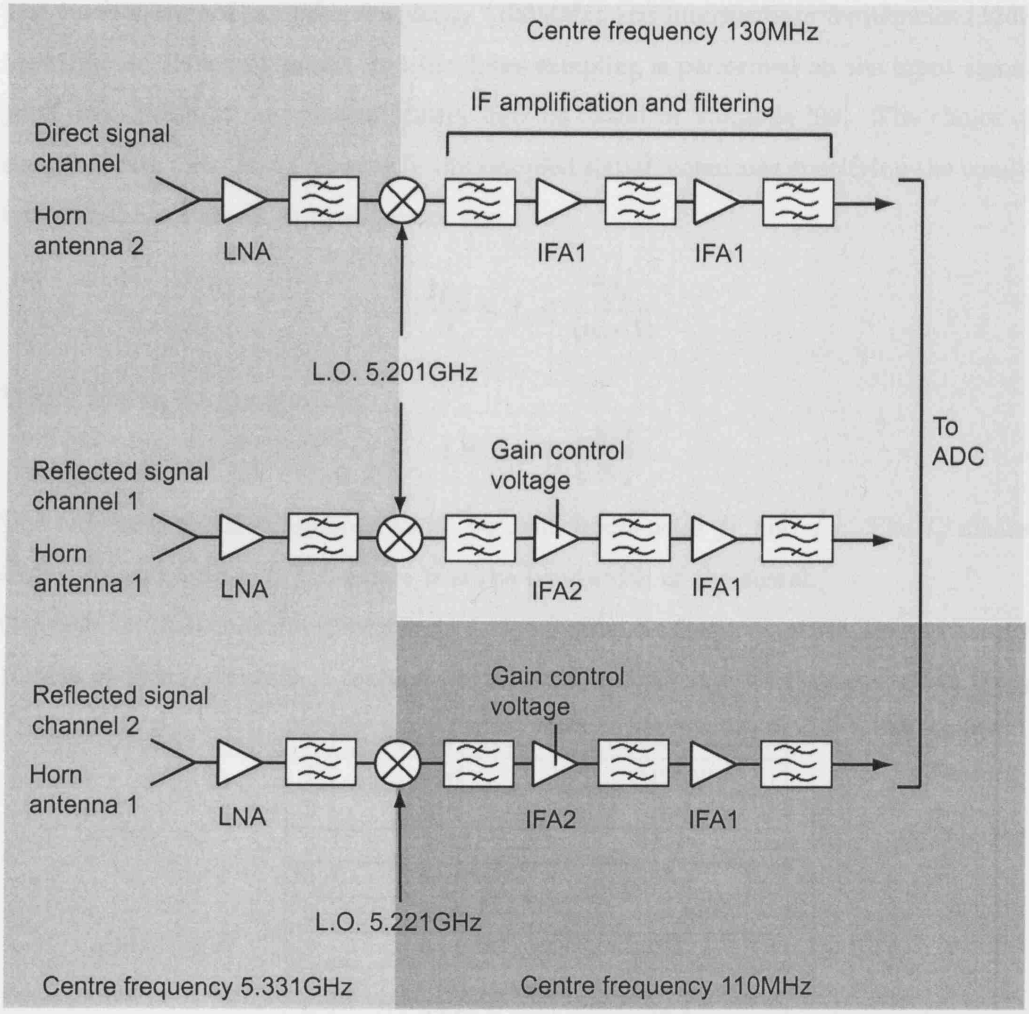

Figure 4-17: Three-channel receiver block diagram

table below. Software supplied with the board is used to select a resolution of 14 bits.

Inputs	Two single-ended analogue AC coupled
Input bandwidth	100kHz - 250MHz
Input impedance	50Ω
Full scale input power	5.5dBm (+/-1.2V pk-pk)
Sampling frequency	100MHz
Sampling resolution	8 - 14 bit (software selectable)

Table 4.15: Specifications of the Parsec PM480 analogue-to-digital converter board

The combination of sampling frequency (100MHz) and intermediate frequencies (124MHz, 110MHz and 130MHz) means that bandpass sampling is performed on the input signals. A good description of the relevant theory may be found in Vaughan [96]. The choice of the sampling rate must avoid aliasing in the sampled signal, equations specifying the conditions for acceptable uniform sampling rates are:

$$\frac{2f_U}{n} \leq f_s \leq \frac{2f_L}{(n-1)} \tag{4.2}$$

Where n is an integer given by:

$$1 \leq n \leq I_g \left[\frac{f_U}{B}\right] \tag{4.3}$$

The bandpass signal is assumed to lie between frequencies f_L and f_U. The I_g means the largest integer within f_U/B, where B is the bandwidth of the signal.

Consider the two-channel receiver first. A signal of centre frequency 124MHz and bandwidth 16MHz must be sampled. A table of the allowed uniform sampling rates is given below.

n	f_s lower/MHz	f_s upper/MHz
1	264	infinity
2	132	232
3	88.0	116
4	66.0	77.3
5	52.8	58.0
6	44.0	46.4
7	37.7	38.7
8	33.0	33.1

Table 4.16: Allowable sampling rates for bandpass sampling of the Envisat IF chirp

It is evident that the sampling frequency of 100MHz is acceptable and will not produce aliasing. The spectrum of the sampled signal is shown in Figure 4-18.

For the three-channel receiver, there is one IF signal of centre frequency 110MHz and 16MHz bandwidth, and a second of centre frequency 130MHz, also with a 16MHz bandwidth. Using the Equations (4.2) and (4.3), with a sampling frequency of 100MHz and n=3, the allowable centre frequencies of a 16MHz bandwidth signal lie in the range 108MHz to 142MHz. So if the lower DPCA signal is at a centre frequency of 110MHz, then the upper must be at 130MHz, and these both satisfy the sampling requirements laid out in Vaughan [96]. The spectrum of the sampled signal is given in the Figure 4-19, where the application of a

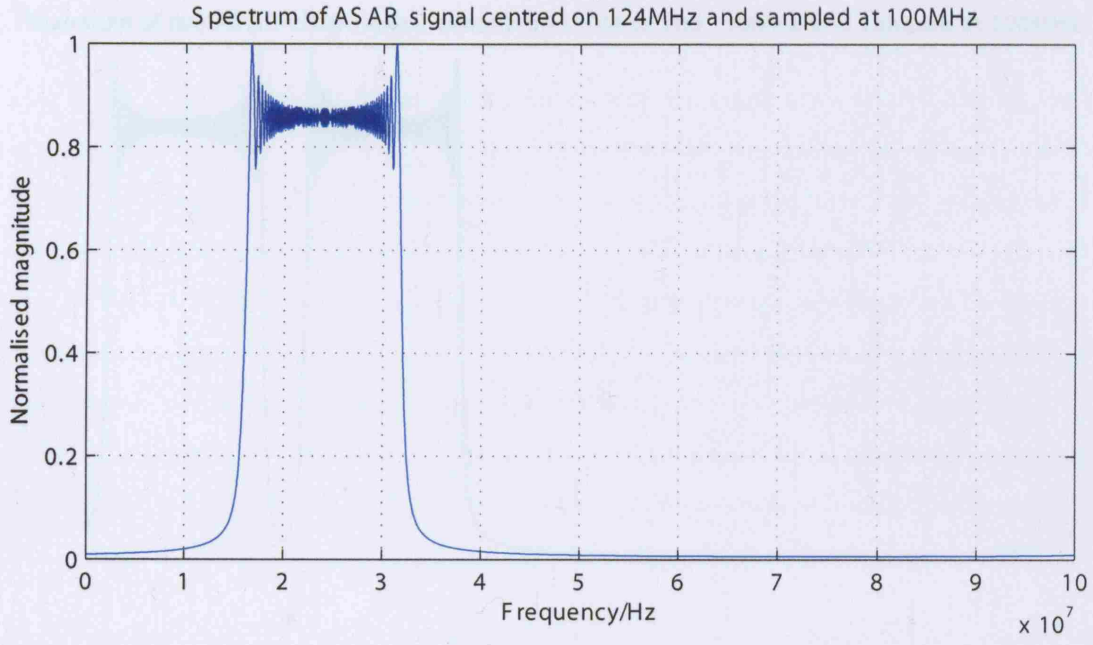

Figure 4-18: Spectrum of the Envisat IF chirp bandpass sampled at 100MHz

100MHz sampling frequency has shifted the centre frequencies of the inputs to 10MHz and 30MHz.

The ADC board was found and purchased in the second year of the research programme after much of the receiver had been constructed (and an intermediate frequency of greater than 100MHz had been decided upon), hence the use of bandpass sampling instead of the more conventional lowpass sampling. The value of 124MHz is in fact the intermediate frequency used on-board the Envisat satellite for the ASAR received signal.

The use of bandpass sampling as described requires several compromises in performance to be made. Referring to Vaughan [96] and Akos [97], the principal advantage of this sampling approach is that the sampling frequency used may be lower, so reducing the data rate. This must be weighed against the disadvantages, which include the aliasing of noise - all energy from dc to the input analog bandwidth of the ADC will fold into each of the $f_s/2$ bands. The resultant degradation in signal-to-noise ratio compared to a lowpass sampling system (where the sampling rate is at least twice the highest frequency component of the input signal) may in theory be offset by using a higher performance bandpass filter at the ADC

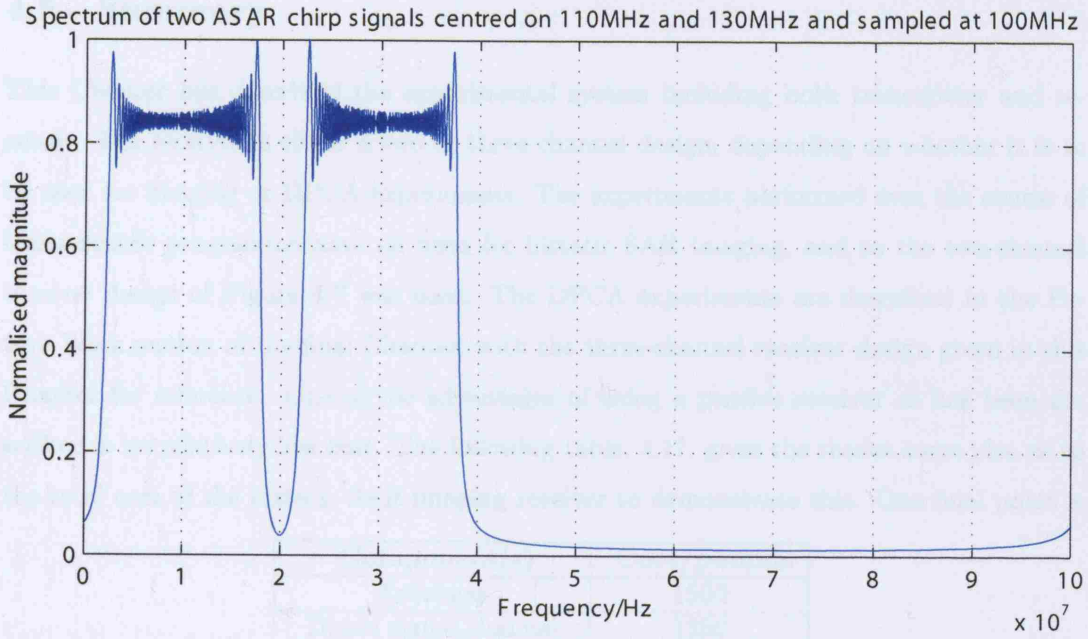

Figure 4-19: Spectrum of two Envisat IF chirp signals at 110MHz and 130MHz bandpass sampled at 100MHz

input. From Vaughan [96], the SNR degradation may be expressed by:

$$D_{SNR} = 10\log_{10}(n)$$

n is the number of bands between dc and the passband of the input signal. For the ASAR chirp, a bandwidth of 16MHz and lower passband frequency of 116MHz means n=8. The degradation $D_{SNR} = 9dB$. The discrepancy between theoretical and measured direct signal channel noise powers may be partially explained by this noise aliasing effect. That this is not seen in the reflected signal channel may be because this channel uses an extra IF filter, so providing additional noise attenuation. In addition to the increase in noise, the analog input bandwidth of the ADC must accommodate the highest frequency components of the input signal (a requirement which is met by the Parsec ADC for the ASAR IF chirp).

4.5 Summary

This Chapter has described the experimental system including both transmitter and receiver. The receiver is either a two or three-channel design, depending on whether it is to be used for imaging or DPCA experiments. The experiments performed over the course of this research programme have all been for bistatic SAR imaging, and so the two-channel receiver design of Figure 4-7 was used. The DPCA experiments are described in the Future Work section of the final Chapter, with the three-channel receiver design given in this Chapter for reference. One of the advantages of using a passive receiver as has been described is its relatively low cost. The following table, 4.17, gives the reader some idea as to the total cost of the bistatic SAR imaging receiver to demonstrate this. One final point is

Component(s)	Cost/pounds
Antennas	1500
Direct signal channel	1850
Reflected signal channel	1920
ADC board and PC	6000
Total	**11270**

Table 4.17: Total cost of the bistatic SAR imaging receiver

with regard to the antennas. They are all mounted on tripods, with the antenna pointing direction calculated using a compass for the horizontal direction (accurate to within one degree) and an inclinometer for the vertical direction (again, accurate to within one degree). Typically for an imaging experiment, the reflected channel antenna would be pointing at an elevation angle two degrees down from the horizontal.

Chapter 5

Predicted system performance

5.1 Synchronisation

Both time and phase synchronisation are necessary between the transmitter and receiver.

5.1.1 Time synchronisation

The first, time synchronisation, is achieved by direct signal reception, which obviously requires adequate line-of-sight with the satellite. From Weib [28] the time stability requirement can be calculated from the following equation,

$$\delta t = \frac{1}{20B\tau_n} \tag{5.1}$$

δt is the time difference or accuracy, B is the bandwidth of the transmitted pulse, and τ_n is the update rate of the two clocks. Inserting the ASAR parameters, with the assumption of a worst-case update rate of 6.05×10^{-4}s, corresponding to the IS2 PRF (pulse repetition frequency), produces a requirement of:

$$\delta t = \frac{1}{20 \times 16 \times 10^6 \times 6.05 \times 10^{-4}} = 5.16 \times 10^{-6} s$$

In order to check that this requirement may be realised, the variance in a time delay measurement of the direct signal after matched filtering must be known. This is calculated with the aid of parameter estimation theory, as described in Cook [98]. The matched filter is the optimum way of processing a signal in the presence of white Gaussian noise, and will

give a maximum accuracy estimate of time delay and Doppler frequency. It is a maximum-likelihood estimator for these parameters, and so the measurement errors approach the Cramér-Rao bound for large signal-to-noise ratios. Application of this theory to a practical rectangular envelope linear frequency modulated pulse gives a minimum time measurement error variance of:

$$\sigma^2_{\tau,min} = \frac{N_0}{2E\beta^2}$$

With E representing the signal energy, N_0 is the single-sided noise power spectral density, and 2β is the effective bandwidth of the waveform, expressed in radian dimensions. The equation for β in terms of the signal bandwidth B is,

$$\beta^2 = \frac{\pi^2 B^2}{3}$$

Therefore,

$$\beta^2 = \frac{\pi^2(16 \times 10^6)^2}{3} = 8.42 \times 10^{14} rad^2/s^2$$

Assuming a signal-to-noise ratio $2E/N_0$ of at least 10dB, this gives a minimum time variance of:

$$\sigma^2_{\tau,min} = 1.19 \times 10^{-16} s^2$$

And a minimum time standard deviation, or error of:

$$\sigma_{\tau,min} = 1.10 \times 10^{-8} s = 11.0 ns$$

From the paper by Weib [28] an achievable accuracy of less than $10ns$ is given for this method of synchronisation, similar to the value just produced. Both values are much lower than the requirement of $5.16\mu s$ error calculated at the beginning of this section. The minimum time standard deviation for a signal-to-noise ratio of 0dB is 34.5ns, also much smaller than the requirement.

5.1.2 Phase synchronisation

Phase stability

Phase synchronisation is required for coherent operation, necessary for the generation of SAR imagery and moving target detection. From Willis [11], oscillator stability for direct

phase synchronisation (on a pulse-by-pulse basis) is given by the equation:

$$\delta\phi_{direct} = \frac{\Delta\phi}{2\pi f_c \Delta T_{rt}} \tag{5.2}$$

$\Delta\phi$ is the allowable rms phase error in radians, f_c is the transmitted centre frequency in Hertz and ΔT_{rt} is the propagation time difference between the reflected and direct signals. A bistatic SAR system is sensitive to high frequency or sinusoidal phase errors over ΔT_{rt}. From Willis [11] a typical value for the rms phase error is $\Delta\phi = 0.07rad = 4^0$. For the system considered, $\Delta T_{rt} = 6.67 \times 10^{-5}s$, equivalent to a (worst case) path length difference of 20km, $f_c = 5.331GHz$, and so,

$$\delta\phi_{direct} = \frac{0.07}{2\pi \times 5.331 \times 10^9 \times 6.67 \times 10^{-5}} = 3.13 \times 10^{-8}rad$$

Therefore the stability required is approximately 3 parts in 10^8 over $67\mu s$. From Willis [11], a Quartz oscillator should be able to meet this requirement.

The phase must be measured from the compressed direct signal pulses. As for the time synchronisation, this process has a minimum measurement error variance, which is again derived by applying the theory presented in Cook [98]:

$$\sigma^2_{\phi,min} = \frac{N_0}{2E}$$

The error variance is inversely proportional to the signal-to-noise ratio of the compressed pulse. As for the time synchronisation case, assuming a signal-to-noise ratio of at least 10dB yields a phase measurement error variance of 0.1rad, and a standard deviation of 0.32rad. This is equivalent to a range error of $2.9 \times 10^{-3}m$. For a SNR of 0dB, the measurement standard deviation is 1 radian, a range error of $8.96 \times 10^{-3}m$.

It is worth examining the indirect phase synchronisation case and comparing the requirement to the value just calculated. Again, from Willis [11], the equation for stability is:

$$\delta\phi_{indirect} = \frac{\Delta\phi}{2\pi f_c T} \tag{5.3}$$

The symbols are the same as used in the previous equation, with T representing the integration time. The SAR system is sensitive to quadratic phase errors over the integration time

T, and so the allowable rms phase error, $\Delta\phi = 1.57rad = 90^0$. The data for an acquisition is typically captured over a period of seven seconds, with the peak received signals from the satellite and the imaged scene being present approximately in the middle of the capture. If the receiver is not synchronised to the transmitter over this period of time, it is equivalent to the indirect phase synchronisation method, but with a constant phase offset between transmitter and receiver oscillators (they are not matched at the beginning of the receiver data capture). So, assuming an integration time of 3.5 seconds, the stability requirement becomes,

$$\delta\phi_{indirect} = \frac{0.5\pi}{2\pi \times 5.207 \times 10^9 \times 3.5} = 1.37 \times 10^{-11} rad$$

Again, a quartz oscillator should be able to meet this requirement.

Phase noise

With the use of independent oscillators in the transmitter and receiver, the resultant overall phase noise of the system is the summation of the individual noise contributions of the two oscillators. There is no phase noise cancellation as would occur in a monostatic system. Given information on the spectra for transmit and receive oscillators and the coherent integration time of the bistatic imaging system, it is possible to determine a value for the Integrated Sidelobe Ratio (ISLR) that results. From Willis, [11], the ISLR due to phase noise alone should ideally be no more than -30dB. The single-sideband phase noise of the signal generators used in the experiments may be obtained from their respective data sheets, with offset frequencies less than 10Hz being of relevance. L_R is the receiver oscillator single-sideband phase noise (absolute value) at an offset frequency of 1Hz and at the correct centre frequency for L.O. generation. L_T is the corresponding phase noise of the transmitter oscillator, for the transmit frequency. T_i is the coherent integration time. The bistatic ISLR, from Willis [11], is given by:

$$ISLR_B = 10log_{10}(L_T + L_R) + 20log_{10}(T_i) \tag{5.4}$$

Two different signal generators were used in the experiments, an HP83732A for the experiment at DSTL Portsdown West on 5th December 2005, and a Rhode and Schwartz SMP04 for all of the other acquisitions. The Rhode and Schwartz SMP04 is considered first. The single sideband phase noise, L(f), expressed in dBc/Hz, is given in Figure 5-1. The plot was

taken from the data sheet for this device.

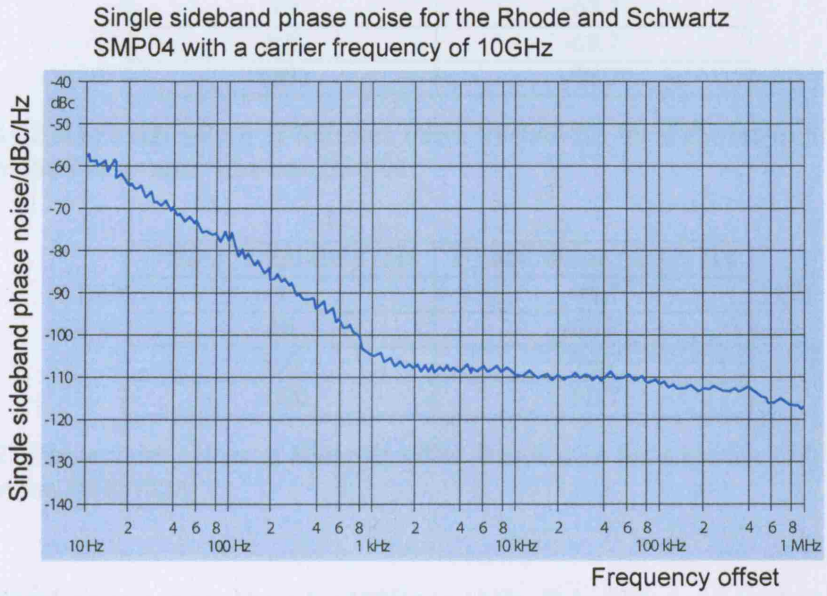

Figure 5-1: Single sideband phase noise of the Rhode and Schwartz SMP04

The Figure is given for an oscillator frequency of 10GHz. From Robins [99], it is expected that the phase noise spectrum follows a $1/f_o^3$ law for small offset frequencies f_o due to intermodulation of carrier and flicker noise, and then after some transition frequency to follow a $1/f_o^2$ law. From Figure 5-1, in the region 10Hz to 1kHz the $1/f_o^2$, relationship (or 20dB/decade decrease) holds, and so it shall be assumed that for 1Hz to 10Hz offset, the phase noise spectrum falls off with $1/f_o^3$, 30dB/decade. At 10Hz the phase noise is -58dBc/Hz and so it will be approximately -28dBc/Hz at 1Hz offset. To convert the values based on oscillator frequency, the following equation, from Robins [99] may be used:

$$L_{f2} = M^2 L_{f1}$$

Where the phase noise values are absolute and apply to different oscillator frequencies f1 and f2. M is the frequency ratio $M = f2/f1$.

The results for the Rhode and Schwartz signal generator are shown in Table 5.1, given a frequency ratio of $M = 5.207/10$. The values for the HP83732A signal generator may be produced in a similar way, giving Table 5.2. The actual values supplied on the data sheet for

Offset frequency/Hz	Phase noise/dBc/Hz
1	-33.7
10	-63.7
100	-69.7
1000	-98.7

Table 5.1: Phase noise values at different offset frequencies for a carrier of 5.207GHz generated by the Rhode and Schwartz SMP04

Offset frequency/Hz	Phase noise/dBc/Hz
1	-24.7
10	-54.7
100	-74.7
1000	-80.7

Table 5.2: Phase noise values at different offset frequencies for a carrier of 5.207GHz generated by the HP83732A

the HP signal generator are those for 100Hz to 1kHz. It has been assumed that the roll-off is 20dB/decade between 10Hz and 100Hz, and 30dB/decade between 1Hz and 10Hz. The phase noise data for the oscillator in ASAR was obtained from the Envisat helpdesk [69], with values reproduced in Table 5.3. These have been converted to the 5.331GHz centre frequency of transmission, from an original frequency of 124MHz. Using Equation 5.4 with the 1Hz offset phase noise values of each signal generator combined with the phase noise of the ASAR oscillator, produces the following integrated sidelobe ratios.

$$ISLR_{Rhode\&Schwartz} = -26.4 + 20log_{10}(T_i)$$

$$ISLR_{HP83732A} = -22.8 + 20log_{10}(T_i)$$

These are plotted in Figure 5-2. The integration time for the bistatic data processing will be less than 0.5 second, and from the graph it is apparent that both combinations of ASAR

Offset frequency/Hz	Phase noise/dBc/Hz
1	-27.3
6.25	-51.3
1000	-107

Table 5.3: Phase noise values at different offset frequencies for a carrier of 5.331GHz generated by the oscillator within ASAR

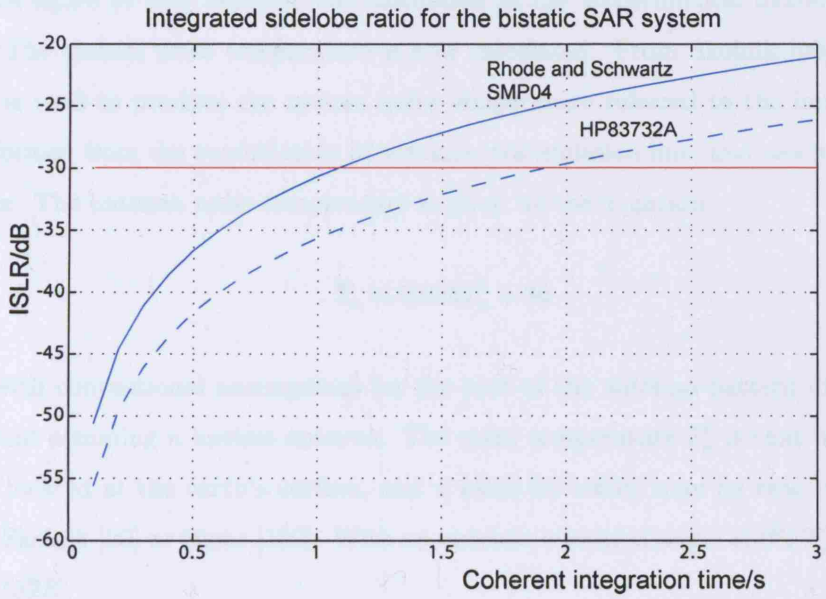

Figure 5-2: Integrated sidelobe ratio simulation

oscillator and receiver oscillator meet the requirement of an $ISLR < -30dB$. Given the potential error in extrapolating receiver phase noise values to a 1Hz offset, both of these predictions are approximate.

This analysis has assumed that direct phase synchronisation is being applied to the received data. If indirect phase synchronisation were used instead (effectively no synchronisation over a data capture time or integration time of 3.5 seconds), the ISLR would increase to -12dB and -15dB for the SMP04 and HP83732A signal generator respectively. These values are unacceptable compared to the requirement of -30dB.

Both direct synchronisation and no synchronisation will be used to generate the first experimental bistatic image in order to compare the results and demonstrate this difference in performance, but the remainder of the images will be produced using the direct phase synchronisation method only.

5.2 Detection

In this section the detection performance of the system will be analysed through use of the radar range equation and associated theory.

The noise figure of each receiver was calculated in the Experimental System Chapter as 1.53dB. The system noise temperature is now calculated. From Skolnik [90], the referral concept is used to produce the system noise temperature referred to the input terminals. This is formed from the combination of antenna, transmission line, and receiver noise temperatures. The antenna noise temperature is given by the equation:

$$T_a = 0.876T'_a + 36$$

This is with conventional assumptions for the part of the antenna pattern directed at the ground and assuming a lossless antenna. The noise temperature T'_a is that of an idealised antenna located at the earth's surface, and a value for which may be read off a graph as given in Skolnik [90] or Blake [100]. With an antenna elevation angle of 0^0, $T'_a = 110K$ and so $T_a = 132K$.

The transmission line noise temperature is that of the cable between the antenna and receiver. The relevant equation is,

$$T_r = T_{tr}(L_r - 1)$$

A conventional value for T_{tr} is 290K, while L_r is the loss of the transmission line. Typically the cable used is of RG316-DS type, which has a loss of approximately 0.3dB/ft at 5GHz. This equates to 1dB of loss for 1m (the typical length), and so $T_r = 290(1.259 - 1) = 75.1K$. The effective input noise temperature of the receiver is given by:

$$T_e = 290(NF_{overall} - 1) = 290(1.427 - 1) = 124K$$

The system noise temperature is:

$$T_s = T_a + T_r + L_r T_e = 363K$$

The bistatic radar range equation may be expressed in terms of signal-to-noise ratio,

$$SNR = \left(\frac{P_T G_T G_R \lambda^2 \sigma_B F_T^2 F_R^2}{(4\pi)^3 k T_s B_n R_T^2 R_R^2 L_T L_R} \right) I \tag{5.5}$$

I is the improvement factor, which takes into consideration the processing gain due to range

and azimuth compression in SAR imaging. It may be expressed as,

$$I = \left(\frac{\tau_i}{\tau_o}\right)\left(\frac{N}{L_p}\right)$$

The processing gain from compression of the chirp pulse (matched filtering) is equal to the ratio of uncompressed to compressed pulse length, (τ_i/τ_o). The former depends on the swath, while the latter is $\tau_o = (0.886/B) = 5.54 \times 10^{-8}s$ (where B is the chirp bandwidth of 16MHz). The second gain is equal to N, the number of pulses integrated or used for SAR image generation. There is also a processing loss term L_p, to account for windowing function loss. As Taylor weighting is applied during both range and azimuth compression, its effect on the impulse response in both dimensions is shown in Table 5.4. The window

Window function	**Mainlobe broadening**	**Processing loss/dB**	**PSLR/dB**	**Sidelobe decay/dB/decade**
None (uniform)	1.0	0	-13.3	-20
Taylor (n)	1.41	1.23	-40	-20

Table 5.4: Taylor window compared to uniform weighting

function loss of 1.23dB will reduce the final signal-to-noise ratio achieved; this is applied for range and azimuth compression, giving an overall loss of 2.46dB. The processing gain for range compression is given for the various ASAR image swaths in Table 5.5, taking into account the loss introduced by the Taylor weighting (1.23dB). The corresponding azimuth

Swath	Processing gain with windowing loss for range compression/dB
IS1	25.6
IS2	25.7
IS3	24.6
IS4	25.6
IS5	24.7
IS6	25.5
IS7	24.7

Table 5.5: Processing gain for range compression of the ASAR chirp pulse with windowing function loss attributed to Taylor weighting ($\overline{n} = 6$) taken into account

compression gain values are dependent on the number of pulses used. In addition, there will be some amplitude taper in the azimuth dimension as a result of the transmit antenna

pattern, which will introduce an extra, albeit small loss. For imaging, the azimuth resolution in the experimental results is 24m, given the processed bandwidth chosen and mainlobe broadening introduced by the Taylor weighting. The Doppler centroid is taken to be zero in the following analysis. Using the exposure time values from Table 6.1 in the Experimental System Chapter and multiplying by the pulse repetition frequency gives some example values that are applicable to SAR imaging. After calculation, these vary between 29.1dB and 30.9dB (taking the loss of 1.23dB into account). The overall processing gain in image generation will therefore be approximately 55dB (the actual processing gain will be less than this as the full azimuth bandwidth will not be processed, and as mentioned earlier the antenna pattern will exhibit a small amount of taper over the processing time).
The signal-to-noise ratio in the SAR image will be approximately equal to:

$$SNR_{image} \approx P_g + SNR_{pulse} \tag{5.6}$$

Where P_g is the combined processing gain for range and azimuth compression, taking into account the windowing function loss, and SNR_{pulse} is the signal-to-noise ratio of a single received pulse, in the centre of the transmit beam.
A summary of the fixed parameters used in the radar range equation may be found in Table 5.6. The antenna pattern loss, or beamshape loss is given by the pattern propagation factors,

Parameter	Value
P_T	1365W
λ	0.0563m
F_T	1
F_R	1
T_s	363K
B_n	16MHz
L_T	0.281dB
L_R	1

Table 5.6: Fixed-value parameters used in the range equation calculations

F_T and F_R, and accounts for the loss introduced by transmitting and receiving off-boresight. It is assumed that both F_T and F_R are equal to 1 (the target is illuminated by the peak of the antenna beam in each case). The effects of multipath, diffraction and refraction have been discounted. Certainly multipath will have an effect on the received signal, but given the

typically urban environment in which the receiver system is operating this will be difficult to quantify theoretically. The value of L_T takes into account transmitting system losses - these have been assumed to arise from atmospheric attenuation of the signal. From Blake [100], such attenuation is a function of range. For the satellite-to-target ranges indicated in the Experimental System Chapter for the various swaths (838km to 1050km), the total one-way absorption loss is approximately 0.281dB, due to oxygen, water vapour and lens effect losses, and assuming an antenna elevation angle of 0^0. The receiving system losses not accounted for elsewhere are taken to be negligible.

Applying the bistatic radar equation to the IS1 and IS7 swaths, assuming that the receiver antenna gain is 23.3dBi (the value for parabolic antenna 2), that the range from transmitter to target is equal to the ASAR range to scene centre values given in the last Chapter, and assuming that range compression has been performed with the Taylor weighting previously described gives the results shown in Figure 5-3. The bistatic radar cross-section in the plots is $1m^2$, $10m^2$ and $100m^2$, increasing as shown.

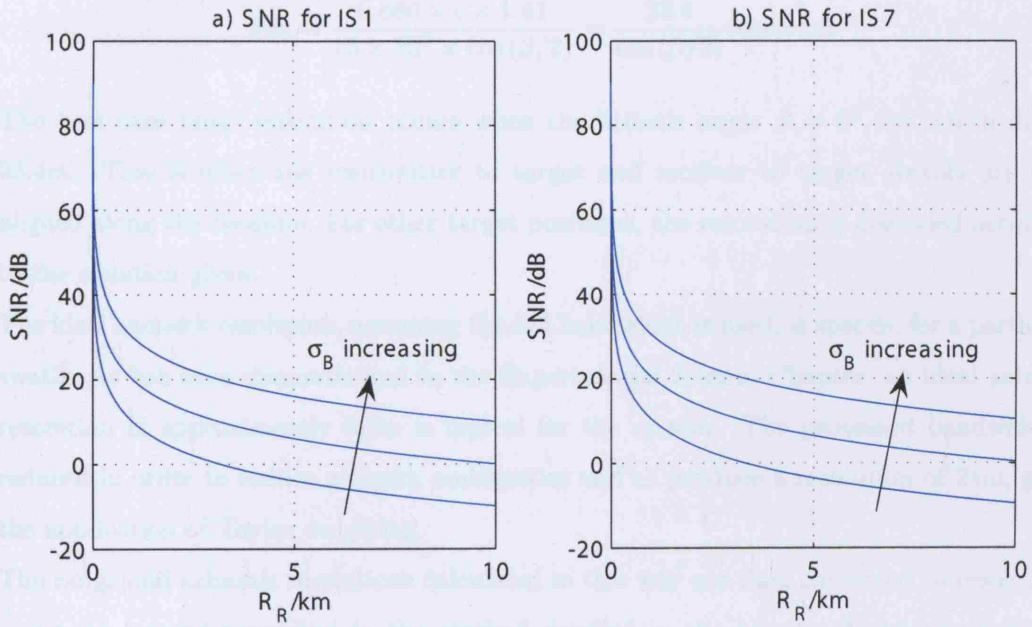

Figure 5-3: Signal-to-noise ratio after range compression using parabolic antenna 2 in the receiver and for the IS1 and IS7 swaths

For a target of bistatic RCS $1m^2$, the range R_R at which the SNR=0dB is just over 3km for IS1 and IS7. For local area imaging with $R_R < 2km$, the signal-to-noise ratio is acceptable

for an RCS of at least $10m^2$. Given the subsequent azimuth compression and the resultant extra processing gain, the SNR in the image should be adequate. Use of parabolic antenna 1 implies additional gain (35dBi), and so the SNR achievable will increase by 11.7dB.

5.3 Resolution

Using the expressions for range and azimuth resolution in the Bistatic Radar Theory Chapter, (3.24) and (3.26) as well as the ground resolution cell size (3.30), together with the simulated geometry for a particular experiment will enable prediction of resolution performance. A window function is applied in the range and azimuth dimensions in order to reduce the peak to sidelobe ratio in the resultant impulse response. A Taylor window was chosen for this task, its effect on the impulse response has already been summarised in Table 5.4.

With the above taken into account, the bistatic range resolution is

$$\delta R_b = \frac{0.886 \times c \times 1.41}{16 \times 10^6 \times \cos(\beta/2)} = \frac{23.4}{\cos(\beta/2)}(metres)$$

The best case range resolution occurs when the bistatic angle $\beta = 0^0$, for which $\delta R_b = 23.4m$. This is when the transmitter to target and receiver to target vectors are both aligned along the baseline. For other target positions, the resolution is degraded according to the equation given.

The ideal azimuth resolution, assuming the full bandwidth is used, is specific for a particular swath. As has been demonstrated in the Experimental System Chapter, an ideal azimuth resolution of approximately 8.9m is typical for the system. The processed bandwidth is reduced in order to reduce azimuth ambiguities and so produce a resolution of 24m, given the application of Taylor weighting.

The range and azimuth resolutions calculated in this way are then converted to resolutions along the ground according to the method detailed in the bistatic Ambiguity Function theory. The directions on the ground plane are aligned with the Easting and Northing axes on an ordnance survey map.

The theoretical resolution performance for each experiment will be given alongside the experimental bistatic image results in the Experimental Imagery and Analysis Chapter.

Chapter 6

Bistatic SAR signal processing and simulations

6.1 Data Preparation

6.1.1 Overview

This section covers the theory and method of data pre-processing, before any subsequent application of a bistatic SAR processor. Raw data is produced by all of the channels at an intermediate frequency and is bandpass sampled at 100MHz by the ADC board. These sets of bandpass sampled data are down-converted to baseband by multiplication with a local oscillator and application of a low-pass filter, both generated in Matlab. The method for the imaging receiver is shown in Figure 6-1.

The low-pass filter is necessary for removal of the frequency sum term produced by the mixing operation (in this case a replica of the received signal centred on 48MHz). The filter used is a Finite Impulse Response digital filter generated using the 'fdatool' function in Matlab, specifically a Blackman window with a length of 41 and a cut-off frequency of 25MHz.

As described previously in the section on synchronisation, the receiver must periodically synchronise itself with the transmitter, through the use of the direct signal, in order to establish adequate time and phase references. For timing, a replica of the ASAR transmitted chirp is used as a matched filter to pulse compress the direct signal data. This provides a maximum accuracy estimate of the start time of each direct signal pulse, which is used as

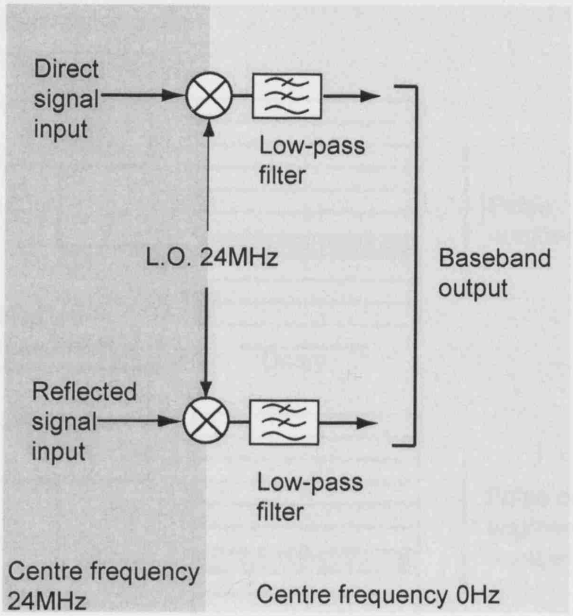

Figure 6-1: Imaging receiver down-conversion to baseband

the corresponding start time for the reflected signal data extracted for each pulse repetition interval.

Each direct signal pulse and the corresponding reflected signal data segment are then placed in separate matrices as shown in Figure 6-2.

Each reflected signal segment consists of returns from the imaged scene, from very close range to the receiver (for example energy scattered by the building on which the receiver is positioned) to some scatterer perhaps a few kilometres away. Phase synchronisation between the receiver and transmitter is required in order to provide coherent data for signal processing. As was mentioned earlier in this document, this may be performed on a pulse-to-pulse basis using the direct signal from the transmitter. The local oscillator used in the receiver is not phase locked to the oscillator(s) used for transmit signal generation on board Envisat. The phase of the received signal in each channel therefore experiences a drift over time relative to the transmitted signal phase. This drift is the same for each channel and so the phase of one channel may be subtracted from that of the other in order to establish coherency with the transmitter. Each reflected signal section is compressed with a replica of the ASAR chirp that also includes the phase of the corresponding direct signal pulse. In this way the direct signal acts as a phase reference and at the same time a matched filtered

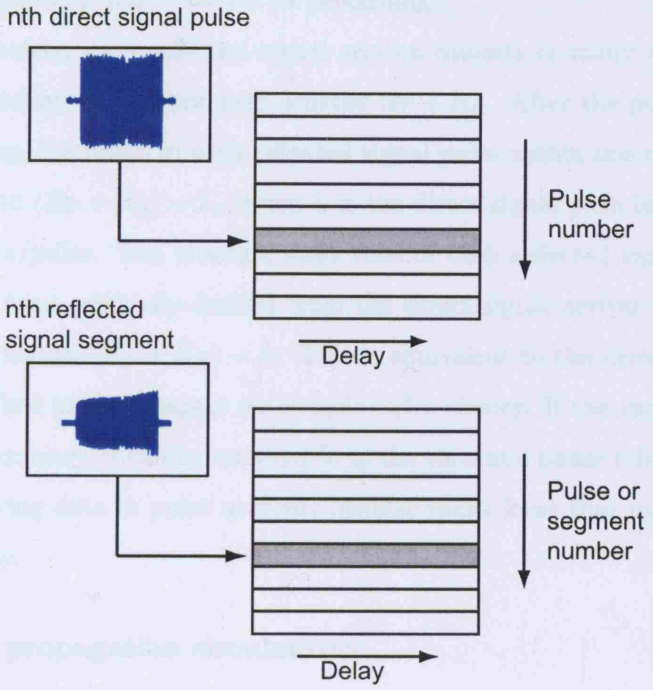

Figure 6-2: Arrangement of raw data pulses/segments in matrix format

(or range compressed) output is provided. The combined operation of matched filtering and phase compensation are separable, as the direct signal phase is a function of pulse number, not delay. The operation for one pulse may be described as:

$$s_{rc}(\tau_o) = e^{(-j\theta_d)} \int_{-\infty}^{+\infty} f(\tau)h(\tau_o - \tau)d\tau$$

Where s_{rc} is the output signal, θ_d the direct signal phase, f represents the reflected signal section and h is the ASAR chirp replica. The phase referencing operation, multiplication by $e^{(-j\theta_d)}$, may be thought of to occur after pulse compression of the reflected signal data. In order for the referencing to produce a maximum accuracy output phase, the measured phase of both the direct and reflected signal data must also be of maximum accuracy. As a result, θ_d is measured from the pulse compressed direct signal. The reflected signal is compressed as part of the overall operation already described and so the output phase of s_{rc} is of maximum accuracy. These steps lead to the condition that the raw data input to the subsequent SAR processor has already been range compressed, and so the accelerated

chirp scaling algorithm must be used for processing.

As mentioned before, each reflected signal section consists of many echo pulses superimposed, corresponding to different path lengths $R_T + R_R$. After the pulse compression and phase referencing, the phase of each reflected signal pulse within one reflected data section is proportional to $(R_T + R_R) - L$, where L is the direct signal path length for that particular data section/pulse. The absolute start time of each reflected signal pulse within the section, having been originally derived from the direct signal arrival time at the receiver, is also proportional to $(R_T + R_R) - L$. This is equivalent to the direct method for target detection described in the Chapter on bistatic radar theory. If the variation of L is known with sufficient accuracy, it can be removed from the time and phase relations of the reflected signal data, leaving data in pulse number, bistatic range form that may be processed in a conventional way.

6.1.2 Orbit propagation simulations

Knowledge of the baseline length L comes from a satellite orbit propagation simulation, coupled with the position of the receiver, measured with a GPS receiver. The simulation was performed with the aid of the CFI software, a group of precompiled C libraries for such operations as timing, coordinate conversions, and orbit propagation, from the Envisat website [69]. Various C files were written using these libraries, and accessed from within Matlab by writing a gateway routine and performing a mex file compilation. For example, the 'ppf_orbit' software library, and in particular the 'po-ppforb' function is used to predict Cartesian and Kepler state vectors for Envisat, at some time defined by the user. The sequence of function calls consists of two or more steps, initialisation and then one or more propagation calls. The initialisation call makes use of an initial orbit state vector obtained from DORIS data, all output state vectors obtained in the propagation calls are calculated relative to this.

DORIS stands for Doppler ORbitography Integrated by Satellite, and is a system used for precise position determination. For the application of orbit determination, the system uses a collection of ground beacons which act as transmitters and a receiver mounted on the satellite. Signals are transmitted from the ground beacons, and every ten seconds the Doppler shift of these is measured by the receiver. The satellite relays the acquired and stored data to the DORIS mission control centre at regular intervals, and it is subsequently

processed in order to generate the highly accurate satellite position information. The precision orbit thus generated for Envisat has a radial rms error of less than 2.5cm and a 3D rms error of less than 10cm.

As a result, satellite position and velocity vectors are produced over time for an earth-fixed coordinate system. The spacing in time of subsequent position and velocity vectors is set to the pulse repetition interval for the particular swath. Note that the effects of earth rotation are included within the coordinate system, and so the minimum range between a point on the earth and the satellite is the true zero Doppler position, not necessarily coincident with the satellite antenna boresight however. The satellite position with time, coupled with the position of the receiver may also be used to generate the Doppler rate f_R variation with time for the receiver point. This is based on Appendix B3 from Curlander [101], which gives expressions for the Doppler rate calculated from satellite attitude parameters.

6.1.3 Baseline compensation in received data

As described previously in the overview, we have a set of received signal data which has a delay and phase proportional to $(R_T + R_R) - L$. In order to remove the L dependance, the simulated baseline length L_{sim} is used to interpolate and phase shift the data array. One question that arises is which azimuth time sample in the data array corresponds to the minimum range between satellite and receiver, L_{min}, as L_{sim} must be aligned with this true minimum in order for accurate compensation to be performed. The direct signal received from the satellite in the direct signal channel may be examined to give an approximate form for L, which shall be denoted L_{app}. This is approximate because examining the received signal from one channel in isolation implies no phase synchronisation (with the transmitter) has been performed on that data, and as a result the phase will drift relative to the true value. In effect this is the same as if indirect phase synchronisation were used, with an additional phase offset. As was shown in the last Chapter, having no phase synchronisation in this way will lead to a phase error between transmitter and receiver local oscillators. It was demonstrated that an rms phase error of approximately 90^0 would be expected over a period of several seconds, which equates to an rms range error of $\lambda/4$, equal to $1.41 \times 10^{-2} m$. In the indirect synchronisation case, the processing is sensitive to quadratic phase errors

and so this phase drift may be modelled as a quadratic function of azimuth time t:

$$\epsilon_p(t) = \epsilon_0 + \epsilon_1 t^2$$

It is assumed that linear and other terms in t have negligible effect. At the start of the signal capture, the error is zero, and it is assumed that after 3.5 seconds (half of the total signal capture length), the rms error has reached a value of 90^0. The measured direct signal range variation in the single channel will therefore follow:

$$L_{app} = \sqrt{r_0^2 + V_{FM}^2(t - t_0)^2} + \epsilon_r$$

Where,

$$\epsilon_p = \frac{2\pi\epsilon_r}{\lambda}$$

If no error were present, the direct signal range would have a minimum value, r_0, which occurs at time t_0. The time of range minimum for L_{app} is calculated by producing an expression for the stationary point of this function, where $d(L_{app})/dt = 0$. Assuming that $t_0 = 0$, this gives:

$$\frac{V_{FM}^2 t}{\sqrt{r_0^2 + V_{FM}^2 t^2}} + 2\epsilon_1 t = 0$$

The solution to this equation that is of interest is $t = 0$, and so the time of minimum range has not been shifted by the error function. Assuming that the quadratic phase error term ϵ_1 has the most effect on the overall phase error, it may be assumed that the time of range minimum measured in L_{app} is accurate for processing purposes.

The minimum of the simulated baseline length, $L_{sim,min}$ is aligned with the $L_{app,min}$ determined from the direct signal phase and then the interpolation and phase shift are applied. The operations just described are summarised in Figure 6-3.

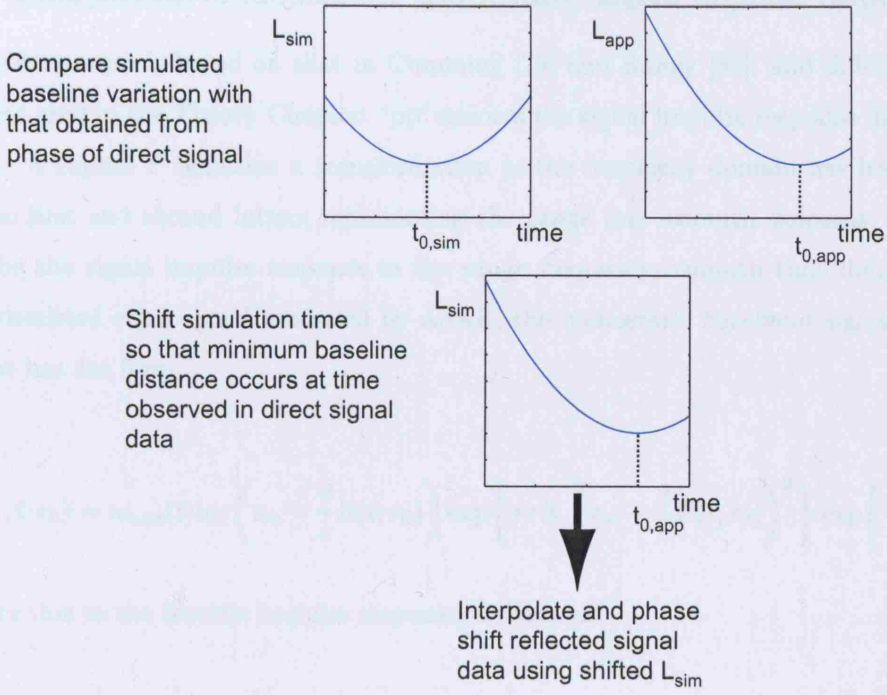

Figure 6-3: Interpolation and phase shifting operations to compensate for the baseline variation, L

6.2 Bistatic SAR Signal Processing

6.2.1 Overview

The bistatic SAR processing is based on the monostatic Chirp Scaling algorithm. In a monostatic system, there is a two-way varying path length from transmitter to target and back to the receiver. In the bistatic system the time-varying path length is one-way, from transmitter to target, and so this factor of two may be applied to the processing algorithm to convert a monostatic SAR processor to a narrow-focus bistatic SAR processor. In addition, the standard chirp scaling algorithm is designed to operate on raw data, whereas the data input to the bistatic algorithm will have already been range compressed as part of the pre-processing. As a result, a variant of the standard approach called the accelerated chirp scaling algorithm [37], used for range compressed data, has been adapted to the bistatic case. The following compares monostatic and bistatic processing with the accelerated chirp scaling algorithm.

6.2.2 Comparison of monostatic and bistatic signal impulse responses

The notation used is based on that in Cumming [79] and Raney [83], and differs slightly from that used in the Theory Chapter. 'pp' denotes the signal impulse response in the time domain. A capital P indicates a transformation to the frequency domain has been made, with the first and second letters representing the range and azimuth domains. So, 'Pp' would be the signal impulse response in the range frequency/azimuth time domain. For the transmitted chirp signal produced by ASAR, the monostatic baseband signal impulse response has the form,

$$pp_m(\tau_m, t; r_0) = w_{a,m}(t) w_r \left(\tau_m - \frac{2}{c} R(t; r_0)\right) \exp\left\{j\pi K \left(\tau_m - \frac{2}{c} R(t; r_0)\right)^2\right\} \exp\left\{-j\frac{4\pi}{\lambda} R(t; r_0)\right\} \tag{6.1}$$

Compare this to the bistatic impulse response, written as:

$$\begin{aligned} pp_b(\tau_b, t; r_0) &= w_{a,b}(t) A_R w_r \left(\tau_b - \frac{1}{c}(R_R + R(t; r_0))\right) \exp\left\{j\pi K \left(\tau_b - \frac{1}{c}(R_R + R(t; r_0))\right)^2\right\} \\ &\quad . \exp\left\{-j\frac{2\pi}{\lambda}(R_R + R(t; r_0))\right\} \end{aligned} \tag{6.2}$$

In both of the above, it has been assumed that $t_0 = 0$ and monostatic and bistatic delay τ have also been differentiated between through the use of appropriate subscripts. w_a and w_r are the azimuth and range signal envelopes. ASAR transmits an up-chirp with chirp rate K as may be observed with the first phase function in the two previous equations. The second phase function shows the azimuth modulation, which is dependent on (time-varying) range. The range to target in the bistatic case is formed from the bistatic range sum, consisting of a time-varying term, the range from satellite to target, and a fixed term representing the range from receiver to target.

It is useful to examine the azimuth Fourier transform of the impulse response. A direct calculation may not be performed when the range curvature is present in the signal envelope, and so the method presented in Cumming [79] for monostatic signals is applied to this bistatic case. This involves performing subsequent range and azimuth Fourier transforms and finally a range inverse Fourier transform using the method of stationary phase. The azimuth Fourier transform, firstly for monostatic, and then for the bistatic system are given

in Equations (6.3) and (6.4). These have been derived making use of an approximation in the phase of the range frequency, azimuth frequency signal, which means that the results are accurate for moderate synthetic aperture length and squint. Details of the working are given in Appendix C.

$$\begin{aligned} pP_m(\tau_m, f; r_0) &= C_{a,m} W_{a,m}(f - f_{DC}) w_r \left(\frac{1}{1 - K_r Z_m} \tau_m - \frac{2r_0}{cD(f, V_{FM})} \right) \\ &\quad . \exp\left\{ j\pi K_{m,m} \left(\tau_m - \frac{2r_0}{cD_m(f, V_{FM})} \right)^2 \right\} \\ &\quad . \exp\left\{ -j \frac{4\pi r_0 D_m(f, V_{FM})}{\lambda} \right\} \end{aligned} \tag{6.3}$$

$$\begin{aligned} pP_b(\tau_b, f; r_0) &= C_{a,b} W_{a,b}(f - f_{DC,b}) A_R w_r \left(\frac{1}{1 - K_r Z_b} \tau_b - \frac{r0}{cD_b(f, V_{FM})} - \frac{R_R}{c} \right) \\ &\quad . \exp\left\{ j\pi K_{m,b} \left(\tau_b - \frac{r0}{cD_b(f, V_{FM})} - \frac{R_R}{c} \right)^2 \right\} \\ &\quad . \exp\left\{ -j \frac{2\pi (r_0 D_b(f, V_{FM}) + R_R)}{\lambda} \right\} \end{aligned} \tag{6.4}$$

The first item in each equation, C, is a complex constant that arises as a result of the stationary phase method. This is followed by the antenna azimuth pattern W_a in the azimuth frequency domain, centred on the Doppler centroid. For the bistatic signal, the factor A_R is a constant representing the receiver antenna gain for the target point. w_r is the range signal envelope (a rectangle function). The pulse length has been altered by a factor $1/(1 - K_r Z)$. $|K_r Z| << 1$ so this change is small. Range cell migration has caused a shift of the signal envelope by $r0/cD(f, V_{FM})$. $D(f, V_{FM})$ is related to the range curvature factor given in Raney [83], and describes range migration in the azimuth frequency domain. It is given by,

$$D_m(f, V_{FM}) = \sqrt{1 - \left(\frac{\lambda f}{2V_{FM}} \right)^2} \qquad D_b(f, V_{FM}) = \sqrt{1 - \left(\frac{\lambda f}{V_{FM}} \right)^2}$$

The factor of two difference in the two D terms of the previous equation is as a direct result

of the one-way as opposed to two-way varying path length in the bistatic system. Also note that this term does not alter the (bistatic) range to receiver R_R. This range is constant with azimuth time and so this is expected. The first phase term gives the range modulation, with a modified FM chirp rate of K_m.

$$K_{m,m} = \frac{K_r}{1 - K_r Z_m} \qquad K_{m,b} = \frac{K_r}{1 - K_r Z_b}$$

This has been altered as a result of coupling between range and azimuth, with the modifying factor being range dependent:

$$Z_m(r_0, f) = \frac{\lambda^3 r_0 f^2}{2V_{FM}^2 c^2 D_m(f, V_{FM})^3} \qquad Z_b(r_0, f) = \frac{\lambda^3 r_0 f^2}{V_{FM}^2 c^2 D_b(f, V_{FM})^3}$$

$1/Z$ is the secondary range compression filter, thus compensation for this coupling is known as secondary range compression.

Accelerated chirp scaling operates on range compressed data. Assuming a replica of the ASAR chirp with chirp rate K is used for the range compression, the resultant signal will have a residual chirp that results from the range distortion term of K_{bs}. This residual chirp has a low time-bandwidth product and so the method of stationary phase may no longer be applied - as a result, an analytic formulation for the range compressed impulse response in the delay/azimuth time or delay/Doppler domains may not be given. However, the accelerated chirp scaling processing, from Hawkins [37] performs the same operations as conventional chirp scaling, without the phase multiply for range compression. As a result, the phase functions for conventional chirp scaling processing of the bistatic impulse response are first derived, then these are used for the accelerated chirp scaling processing, with the adaption to the range compression phase term already mentioned. For the processing, it is assumed that the range variation of the signal input to the processor is:

$$R_{app}(t - t_0; r_0) = \sqrt{(R_R + r_0)^2 + V^2(t - t_0)^2} \approx R_R + \sqrt{r_0^2 + V^2(t - t_0)^2}$$

The phase is given by,

$$\phi_{app}(t - t_0; r_0) = -\frac{2\pi}{\lambda} R_{app}(t - t_0; r_0)$$

The above approximation only holds for R_R values that are small in comparison with r_0 and for small ranges of azimuth time t. Given the relatively small imaged area of the experimental system, these conditions hold, as shall be demonstrated with the effect on Quadratic Phase Error in the simulations in later in this Chapter. The phase functions used in the bistatic processor are those that would compress a signal with phase variation ϕ_{app} exactly.

6.2.3 Bistatic chirp scaling algorithm phase functions

The phase functions used in the narrow-focus bistatic chirp scaling algorithm are described. Note in the following that $f_0 = \frac{c}{\lambda}$ is the centre frequency of transmission of the radar system.

Phase function 1 and range FT

The signal input to this stage is as given in (6.4). The first phase function of the processor, below, performs chirp scaling on this input in the range/Doppler domain.

$$\phi_1 = \exp\{j\pi K_{m,b}\left[\frac{D_b(f_{ref}, V_{FM,ref})}{D_b(f, V_{FM,ref})} - 1\right](\tau_{b,ref})^2\} \tag{6.5}$$

The azimuth frequency f_{ref} and effective velocity $V_{FM,ref}$ correspond to the reference range r_{ref}, which is contained within the $\tau_{b,ref}$ term:

$$\tau_{b,ref} = \tau_b - \frac{r_{ref}}{cD(f, V_{FM,ref})} \tag{6.6}$$

In the chirp scaling operation, the range migration of all scatterers are altered to be equal to that of a scatterer at a reference range, r_{ref}.

The phase of the signal after multiplication by the first phase function and subsequent application of a range Fourier transform is given in Equation (6.7). These terms were calculated using the 'Maple' software package, which performs simplification of symbolic expressions.

$$\begin{aligned}\phi_{stage1,out} = & -\frac{\pi D_b(f,V_{FM}) f_{\tau,b}^2}{D_b(f_{ref},V_{FM})K_{m,b}} - \frac{2\pi}{c}\left(\frac{r_0}{D_b(f_{ref},V_{FM,ref})+R_R}\right) f_{\tau,b} \\ & -\frac{2\pi r_{ref} f_{\tau,b}}{c}\left(\frac{1}{D_b(f,V_{FM,ref})} - \frac{1}{D_b(f_{ref},V_{FM,ref})}\right) \\ & -\frac{2\pi f_0(r_0 D_b(f,V_{FM})+R_R)}{c} + \theta_e\end{aligned} \tag{6.7}$$

The first three phase functions of Equation (6.7) appear in the output of the monostatic chirp scaling function at this point, although the second and third have an extra factor of two in the numerator as a result of monostatic as opposed to bistatic operation.
θ_e represents a complicated expression of extra phase terms, again produced using Maple, involving combinations of r_0, r_{ref}, R_R, and D_b (but no terms with $f_{\tau,b}$).

Phase function 2 and range IFT

The second phase function to be applied is:

$$\phi_2 = \exp\left\{j\frac{\pi D_b(f,V_{FM}) f_\tau^2}{D_b(f_{ref},V_{FM})K_{m,b}}\right\}\exp\left\{j\frac{2\pi r_{ref} f_{\tau,b}}{c}\left(\frac{1}{D_b(f,V_{FM,ref})} - \frac{1}{D_b(f_{ref},V_{FM,ref})}\right)\right\} \tag{6.8}$$

This phase function compensates for the first and third phase terms in Equation (6.7), performing range compression (including secondary range compression), and bulk range cell migration correction. Note that bulk range cell migration is the total RCM of the target at the reference range r_{ref}. For accelerated chirp scaling, the range compression operation is removed. Application of a range inverse Fourier transform gives the output phase shown in Equation (6.9).

$$\phi_{stage2,out} = -\frac{2\pi f_0(r_0 D_b(f,V_{FM})+R_R)}{c} + \theta_e \tag{6.9}$$

The signal has been range compressed to a position,

$$\tau_b = \frac{r_0}{cD_b(f_{ref},V_{FM,ref})} + \frac{R_R}{c}$$

The envelope of this signal in range is a sinc function if the original range pulse was rectan-

gular.

The phase terms remaining in Equation (6.9) are azimuth modulation (for the first) and residual phase (for the second). These shall be partially compensated for in the next stage of processing.

Phase function 3 and azimuth IFT

The final phase function to be applied is:

$$\phi_3 = \frac{2\pi f_0 D_b(f, V_{FM})(r_0 + R_R)}{c} - \frac{2\pi K_{m,b}}{c^2}\left[1 - \frac{D_b(f, V_{FM,ref})}{D_b(f_{ref}, V_{FM,ref})}\right]\left[\frac{r_0}{D_b(f, V_{FM})} - \frac{r_{ref}}{D_b(f, V_{FM})}\right]^2 \tag{6.10}$$

The azimuth modulation of (6.9) is partially compensated for by the first term of this third phase function, while the second term of the phase function combines with the θ_e to give a new phase residual. The phase terms left over are functions of azimuth frequency and range, and as a result of this coupling between the two, the inverse azimuth Fourier transform can not be calculated. The residual phase that has not been compensated at this stage will lead to defocusing of the azimuth impulse response.

6.3 Conversion to map coordinates

The last operation to be performed is that of data conversion from the bistatic image plane, azimuth distance x versus bistatic range $R_T + R_R$, to a grid coordinates plane, Eastings versus Northings. These coordinates are those used in United Kingdom maps and will enable comparison of the bistatic images with aerial or satellite photographs, maps of the area, and the monostatic SAR images supplied by ESA. Given the satellite and receiver position for a data acquisition (the former is obtained through the orbit propagation simulations detailed earlier), which are in cartesian earth-fixed coordinates, the first step is to find a (cartesian) target point corresponding to each point in the image. For a given image point, the range sum $R_T + R_R$ is known from the delay difference between this point and that of the receiver, which has a range L_{min}. The azimuth time relative to L_{min}, the minimum range between satellite and receiver, is also known, which gives a single satellite position and single satellite velocity vector. The Earth's surface around the receiver is represented by a plane (flat Earth model). From the position of satellite and receiver, together with a constant bistatic range

sum, an ellipsoid is defined. This may intersect with the (Earth surface) plane, and if it does, will either define a single point or an ellipse. Effectively, there are now two equations for three unknowns. The final equation constrains the satellite to target vector to lie in the zero Doppler plane of the satellite, in other words this vector is perpendicular to the velocity of the satellite. The three equations to be solved simultaneously may therefore be written:

$$\sqrt{(x_t - x_r)^2 + (y_t - y_r)^2 + (y_t - y_r)^2} + \sqrt{(x_t - x_s)^2 + (y_t - y_s)^2 + (z_t - z_s)^2} = C \quad (6.11)$$

$$ax_t + by_t + cz_t = p \quad (6.12)$$

$$V_{sx}(x_t - x_s) + V_{sy}(y_t - y_s) + V_{sz}(z_t - z_s) = 0 \quad (6.13)$$

(x_s, y_s, z_s), (x_r, y_r, z_r) and (x_t, y_t, z_t) are the satellite, receiver and target positions respectively. (V_{sx}, V_{sy}, V_{sz}) is the satellite velocity and a, b, c and p define a plane. So, the first equation defines a constant bistatic range sum, equal to C, the second that the target point should lie on a flat plane defining the Earth's surface, and the third that the satellite to target vector is perpendicular to the satellite velocity. The (lengthy) solution to this set of equations was found using Maple and coded as a function in Matlab. For a given bistatic configuration, there may be some points in the image that do not have a valid solution to the equation set, giving a complex answer. These will be described in more detail in the image results Chapter.

It is necessary to convert the Cartesian coordinates given from the solution to grid Eastings and Northings. The National GPS Network website [86] has several descriptions of the mathematical operations necessary to convert to and from Cartesian, elliptical (latitude, longitude and height) and grid coordinates (Eastings, Northings). These were coded as functions in Matlab and tested against example coordinate sets provided on the aforementioned website. The Cartesian target points are thus converted first to elliptical and then to grid coordinates.

The final stage is to convert the bistatic image to the newly calculated grid coordinates,

using a data gridding function. The function 'griddata', supplied with Matlab is used to this effect, with a triangle based cubic interpolation applied to the image points.

6.4 Processing Algorithm Tests

6.4.1 Overview

This section of the thesis covers the imaging simulations performed to validate the SAR processing operation and demonstrate the depth of focus of the bistatic processor. Some tests of a monostatic chirp scaling algorithm may be found in Appendix D, where experimental data from an airborne SAR trial (supplied by QinetiQ) has been processed.

6.4.2 Depth of focus

The processing tests will illustrate the depth of focus of the system, and so the impulse response broadening and increase in peak-to-sidelobe ratio, as a result of mismatch between the azimuth compression filter FM rate and that in the actual received signal. The depth of focus of SAR processing may be quantified through the use of the Quadratic Phase Error (QPE), which from Cumming [79] is defined as:

$$QPE = \pi \Delta K \left(\frac{T}{2}\right)^2 \tag{6.14}$$

ΔK is the error in FM rate K of the compression filter and T is the time duration of the filter. In this way, the QPE is the relative phase mismatch at either end of the signal (whichever is greater).

From Cumming [79], the azimuth matched filter phase is approximately,

$$\phi_{az} \approx \pi K_a (t - t_c)^2$$

With azimuth FM rate (bistatic),

$$K_a = \frac{V_{FM}^2 \cos(\theta_{r,c})^2}{\lambda R(t_c)}$$

The previous equation for azimuth FM rate is equal to $f_{R,b}$, the bistatic Doppler rate given in (3.22). The azimuth matched filter phase has been approximated by the quadratic

component, obtained from the expansion of the hyperbolic range equation about the beam centre time t_c:

$$R(t) = R(t_c) - V_{FM}\sin(\theta_{r,c})(t - t_c) + \frac{1}{2}\frac{V_{FM}^2\cos(\theta_{r,c})^2}{R(t_c)}(t - t_c)^2 + ... \tag{6.15}$$

It is this quadratic term that dominates the resultant phase error for processing and results in the impulse response width broadening and increase in first sidelobe level.

The increase in mainlobe width, or impulse response width (IRW) broadening, and first sidelobe level as a function of the QPE in the azimuth matched filter (which has a Taylor weighting $\overline{n} = 6$ applied, in order to maintain consistency with the processed bistatic images given later in this thesis) is plotted in Figure 6-4. The quadratic phase error in

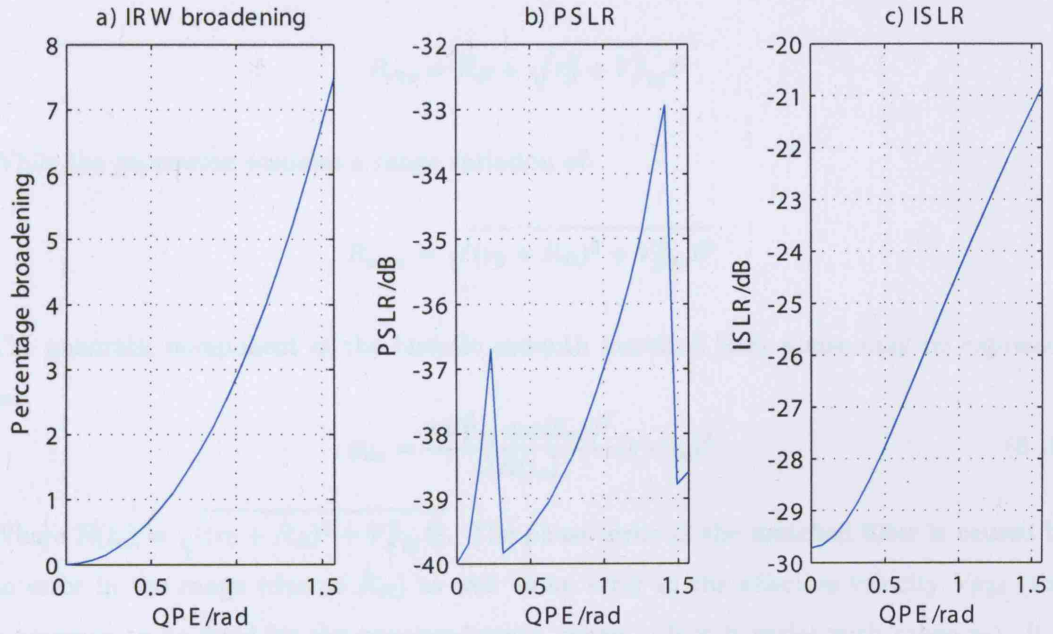

Figure 6-4: Impulse response width broadening, peak-to-sidelobe ratio increase, and integrated sidelobe ratio increase with quadratic phase error for a matched filter with Taylor weighting, $\overline{n} = 6$

this Figure varies from zero to $\pi/2$ radians (or 90^0). As was discussed in the Predicted System Performance Chapter, the acceptable quadratic phase error is typically 90^0. The mainlobe width experiences a broadening of up to 7.5% over this range. The PSLR has two downward jumps, at 0.24rad and 1.42rad. For the first jump, the first sidelobes have been

absorbed into the mainlobe, and so the PSLR is then measured relative to the next sidelobes along, which have a much smaller magnitude. These 'new' first sidelobes then increase with increasing QPE until the second jump when they are absorbed into the mainlobe. This effect is noted in Cumming [79], and it is recommended that ISLR be used instead to quantify the QPE effect on sidelobe energy. Plot c) shows the ISLR as a function of QPE increase. The calculation for ISLR is based on integrating the plot of impulse response magnitude squared (proportional to signal power) over the mainlobe and over the entire impulse response width. The mainlobe width is defined here as 2.8 times the -3dB width of the impulse response produced with no quadratic phase error. The ISLR has risen by 8.9dB for the QPE increase to 1.57rad, a significant amount.

In the bistatic system, the received signal due to a single point target has range variation:

$$R_{rec} = R_R + \sqrt{r_0^2 + V_{FM}^2 t^2}$$

While the processing assumes a range variation of:

$$R_{proc} = \sqrt{(r_0 + R_R)^2 + V_{FM}^2 t^2}$$

The quadratic component of the bistatic azimuth matched filter phase may be expressed as:

$$\phi_{az} = \frac{\pi V_{FM}^2 \cos(\theta_{r,c})^2}{\lambda R(t_c)}(t - t_c)^2 \tag{6.16}$$

Where $R(t_c) = \sqrt{(r_0 + R_R)^2 + V_{FM}^2 t_c^2}$. The phase error in the matched filter is caused by an error in the range (due to R_R) as well as an error in the effective velocity V_{FM} (this is assumed to be fixed for the processed scene, when in fact it varies with range r_0). It is necessary to know the variation of V_{FM} with slant range r_0 in order to quantify the overall phase error produced in the matched filter. For this, the method outlined in Cumming [79] may be applied, based on the approximate relation:

$$V_{FM} \approx \sqrt{V_s V_{gr}} \tag{6.17}$$

This equation will yield results that are adequate for the analysis given here in terms of establishing some approximate limits on scene size for the bistatic processing, but are

not suitable for precision image processing. After producing the relevant V_{gr} values using the method detailed in the Experimental System Chapter and described in Appendix A, application of Equation (6.17) yields the effective velocity V_{FM}. The results of V_{FM} versus slant range for the ASAR image mode swaths IS1 and IS7 are reproduced in Figure 6-5, below. It is apparent that the relationship is approximately linear over the swath width.

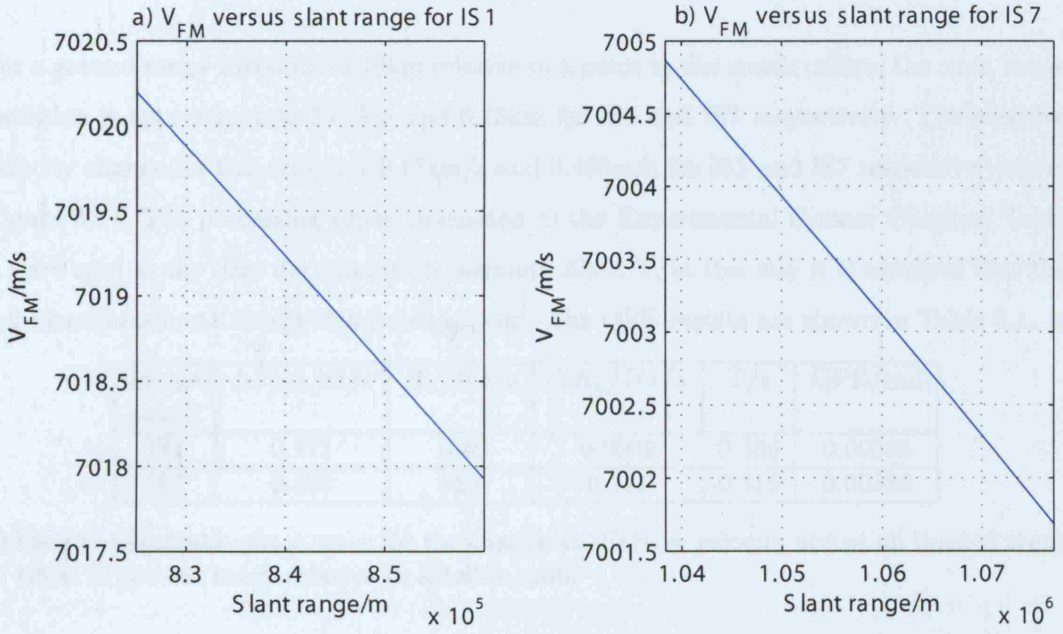

Figure 6-5: Effective velocity versus slant range across the swath for IS1 and IS7

The decrease in effective velocity is relatively small over the entire swath in each case, for example 2.27m/s over a slant range variation of 35.0km for IS1. As the V_{FM} values are calculated with a method that applies to zero Doppler pointing of the antenna beam, the Doppler centroid is taken to be 0Hz for all calculations, and so the squint angle $\theta_{r,c}$ is also zero. Considering the QPE as a result of a velocity error only, gives,

$$QPE_{vel} = \pi \Delta K_{a,vel} \left(\frac{T}{2} \right)^2$$

Where,

$$\begin{aligned}\Delta K_{a,vel} &= \frac{\partial K_a}{\partial V_{FM}}\Delta V_{FM} \\ &= \frac{2V_{FM}}{\lambda r_0}\Delta V_{FM}\end{aligned}$$

For a ground range variation of 10km relative to a point in the swath centre, the slant range variation is approximately 2.64km and 5.75km for IS1 and IS7 respectively. The effective velocity change for this region is 0.171m/s and 0.469m/s for IS1 and IS7 respectively, from Figure 6-5 . The processing times calculated in the Experimental System Chapter, Table 6.1 are used as the time duration of the azimuth filter, T, in this way it is assumed that the full bistatic azimuth bandwidth is being used. The QPE results are shown in Table 6.1. It

Image swath	$\Delta V_{FM}/m/s$	$K_a/Hz/s$	$\Delta K_a/Hz/s$	T/s	QPE/rad
IS1	0.171	1040	0.0509	0.386	0.00596
IS7	0.469	828	0.111	0.319	0.00888

Table 6.1: Quadratic phase error for the change in effective velocity across an imaged scene of 10km in ground range relative to satellite nadir

is apparent from the QPE results table that the change in effective velocity will not have a significant effect on image focus. For the relatively small imaged area of the bistatic system (on the order of a few kilometres square), it shall therefore be assumed that the effective velocity is constant and that the QPE in the azimuth matched filter is due to R_R (a range mismatch) only. The QPE resulting from a range error for zero Doppler pointing is:

$$QPE_{range} = \frac{-\pi V_{FM}^2}{\lambda r_0}\Delta r_0^2 \left(\frac{T}{2}\right)^2 \tag{6.18}$$

The Δr_0 term, representing the range error, is equivalent to R_R. The next section will outline the bistatic imaging geometry and quantify the defocusing that will result.

6.4.3 Simulation scenario

The arrangement is as illustrated in Figure 6-6. A flat earth model is used for the illuminated area around the receiver. The receiver antenna may be pointed in any direction

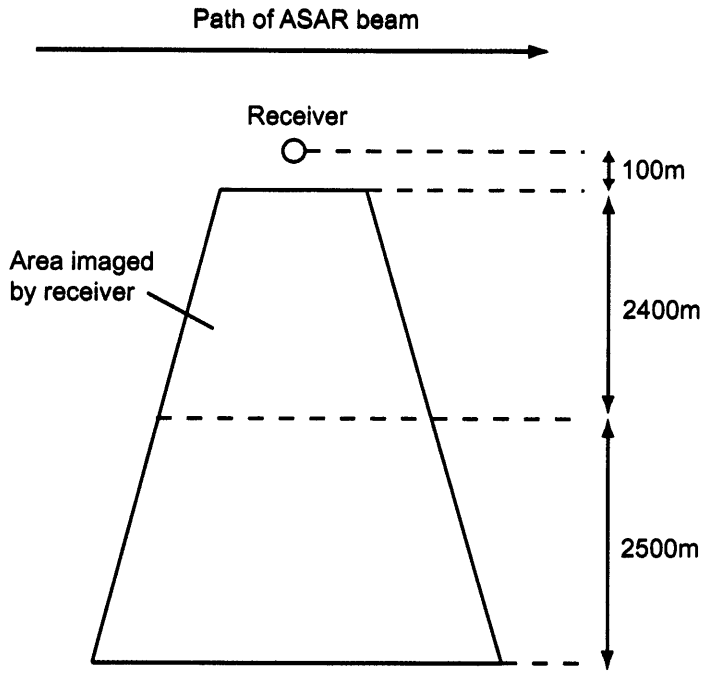

Figure 6-6: Geometry for bistatic SAR point target simulations

relative to the satellite ground track (azimuth), or path of ASAR beam, but the perpendicular direction as illustrated will give the greatest satellite-to-target range variation and so potential defocusing.

A rectangular antenna pattern shall be assumed for both transmitter and receiver, with three point targets considered in the illuminated area corresponding to the three different ground ranges from the receiver of the polygonal illuminated area. These are 100m, 2500m and 5000m from the receiver. The simulations will use typical values for the IS1 and IS7 swaths, as calculated in the Experimental System Chapter, and the processing of the point targets will be performed assuming bistatic operation. The receiver is 15m above the surrounding flat target area at a point in the centre of the illuminated swath. The application of Taylor weighting (with $\overline{n} = 6$) along range and azimuth will be considered as the effects of defocusing covered in the last section assume this. The azimuth resolution is 24m for the simulations, as this is consistent with the resolution of the experimental bistatic images.

6.4.4 Simulation results

From Equation (6.18), the quadratic phase error for these three target points may be calculated and used to predict the defocusing of the impulse response in each case, the results of which are summarised in Table 6.2, for IS1 and IS7 swaths. It may be noted that the IRW

	IS1 swath			IS7 swath		
Ground range of target from receiver/m	QPE/rad	IRW broadening (%)	ISLR/dB	QPE/rad	IRW broadening (%)	ISLR/dB
100	0.0107	-	-29.8	0.0107	-	-29.8
2500	0.266	0.2	-28.9	0.265	0.2	-28.9
5000	0.531	0.8	-27.5	0.529	0.8	-27.5

Table 6.2: Defocusing due to a slant range error (non-zero range R_R) for the IS1 and IS7 ASAR image mode swaths

broadening is very small for the ground range variation (a dash is equivalent to a negligible broadening, for 100m ground range), while the maximum ISLR increase is 2.3dB for both swaths. The simulated impulse responses, generated using the narrow focus bistatic accelerated chirp scaling algorithm, are compared in the following Figures. Figure 6-7 shows the image plots of the response produced at the receiver for IS1 and IS7 simulations, while 6-8 and 6-9 illustrate the cuts along azimuth and bistatic range sum for each of these.

The effect of a finite R_R on the azimuth impulse response is shown in Figures 6-10 and 6-11 for IS1 and IS7 simulations respectively.

The increase in ISLR is obvious in these plots. The mainlobe width broadening is also apparent, but is not significant.

The limit on scene size in terms of R_R may be calculated using Equation (6.18), with the QPE set to 90^0. For the azimuth time duration considered above (giving an azimuth resolution of 24m), this results in a maximum R_R of 10.8km for IS1 and 24.9km for IS7.

The analysis has assumed zero Doppler pointing of the beam. Given that the ASAR instrument employs yaw steering, the maximum bistatic Doppler centroid expected is $f_p/4$, with f_p equal to the pulse repetition frequency. This is a relatively small centroid value and so the results produced here should be fairly representative of the real system.

For the experimental geometry, the combination of receiver height (typically 15m or less above the imaged area) combined with the elevation beamwidth and obstructions in the

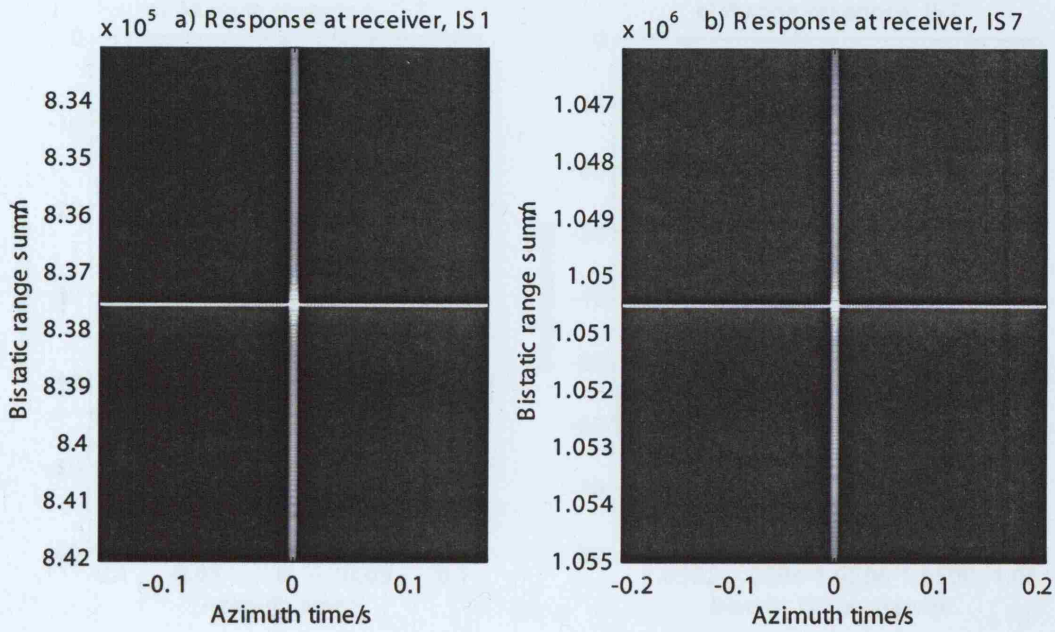

Figure 6-7: Responses produced at the receiver for the IS1 and IS7 simulations

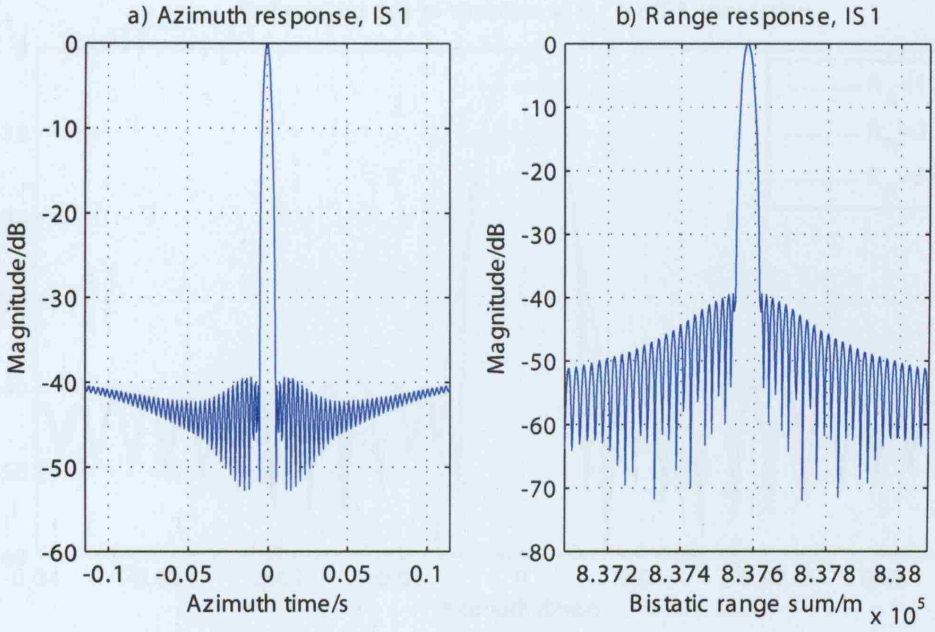

Figure 6-8: Cuts of response produced at receiver, IS1 swath simulation

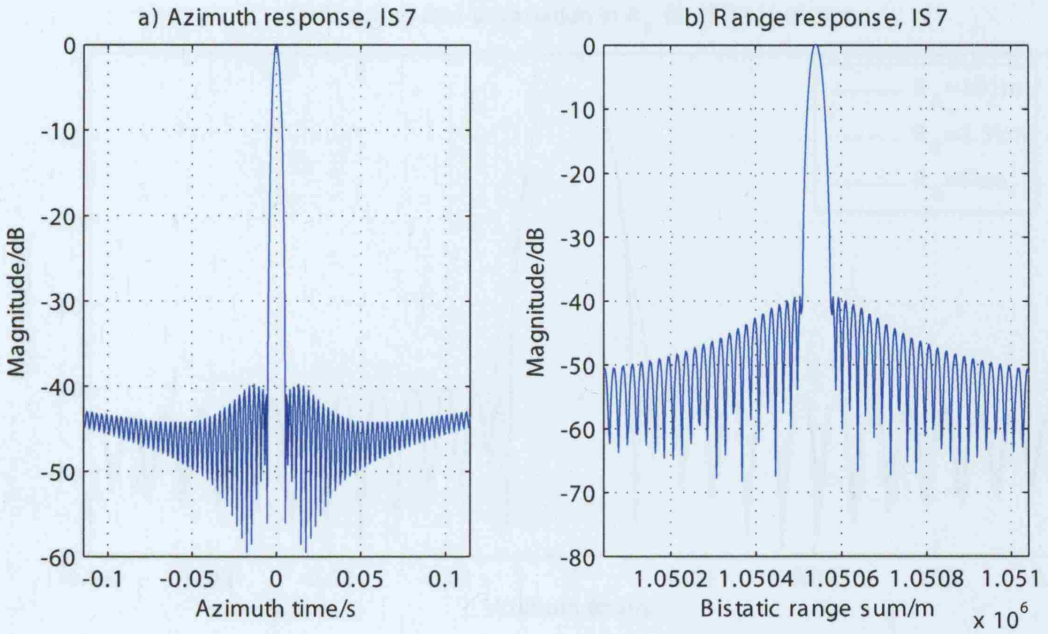

Figure 6-9: Cuts of response produced at receiver, IS7 swath simulation

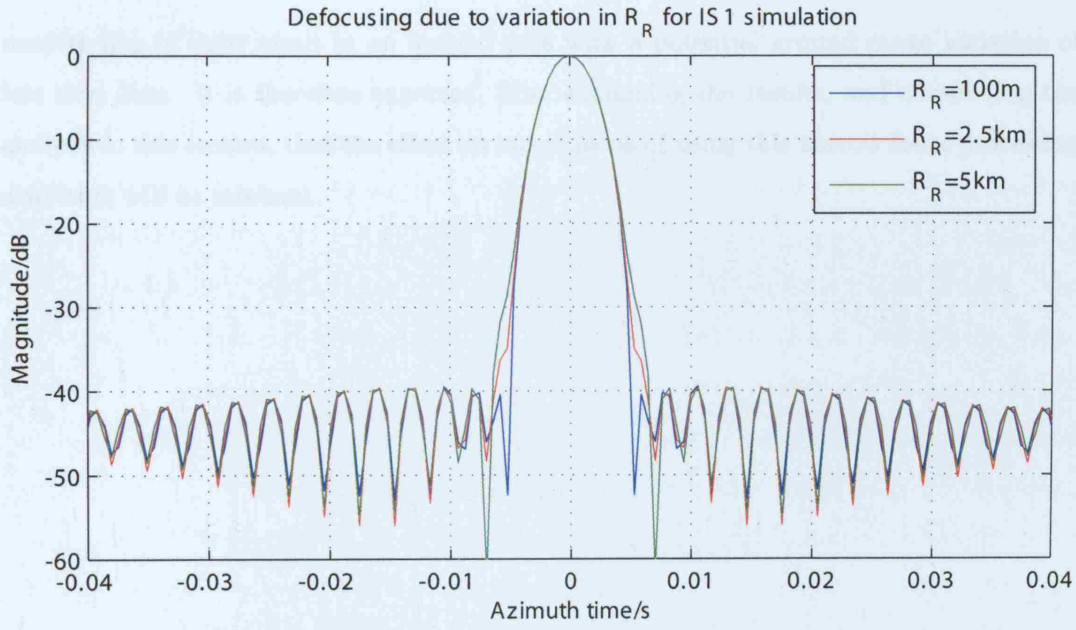

Figure 6-10: Defocusing of azimuth impulse response due to R_R, IS1 swath simulation

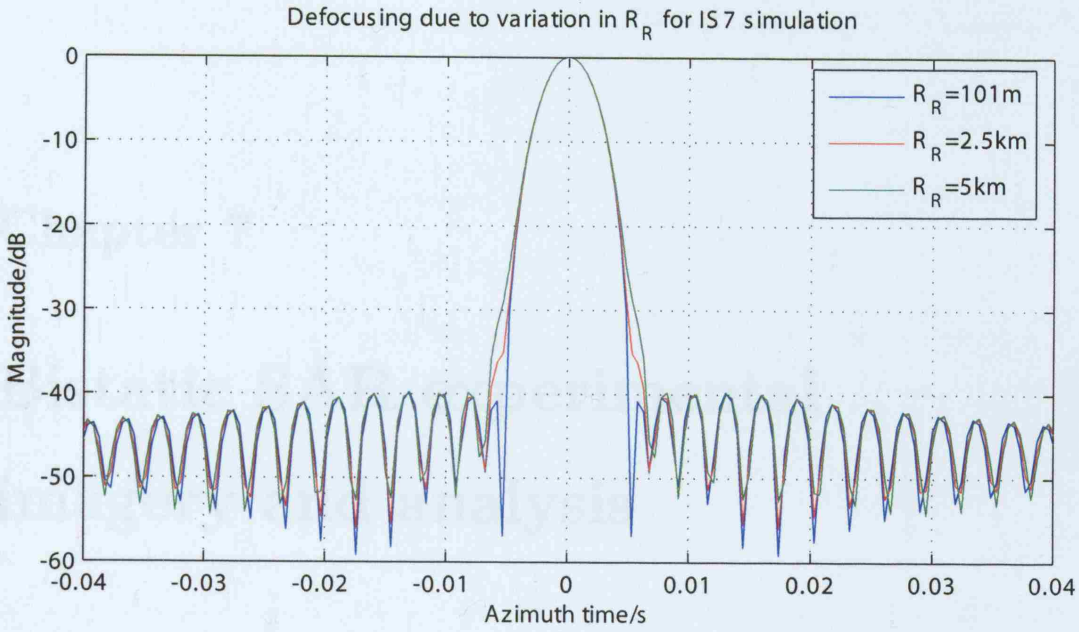

Figure 6-11: Defocusing of azimuth impulse response due to R_R, IS7 swath simulation

receiver line of sight result in an imaged area with a potential ground range variation of less than 2km. It is therefore expected, from examining the results, and considering the analysis in this section, that the effect on image focus of using this narrow focus processing algorithm will be minimal.

Chapter 7

Bistatic SAR experimental imagery and analysis

7.1 Introduction

This Chapter gives the results obtained with regard to the imaging experiments, as well as a discussion of the observations. Experiments may be categorised according to type, location and date. For the type, an experiment may be either a direct signal detection (performed early in the PhD programme in order to validate receiver channel operation and experimental planning) or an imaging acquisition (performed with two channels). The locations include two rooftops in central London as well as a laboratory roof at DSTL Portsdown West in Hampshire. The order in which the results shall be presented is as follows. The Portsdown site results are given at the beginning, the central London acquisition data then follow. The reason for this ordering is due to the nature of the scenes imaged - in the Portsdown case there are far fewer scatterers than in central London, and so these results act as a control, to which the highly cluttered central London images may be compared. A summary of the bistatic imaging experiments performed, in the order in which they are presented in this thesis, is given in Table 7.1, below.

The experiments are not ordered chronologically, but according to site. Also note that the imaged swath is IS2 for all experiments apart from the last. For the London area, the most likely acquisition that could be booked corresponded to an IS2 swath, due to conflicts between different users of ASAR. Also note the different reflected signal channel antennas -

Experiment description	Date	ASAR swath	Receiver reflected channel antenna
DSTL Portsdown West	5th December 2005	IS2	Parabolic antenna 2
Torrington Place experiment 1	12th November 2004	IS2	Parabolic antenna 1
Torrington Place experiment 2	1st December 2004	IS2	Parabolic antenna 1
Torrington Place experiment 3	19th August 2005	IS2	Parabolic antenna 2
Gower Street experiment 1	25th July 2005	IS2	Parabolic antenna 2
Gower Street experiment 2	25th October 2005	IS4	Parabolic antenna 2

Table 7.1: Summary of bistatic imaging acquisitions performed

parabolic antenna 1 was used for the first two experiments performed on Torrington Place in 2004, after which parabolic antenna 2 was used for all experiments. The results of some direct signal captures which preceded the experiments described here (performed during 2003) are presented in the research paper submitted to the International Conference on Radar 2003 in Adelaide, see Whitewood [60].

7.2 Experimental planning and method

For the experiments, the ASAR instrument on Envisat must be in Image Mode and information is also needed on the exact acquisition area and time. A Category 1 Project Proposal was submitted to ESA in January 2003, and subsequently accepted. This allows the 'principal investigator' (the author) to request and effectively reserve acquisitions by using the EOLI Catalogue and a software program called DESCW (obtainable from the Envisat website, [69]). On the Catalogue, the user selects an area on a map (in this case, Central London), a range of times (of the order of days) and an ASAR mode. Potential acquisitions that meet these criteria are then listed.

The orbit numbers and swath details given for these are input into DESCW, which writes a parameters file. The parameters file is then emailed to ESA in order to make the acquisition request, and the status of the acquisition then becomes 'planned' on the Catalogue. The following sections give the results for all of the bistatic SAR image acquisitions.

7.2.1 DSTL Portsdown West site

Overview and geometry

This experiment was performed on 5th December 2005 at DSTL Portsdown West, near Portsmouth in Hampshire. The ASAR acquisition details are given in the next table, followed by a diagram illustrating the receiver look direction and satellite subtrack. The smaller parabolic antenna was used in the reflected signal channel (parabolic antenna 2).

Swath	IS2
Satellite pass	Descending
Polarisation	VV
Pulse repetition frequency/Hz	1652.4156
Pulse length/s	27.1776×10^{-6}
Receiver position (Easting,Northing)/m	(461632,107065)
Receiver look direction (bearing)/degrees	282

Table 7.2: Acquisition details for DSTL Portsdown West experiment

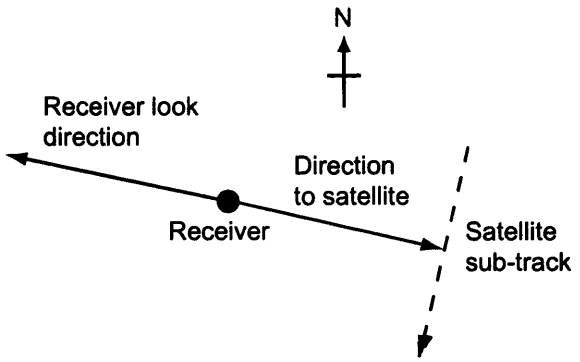

Figure 7-1: Imaging geometry for 5th December 2005 acquisition

Raw data: direct signal channel

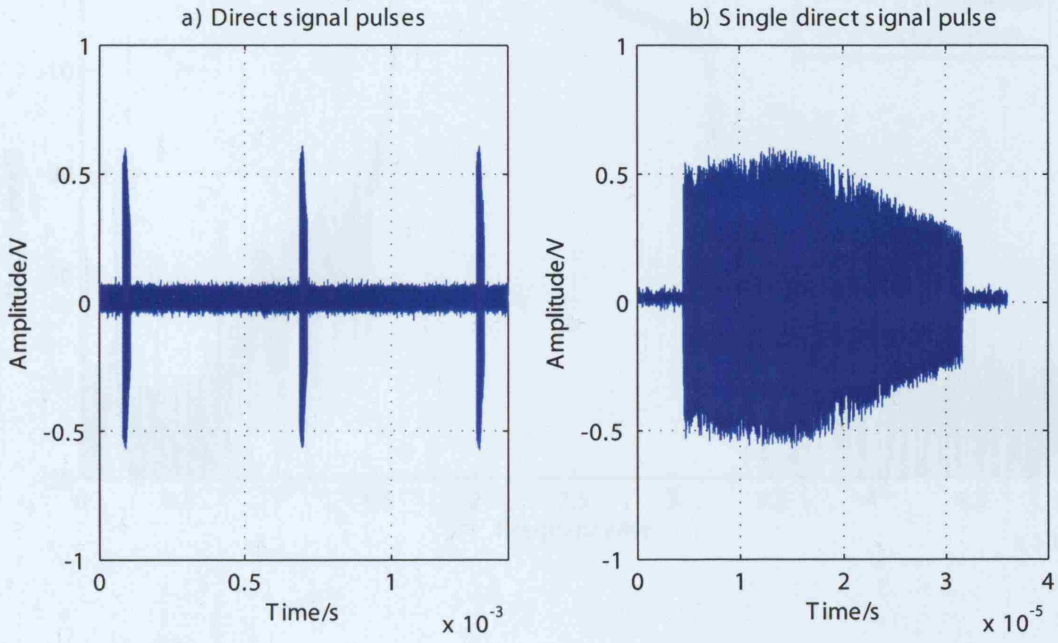

Figure 7-2: Direct signal channel IF pulses captured by the Parsec ADC

Figure 7-2 shows the form of the direct signal pulses captured in the ADC, at a time within the capture for which the pulse amplitudes are at a maximum. They are at a centre frequency of 24MHz, with a) illustrating three pulses and therefore the pulse repetition interval of approximately 0.6ms (equal to the inverse of the prf, 1/1652.4156). After taking the FFT of the direct signal pulse of Figure 7-2 b), Figure 7-3 is produced. It compares the measured frequency response of the captured pulse with a theoretical plot in red. The response is centred on 24MHz, as expected. The IF filter response has attenuated the higher frequencies measured by up to 6dB, although the response is fairly level for frequencies below 24MHz. The maximum signal-to-noise ratio, for the lower frequencies in the pulse bandwidth, is approximately 18dB. This high frequency attenuation may also be observed in the pulse shape of Figure 7-2 b). The IF filter response is designed to have a symmetrical roll-off about 124MHz of approximately 1dB over the 16MHz bandwidth of the ASAR chirp, however the filters are implemented using lumped tunable components whose values have obviously drifted away from their set values. It will be noted that for the other acquisitions the response is much more uniform over the pulse bandwidth. It is perhaps the case that

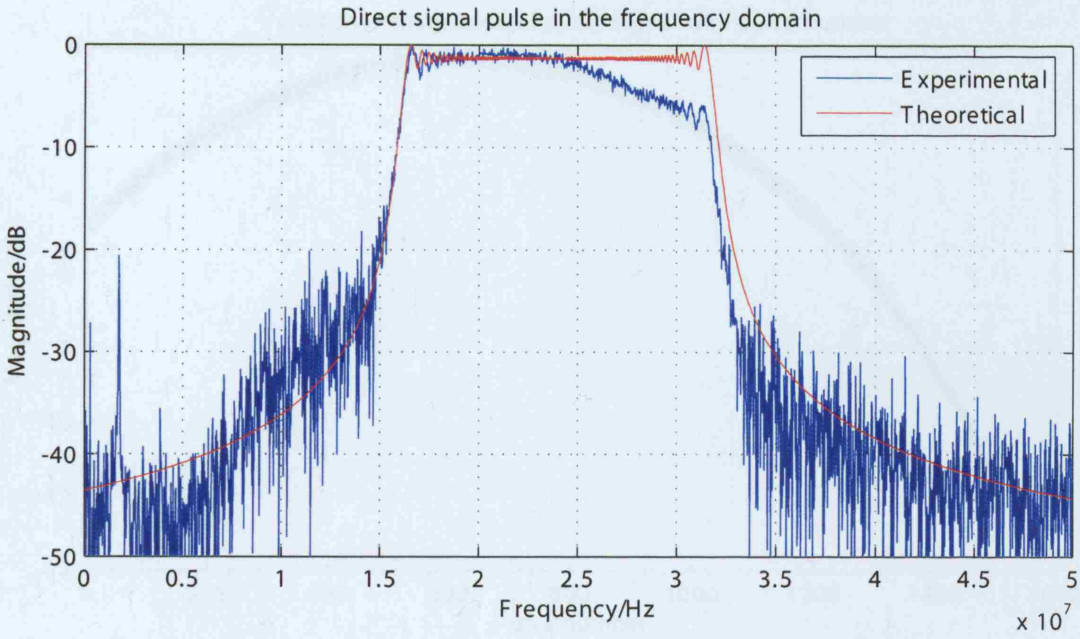

Figure 7-3: Direct signal channel IF pulse in the frequency domain

the transportation of the bistatic receiver to the Portsdown site for this last experiment including possible mechanical vibrations/shocks during the journey resulted in the filter drift.

The direct signal channel will be used for phase measurement, the accuracy of which depends on the signal-to-noise ratios of the pulses used. The attenuation noticed here will reduce the final signal-to-noise ratio after matched filtering of all of the pulses, and the variation in amplitude of the direct signal pulses over a signal capture as a result of the transmitter and receiver antenna patterns will also have an effect. The magnitude of the direct signal pulses for this acquisition is shown in Figure 7-4. The plot has been normalised to have a maximum magnitude of 0dB. The amplitude taper is 13dB across the data capture time of the graph. For the higher frequencies of each pulse the maximum signal-to-noise ratio is approximately 12dB, from the measurements made previously. The direct pulse SNR will therefore be approximately -1dB for pulse numbers approaching 1500. After pulse compression, this signal-to-noise ratio will rise by the compression gain of 26.4dB for IS2 swath to give 25.4dB. The measured phase will have a standard deviation of $2.88 \times 10^{-3} rad$, which is negligible.

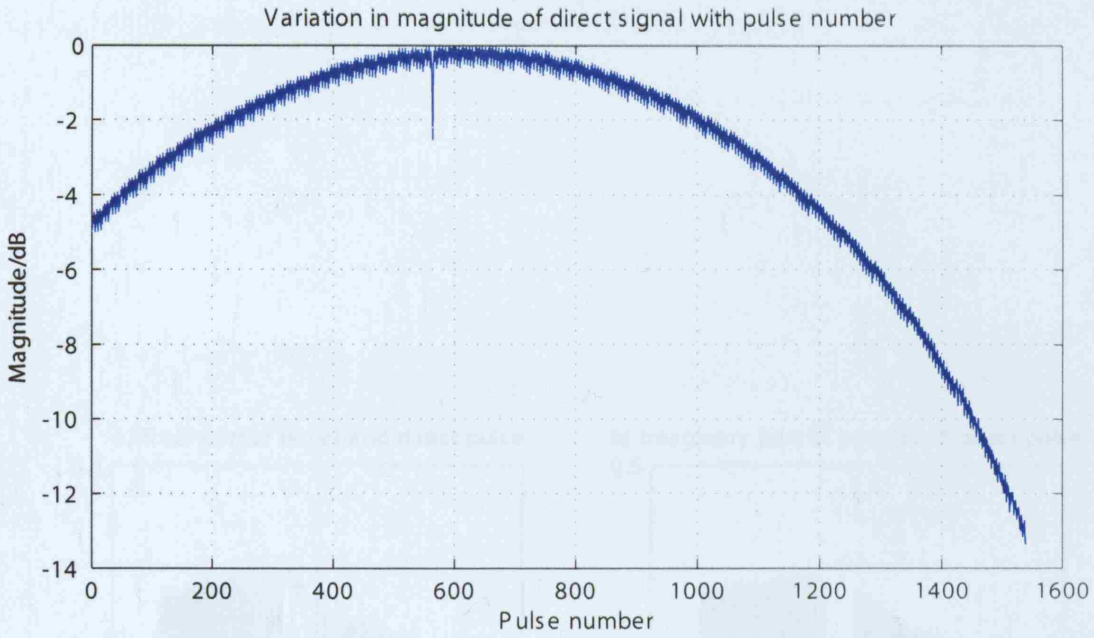

Figure 7-4: Direct signal pulse magnitude versus pulse number for the 5th December 2005 acquisition

In addition, the data to be used for the SAR processing will lie in a region centred about the peak magnitude as seen in this Figure, corresponding to less than half of the ASAR exposure time. This processing time is approximately 0.3s or 500 pulses, which would result in a magnitude taper of 4dB. The SNR values of the direct signal pulses used to process data will therefore be higher than the value calculated here.

The last plot in this section, Figure 7-5, illustrates a direct signal pulse after conversion to baseband.

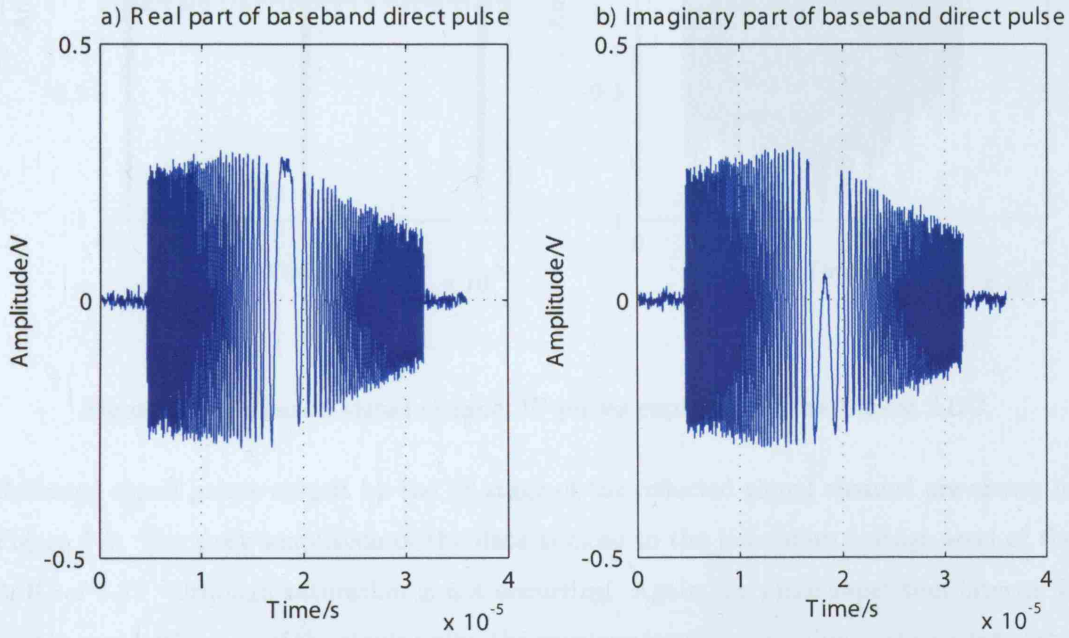

Figure 7-5: Real and imaginary parts of a direct signal pulse after down-conversion to baseband within Matlab

Raw data: reflected signal channel

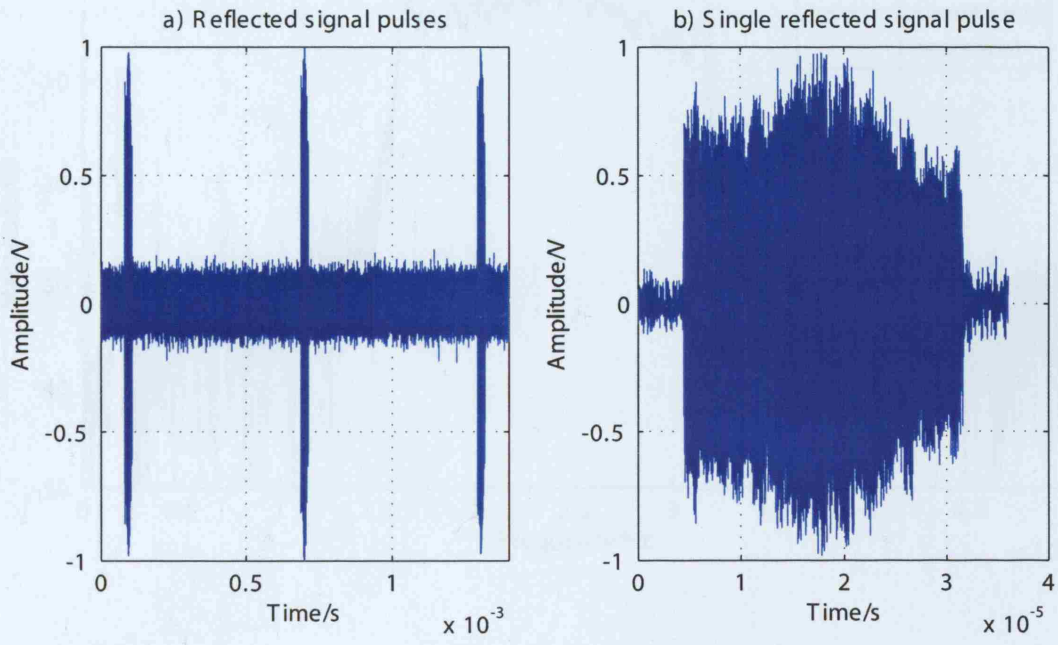

Figure 7-6: Reflected signal channel IF pulses captured by the Parsec ADC

Reflected signal pulses output by the IF stage of the reflected signal channel are shown in Figure 7-6. The peak amplitude of the data is close to the maximum voltage level of the ADC of 1.2V, although saturation is not occurring. Again the pulse repetition interval is visible, and in the case of the single pulse, the envelope is at a peak value in the centre of the pulse, with tapering at each end. The peak noise amplitude is higher in this case than for the direct signal as a result of the higher gain used in this channel. Again, after taking the FFT of the single reflected signal pulse, the graph of Figure 7-7 is produced. The amplitude taper across the signal bandwidth is approximately 1.6dB for the lower frequencies and 4dB for the higher frequencies. Several interfering peaks may be observed below 7MHz, giving a signal-to-noise ratio of 9dB.

A baseband reflected signal pulse is shown in Figure 7-8.

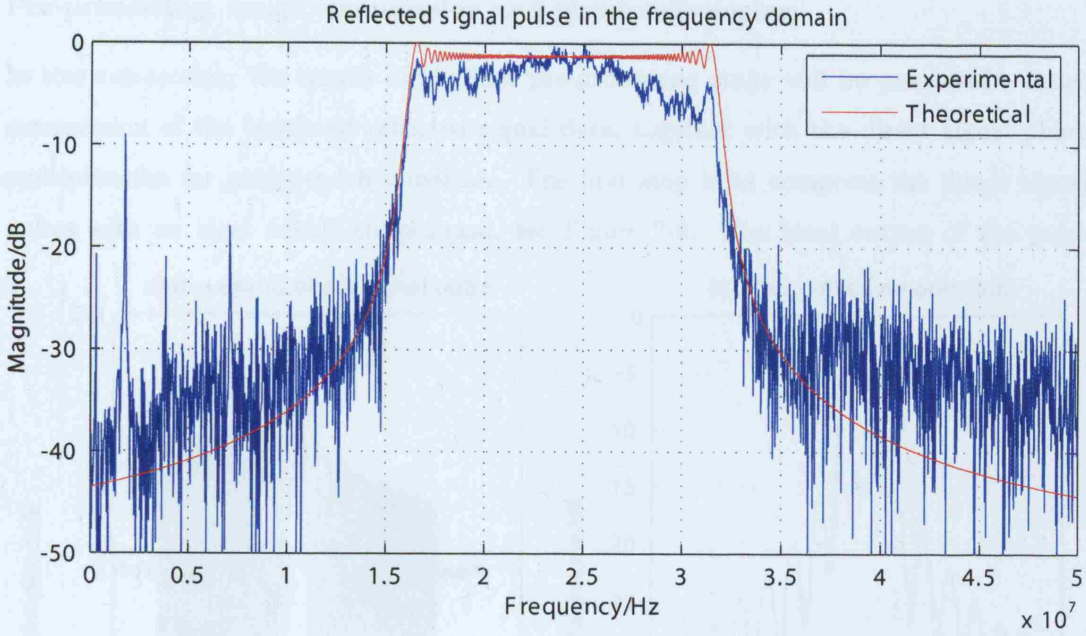

Figure 7-7: Reflected signal channel IF pulse in the frequency domain

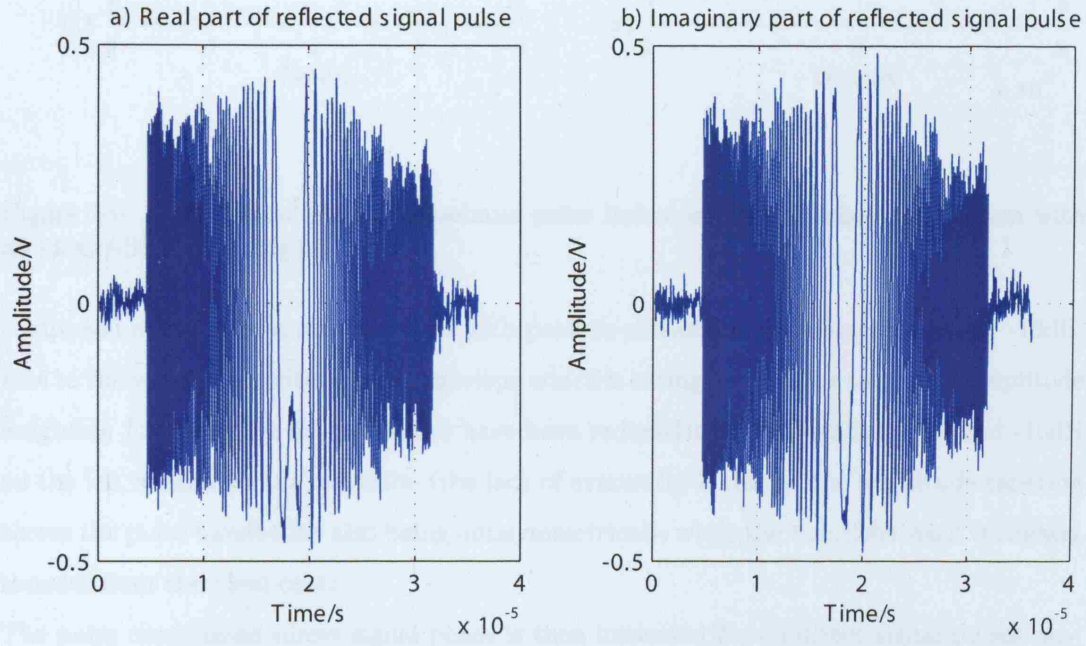

Figure 7-8: Real and imaginary parts of a direct signal pulse after down-conversion to baseband within Matlab

Pre-processing: range compression and phase referencing

In this sub-section, the results of the first pre-processing stage will be presented - range compression of the baseband reflected signal data, together with the direct signal phase multiplication for phase synchronisation. The first step is to compress the direct signal pulses with an ideal ASAR chirp signal, see Figure 7-9. The ideal output of the pulse

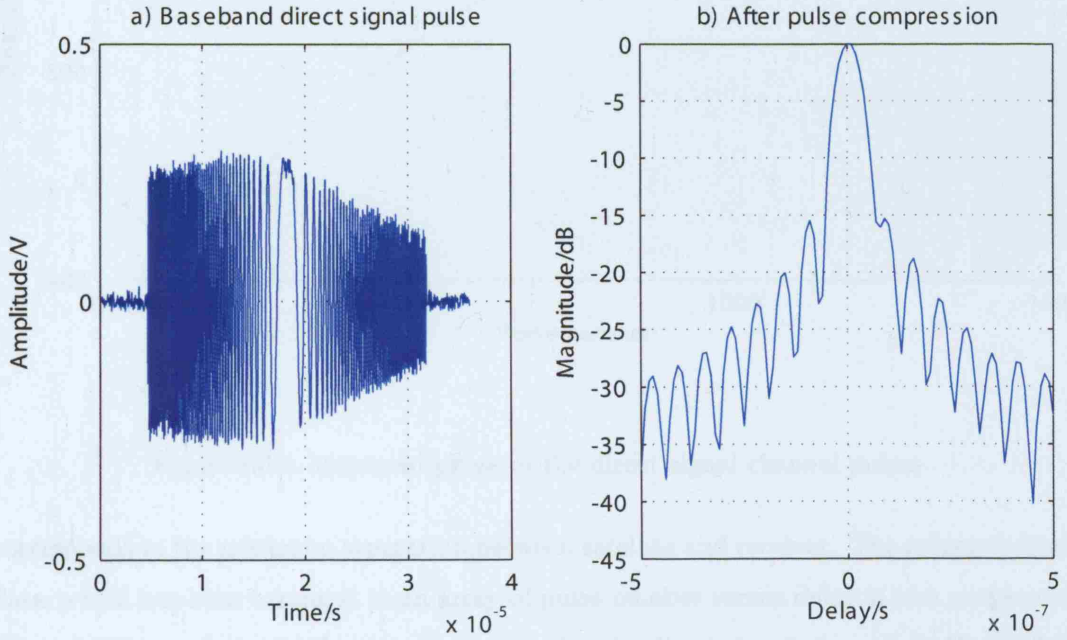

Figure 7-9: Direct signal channel baseband pulse before and after pulse compression with an ideal ASAR chirp signal

compression would be a sinc response with peak-to-sidelobe ratio of approximately -13dB. Due to the varying amplitude pulse envelope which is acting in a similar way to an amplitude weighting function, the first sidelobes have been reduced to -15dB on the right and -16dB on the left relative to the mainlobe (the lack of symmetry is due to the amplitude tapering across the pulse bandwidth also being antisymmetrical), while the mainlobe itself is slightly broader than the ideal case.

The pulse compressed direct signal phase is then measured for all direct signal pulses captured, producing the following plot, where the phase has been unwrapped, Figure 7-10. 1500 pulses are considered out of the larger total number captured for this experiment. Pulse number 1403 corresponds to the maximum value of the unwrapped phase, which in turn

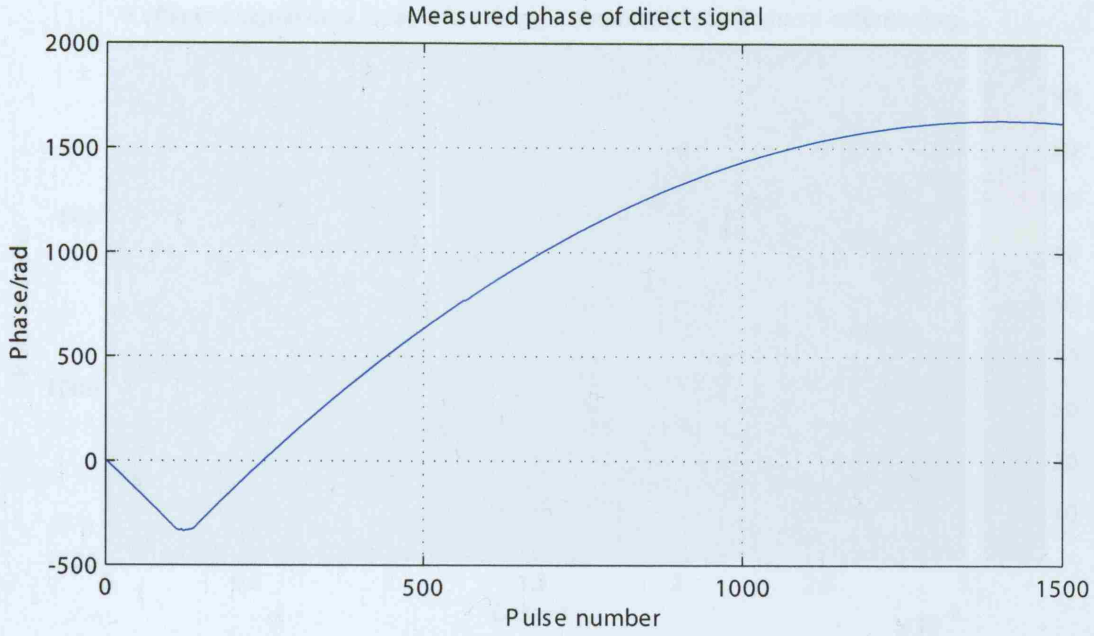

Figure 7-10: Measured phase of the direct signal channel pulses

corresponds to the minimum separation between satellite and receiver. The reflected signal data, which has been arranged in an array of pulse number versus delay is now range compressed with an ideal ASAR chirp, which includes the direct signal phase from Figure 7-10 and a Taylor amplitude weighting. The resultant array is given in Figure 7-11. The plot is given for the magnitude of the range compressed data normalised to a peak value of 100. For each pulse number we have a reflected signal data section, of time duration $30\mu s$. The delay axis is for bistatic delay and so is proportional to bistatic range sum $R_T + R_R$. The peak response within the array occurs at a delay of $10\mu s$ - this is the point at which energy from very close to the receiver parabolic antenna (for example the edge of the building on which it is mounted) is received. It therefore marks the position of the receiver along the delay axis of the data array. Several other relatively high amplitude lines may be observed at delays greater than $10\mu s$, corresponding to targets within the illuminated scene.

A plot of the unwrapped phase along the $10\mu s$ delay line for all of the pulses is shown in Figure 7-12. As the phase referencing has been performed, each point scatterer within the imaged scene has a phase proportional to $(R_T + R_R) - L$, where both R_T and L (the baseline distance) are functions of time. If there was a single point scatterer with a much greater RCS

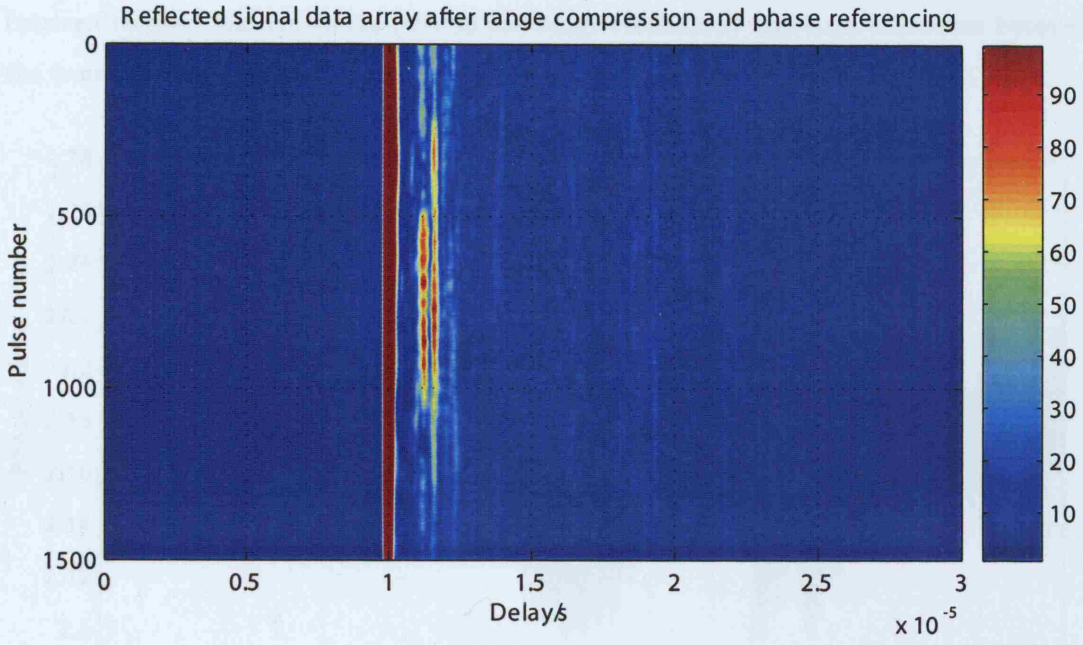

Figure 7-11: Reflected signal channel array after range compression and phase referencing

than all of the others at this particular bistatic range sum (very close to the receiver), then it would dominate the phase plot and the observed shape would be dependent on the function $(R_T + R_R) - L$, where $R_T + R_R$ is the range sum for this dominant scatterer. The variation of $R_T + R_R$ and L are both hyperbolic, with a minimum range that is approximately equal. This minimum range would probably occur at different pulse numbers (or azimuth times) and so the resulting phase plot would therefore be approximately linear (from the difference between two hyperbolic range functions with a time shift between them). In contrast to this hypothetical scenario, the fluctuating form of the phase graph in Figure 7-12 indicates that several point scatterers with similar responses are contributing.

Examining the (normalised) magnitude of the reflected signal data along this $10\mu s$ delay line gives Figure 7-13. As was mentioned previously, this corresponds to reflections from points close to the receiver. As the satellite moves and illuminates the scene, these points are illuminated and reflect energy towards the receiver antenna. The nature of the scatterers and their placement relative to the receiver will determine the form of the magnitude pattern. The peak of this pattern will occur at a time that may not correspond exactly to the peak of the transmitter antenna beam passing over the receiver. However, due to the close proximity

between receiver and scatterers (within the range resolution) any time difference between the transmit beam peak time and that measured using Figure 7-13 will be small.

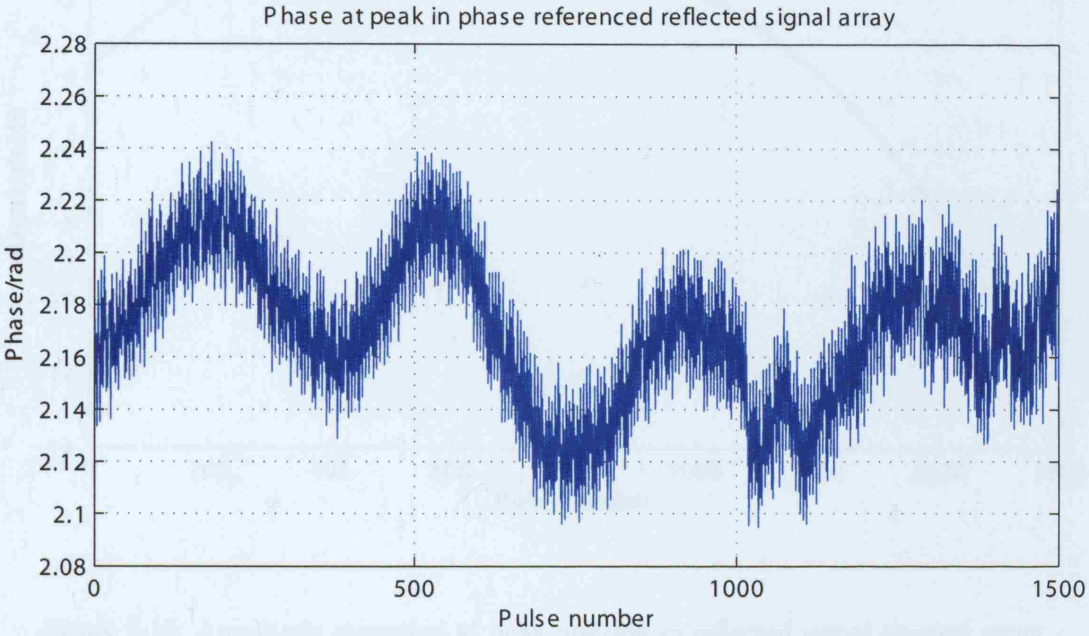

Figure 7-12: Phase measured at peak position in reflected signal channel array

A decrease in signal amplitude for pulse numbers 563 and 564 may be observed on the same graph. This amplitude discontinuity is due to a temporary loss of data by the ADC. As the ADC board is mounted in a PC and transfers data to a ramdisk in real-time across the PC bus, such data loss does occur (the frequency of such events increases with increasing resolution for the capture and increasing data capture size). Plotting the measured pulse repetition interval versus pulse number for the direct signal data gives Figure 7-14. It is apparent that as well as a pulse amplitude decrease, the pulse repetition interval appears to have been altered. The IF pulses in this channel for the pulse numbers 562 to 565 are given in Figure 7-15. Examining the pulse train in the Figure, plot a) shows pulse number 562 and 565 with the expected amplitude, while pulse number 563 and 564 have a reduced amplitude. Plot b) indicates that an extra pulse, occurring before number 563 is present in the data. This is the pulse repetition interval that has suffered a partial loss of data and large reduction in amplitude. As a result, the pulse repetition interval for pulse number 563 appears longer than normal in Figure 7-14, while that for number 564 is shorter. This type

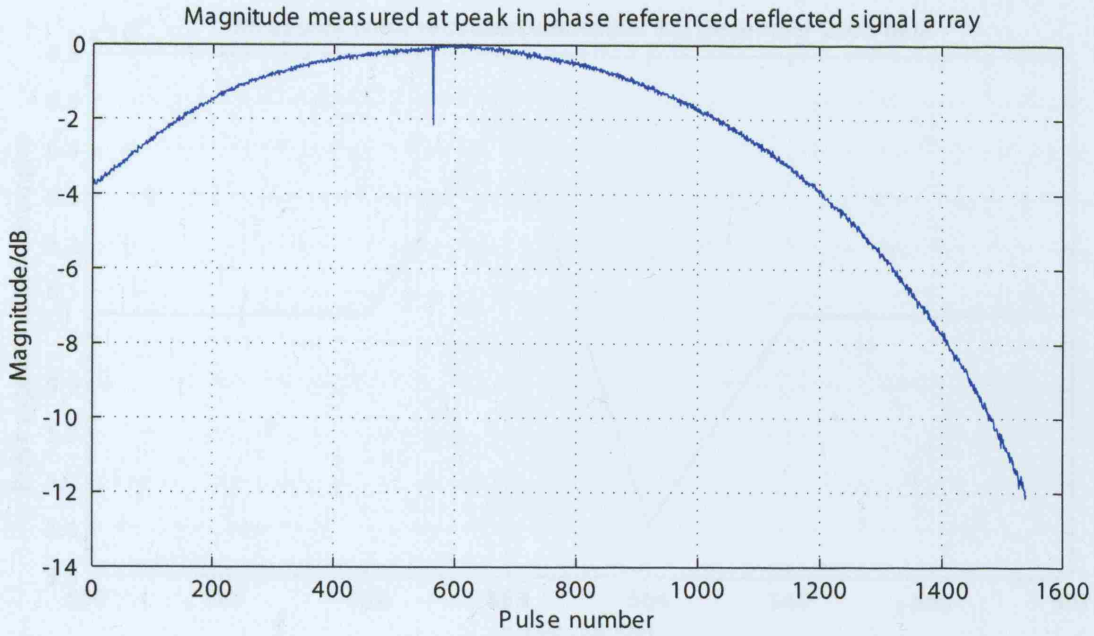

Figure 7-13: Amplitude measured at peak position in reflected signal channel array

of data loss typically occurs only once over one second.

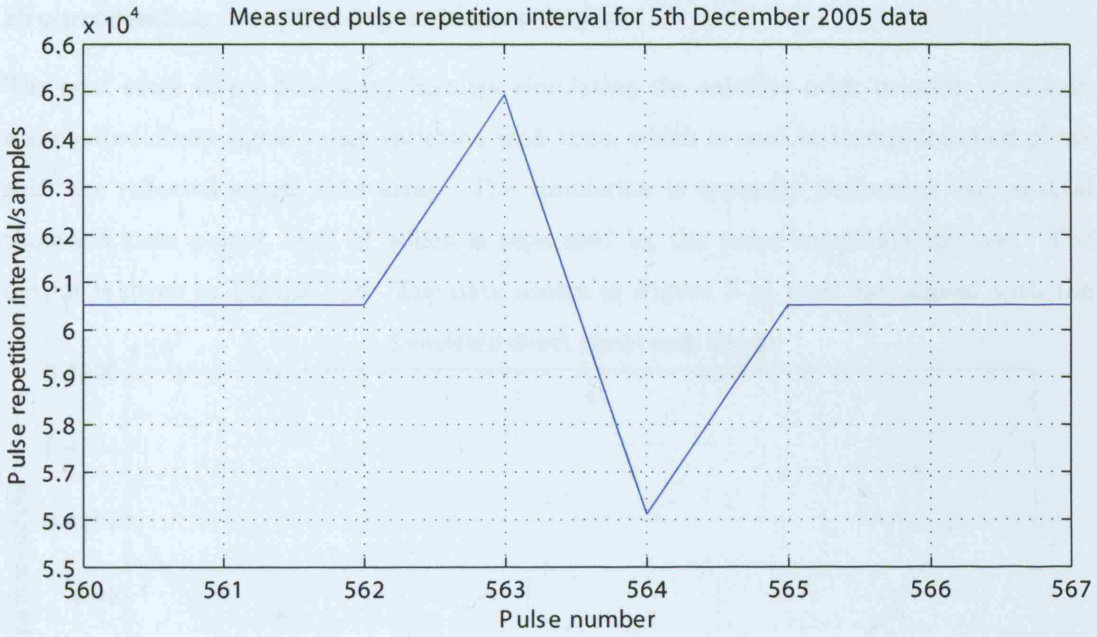

Figure 7-14: Measured pulse repetition interval for the direct signal data captured for the 5th December 2005 acquisition

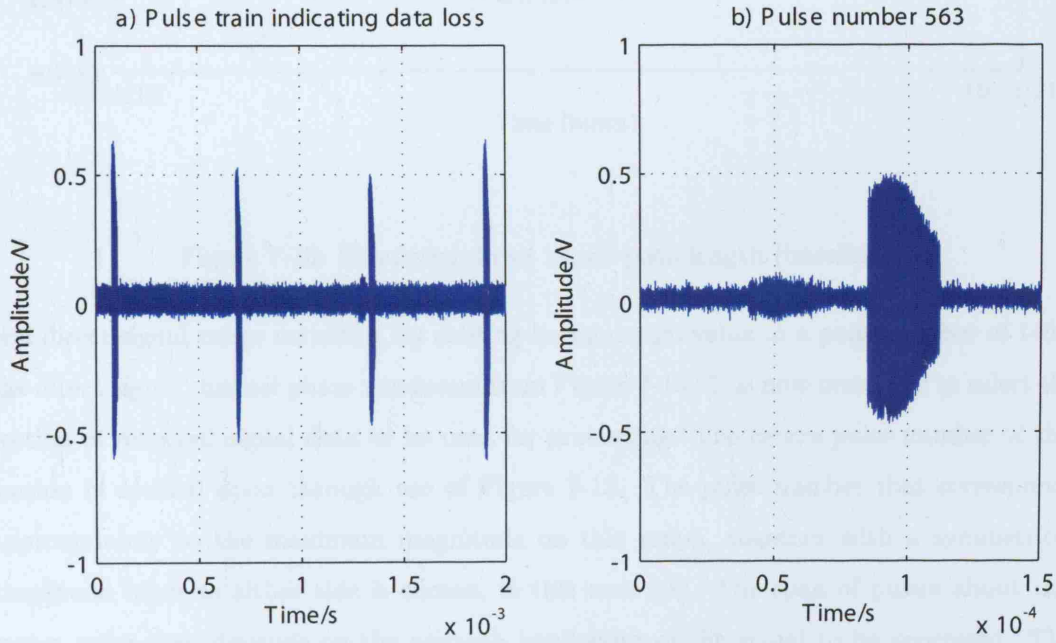

Figure 7-15: Data loss for the direct signal data captured for the 5th December 2005 acquisition

Pre-processing: baseline dependence removal

The next stage of pre-processing involves simulating the satellite orbit in order to obtain a simulated direct signal range variation with time, which is used to interpolate and phase shift the reflected signal data array. The simulation is typically performed over several thousand time points, each of which is separated by the pulse repetition interval. The output is given in Figure 7-16. The data shown in Figure 7-16 must be aligned with the

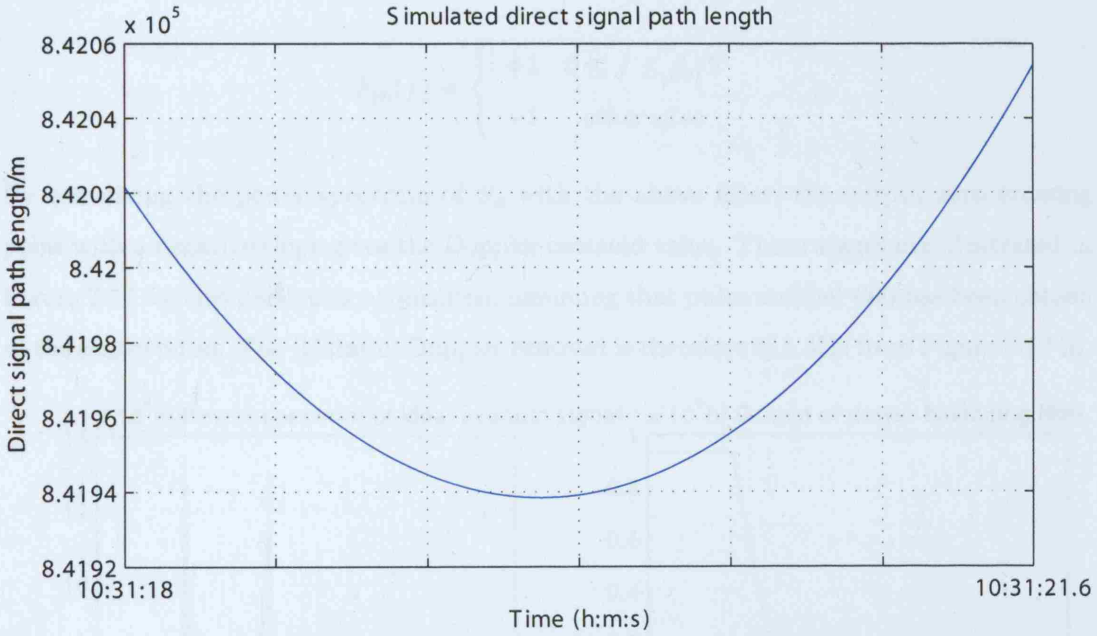

Figure 7-16: Simulated direct signal path length (baseline)

real direct signal range variation, by shifting its minimum value to a pulse number of 1403, the direct signal channel phase maximum from Figure 7-10. It is now necessary to select the section of reflected signal data to be used for processing. The centre pulse number of this section is decided upon through use of Figure 7-13. The pulse number that corresponds approximately to the maximum magnitude on this graph, together with a symmetrical amplitude taper to either side is chosen, in this case 600. The span of pulses about this centre pulse then depends on the azimuth bandwidth of the signal to be processed. The method for determining this pulse span is as follows. From the orbit propagation simulation performed, the baseline variation is known, together with the platform velocity V_s and Doppler rate f_R (with respect to the receiver position). The baseline variation about the

centre pulse may be used to generate an ideal azimuth signal. If the baseline variation is L_{sim}, the signal takes the form:

$$S_a = \exp\left(-j2\pi L_{sim}/\lambda\right)$$

If the FFT is taken of this signal, the bistatic Doppler centroid may be obtained by the power balancing method given in Cumming [79]. This uses a filter, defined by:

$$F_{pb}(f) = \begin{cases} +1 & 0 \leq f \leq f_p/2 \\ -1 & otherwise \end{cases}$$

By convolving the power spectrum of S_a with the above filter, the output zero crossing point with a negative slope gives the Doppler centroid value. These stages are illustrated in Figure 7-17 for this particular acquisition, assuming that pulse number 600 has been chosen as the centre pulse. The (bistatic) Doppler centroid is therefore 518.3Hz from Figure 7-17 b).

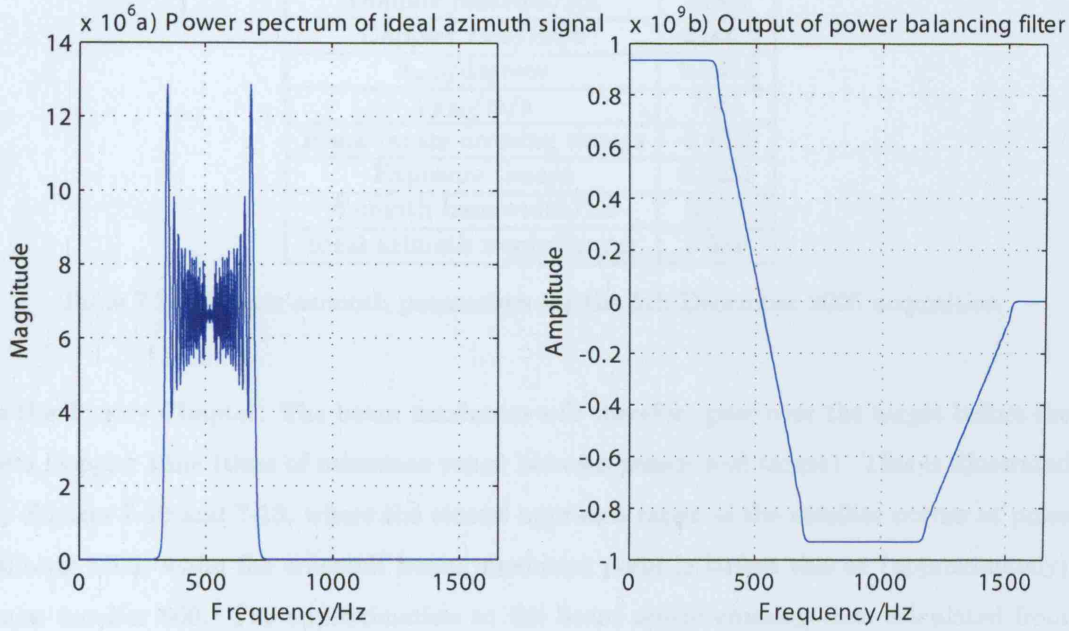

Figure 7-17: Power balancing method applied to simulated azimuth signal

Envisat uses yaw steering and so the unaliased Doppler centroid value calculated in this way is correct for the system. Equation 3.21 from the Theory Chapter gives the bistatic Doppler

centroid as a function of platform velocity and $\theta_{sq,c}$. Using the simulated satellite velocity and the value of $f_{DC,b}$ will enable calculation of $\theta_{sq,c}$. The satellite velocity value used here corresponds to the minimum direct signal range time, or zero Doppler time for ASAR with respect to the receiver. The velocity at the beam centre crossing time should strictly be used, although the variation in the satellite velocity magnitude over the entire simulation (3.6 seconds) is only 0.05m/s and so the error arising is negligible. For most of the azimuth parameter equations, the squint angle $\theta_{r,c}$ is used. From Cumming [79], assuming the squint angle is less than 6^0, then the cosine of $\theta_{sq,c}$ and $\theta_{r,c}$ will differ by less than 0.08%. As a result, Equation 3.22 for the bistatic Doppler rate may be used with a $\cos(\theta_{sq,c})^3$ instead of $\cos(\theta_{r,c})^3$, together with the simulated Doppler rate to calculate V_{FM}. In addition, $\cos(\theta_{sq,c})$ may be used in the remainder of the azimuth parameter equations, in order to calculate azimuth bandwidth and target exposure time. The results are summarised in Table 7.2.1. The beam centre crossing time given is negative in accordance with the convention adopted

Parameter	Value
Doppler centroid/Hz	518.3
Doppler rate/Hz/s	-2146.5
$\theta_{sq,c}$/degrees	0.2214
V_{FM}/m/s	7131
Beam centre crossing time/s	-0.4829
Exposure time/s	0.6231
Azimuth bandwidth/Hz	668.7
Ideal azimuth resolution/m	8.926

Table 7.3: Bistatic azimuth parameters for the 5th December 2005 acquisition

in the Theory Chapter. The beam maximum will therefore pass over the target before the zero Doppler time (time of minimum range between sensor and target). This is illustrated by Figures 7-10 and 7-13, where the closest approach range of the satellite occurs at pulse number 1403, while the transmit beam maximum point is before this at (approximately) pulse number 600. The approximation to the beam centre crossing time calculated from these values is $-(1403-600)/f_p = -0.486$s, in fairly good agreement with the value in Table 7.2.1. Also, the squint angle is much smaller than the 6^0 example given in the discussion on accuracy earlier, and so the use of $\cos(\theta_{sq,c})$ in the equations is acceptable.

The azimuth resolution in the output image is chosen to be 24m. The definition for resolution used is based on the full -3dB width of the impulse response, but the system will

be able to distinguish between targets separated by half this distance, in this case 12m. The azimuth broadening factor γ_a takes into account the Taylor weighting to be applied, and also the additional weighting introduced by the transmitter antenna pattern variation. This has a relatively small amplitude taper for the typical data length in azimuth and is represented by an additional broadening of 5%. The broadening factor is therefore 1.67. The processing bandwidth from Equation 3.26 is therefore:

$$B_{p,b} = 0.886\frac{V_{gr}\cos(\theta_{sq,c}) \times 1.67}{24} = 368.1Hz$$

This is 0.55 of the full azimuth bandwidth and will mean a total of $0.55 \times T_{3dB} \times f_p = 567$ pulses must be used in the processing. The processing gain as a result of range and azimuth compression, taking into account the weighting function loss is, in dB:

$$P_g = 25.7 + 10\log_{10}(567) - 1.23 = 52dB$$

From Equation (5.6), the signal-to-noise ratio in the image is approximately,

$$SNR_{image} \approx 52 + 9 = 61dB$$

The magnitude of the reflected signal data at the receiver position and the simulated direct signal path variation for the processing interval are given in Figure 7-18. Plot a) shows the approximate form of the transmitter antenna pattern for the data, with a taper of 0.9dB. This may be simulated by a Kaiser window with factor 0.7. From Cumming [79], the mainlobe broadening as a result of this weighting will be approximately 5%, the value used in the azimuth bandwidth calculation. The range migration, illustrated in plot b), is 10m, or just over 3 range samples.

The interpolation and phase multiplication, based on the simulated direct signal range is now applied to the data, followed by application of the SAR processor.

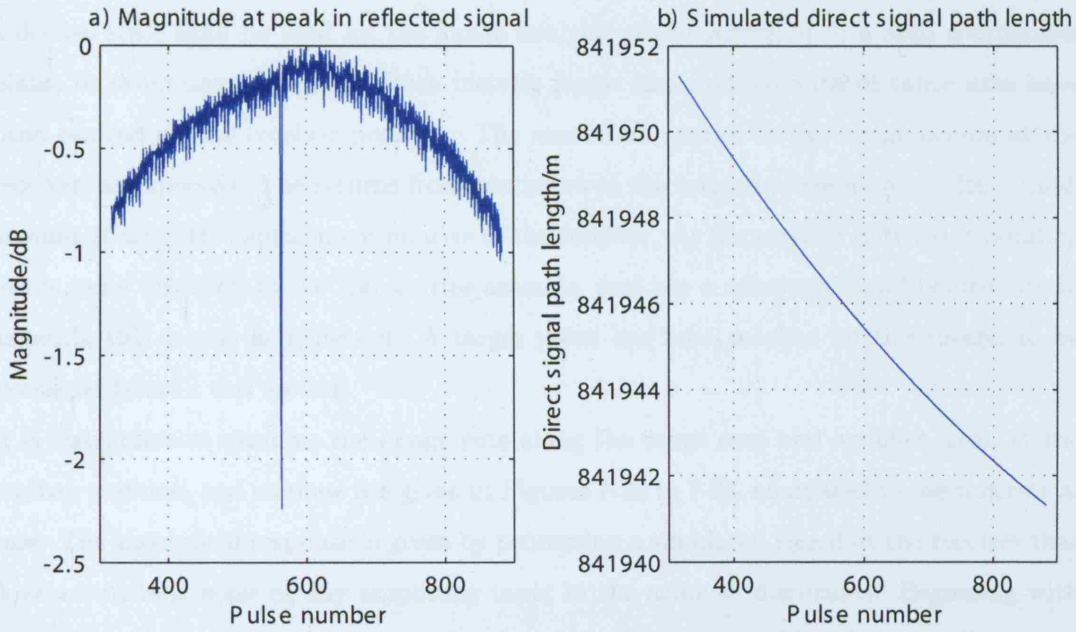

Figure 7-18: Approximate transmit beam variation and simulated baseline variation over the processing interval for the 5th December 2005 bistatic image

Bistatic SAR image

Figure 7-19 illustrates the output of the SAR processing operation. The image given is a magnitude plot, produced using the Matlab 'imagesc' function, with a colormap range of 0 to 100. This means that the magnitude of the image has been scaled to lie within this range. As the actual magnitude varies from close to zero to a number of the order of several thousand, this has the effect of reducing the contrast, with responses of widely varying magnitude being represented by similar colours. It gives a reasonable indication of the higher magnitude regions, without the receiver response dominating the image. Note that a decibel scale shall be used for the image analysis after conversion to a map coordinates plane, to avoid any ambiguity. Both bistatic range sum and azimuth distance axes have been centred on the receiver position. The maximum energy in the image occurs at the receiver, as expected. The returns from scatterers in the imaged scene all occur for a small amount of azimuth displacement relative to the receiver. As the receiver antenna is pointing in the same direction as the transmitter antenna, and has a relatively small beamwidth in azimuth, this is also as expected. A target point has been marked on this image, to be examined later in this section.

It is instructive to examine the image cuts along the range sum and azimuth axes, at the receiver position, and so these are given in Figures 7-20 to 7-23, compared to the theoretical case. The theoretical response is given by processing a simulated signal at the receiver that does not include noise or any amplitude taper in the azimuth dimension. Beginning with the range cuts, several target points may be observed along the bistatic range dimension, all of which are at least 30dB below the receiver response, but above the noise floor of -61dB. The furthest target point corresponds to a bistatic range sum increase of 1300m with respect to the receiver position. The bulge in the mainlobe along the positive range direction may be explained by energy from scatterers close to the receiver.

The range resolution of Figure 7-21 is found by measuring the full -3dB width of the mainlobe. This gives a range resolution of 25.5m, compared to the theoretical value of 23.4m.

For the azimuth cuts, the first point to note is that the theoretical response is above the measured response for the edges of the plot in Figure 7-22. This may be explained from Figure 7-23, where for the experimental data, more of the signal energy is contained in

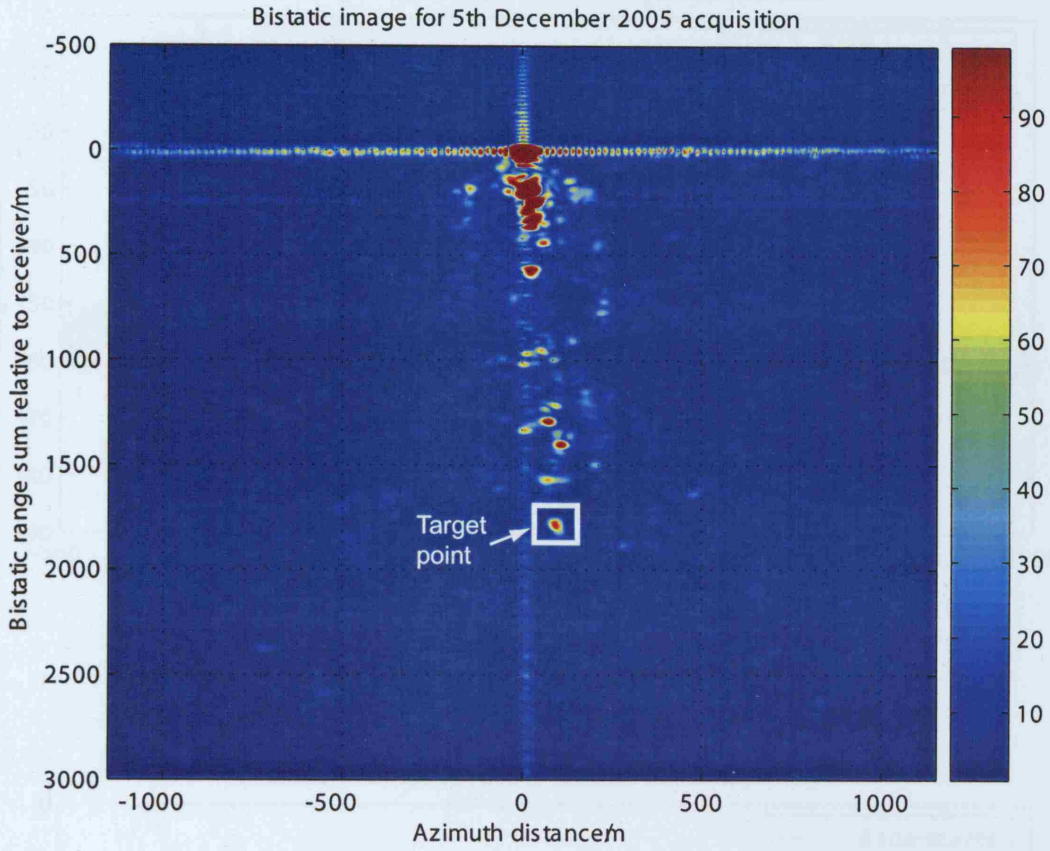

Figure 7-19: Bistatic image for 5th December 2005 acquisition, bistatic range sum versus azimuth

the mainlobe, which has absorbed the first sidelobes as a result. The second sidelobe, seen on the left hand side of the mainlobe is at -35dB, 5dB above the design value. This defocusing of the main response may be due to oscillator instability over the pulse repetition interval, assuming that the simulated satellite propagation parameters are correct, or from the presence of multiple scatterers instead of a single point target forming this receiver response. The measured azimuth resolution after interpolation is 23.9m, in good agreement with the theoretical value of 24m. An additional point to note is that the overall shape of the ideal Taylor weighted signal in the azimuth dimension does not match that in the range dimension. Indeed, the ideal response in Figure 7-20 is similar to those frequently given in text books, such as Carrara [102], whereas the azimuth response differs somewhat. The

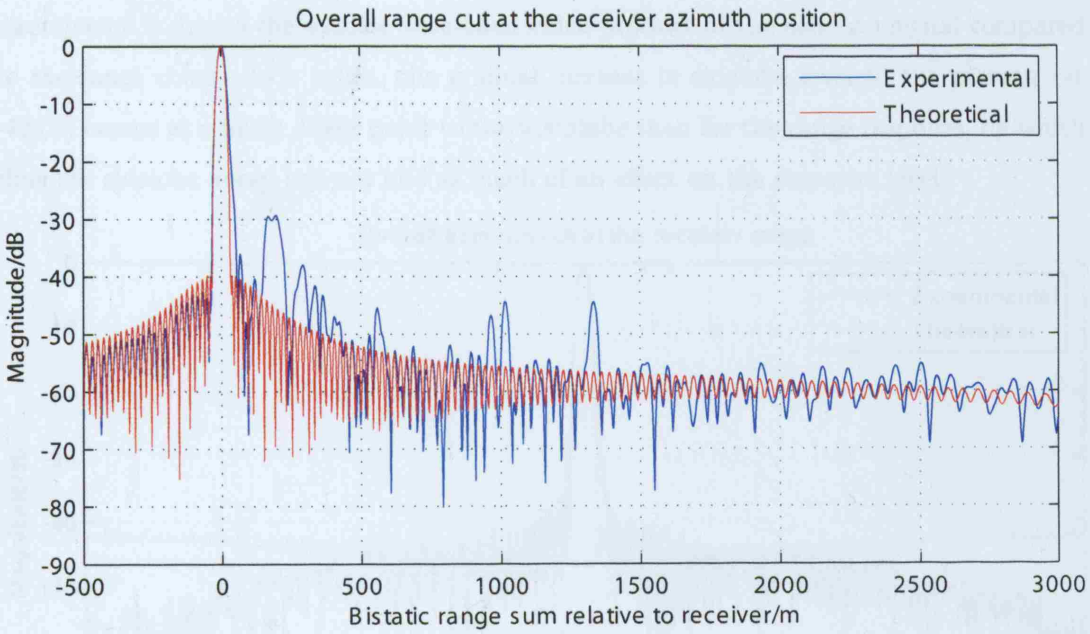

Figure 7-20: Overall range cut at the receiver azimuth position

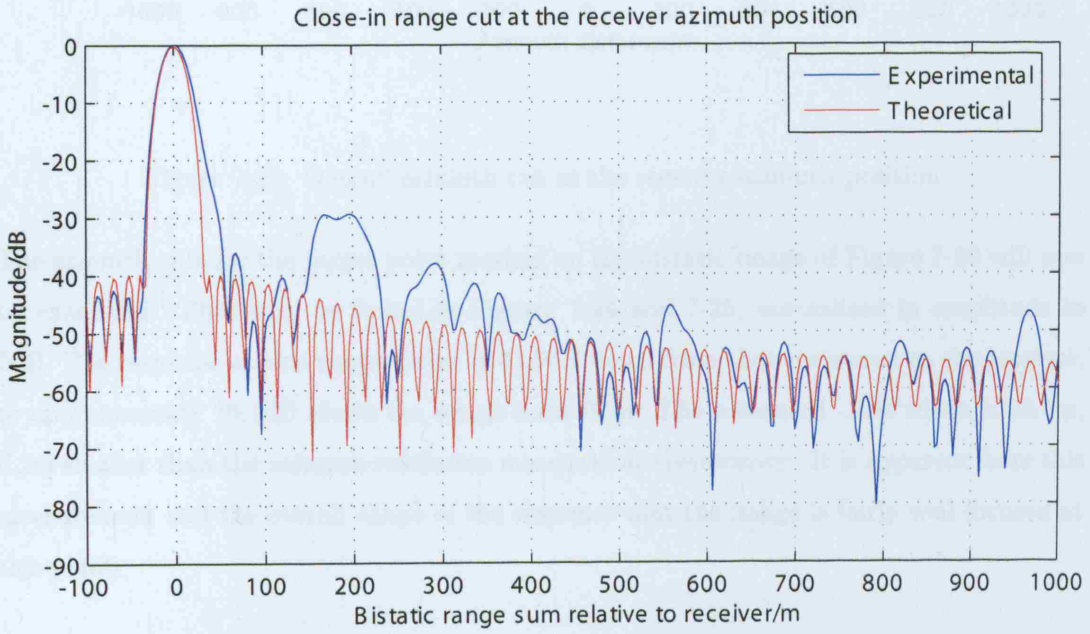

Figure 7-21: Close-in range cut at the receiver azimuth position

discrepancy is due to the smaller time-bandwidth product of the azimuth signal compared to the range chirp. As a result, the gradual increase in sidelobe level to the plateau (at -42dB) occurs at a much closer point to the mainlobe than for the range response, by which time the sidelobe decay has not had as much of an effect on the response level.

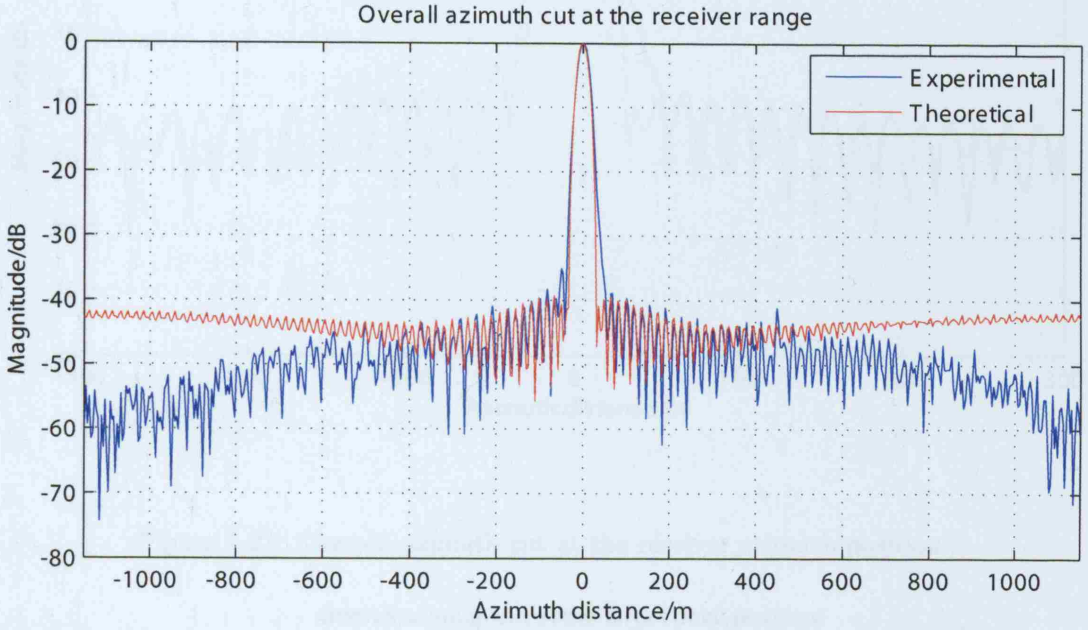

Figure 7-22: Overall azimuth cut at the receiver azimuth position

The azimuth cuts for the target point marked on the bistatic image of Figure 7-19 will now be examined. They may be found in Figures 7-24 and 7-25, normalised in amplitude to 0dB. The response at this target point is 41.9dB down from that measured at the receiver, or approximately 19.1dB above the image noise floor. The measured -3dB width is 23.7m, 0.2m smaller than the azimuth resolution measured at the receiver. It is apparent from this measurement and the overall shape of the response that the image is fairly well focused at this point.

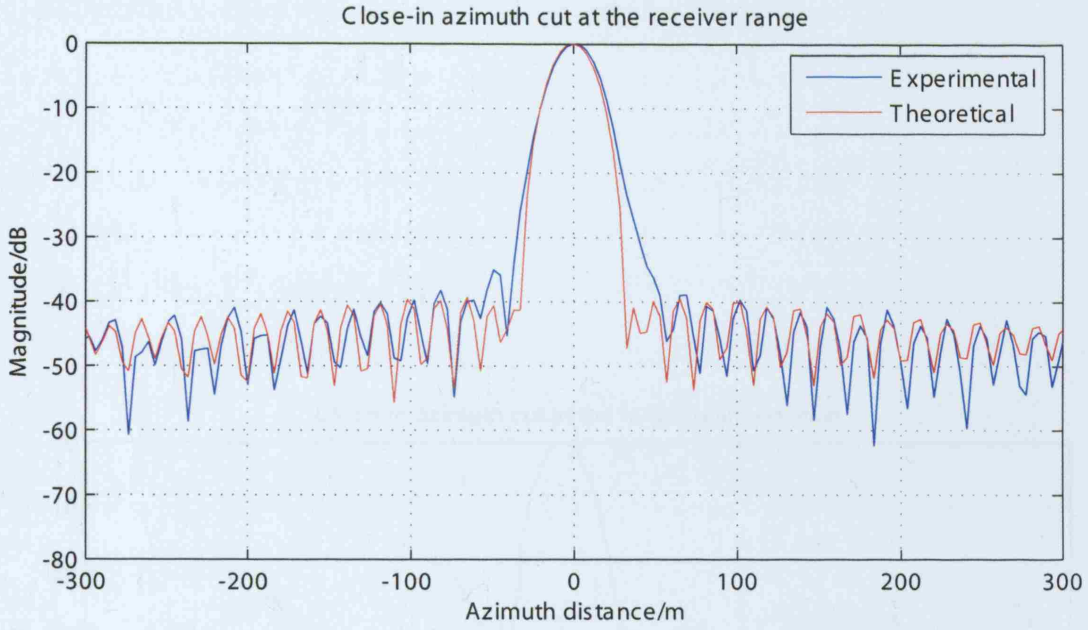

Figure 7-23: Close-in azimuth cut at the receiver azimuth position

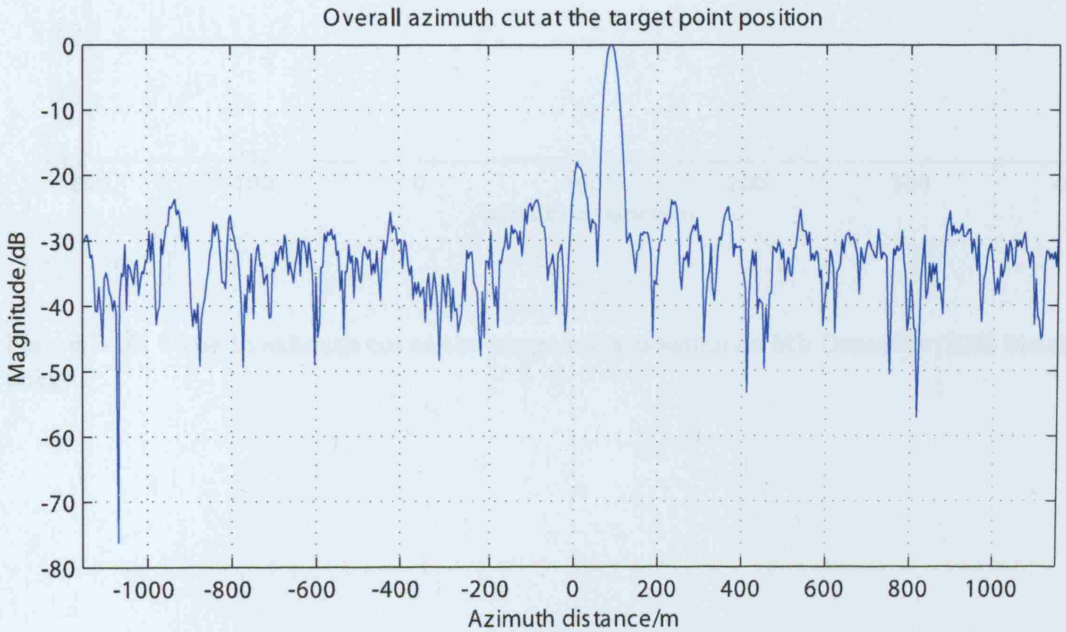

Figure 7-24: Overall azimuth cut at the target point position on 5th December 2005 bistatic image

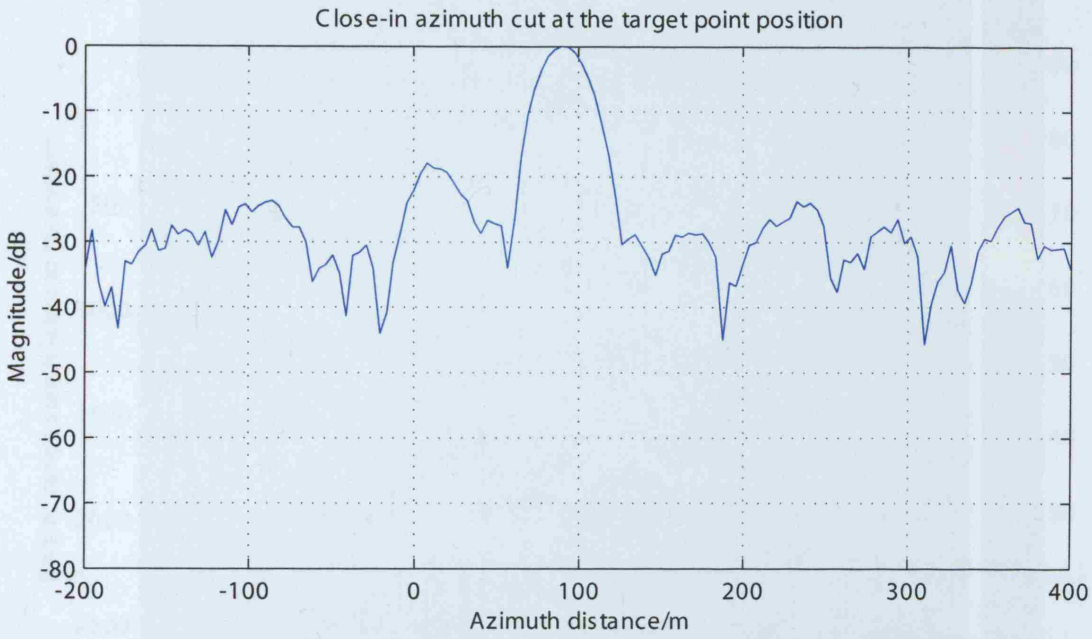

Figure 7-25: Close-in azimuth cut at the target point position on 5th December 2005 bistatic image

Comparison between direct and no phase synchronisation

As has been mentioned before, it is possible to operate the receiver using no phase synchronisation, (equivalent to the indirect phase synchronisation case plus a phase offset), the reflected signal data array is therefore range compressed but not phase referenced to the direct signal data. The remainder of the processing is the same as before. The non-phase synchronised image is given in Figure 7-26. The differences between this image and the

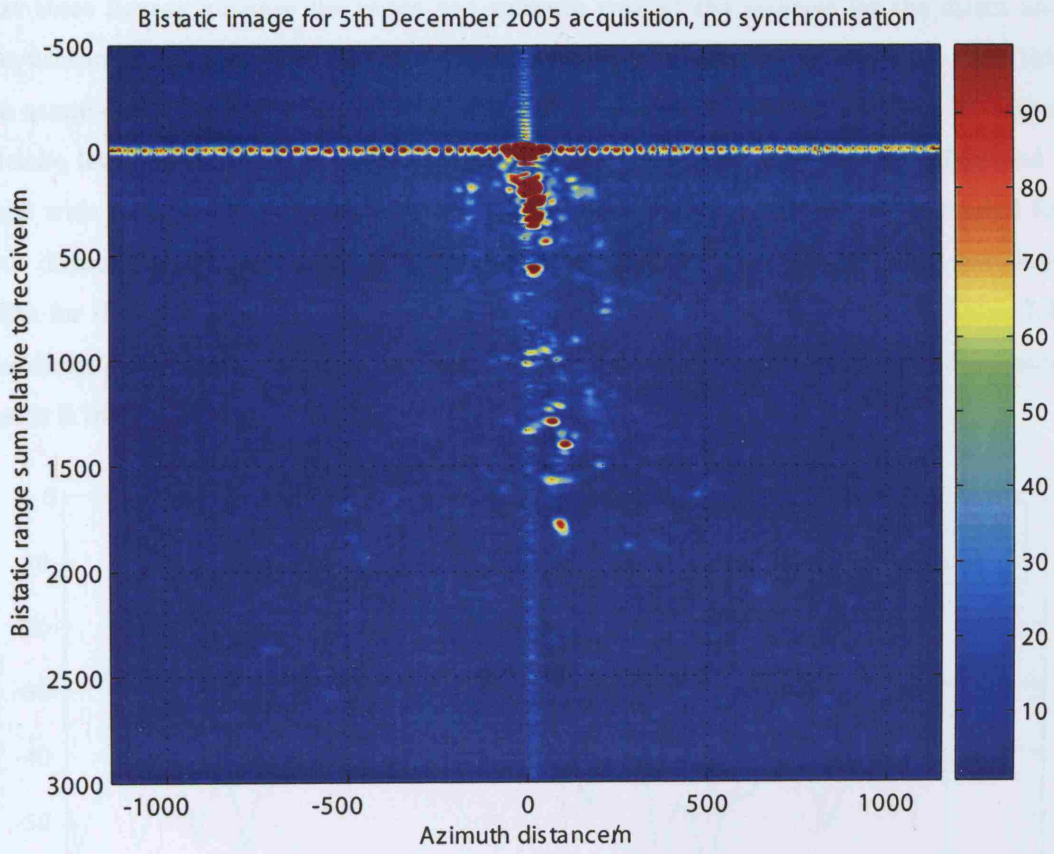

Figure 7-26: Bistatic image for 5th December 2005 acquisition, bistatic range sum versus azimuth, no phase synchronisation

direct phase synchronised version given in Figure 7-19 are not obvious, it is possible to note a higher sidelobe energy along the azimuth dimension in the unsynchronised image however. Other differences include a decrease in the peak signal-to-noise ratio at the receiver position relative to the direct image, in addition to a shift in range of the receiver response. In the

ISLR (direct)/dB	ISLR (unsynchronised)/dB
-25.6	-21.8

Table 7.4: Comparison between ISLR levels for the azimuth cut at the receiver in the direct phase synchronisation and unsynchronised bistatic images

unsynchronised image the peak response in the image occurs at a range approximately 3m less than the true receiver range. This may be attributed to a constant phase error. The next three figures compare the range and azimuth cuts at the receiver for the direct and unsynchronised images. The mis-registration is apparent in the range cut, apart from this one sample shift the two plots are identical. The azimuth cut is characterised by higher sidelobe levels for the entire processing interval, with first sidelobe levels at -27dB and -28dB with respect to the mainlobe. The integrated sidelobe ratio may be calculated for both direct and unsynchronised image cuts for comparison. Assuming that the mainlobe width for the calculation is 2.8 times the -3dB width of 24m gives the results in Table 7.4. The direct phase synchronisation technique leads to an ISLR along the azimuth dimension that is 3.76dB lower.

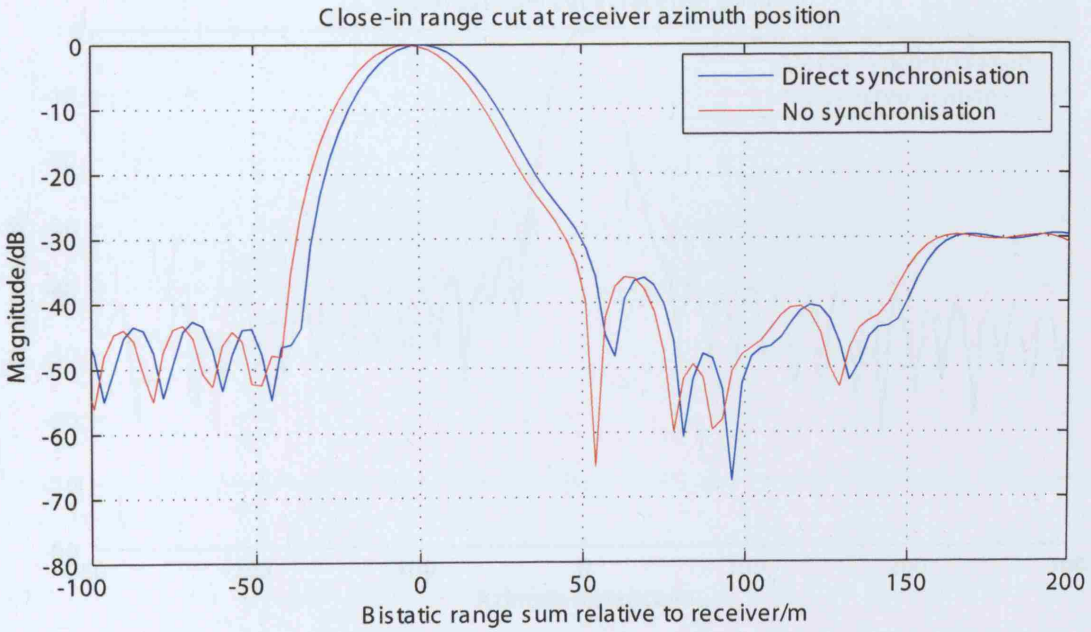

Figure 7-27: Close-in range cut at the receiver azimuth position

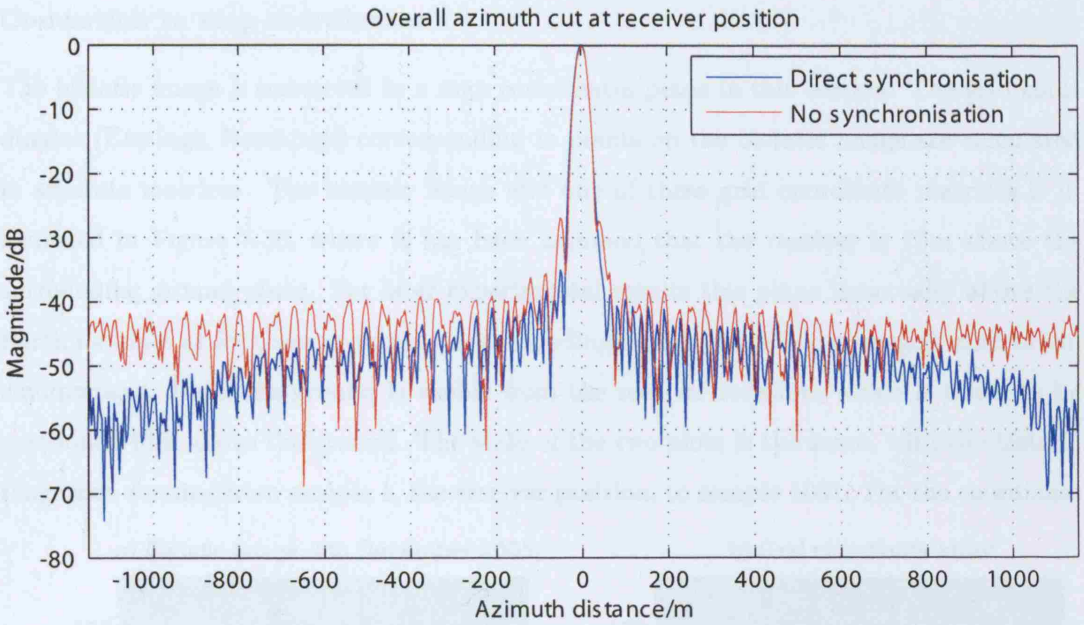

Figure 7-28: Overall azimuth cut at the receiver azimuth position

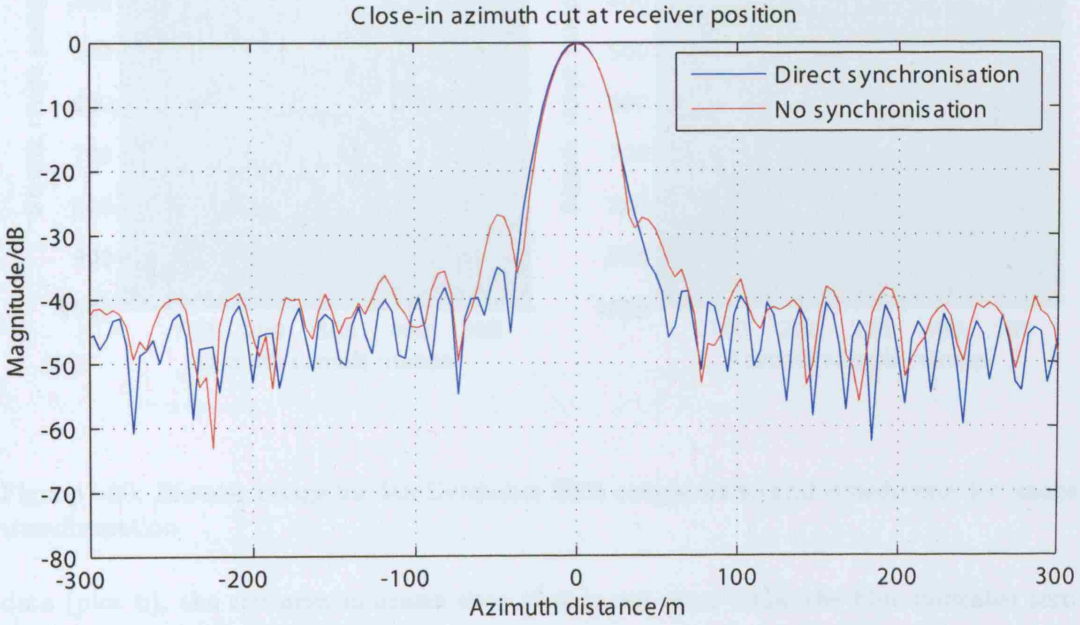

Figure 7-29: Close-in azimuth cut at the receiver azimuth position

Conversion to map coordinates

The bistatic image is converted to a map coordinates plane in this section. The grid coordinates (Eastings, Northings) corresponding to points on the bistatic image are calculated in separate matrices. The bistatic image and one of these grid coordinate matrices is illustrated in Figure 7-30, where it has been assumed that the receiver is 15m above the surrounding ground plane. For later experimental results this plane is actually above the Earth's surface as for these acquisitions surrounding buildings are being imaged in an urban environment. Here, the ground is visible from the receiver location, which is taken to be positioned 15m above the ground. The scale of the two plots is the same, with the bistatic range axis running from sample 1, the receiver position, to sample 1001. For the coordinate

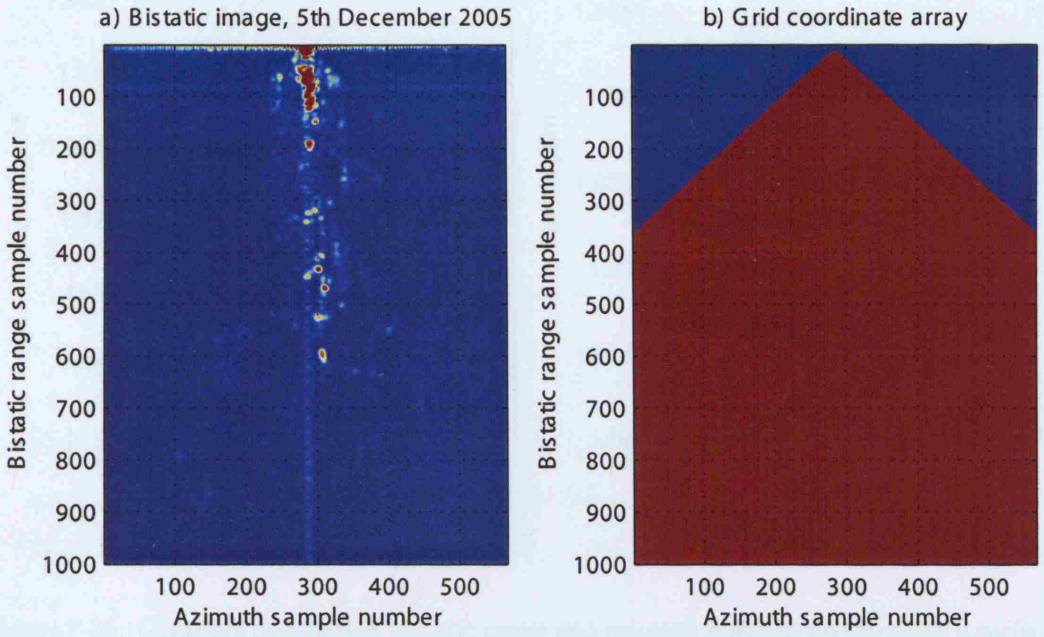

Figure 7-30: Bistatic image for 5th December 2005 compared to grid coordinates for image transformation

data (plot b), the red area indicates data that is not zero, while the blue indicates zero values. The coordinates are therefore only given for a triangular area in the data matrix - these are the solutions to the simultaneous equations that give a real answer. All other points within the data matrix were originally complex but have been set to zero for the purposes of clarity in the Figure.

The next Figure, 7-31 illustrates contours along the (theoretically flat) earth's surface for constant bistatic range values and for constant azimuth positions (of the satellite). The receiver position is marked with a red cross. Isorange contours, as discussed in the Theory Chapter, are formed on the plane of the bistatic triangle, it is therefore the projection of these onto the earth's surface that gives Figure 7-31 a). Not all of the contours from the original bistatic image are shown - the constant range contours have a spacing of 150m (in bistatic range), while the spacing between the constant azimuth contours is 160m, for clarity. The constant range contours are formed from the intersection of iso-range ellipses

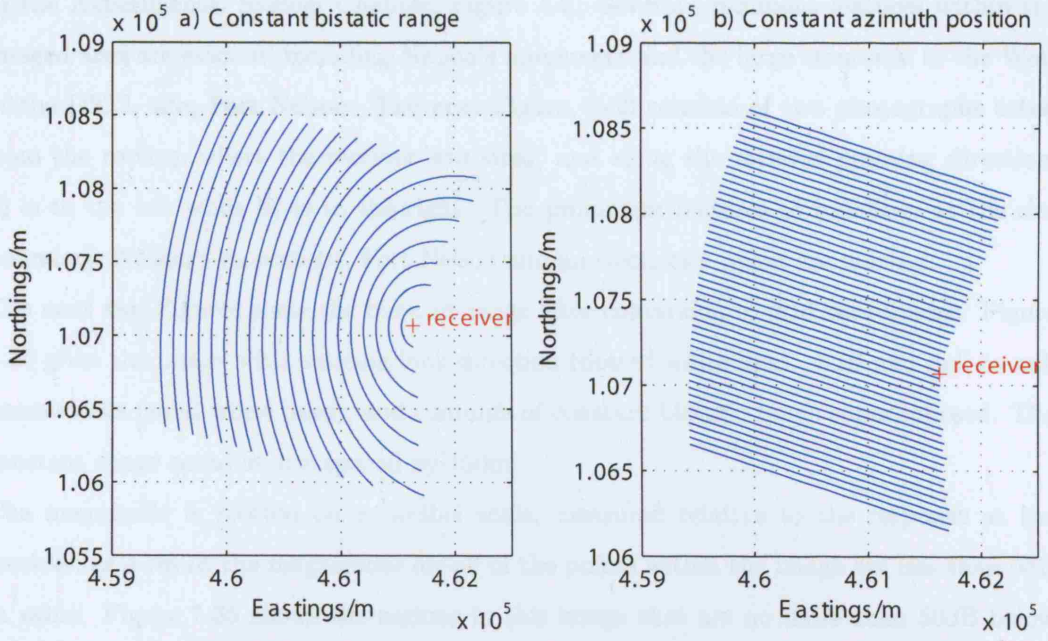

Figure 7-31: Contours of constant bistatic range and azimuth position on the earth's surface for the coordinate conversion of the 5th December 2005 bistatic image

with a plane, and so are elliptical in shape. The contours of constant azimuth position are straight lines perpendicular to the beam footprint velocity of the satellite, as expected.

Grid coordinates image analysis

The bistatic image, after conversion to grid coordinates, may be compared to an aerial photograph and a map, and of course the monostatic image produced by ASAR and supplied by ESA (in the next section). It is useful to first give an idea as to the imaged area

through the use of a map and some photographs. Figure 7-32 on the next page shows the immediate area around DSTL Portsdown West. a) gives a map view while b) shows the same area with a satellite photograph obtained using the 'Google earth' program. The receiver, shown by the red cross, is mounted on top of the Eastern building on the DSTL site. For plot b), the receiver pointing direction (solid white line), towards Nelson's monument and Fort Nelson is also shown, together with the antenna -3dB beamwidth of 11.8^0 and the null-to-null beamwidth (solid black lines). Note that the null-to-null beamwidth is not symmetrical about the boresight of the beam, see parabolic antenna 2 radiation pattern, in the Experimental System Chapter, Figure 4-5. Several prominent features within the imaged area are evident, including Nelson's monument and the large structure to the West of the DSTL site, Fort Nelson. The next Figure, 7-33 consists of two photographs taken from the rooftop where the receiver was sited, and along the receiver pointing direction, a) is to the left while b) is to the right. The prominent features of buildings at the site boundary, Nelson's monument, Fort Nelson and an electricity pylon are marked.

The next two Figures show the bistatic image after conversion to grid coordinates. Figure 7-34 gives the image with antenna look direction (dotted white line), -3dB and null-to-null beamwidths (solid white lines), and contours of constant bistatic range superimposed. The constant range contours are spaced by 150m.

The magnitude is plotted on a decibel scale, measured relative to the response at the receiver, as a result the magnitudes for all of the points within the image are less than 0dB in value. Figure 7-35 shows the regions in this image that are no more than 50dB below the receiver response, superimposed onto the corresponding satellite photograph. For a reflected signal of the same amplitude as the noise floor in the ADC, the signal-to-noise ratio in the image will be equal to the processing gain minus any processing loss. This has already been calculated for this set of results as 52dB, and so 50dB should mean the plot will be of all signals above the noise floor. This cut-off of 50dB will also be applied to the other bistatic images produced later in this Chapter, as the processing gain for each is also approximately 50dB. Again, the beam limits and range contours are also shown. A colorbar is given in both Figures, showing the variation in received signal in dB versus the colormap for the image.

From the overlay image of Figure 7-35, much of the scattering is within the DSTL site itself, from buildings and the car park directly in front of the receiver. This includes a

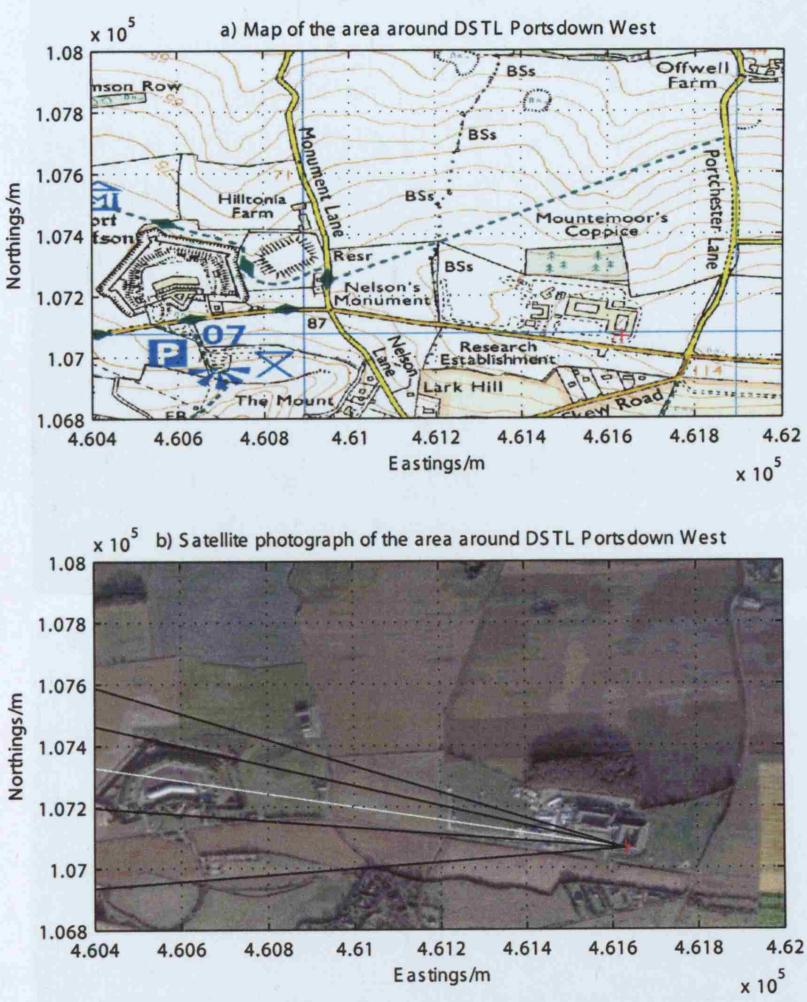

Figure 7-32: Map and satellite photograph of the area around the DSTL Portsdown West site

scatterer at the fence, marked on the Figure. Beyond this, three target points around Nelson's monument may be observed. Several point-like scatterers follow the edges and so indicate an approximate shape for the edges of Fort Nelson, while the furthest image point from the receiver shown in Figure 7-35 probably corresponds to an electricity pylon, as can be seen in the upper photograph of Figure 7-33, to the left of Nelson's column. The target point examined in the original bistatic image (plotted for bistatic range versus azimuth) corresponds to this pylon.

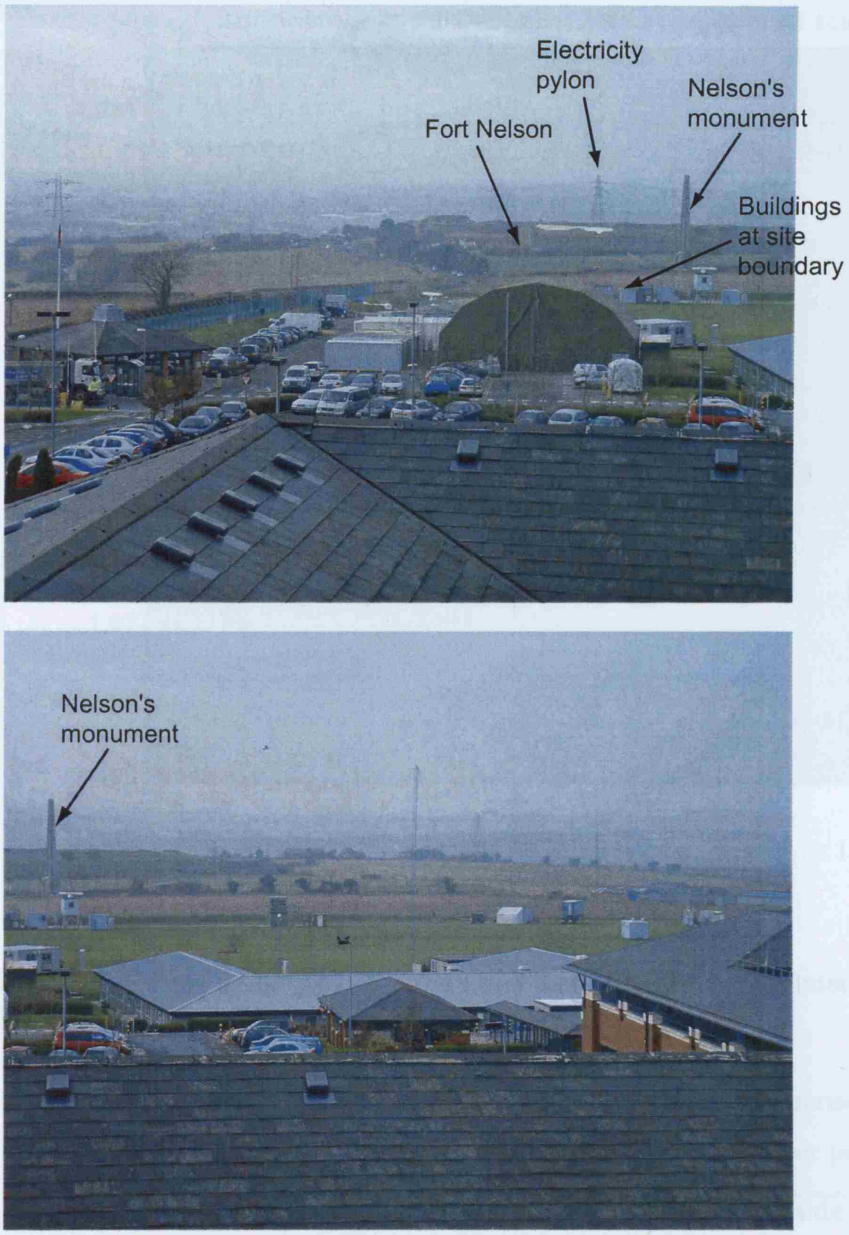

Figure 7-33: Photographs of the imaged area, taken from the receiver position - left of centre (top) and right of centre (bottom)

Examining the cuts along the East and North directions for the buildings at the site edge, Nelson's monument (there are three scatterers for this feature and so the one on the receiver line-of-sight that is closest to the receiver shall be considered only), and the electricity pylon

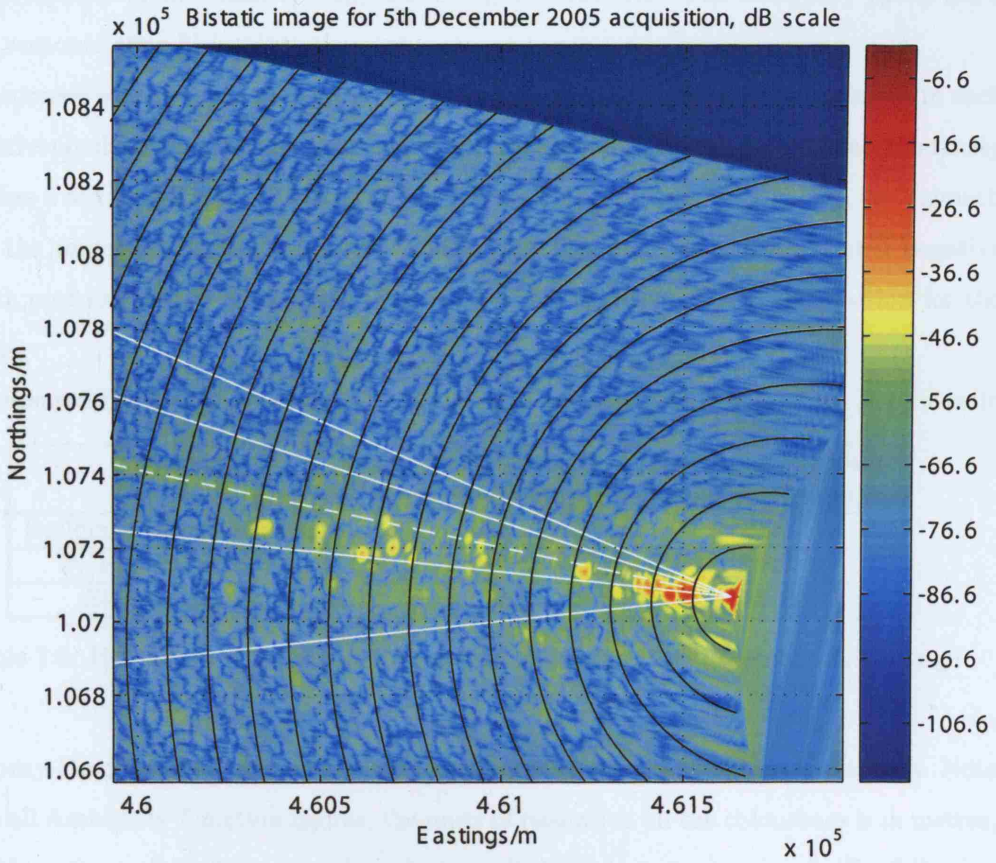

Figure 7-34: Bistatic image from the 5th December 2005 acquisition interpolated onto a grid coordinates plane

gives the following Figures, 7-36 to 7-38. The scatterer details are summarised in Table 7.5. The magnitude of the responses relative to that produced at the receiver position indicate

Feature	Position (Easting,Northing)/m	Magnitude relative to receiver response/dB
Buildings at site boundary	(461231,107134)	-36.9
Nelson's monument	(460947,107204)	-43.2
Electricity pylon	(460345,107254)	-41.9

Table 7.5: Selected features in 5th December 2005 image

the dynamic range between target points within the imaged scene. The buildings at the site boundary feature gives the highest response out of all three, as expected, given that

this corresponds to the smallest range from target to receiver. The electricity pylon has a higher response than Nelson's monument.

The responses all have a single peak at the target. Several other peaks are apparent in each cut, corresponding to the other features in the image. The North cut for the electricity pylon has a second peak to the North of the main one. This is also apparent in the azimuth cut of the target point (the pylon) of Figure 7-25. The secondary peak is at a negative azimuth position relative to the pylon response, which is a more Northerly position for the satellite.

The measured resolutions of these features are given in the next Table, 7.6. The bistatic

Feature	Resolution along East direction/m	Resolution along North direction/m
Buildings at site boundary	23.5	23.5
Nelson's monument	26.5	26.5
Electricity pylon	23.5	25.5

Table 7.6: Resolution of responses for selected features in 5th December 2005 image

Ambiguity Function shall now be applied to the imaging geometry of this acquisition. Note that in all Ambiguity Function figures, the units of resolution on the colourbars is in metres, that of bistatic angle in degrees, and resolution cell size is in metres squared. The following Figure, 7-39 shows the theoretical resolution along the East and North directions for the same scale as the image overlay of Figure 7-35. Figure 7-40 gives the bistatic angle and ground resolution cell size. As before, the receiver antenna boresight and beam limits are shown on the plots. The resolution along the East direction varies to a much greater extent than that along the North direction. The North directed resolution is heavily dependent on the azimuth resolution (but weakly on bistatic range resolution) as the satellite path is approximately from North-North-East to South-South-West. The azimuth resolution has a weak dependence on slant range from satellite to target (which has been discounted for the purposes of this simulation). The East directed resolution has a greater dependence on the bistatic slant range resolution, which varies with bistatic angle β.

Along the boresight of the receiver antenna (the dotted line), the East and North resolutions do not vary by a great deal, and are equal to 16.5m and 22.4m. At the receiver location, the resolutions tend to their maximum values of 104m and 24.7m for East and North respectively. It is apparent that the regions directly to the North and to the South of the receiver

are unsuitable for bistatic imaging, as the resolution along the East direction approaches its maximum value. This area corresponds to the image points where the $\cos(\beta/2)$ and $\cos(\theta_\tau)$ terms in the denominator of the δ_Ω equation tend to zero. The opposite is true for the North directed resolution, which has its maximum in a direction perpendicular to the satellite path.

Comparing the measured and theoretical resolutions for the image features, the resolutions measured along the North direction are in fairly good agreement with the theory. The measured resolutions along the East direction are higher. The features imaged are of course not point targets, which may explain this observation.

The bistatic angle is at a minimum for a small region around the receiver, but for most of the imaged scene, it is approximately 90^0. From the discussion in the Theory Chapter on bistatic angle, the system is operating in the bistatic RCS region, and so it is expected that the RCS of complex targets in the scene will differ from their monostatic values. Bistatic angle varies predominantly in the West to East direction, accounting for the larger change in East directed compared to North directed resolution in the image.

The ground resolution cell size has a typical value of $850m^2$ for the imaged area, close to the minimum for this particular bistatic arrangement. The resolution cell size also approaches a maximum value to the North and South of the receiver, along a line that is in the same direction as the beam footprint path. This is due to the combination of $\cos(\beta/2)$ and $\cos(\eta_g)$ tending to zero in the denominator of the resolution cell equation along this line. It should be noted that the ground resolution cell size plot has been limited to a maximum of $2500m^2$ for all of the acquisitions, for clarity. In fact the resolution cell maximum for this particular set of results is $2.99 \times 10^7 m^2$, obviously a completely impractical value for imaging.

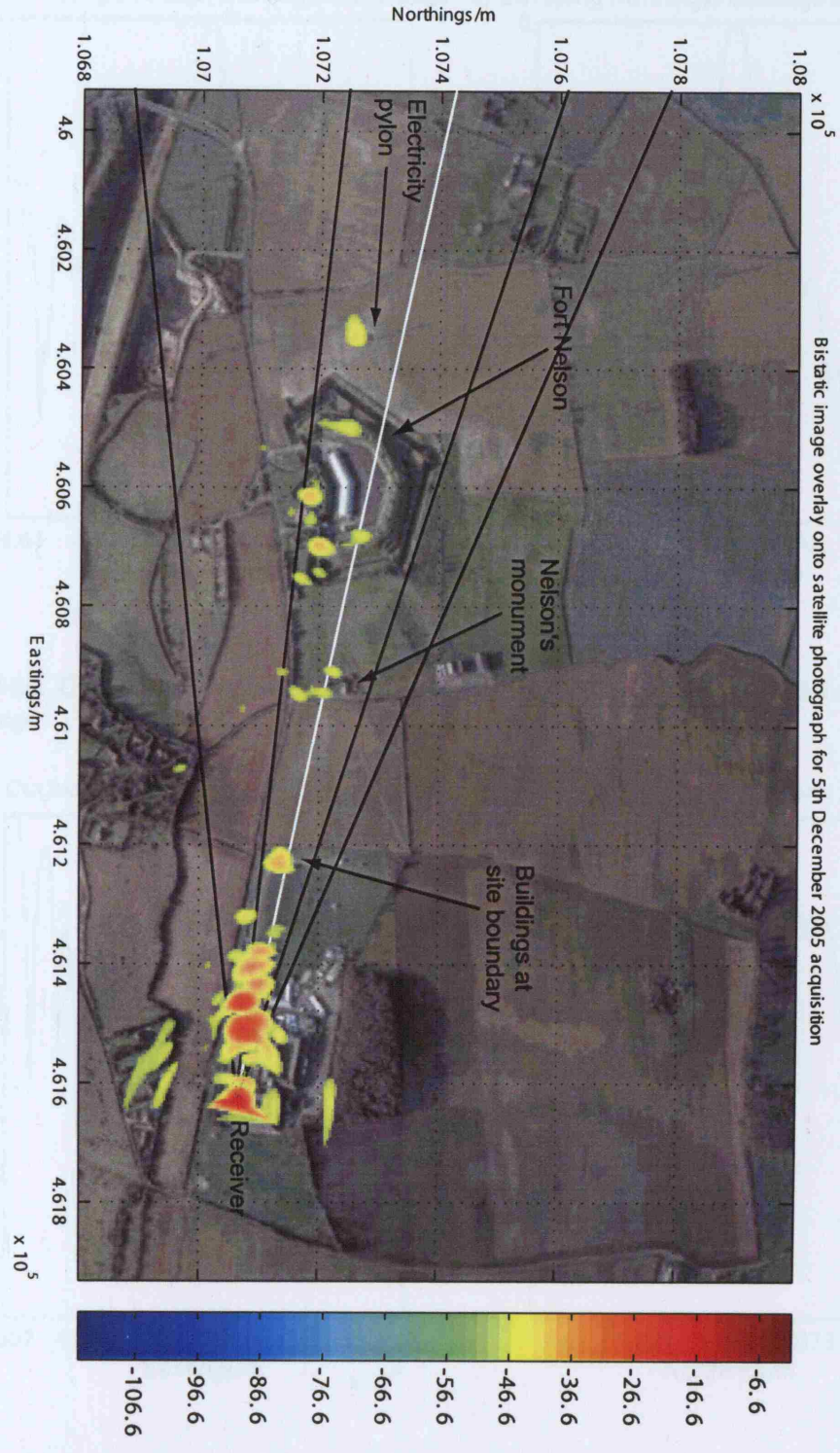

Figure 7-35: Bistatic image overlaid onto a satellite photograph of the area around DSTL Portsdown West

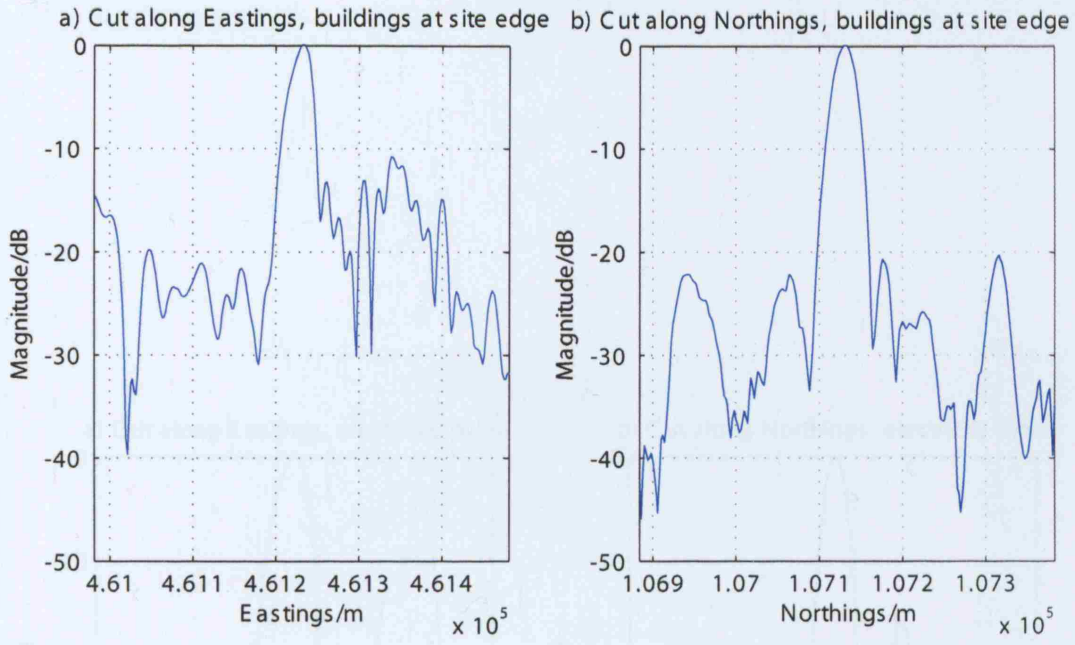

Figure 7-36: Cuts along Eastings and Northings at DSTL site boundary for 5th December 2005 image

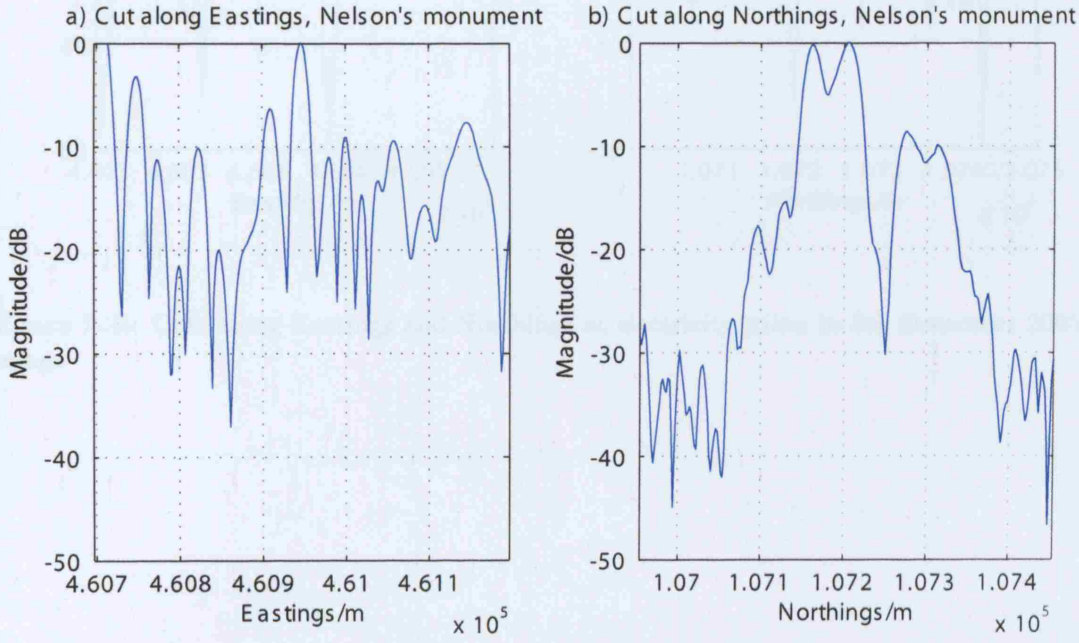

Figure 7-37: Cuts along Eastings and Northings at Nelson's monument in 5th December 2005 image

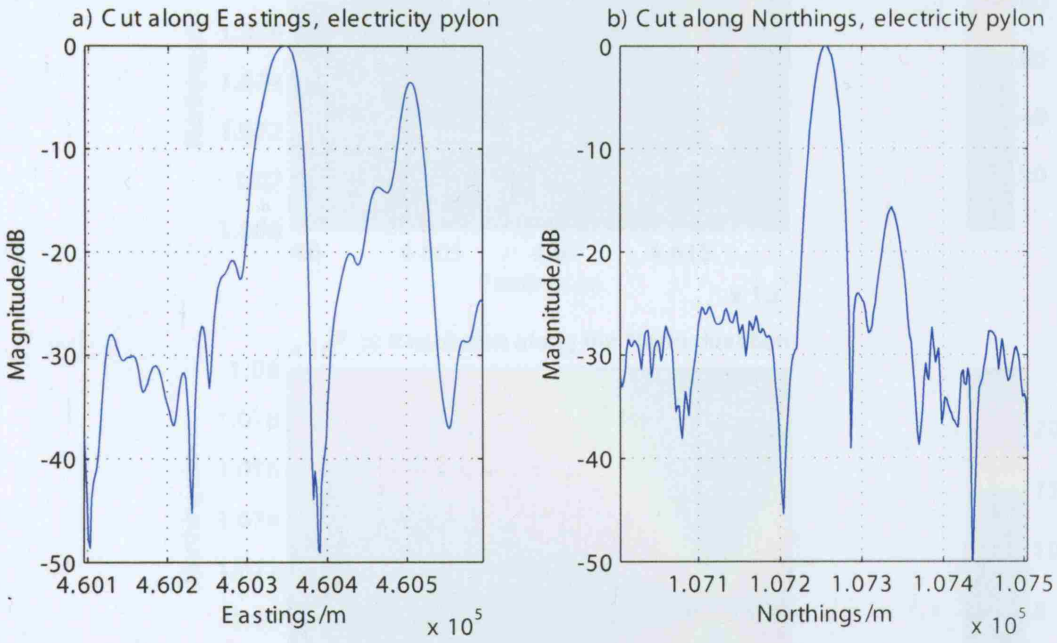

Figure 7-38: Cuts along Eastings and Northings at electricity pylon in 5th December 2005 image

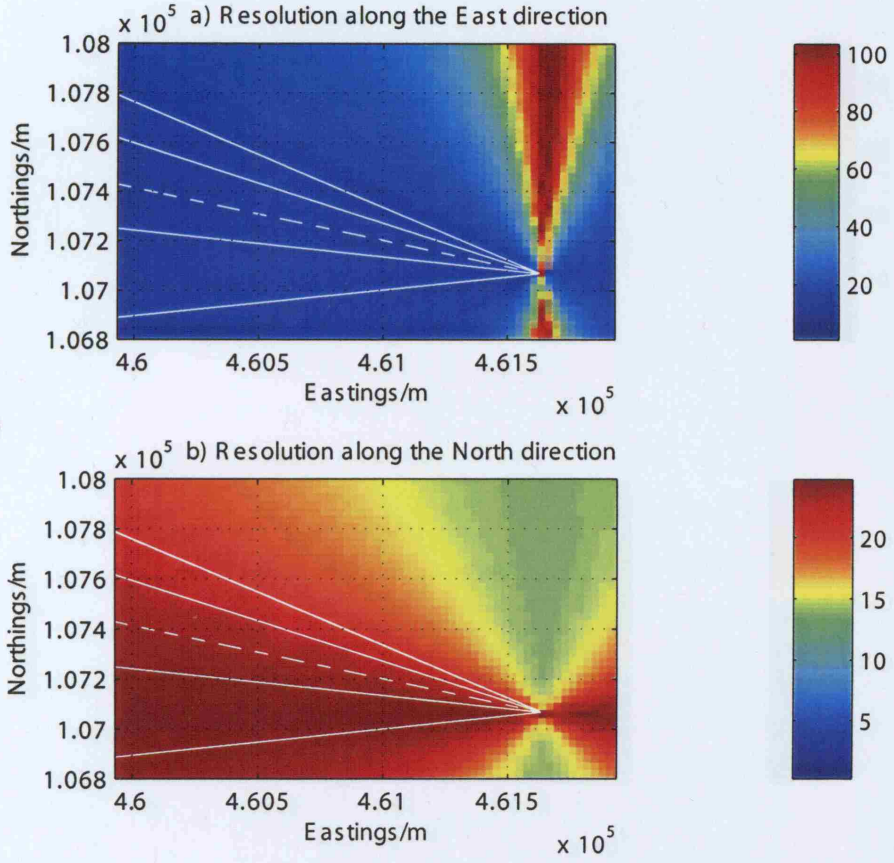

Figure 7-39: Theoretical resolutions along East and North directions for 5th December 2005 image

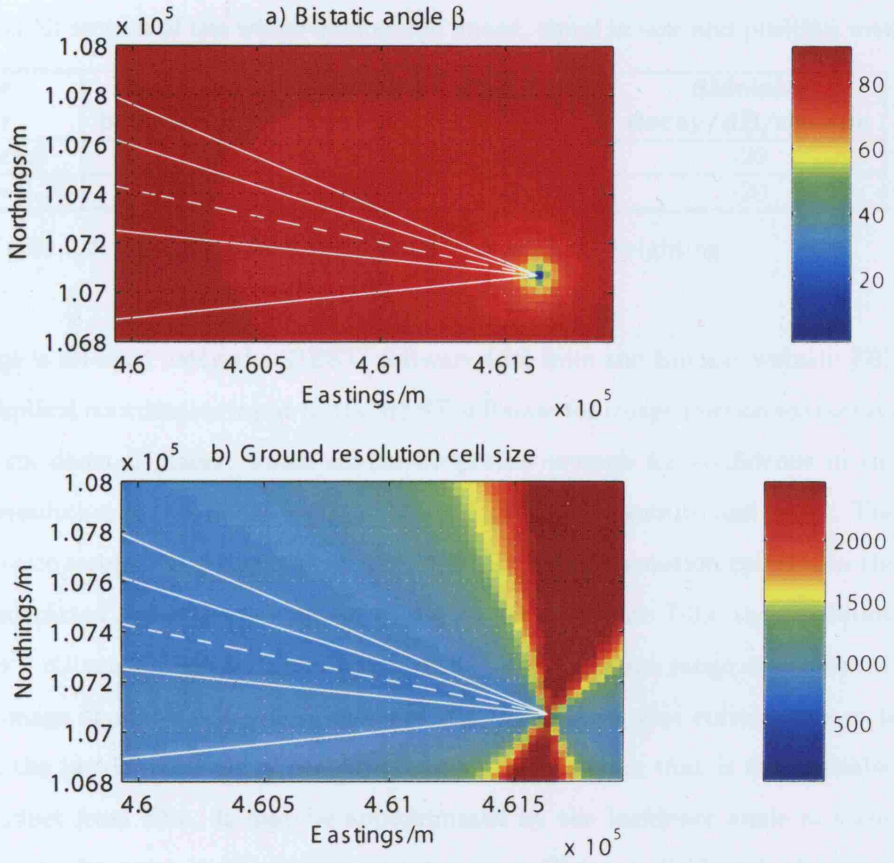

Figure 7-40: Theoretical bistatic angle and ground resolution cell size for 5th December 2005 image

Comparison with the monostatic image

This final section for the Portsdown acquisition results compares the bistatic and monostatic images for this location. The monostatic image is of single look complex type, as described at the start of the Experimental System Chapter. This has a resolution of 6m by 9m in azimuth and range respectively, with a Hamming weighting with $\alpha = 0.75$ applied in both dimensions. The effect of such a weighting function on the impulse response is summarised in Table 7.7. A small section of the whole monostatic image, equal in size and position with

Window function	Mainlobe broadening	Processing loss/dB	PSLR/dB	Sidelobe decay/dB/decade
None (uniform)	1.0	0	-13.3	-20
Hamming $\alpha = 0.75$	1.13	0.63	-21.2	-20

Table 7.7: Hamming window compared to uniform weighting

the bistatic image is selected using the 'BEST' software tool from the Envisat website [69]. Note that the elliptical coordinates input to the BEST software for image portion extraction are accurate to six decimal places, which should be precise enough for confidence in the operation. The resolution of this image section is then degraded in azimuth and range. The degraded monostatic resolution cell size is equal to the minumum resolution cell size in the bistatic image calculated using the Ambiguity Function. From Figure 7-39, the resolution cell size is $850m^2$. Given an azimuth resolution of 24m, the ground range resolution in the monostatic image should be 35.4m. The slant range resolution this corresponds to is dependent upon the incidence angle of the ASAR beam, information that is not available in the image product from ESA. It may be approximated by the incidence angle at scene centre. From the results given in the Experimental System Chapter, Table 4.3, the scene centre incidence angle for the IS2 swath is 22.95^0. Given a ground range resolution of R_g, slant range resolution of R_{sl}, and incidence angle of θ_i, the relevant equation (from Curlander [101]) is:

$$R_g = \frac{R_{sl}}{\sin(\theta_i)}$$

In this case the slant range resolution should be degraded to $R_{sl} = 35.4 \times \sin(22.95) = 13.8m$.

The monostatic image with both full resolution and degraded resolution is plotted in Figures 7-41 and 7-42. The reduced resolution image is very difficult to interpret, and will therefore

be of limited use in the comparison (this is true for all of the acquisitions, and so only the full resolution images will be considered from this point on). Concentrating instead on the full resolution image, the most prominent returns are originating from the DSTL site itself, including the various buildings, structures and the car park. The dark region around these returns, with an almost pentagonal shape, defines the boundary of the site, with another point-like target observable at the lower-left corner of the boundary. This is in the same location as the buildings noted in the bistatic image. Nelson's monument is marked, but not visible in the image. The Fort outline is faintly visible to the West.

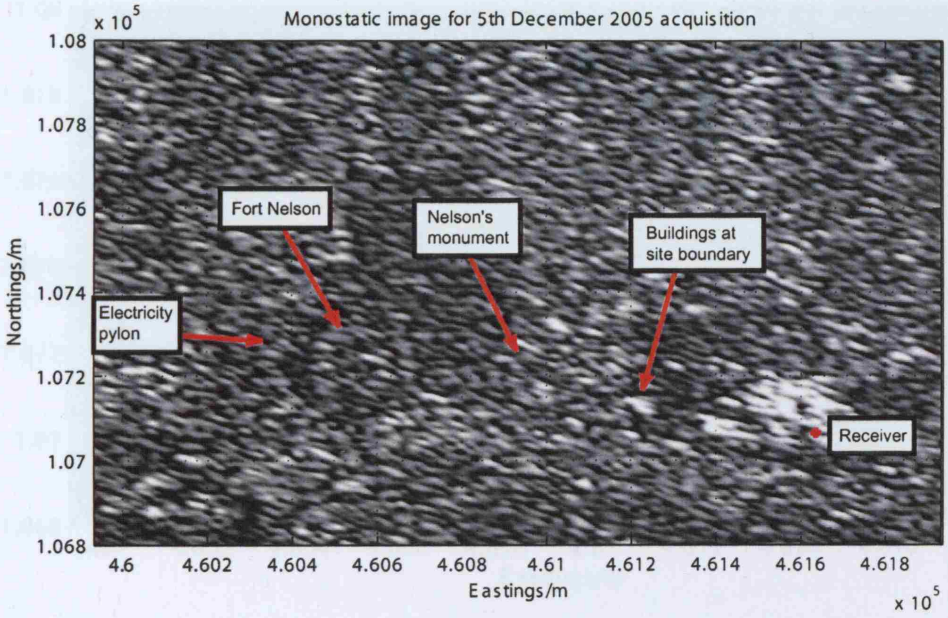

Figure 7-41: Monostatic image for 5th December 2005 acquisition, full resolution

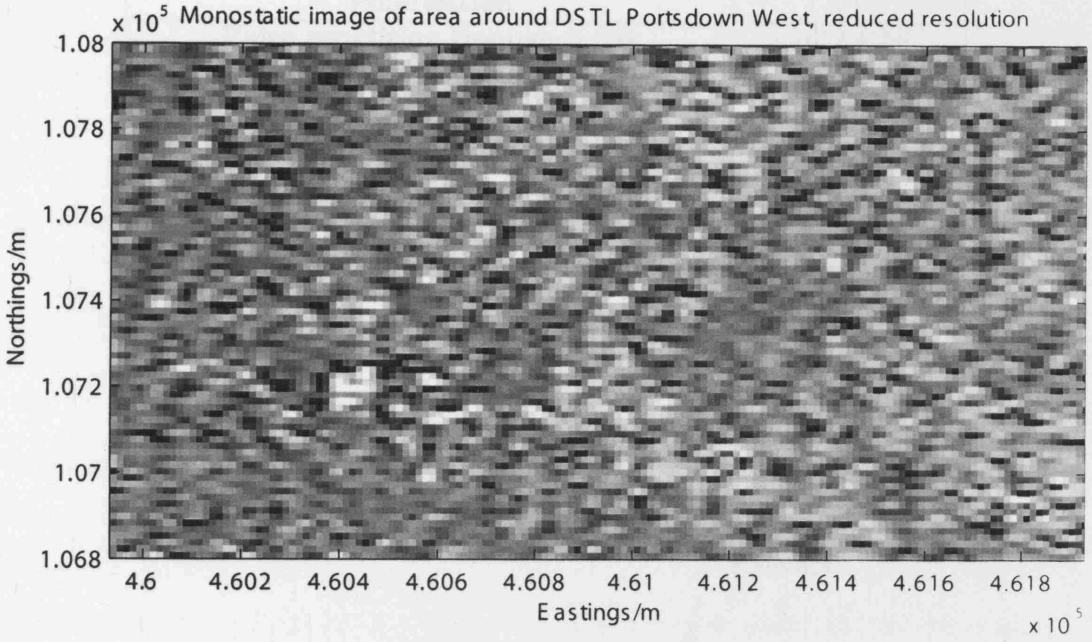

Figure 7-42: Monostatic image for 5th December 2005 acquisition, reduced resolution

7.2.2 Torrington Place site, experiment 1

Overview and geometry

The second experiment to be covered in this document was the first to be performed, on 12th November 2004 on top of a UCL building on Torrington Place, central London. Parabolic antenna 1 was used. Acquisition details, in table 7.8 and a DESCW diagram, Figure 7-43, are given next.

Swath	IS2
Satellite pass	Descending
Polarisation	VV
Pulse repetition frequency/Hz	1652.4156
Pulse length/s	27.1776×10^{-6}
Receiver position (Easting,Northing)/m	(529516,182000)
Receiver look direction (bearing)/degrees	325

Table 7.8: Acquisition details for the first Torrington Place experiment

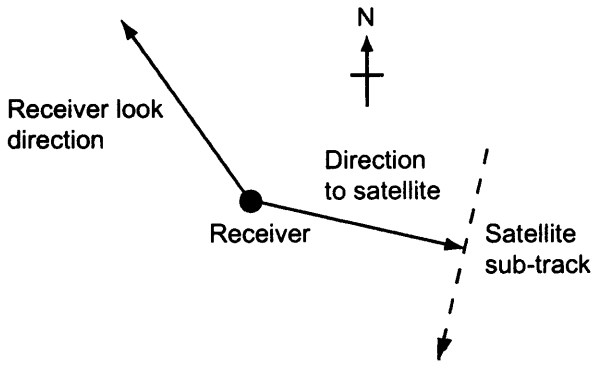

Figure 7-43: Imaging geometry for 12th November 2004 acquisition

Raw data: direct signal channel

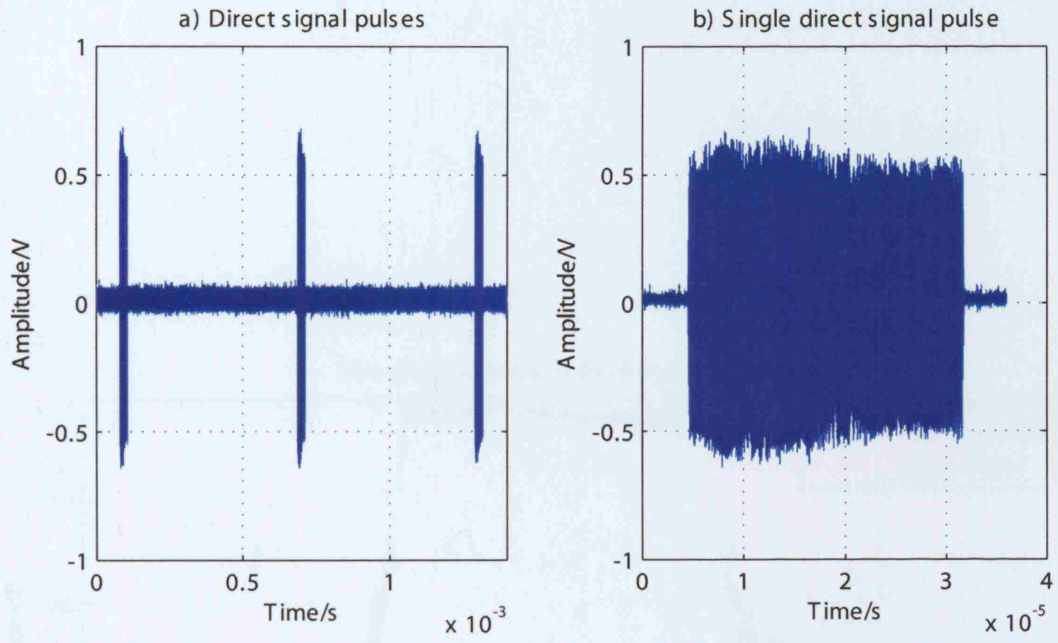

Figure 7-44: Direct signal channel IF pulses captured by the Parsec ADC

Figure 7-44 shows the form of some direct signal pulses at IF. The amplitude is very similar to that exhibited in the 5th December acquisition results, to be expected given the identical direct signal receiver configuration and imaged swath. The pulse repetition interval is also the same. Figure 7-44 b) shows a single direct signal pulse, with a fairly level amplitude across the entire pulse length (the attenuation at high frequencies noted for the last acquisition is not present). The pulse is given in the frequency domain in Figure 7-45, where it is noted that the measured data is in good agreement with theory. The signal-to-noise ratio is approximately 20dB from this Figure. The example baseband pulses and noise histogram will not be shown for any of the acquisition results other than the 5th December 2005.

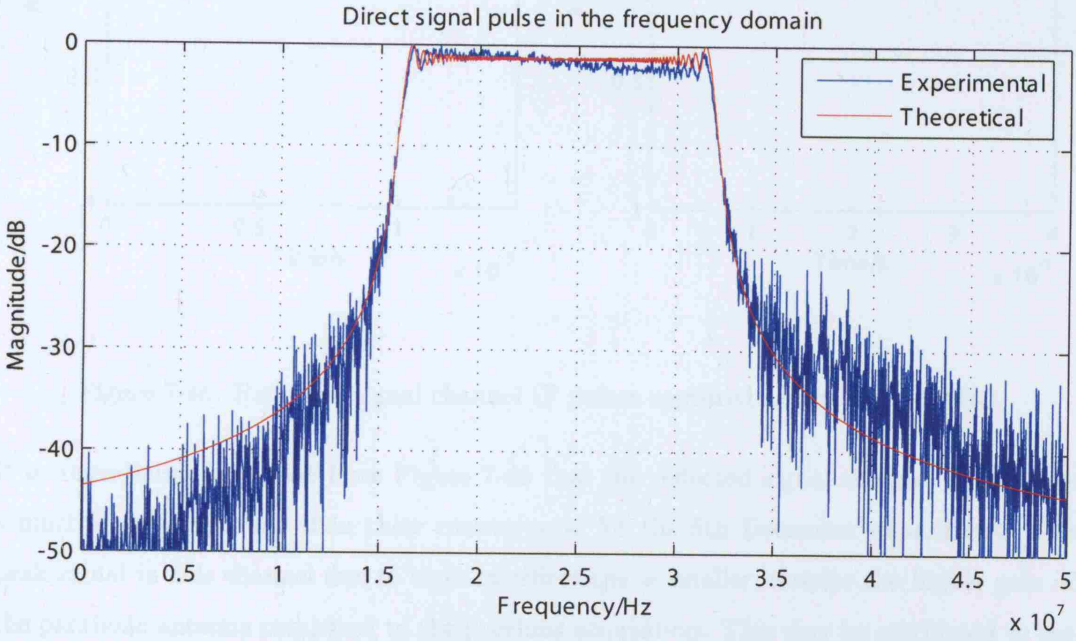

Figure 7-45: Direct signal channel IF pulse in the frequency domain

Raw data: reflected signal channel

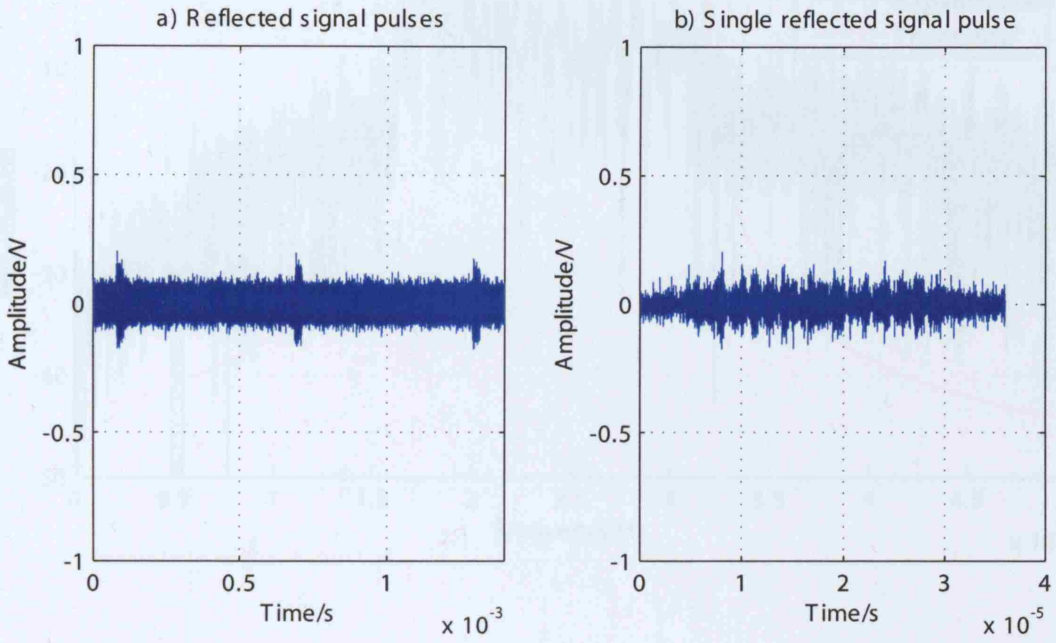

Figure 7-46: Reflected signal channel IF pulses captured by the Parsec ADC

It is immediately apparent from Figure 7-46 that the reflected signal channel pulses have a much lower amplitude than their counterparts for the 5th December experiment. The peak signal in this channel due to close-in reflections is smaller, despite the higher gain of the parabolic antenna compared to the previous acquisition. This may be attributed to the imaging environment for this experiment. Examining Figure 7-47, the signal data is very close in amplitude to the noise, but appears relatively level across the signal bandwidth of 16MHz. A signal-to-noise ratio of 5dB may be observed.

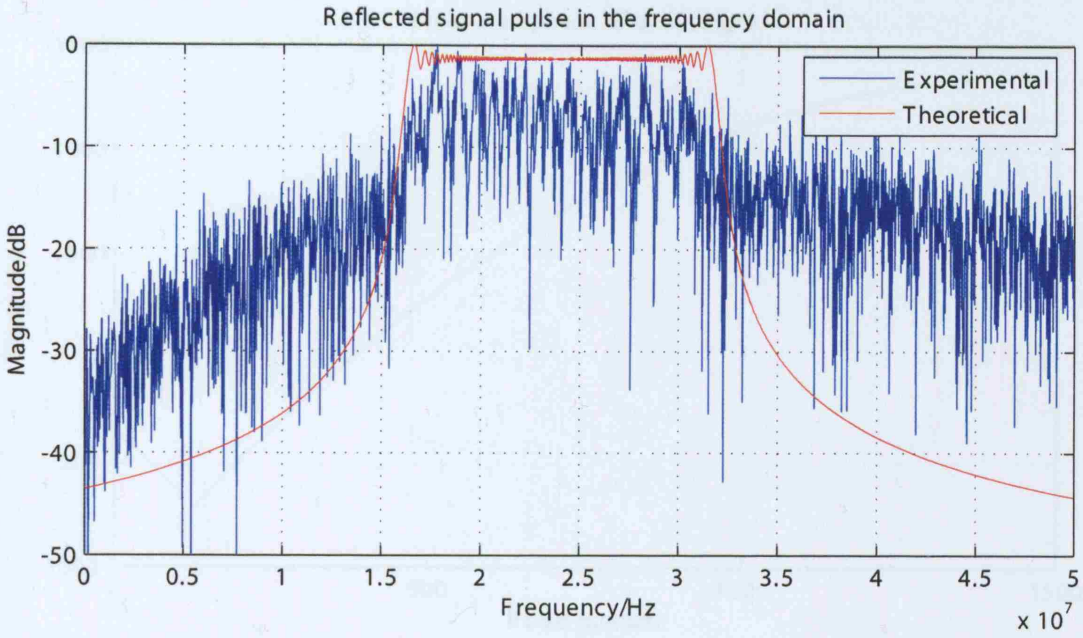

Figure 7-47: Reflected signal channel IF pulse in the frequency domain

Pre-processing

The same procedure as before is followed for this set of experimental data. The reflected signal array is range compressed and phase referenced to the direct signal data. The figures and table over the next three pages illustrate the various outputs of the processing stages. The measured phase of the direct signal pulses is given in Figure 7-48, while the range compressed reflected signal array is shown in Figure 7-49. For the latter, it is noted that there are far more scatterers in the imaged scene with an amplitude close to that of the receiver response than was present in the Portsdown data. Given that the area imaged is a highly cluttered urban scene in this case - compared to the previous semi-rural environment - explains this observation. The phase and magnitude along the pulse number dimension in the compressed reflected signal array for the receiver position are given in Figures 7-50 and 7-51. The residual phase varies by approximately 0.9rad over the 1500 pulses considered and is approximately linear, due to a single dominant point scatterer at the approximate receiver position. The magnitude plot is reasonably symmetrical, with one decrease in pulse amplitude present due to a data loss event as described earlier. The centre pulse for the data to be processed, based on this magnitude plot, is taken to be number 890.

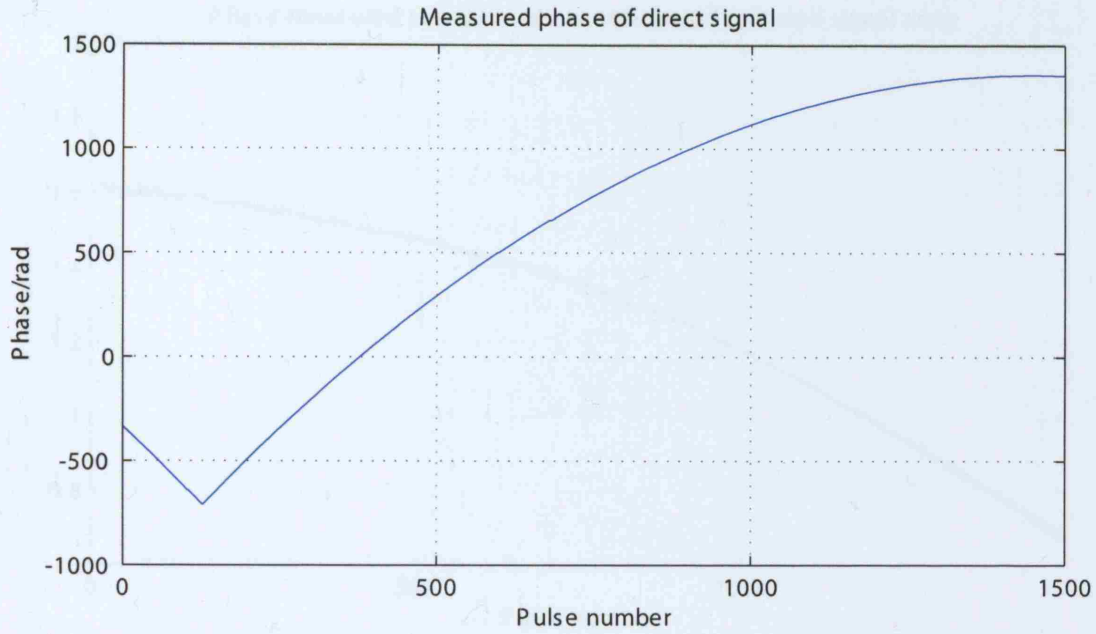

Figure 7-48: Measured phase of direct signal channel pulses

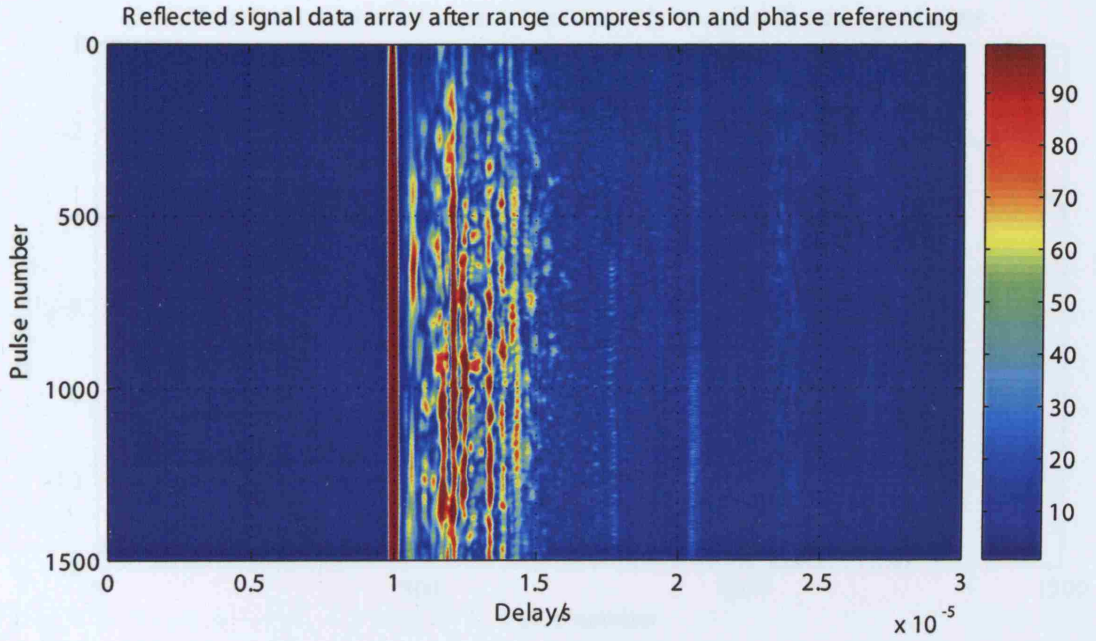

Figure 7-49: Reflected signal channel array after range compression and phase referencing

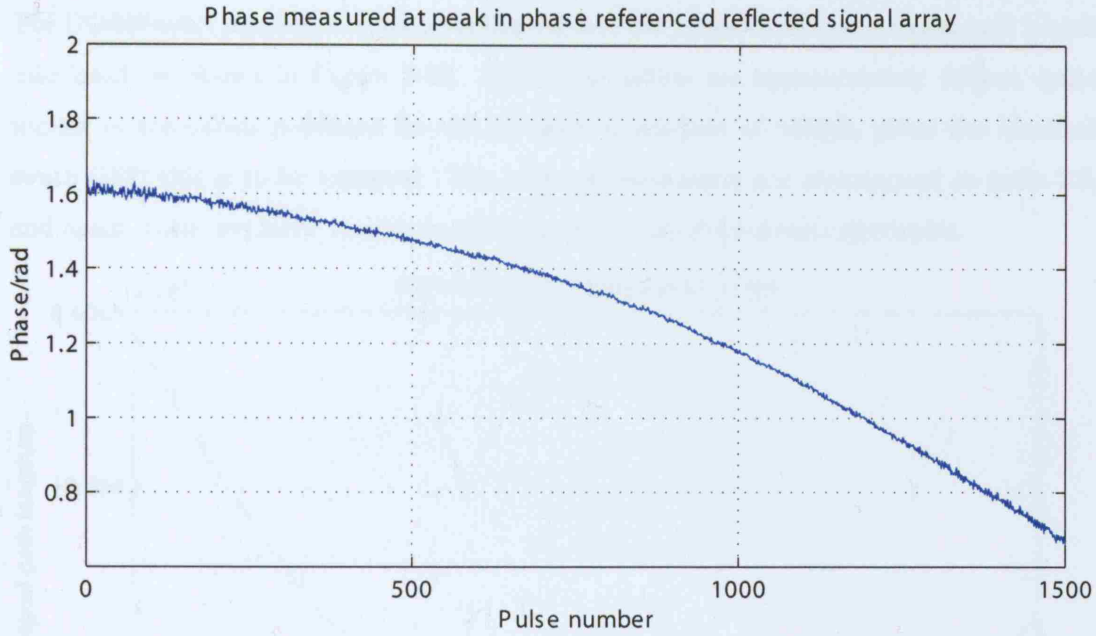

Figure 7-50: Phase measured at peak position in reflected signal channel array

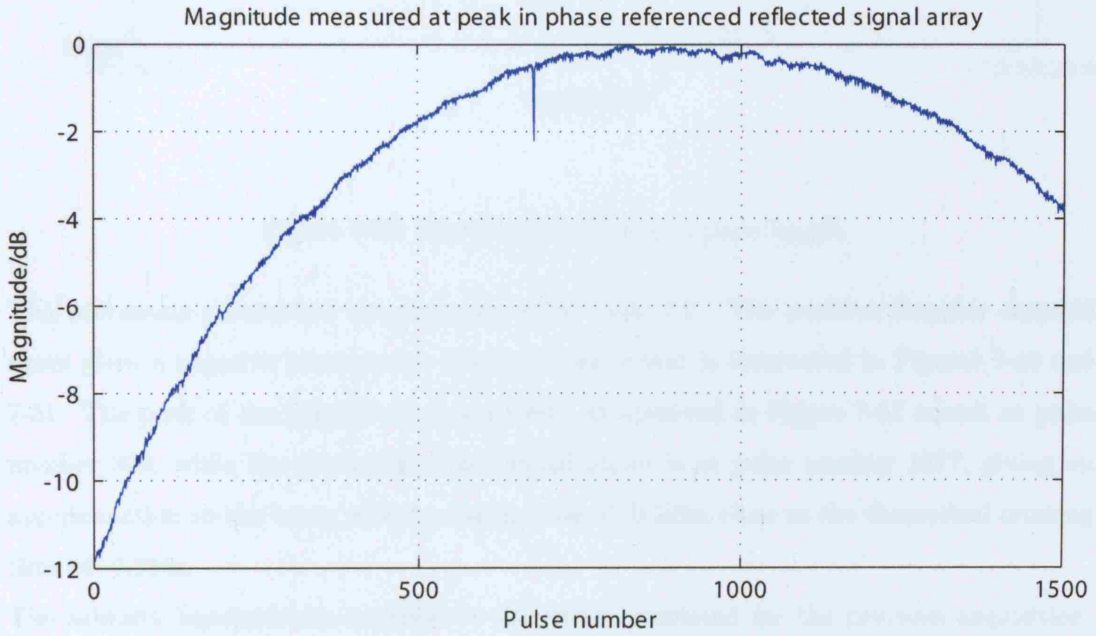

Figure 7-51: Magnitude measured at peak position in reflected signal channel array

The DORIS orbit simulation is then performed, and the variation of direct signal path length calculated, as shown in Figure 7-52. The range values are approximately 860km, quite similar to the values produced for the previous acquisition of 840km, given the identical swath (IS2) this is to be expected. The azimuth parameters are summarised in table 7.9, and again, these are fairly similar to those given for the Portsdown experiment.

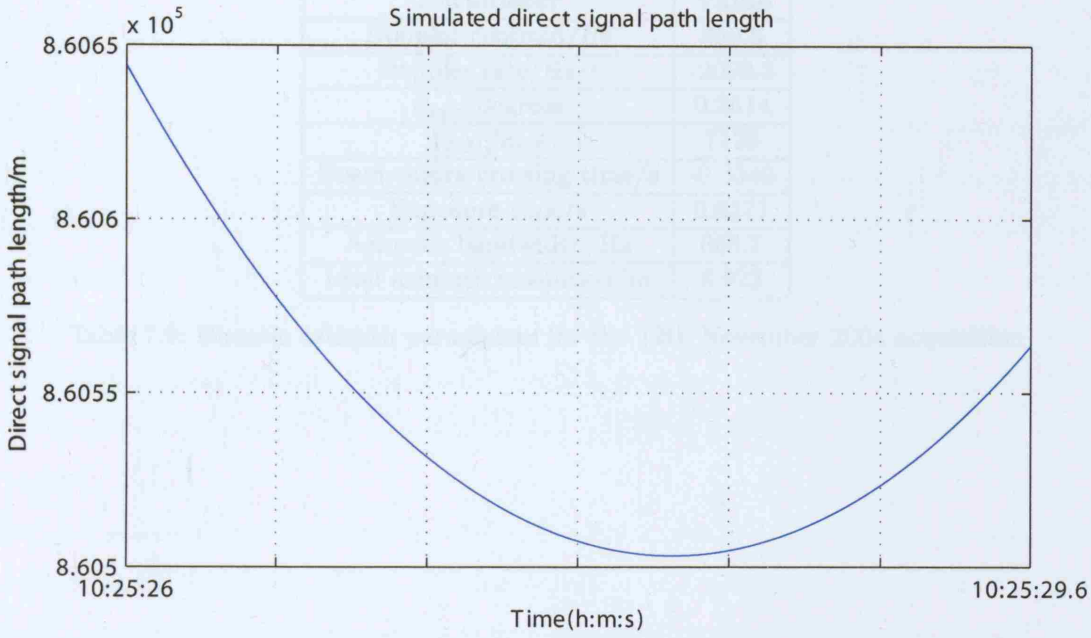

Figure 7-52: Simulated direct signal path length

The processing parameters are summarised in table 7.9. The positive Doppler centroid again gives a negative beam centre crossing time, which is illustrated in Figures 7-48 and 7-51. The peak of the pseudo antenna pattern as observed in Figure 7-51 occurs at pulse number 890, while the minimum direct signal phase is at pulse number 1377, giving an approximation to the beam centre crossing time of -0.295s, close to the theoretical crossing time of -0.334s.

The azimuth bandwidth is identical to the value calculated for the previous acquisition, with a negligible difference in ideal azimuth resolution (8.923m in this case compared to 8.926m previously) between these two acquisitions, as a result of a difference in the squint angle.

The image signal-to-noise ratio may be calculated as,

$$SNR_{image} \approx 25.7 + 10\log_{10}(579) - 1.23 = 52.1dB$$

The second term gives the processing gain due to azimuth compression using 579 pulses.

Parameter	Value
Doppler centroid/Hz	350.6
Doppler rate/Hz/s	-2099.3
$\theta_{sq,c}$/degrees	0.2614
V_{FM}/m/s	7129
Beam centre crossing time/s	-0.3340
Exposure time/s	0.6371
Azimuth bandwidth/Hz	668.7
Ideal azimuth resolution/m	8.923

Table 7.9: Bistatic azimuth parameters for the 12th November 2004 acquisition

Bistatic SAR image

The image produced after processing in Figure 7-53, is presented in the same way as was done previously. As the receiver antenna was not looking in the same direction as the transmitter, the majority of the returns are in this case displaced in azimuth to the left of the receiver in the diagram. As was noted for the reflected channel range compressed data, far more scatterers are visible within the scene.

The range and azimuth cuts at the receiver may be found in Figures 7-54 to 7-57. A few target points may be seen in the range cut at relative range sums of up to 1km with respect to the receiver, although this plane does not contain the majority of scatterer responses in this case due to the receiver look angle. In addition, the bulge in the receiver response in this dimension that was noticed for the previous acquisition is not apparent, and it would therefore seem that there is a clearer delineation between the receiver response and those produced by target points. This can be attributed to the differing rooftop environments for the two experiments. The measured range resolution is 23.6m, compared to 23.4m in theory.

For the azimuth cuts, the same mainlobe broadening and first sidelobe level increase as before may be observed. Again, this can be attributed to the distributed nature of the area iluminated around the receiver, as well as possible receiver oscillator instability. The measured azimuth resolution is 23.4m, theory predicts 24m.

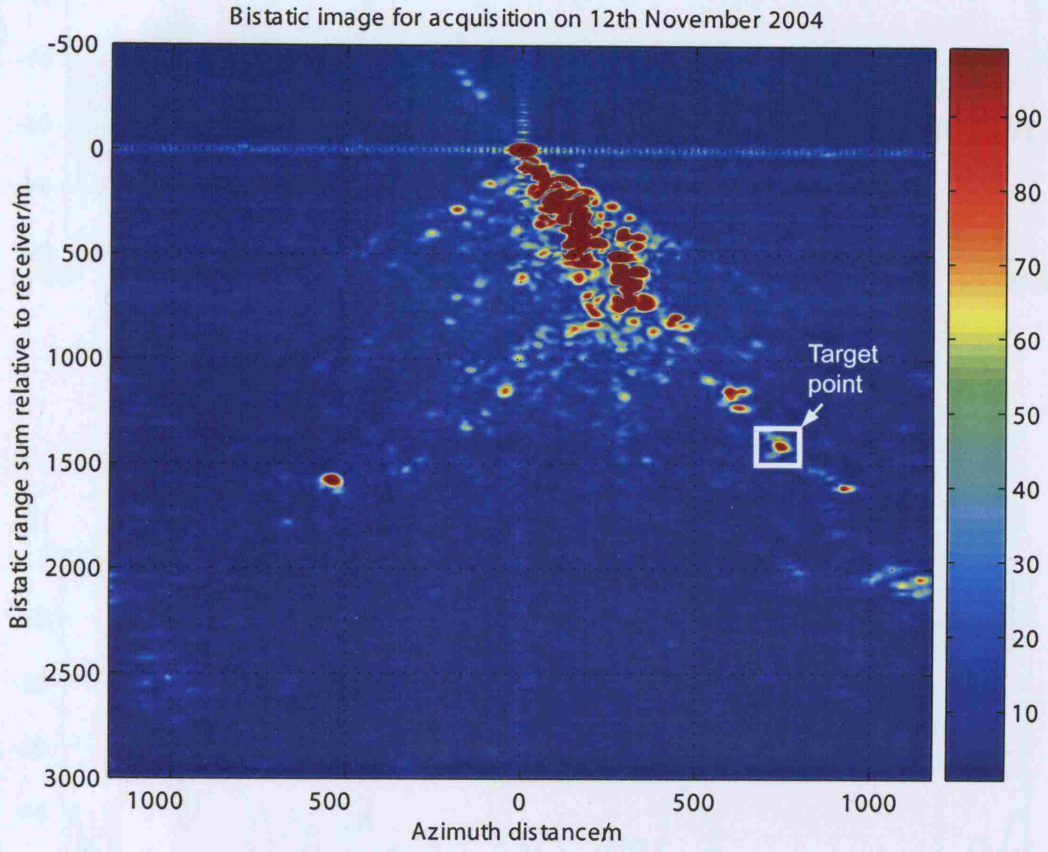

Figure 7-53: Bistatic image for 12th November 2004 acquisition, bistatic range sum versus azimuth

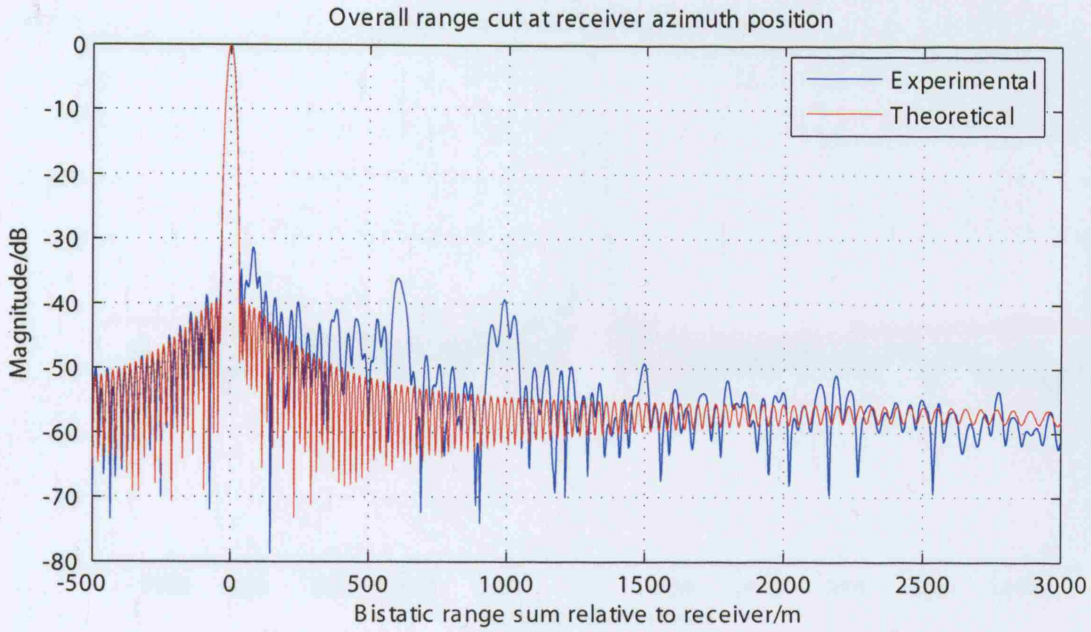

Figure 7-54: Overall range cut at the receiver azimuth position

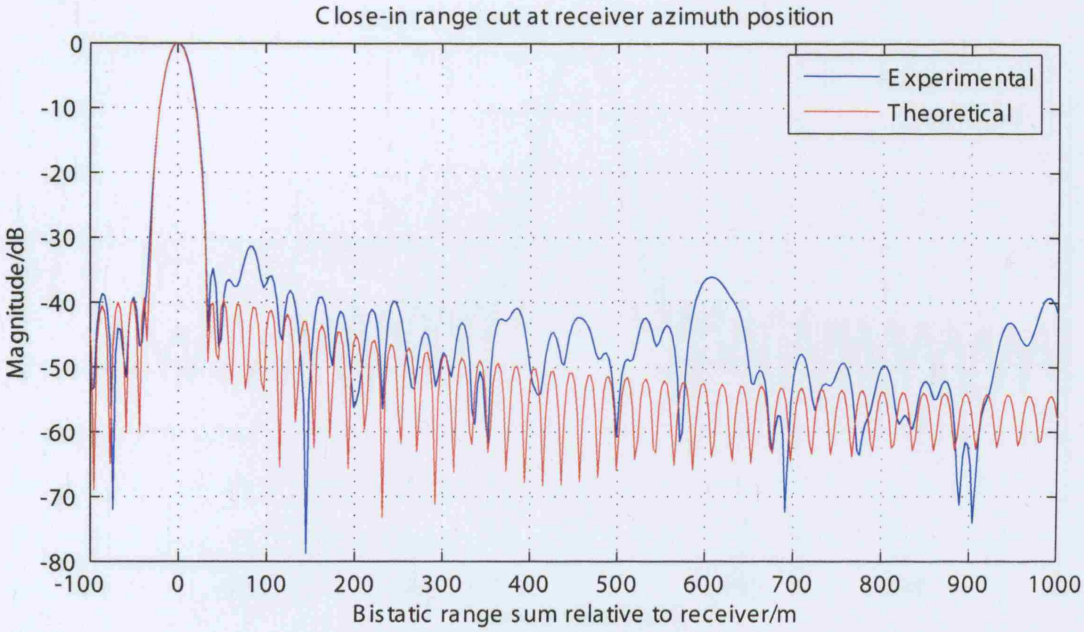

Figure 7-55: Close-in range cut at the receiver azimuth position

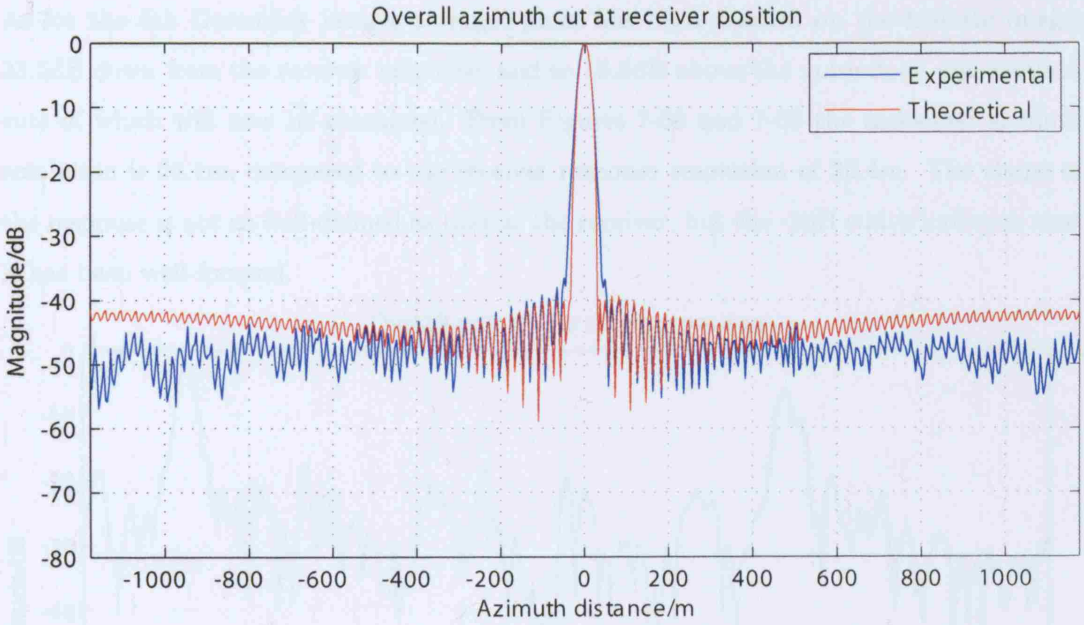

Figure 7-56: Overall azimuth cut at the receiver azimuth position

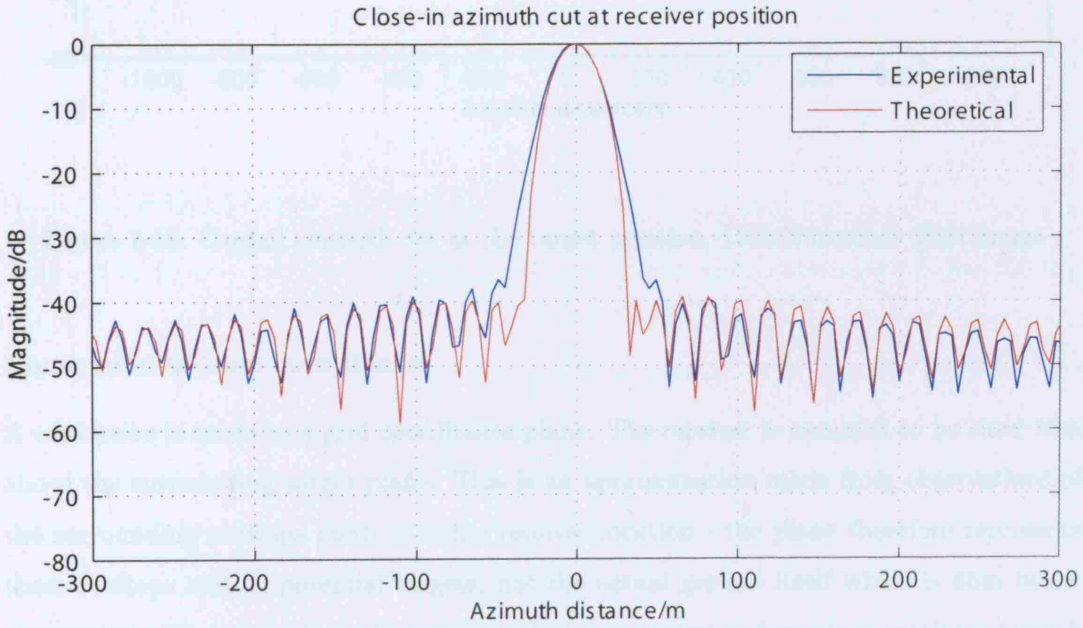

Figure 7-57: Close-in azimuth cut at the receiver azimuth position

As for the 5th December image, a target point has been marked on the bistatic image, 33.5dB down from the receiver response, and so 18.6dB above the noise floor, the azimuth cuts of which will now be examined. From Figures 7-58 and 7-59 the measured azimuth resolution is 23.1m, compared to the receiver response resolution of 23.4m. The shape of the response is not as well-defined as that at the receiver, but the -3dB width indicates that it has been well-focused.

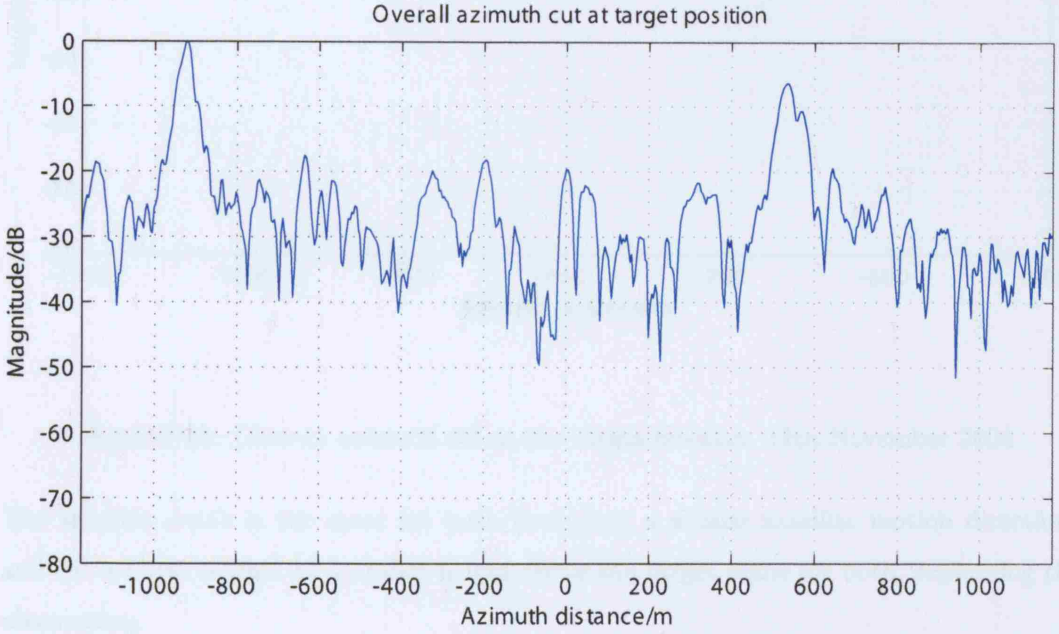

Figure 7-58: Overall azimuth cut at the target position, 12th November 2004 image

Conversion to map coordinates

A conversion is made to a grid coordinates plane. The receiver is assumed to be sited 10m above the surrounding target plane. This is an approximation made from observations of the surrounding rooftops relative to the receiver location - the plane therefore represents these rooftops and so potential targets, not the actual ground itself which is 65m below the receiver. The projections of constant bistatic range sum and constant satellite azimuth position on this plane are given in Figure 7-60. As before, the spacing between each contour is 150m for range and 160m for azimuth, in order that the contour shapes be visible. These are very similar to the contours produced for the previous Portsdown experimental results.

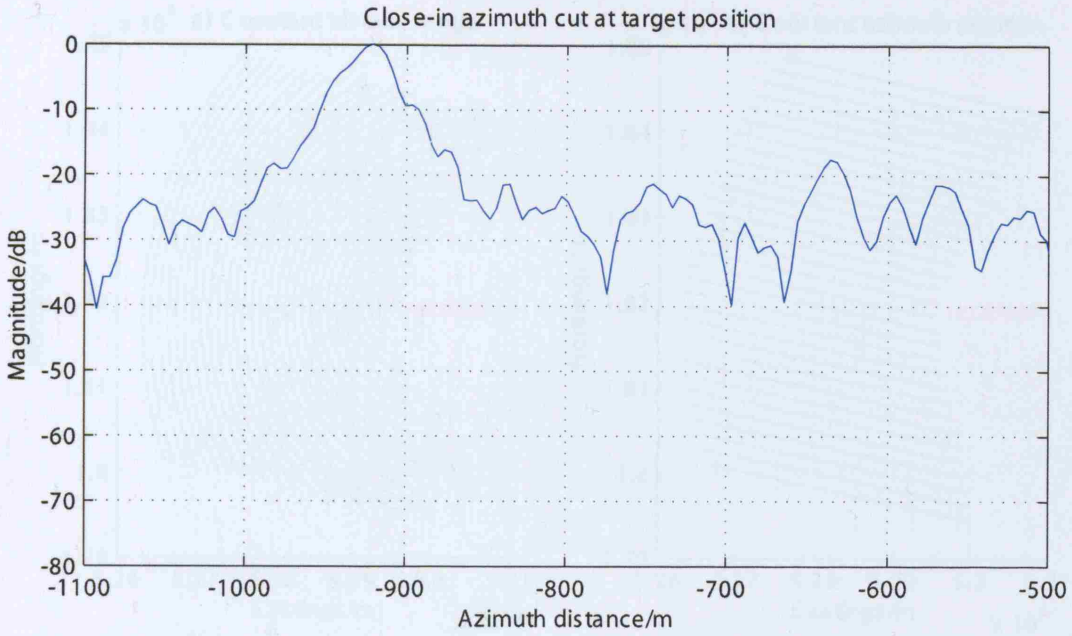

Figure 7-59: Close-in azimuth cut at the target position, 12th November 2004

The satellite swath is the same for both (including a similar satellite motion direction), and the receiver is sited at a similar height above the target plane for both, explaining this observation.

Grid coordinates image analysis

Figure 7-61 shows a satellite photograph of the area around the Torrington Place building where the receiver was sited. Receiver position and beam direction and limits are shown. Contrast the size of the illumination area of this acquisition with that for the last. The parabolic antenna used here has a beamwidth of 3.15^0 while for the Portsdown experiment the antenna beamwidth was 11.8^0. The next Figure, 7-62, is a photo of the observed scene from the point of view of the receiver. It is fairly obvious how cluttered this environment is, with a large number of buildings in the scene. The two main buildings, the Euston tower and the hospital are both marked. Given their size and probable RCS, they should be visible in the bistatic image.

The bistatic image after conversion may be seen in Figure 7-63. The antenna beam and constant range sum contours are superimposed, and the magnitude is plotted with a decibel

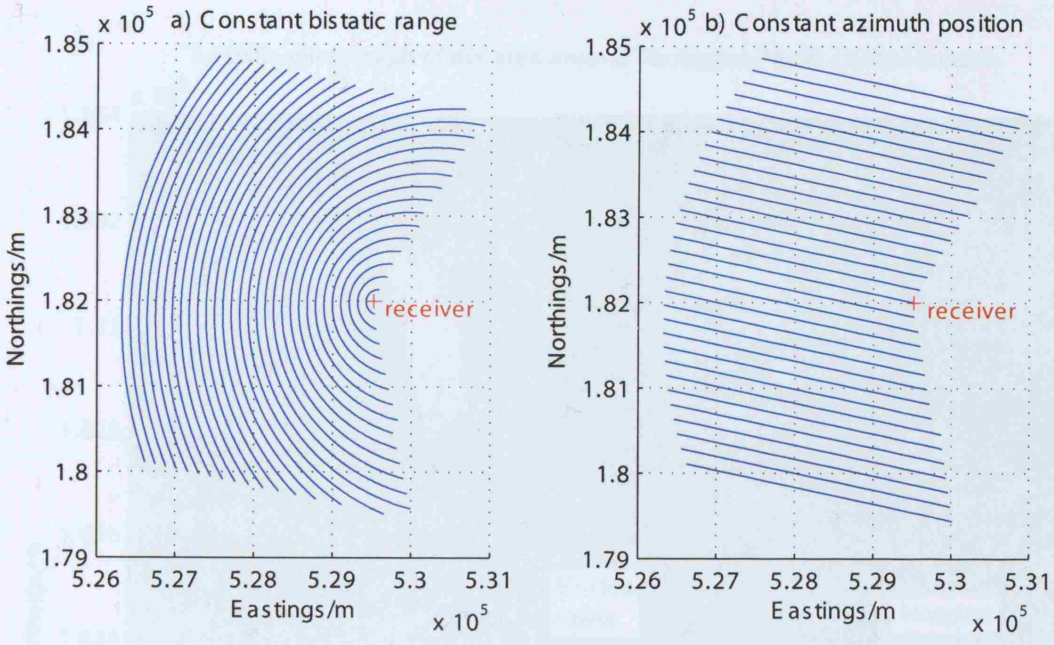

Figure 7-60: Contours of constant bistatic range and azimuth position on the earth's surface for the coordinate conversion of the 12th November 2004 bistatic image

scale, as before. It is obvious that the majority of returns from the imaged scene do not lie within the receiver antenna -3dB or null-to-null beamwidths, for example the scatterer towards the lower left corner of the image. For image generation, a block of data of approximately half the ASAR exposure time is used. Over this period of time, the receiver and surrounding area are within the mainlobe of the ASAR beam. The receiver antenna is fixed, and target points are illuminated by the mainlobe or sidelobes of this antenna. The signals received in the receiver sidelobes may not be separated from the receiver mainlobe returns and will appear in the final image. These responses should be ignored in the image as the sidelobes will apply a phase shift to the signals received, affecting the SAR processing operation. All information outside of the null-to-null beamwidth of the receiver antenna should therefore be ignored.

In addition, it is feasible that azimuth aliasing of the transmit beam pattern is causing azimuth ambiguities to appear in the image. In a monostatic system, the two-way azimuth antenna pattern is sampled at the pulse repetition frequency, which will cause aliasing. The azimuth ambiguities are spaced one "prf time" from each other. From Cumming [79], and

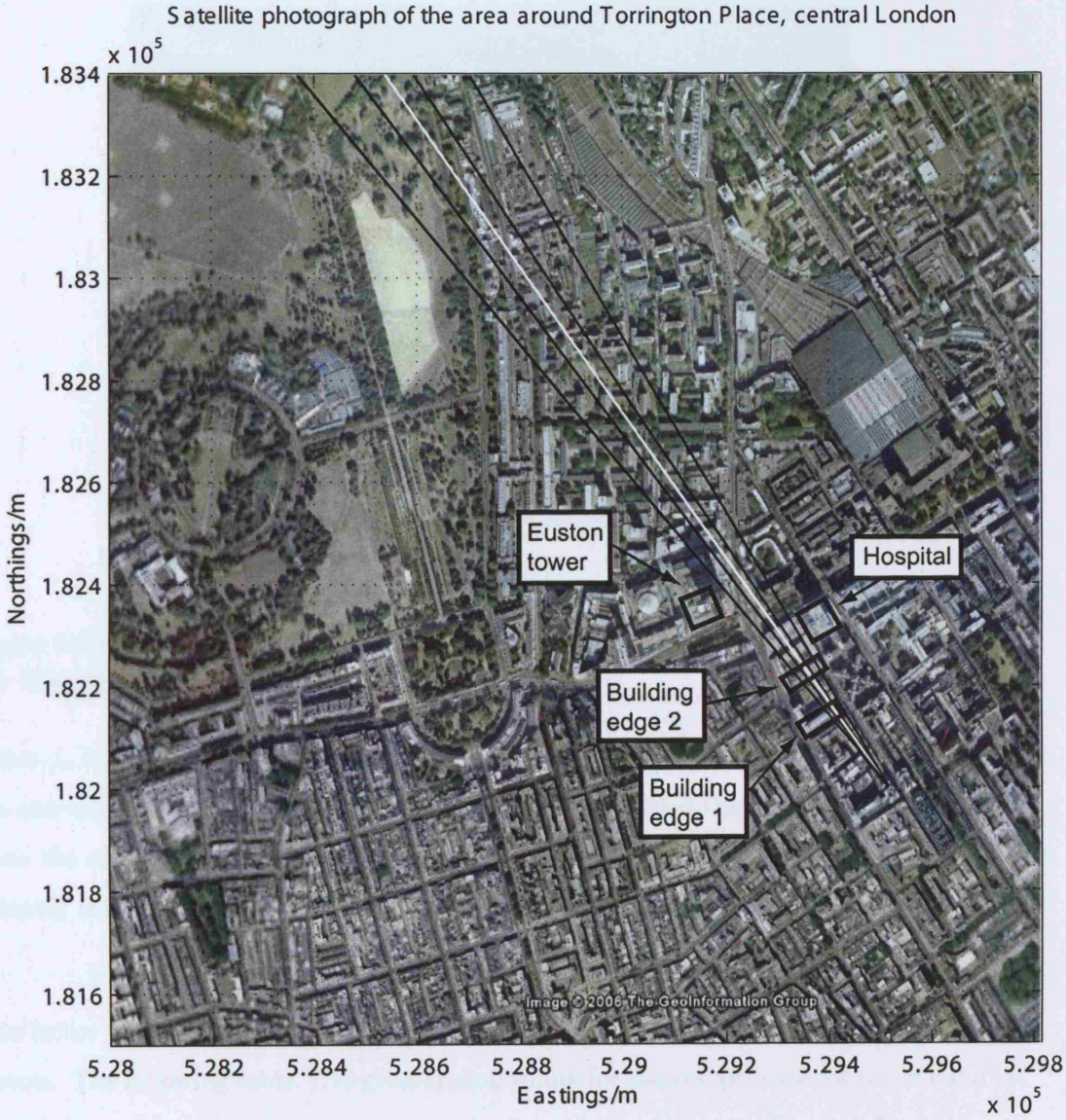

Figure 7-61: Satellite photograph of the area around the Torrington Place site

for zero Doppler pointing, this prf time is equal to,

$$\Delta t_{prf} \approx \frac{\lambda r_0}{2V_{FM}^2} f_p \tag{7.1}$$

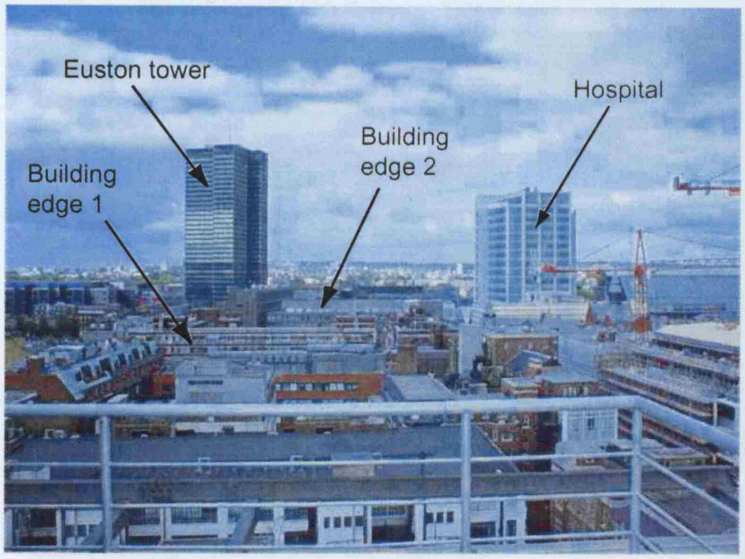

Figure 7-62: Photograph of the imaged area, taken from the receiver position and illustrating the imaged scene

where f_p is the pulse repetition frequency. For the bistatic system, the transmit pattern is the one-way ASAR antenna pattern, with the signal received at the receiver being dependent upon the combined transmit and receive patterns. The bistatic prf time for zero Doppler pointing is equal to,

$$\Delta t_{prf} \approx \frac{\lambda r_0}{V_{FM}^2} f_p \tag{7.2}$$

The factor of two difference arises from the one-way varying path length in the bistatic system. The following table, 7.10 gives typical values for bistatic prf time for the IS1 and IS7 swaths, based on the parameters given in the Experimental System Chapter. For a bistatic

Swath	**Bistatic prf time/s**
IS1	1.64
IS7	2.49

Table 7.10: Bistatic prf time for IS1 and IS7 swaths

image with an R_R variation of approximately 1km, and for a receiver antenna pointing away from the satellite, the prf time will encompass the mainlobe and several sidelobes of the

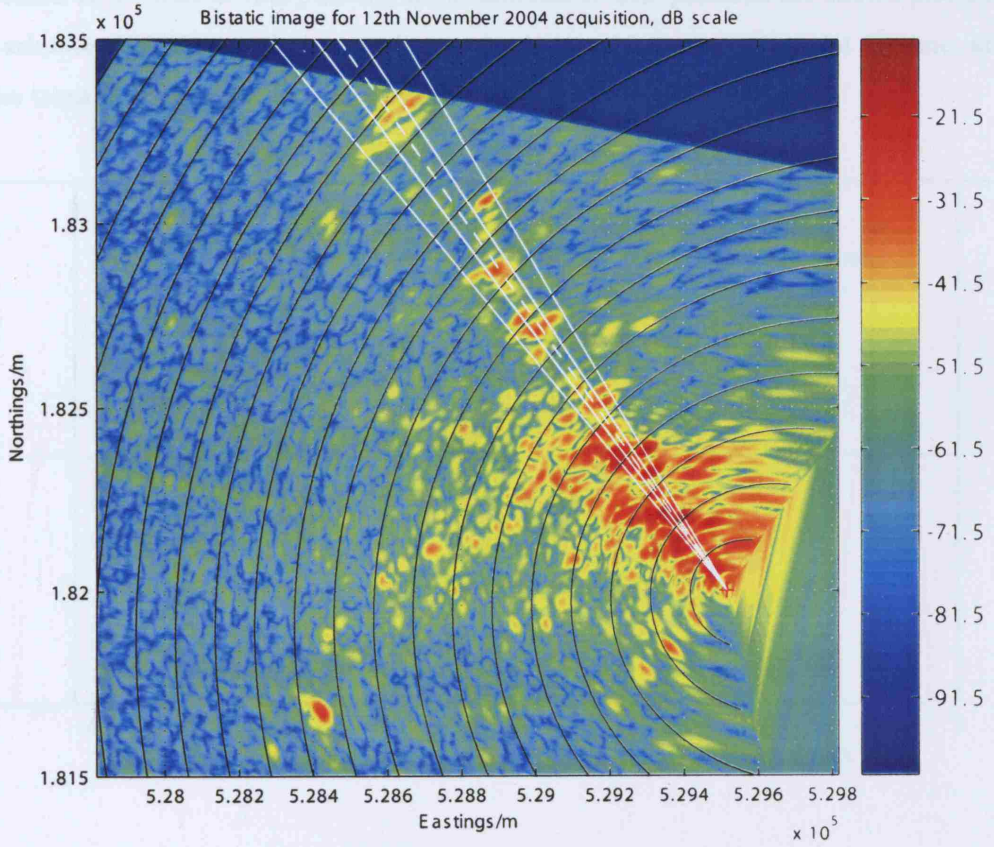

Figure 7-63: Bistatic image from the 12th November 2004 acquisition interpolated onto a grid coordinates plane

receiver pattern response for a particular target point. The following diagrams of Figures 7-64 and 7-65 aid with the explanation. Consider the responses from targets along a line of constant azimuth, a distance of 1km from the receiver. The transmit and receive beams are both represented by sinc functions, the former has both IS1 and IS7 parameters (and is pointing in the zero Doppler direction), while the latter has a beamwidth of 12^0, the largest value used in any of the experiments (see parabolic antenna 2 azimuth beamwidth). The transmit beam is shown in red in the Figures, while the receiver beam is in blue.

The receiver beam may not necessarily be pointing in the same direction as the transmitter beam. An angle of 45^0 (the probable maximum) is assumed between transmit and receive antenna boresights. The plot of the receiver pattern along the constant azimuth line will

be broadened as a result of this pointing angle difference. The patterns are shown plotted against azimuth distance, so the transmit pattern is given for a specific point in time, at which the transmit and receive mainlobes are aligned.

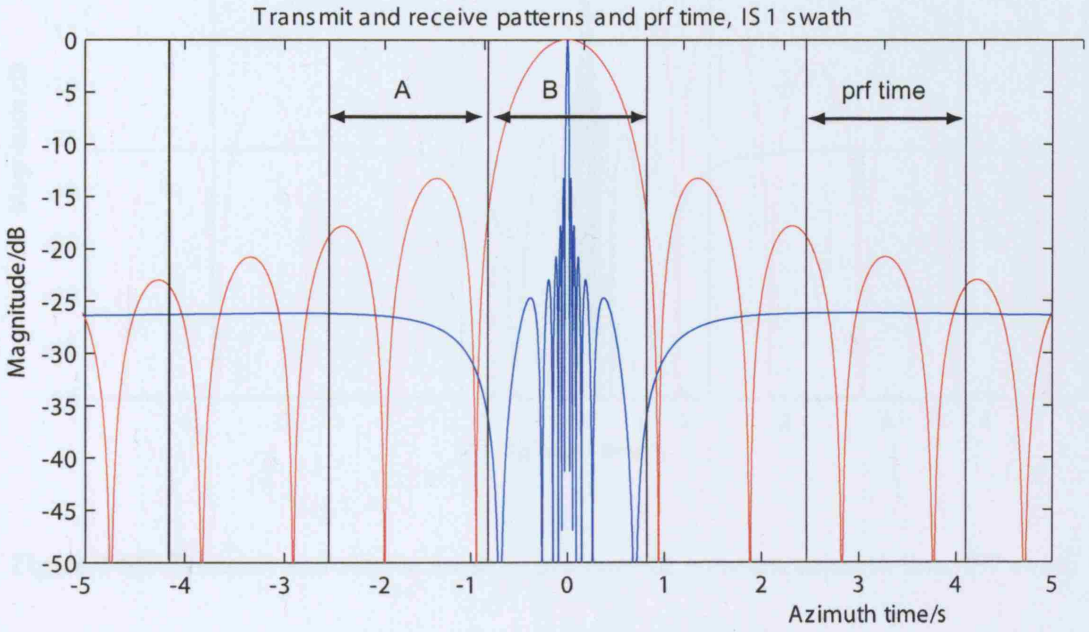

Figure 7-64: Transmit and receive antenna patterns for constant azimuth line, IS1 swath

It is apparent from both Figures that the prf time, shown in terms of azimuth distance is wider than the azimuth extent of the transmit pattern mainlobe, which itself encompasses the mainlobe and several sidelobes of the receiver pattern. As the transmit beam moves across the scene, the mainlobe will illuminate targets on the azimuth line considered, and produce ambiguous responses spaced one/more prf times away. Two regions have been highlighted, A and B, these are adjacent prf time sections. As only data in the receiver mainlobe is important, the ambiguities produced in region B are relevant, produced for instance when the transmit mainlobe is illuminating region A (lower magnitude ambiguities will also be produced in B when the transmitter mainlobe is displaced further away than region A, but these shall be ignored). The ambiguous responses are formed from the combination of the far out receiver sidelobes and transmitter mainlobe. In contrast, the unambiguous (main) response is produced from the combination of transmitter and receiver mainlobes. The ratio between the main response and any ambiguities in region B is therefore likely to be

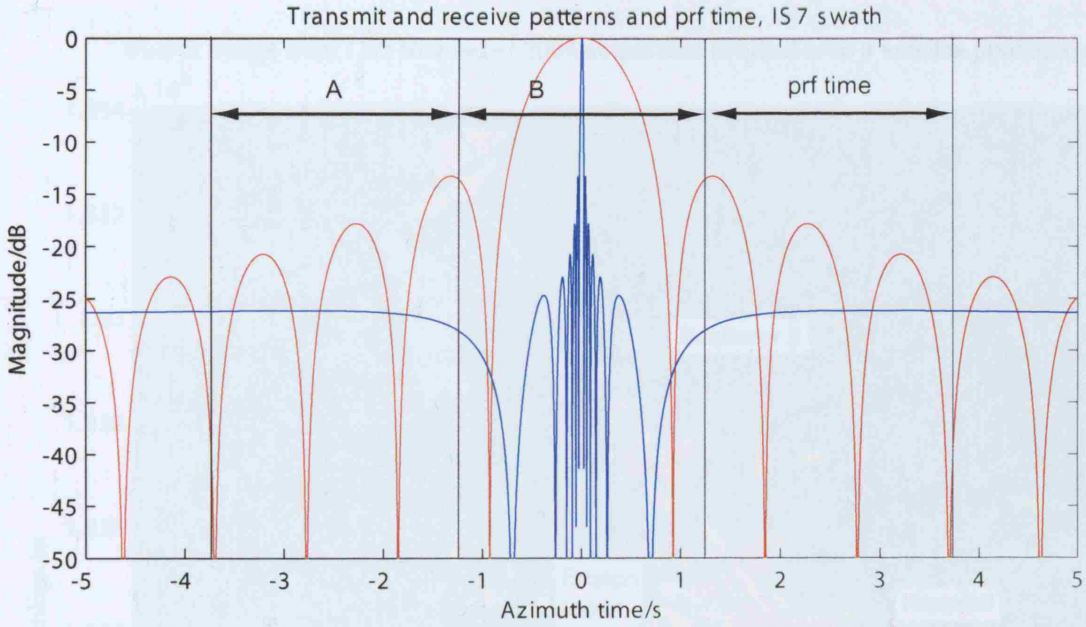

Figure 7-65: Transmit and receive antenna patterns for constant azimuth line, IS7 swath

fairly high, although it is possible that a large bistatic RCS for a target that produces an ambiguous response may reduce this ratio.

As before, the image points that correspond to a magnitude of greater than -50dB with respect to the receiver have been overlaid onto a satellite photograph for Figure 7-66. Given the amount of scattering close to the receiver, it is difficult to match any one scatterer in the image with a feature in the satellite photograph. Nevertheless, it will be attempted in this section to do so. The image results from the next acquisition, for the same receiver location and pointing direction, and similar satellite geometry will be able to at least partially confirm what is discussed here. The features marked on the photographs taken from the receiver position, in Figure 7-62 are reproduced on the satellite photo overlay of Figure 7-66: building edge 1 and 2, the Euston tower and the hospital. Examining this figure, there is a large amount of scattering close to the receiver, and continuing along the receiver line-of-sight until the two large buildings (the tower and the hospital). After this point, the scatterers follow the line-of-sight direction up to a final scatterer approximately 1500m from the receiver. There are no prominent returns from positions behind each of the two large buildings with respect to the receiver position, an area which should be in shadow.

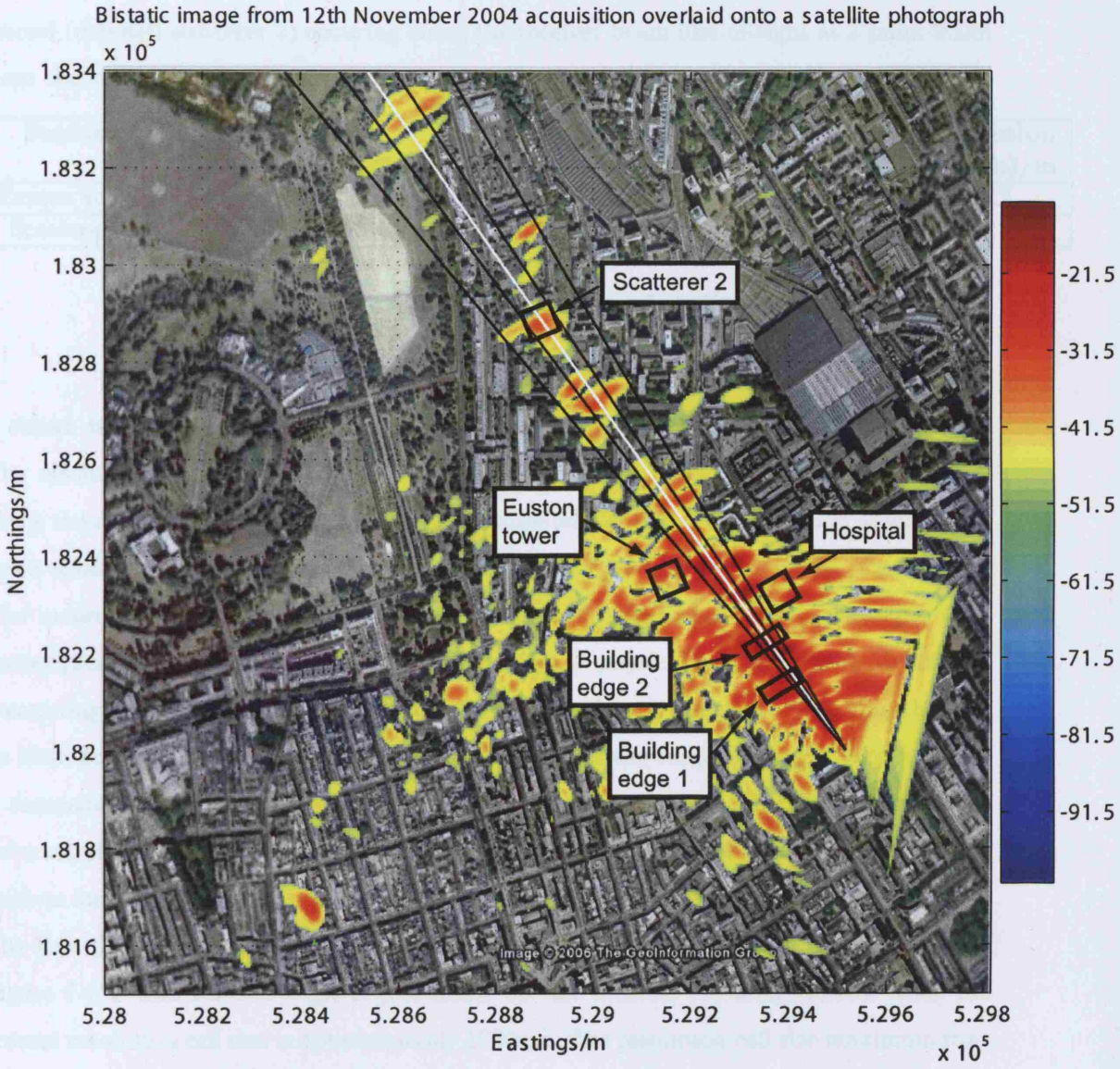

Figure 7-66: Bistatic image overlaid onto a satellite photograph of the area around Torrington Place, 12th November 2004

although there are some points that are yellow in colour behind the Euston tower (approximately -40dB with respect to the receiver). These are low in power and most probably due to sidelobes rather than actual features. Two scatterers are investigated in terms of

returned power and resolution, the first corresponding to the Euston tower position, the second (denoted scatterer 2) occuring along the receiver beam line-of-sight at a point 900m from the receiver, details may be found in Table 7.11. The bistatic Ambiguity Function

Feature	Position (Easting,Northing)/m	Magnitude relative to receiver/dB	Resolution (East)/m	Resolution (North)/m
Euston tower	(529136,182378)	-13.5	19.8	20.7
Scatterer 2	(528892,182870)	-21.6	34.0	28.7

Table 7.11: Selected features in 12th November 2004 image

is shown in Figure 7-67, the bistatic angle and ground resolution cell size in Figure 7-68. The resolution varies from 15.4m to 61.3m in the Eastern direction, with the resolution along the receiver beam direction being approximately 27.9m. The resolution along North has a smaller variation (from 14.9m to 33.8m) and is typically 16.6m in the imaged area. The measured resolutions of the scatterer associated with Euston tower are larger than theory predicts, although the building itself is larger in physical size than these resolutions, accounting for the discrepancy. Scatterer 2 also has a larger measured resolution than for an ideal point scatterer, given the distributed nature of the targets imaged (rooftops) this is reasonable. The response associated with the Euston tower is 8.1dB higher than that for scatterer 2. Given the large physical size of the tower compared to buildings along the receiver antenna boresight (such as that which is causing scatterer 2), this is to be expected. The East-directed resolution maximum along a line running North-South is again noted in Figure 7-67. The bistatic angle is just under 90^0 for most of the imaged area, while the ground resolution cell size is approximately $1200m^2$. The resolution cell size maximum runs along the satellite ground path, in the same way as for the 5th December 2005 results.

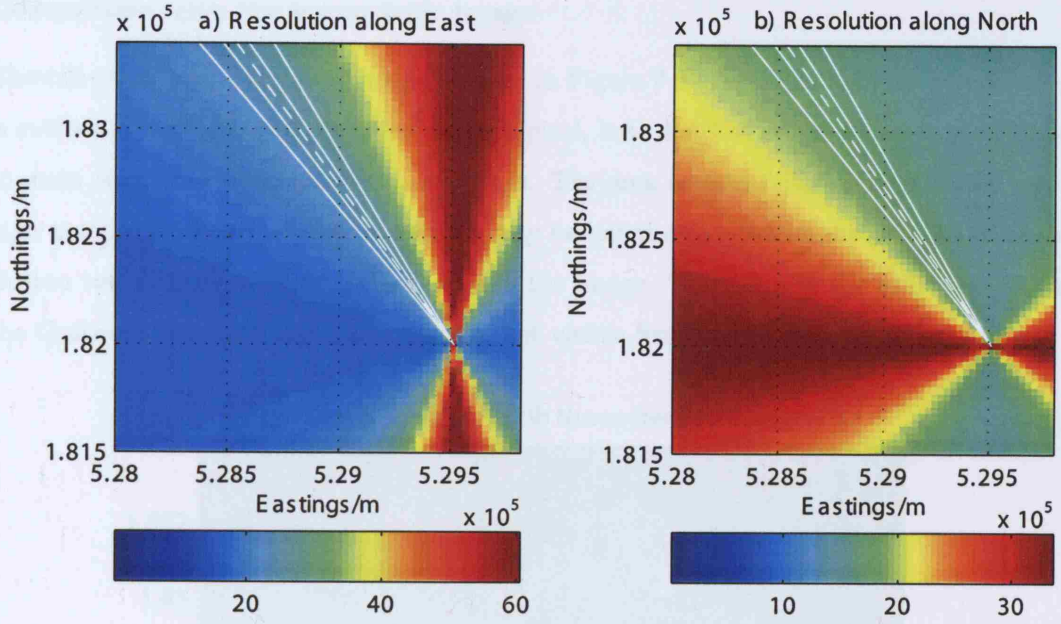

Figure 7-67: Resolutions along East and North directions for 12th November 2004 image

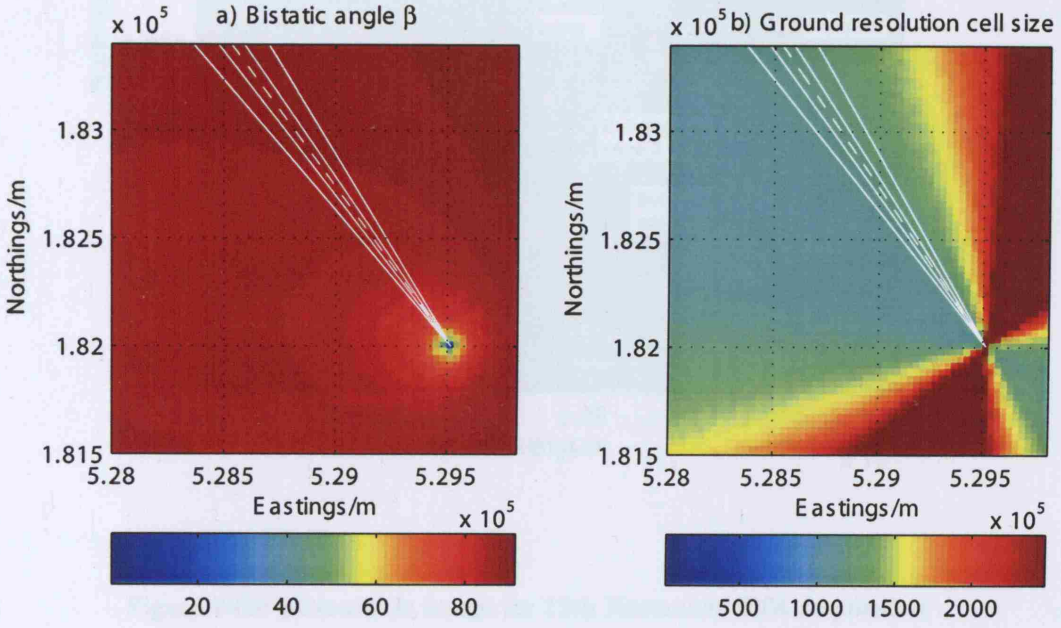

Figure 7-68: Bistatic angle β and ground resolution cell size 12th November 2004 image

Comparison with the monostatic image

The full resolution monostatic image is given in Figure 7-69. A larger amount of scattering is evident around the Euston tower and Hospital, both marked on this image, in addition to some returns between these two buildings. The area around building edge 2 also has a high amplitude. Some prominent returns may be noted at a position directly North of the Euston tower, close to the Northern edge of the image. These are in the same location as the Gasworks behind Kings Cross station, not visible from the bistatic receiver location.

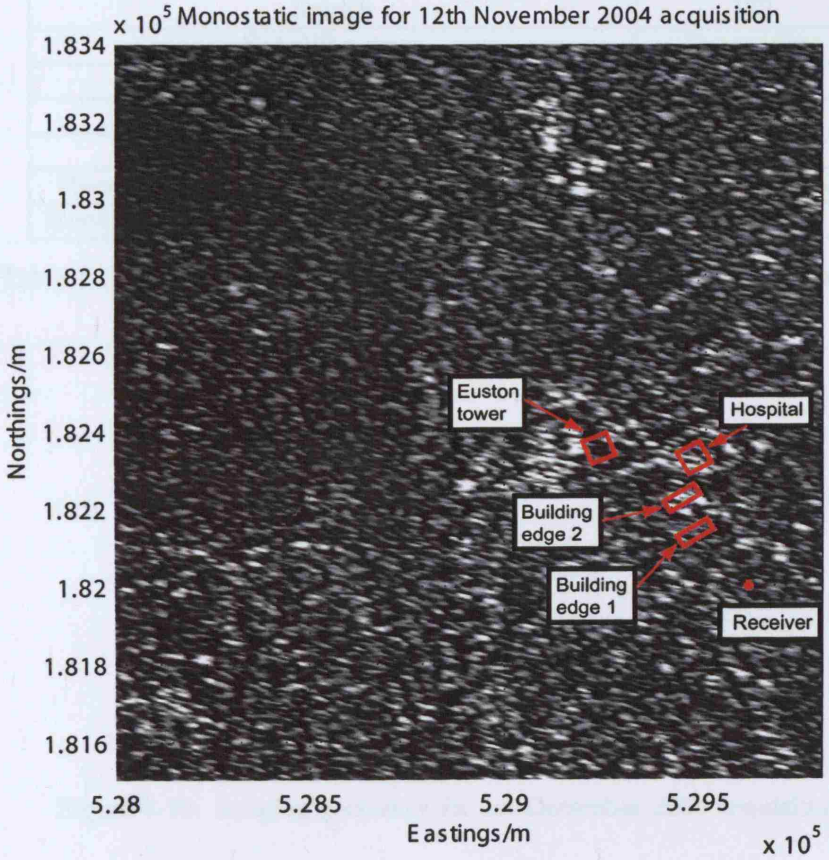

Figure 7-69: Monostatic image for 12th November 2004 acquisition

7.2.3 Torrington Place site, experiment 2

Overview and geometry

This is the second experiment performed at the Torrington Place site in central London. The receiver location and pointing direction are identical to that for the previous acquisition on 12th November 2004, to within the accuracy of the measuring devices. The satellite is again in IS2 mode, with a descending pass, and parabolic antenna 1 is used for the receiver reflected signal measurements. Table 7.12 and Figure 7-70 give the relevant information.

Swath	IS2
Satellite pass	Descending
Polarisation	VV
Pulse repetition frequency/Hz	1652.4156
Pulse length/s	27.1776×10^{-6}
Receiver position (Easting,Northing)/m	(529516,182000)
Receiver look direction (bearing)/degrees	325

Table 7.12: Acquisition details for the second Torrington Place experiment

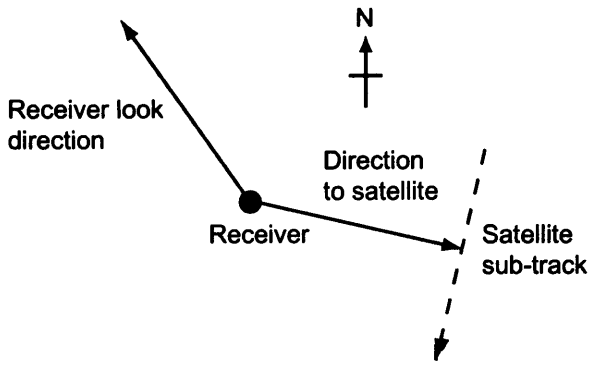

Figure 7-70: Imaging geometry for 1st December 2004 acquisition

Raw data

Example pulses from the direct and reflected signal captures will not be given for this experiment or the others as it has been demonstrated through the previous sets of results that the receiver is capturing the raw pulse data correctly.

Pre-processing

As before, the measured direct signal phase and the pulse compressed reflected signal matrix are given next, in Figures 7-71 and 7-72. The phase plot is fairly similar to that observed for the 12th November signal capture, with a maximum value at pulse number 1272, but the range compressed reflected signal has far fewer peaks in this case, despite the same receiver placement and similar satellite geometry. It is possible that the angle of depression of the parabolic antenna differs for the two experiments - as the accuracy to which this angle can be set is to within 1 degree, this is feasible. The depression angle for this particular acquisition would therefore be less than that for 12th November in order to explain the difference in scattering levels.

The measured reflected signal phase of Figure 7-73 is quite linear, as a result of a single dominant scatterer, and the magnitude plot is fairly symmetrical as a result, Figure 7-74. The magnitude plot peak occurs at pulse number 940.

A minimum baseline length of approximately 841km is noted from Figure 7-75, less than, but consistent with the value calculated for the last set of results. In this case, the processing parameters of Table 7.2.3 include a small Doppler centroid and so minimal squint angle. The measured beam centre crossing time from Figures 7-71 and 7-74 is -0.2s. The theoretical value of -0.03s is very different, although the method for measuring this quantity will be prone to some error.

The image signal-to-noise ratio is,

$$SNR_{image} \approx 25.7 + 10\log_{10}(567) - 1.23 = 52.0dB$$

The second term gives the processing gain due to azimuth compression using 567 pulses.

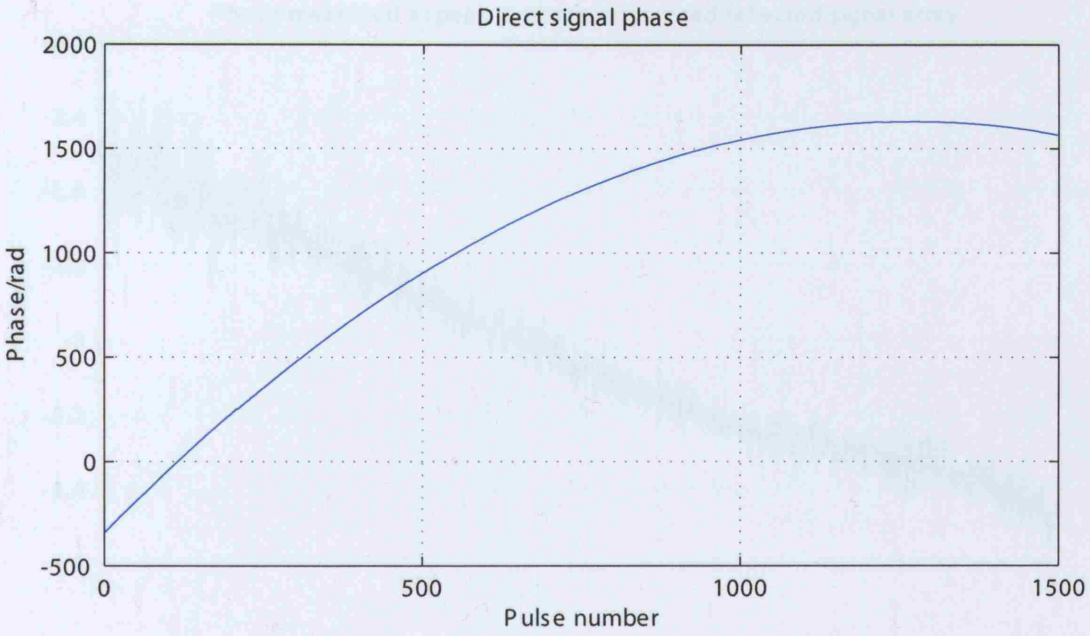

Figure 7-71: Measured phase of direct signal channel pulses

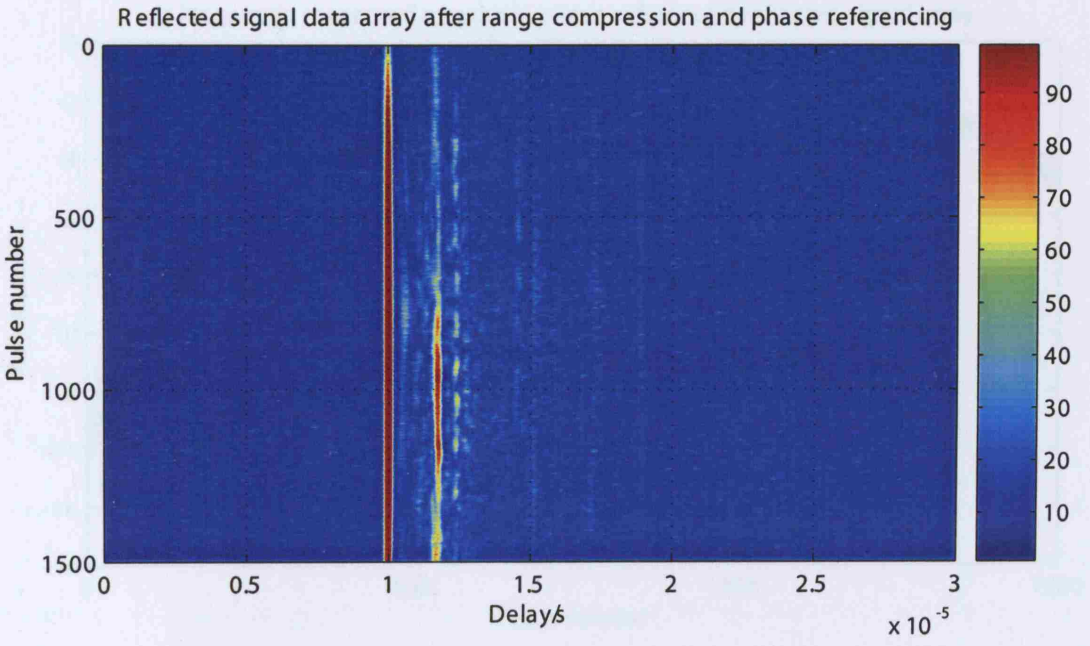

Figure 7-72: Reflected signal channel array after range compression and phase referencing

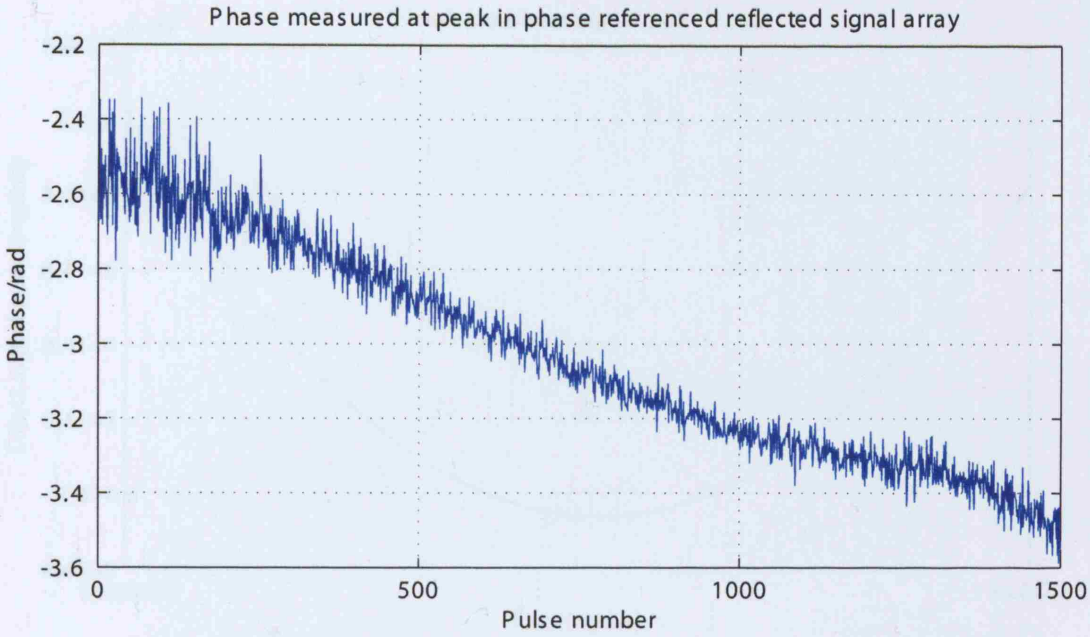

Figure 7-73: Phase measured at peak position in reflected signal channel array

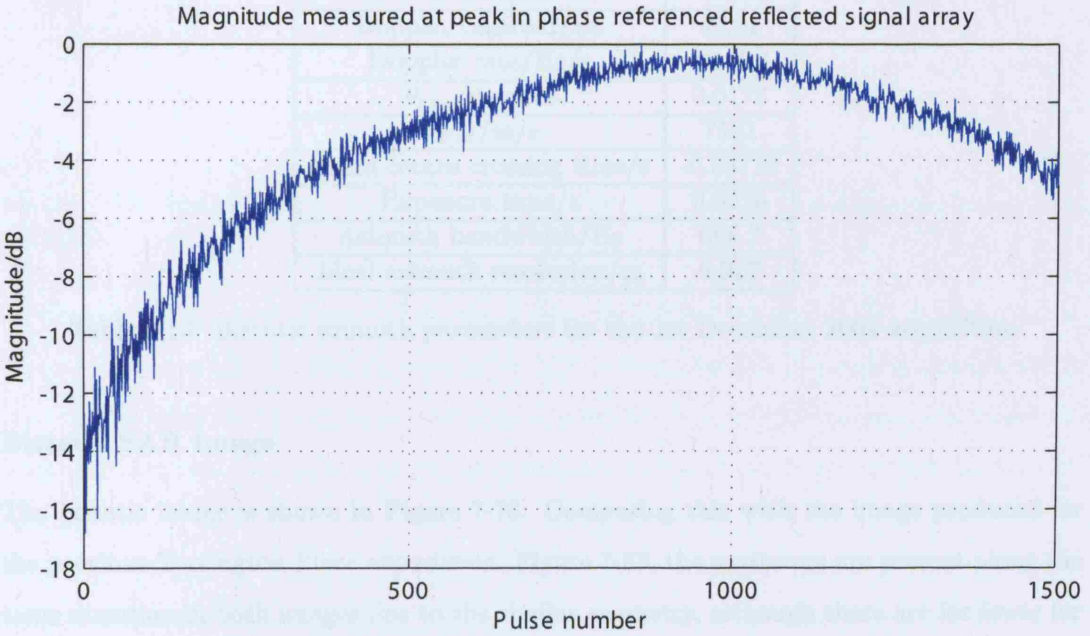

Figure 7-74: Magnitude measured at peak position in reflected signal channel array

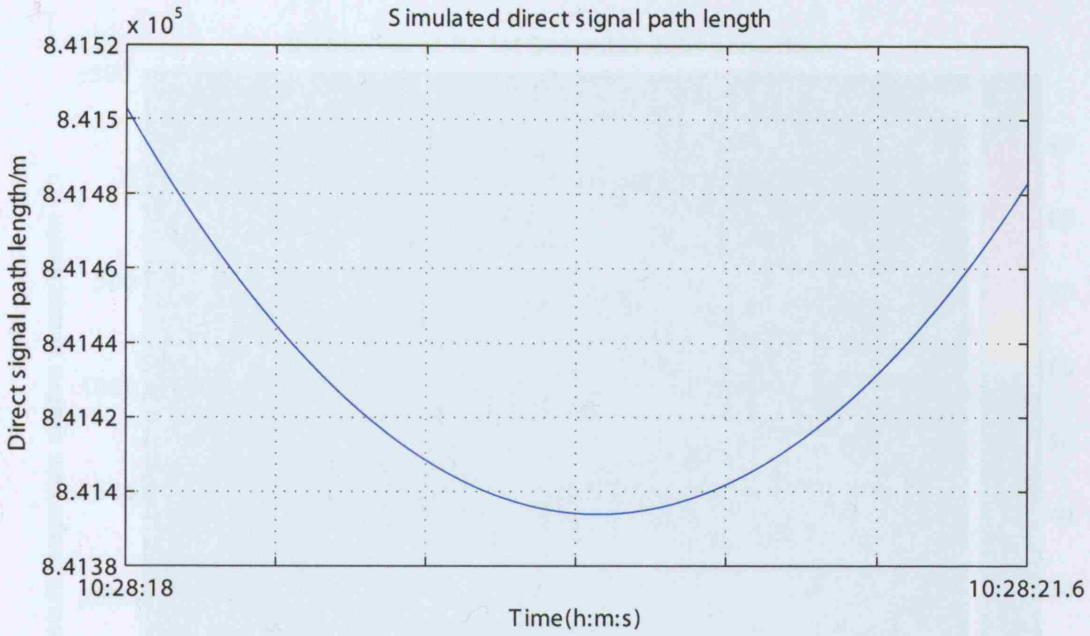

Figure 7-75: Simulated direct signal path length

Parameter	Value
Doppler centroid/Hz	40.51
Doppler rate/Hz/s	-2148.1
$\theta_{sq,c}$/degrees	0.0173
V_{FM}/m/s	7131
Beam centre crossing time/s	-0.03772
Exposure time/s	0.6226
Azimuth bandwidth/Hz	668.7
Ideal azimuth resolution/m	8.927

Table 7.13: Bistatic azimuth parameters for the 1st December 2004 acquisition

Bistatic SAR image

The bistatic image is shown in Figure 7-76. Comparing this with the image produced for the previous Torrington Place experiment, Figure 7-53, the scatterers are present along the same direction in both images due to the similar geometry, although there are far fewer for the 1st December image. This was already noted for the pulse compressed reflected signal data array.

Examining the range cuts of Figures 7-77 and 7-78, these indicate returns from the scene

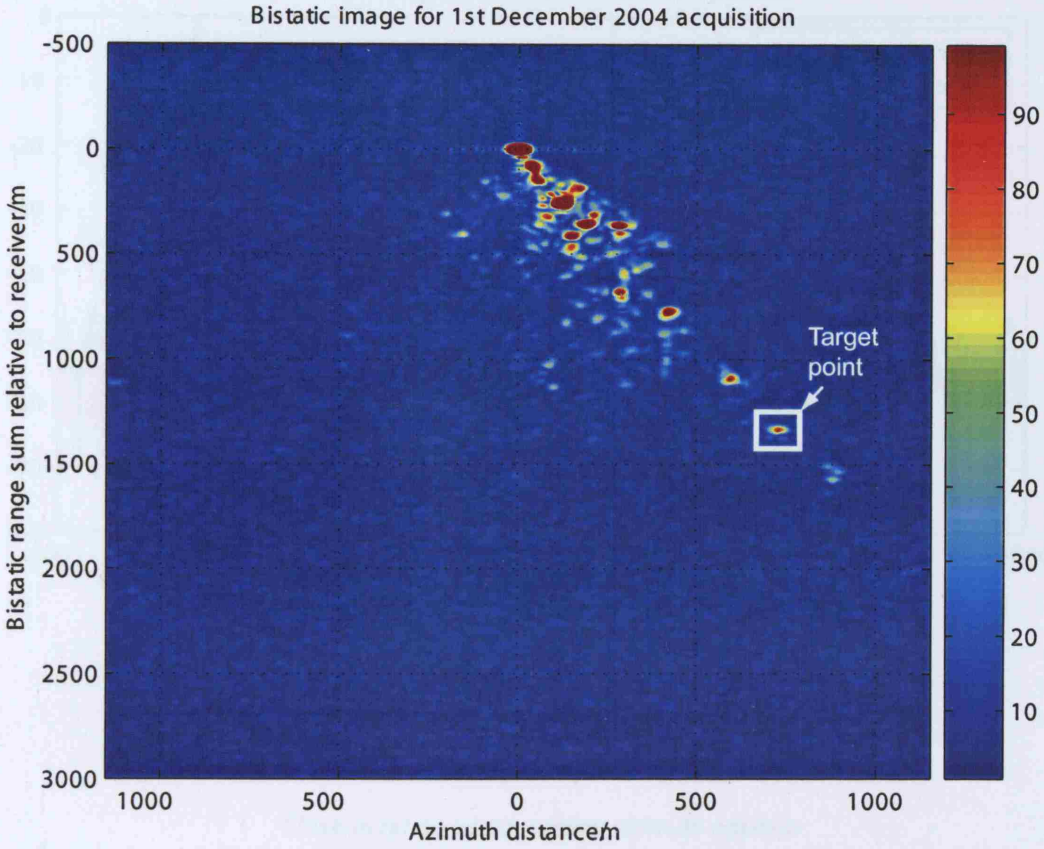

Figure 7-76: Bistatic image for 1st December 2004 acquisition, bistatic range sum versus azimuth

at bistatic range sums of approximately 600m and 1000m relative to the receiver, in the same relative position as may be seen in the 12th November cuts. Therefore objects within the imaged scene are producing a response in both Torrington Place images. The measured range resolution at the receiver is 23.1m, compared to the theory which predicts a value of 23.4m.

The azimuth cuts of Figures 7-79 and 7-80 have a very similar shape to those from the 12th November, with a mainlobe broadening and first sidelobe level increase. The measured resolution in this dimension is 23.7m, with a theoretical resolution of 24m. The azimuth resolution for the same target point as was examined in the 12th November image is measured as 28.2m, fairly close to the ideal.

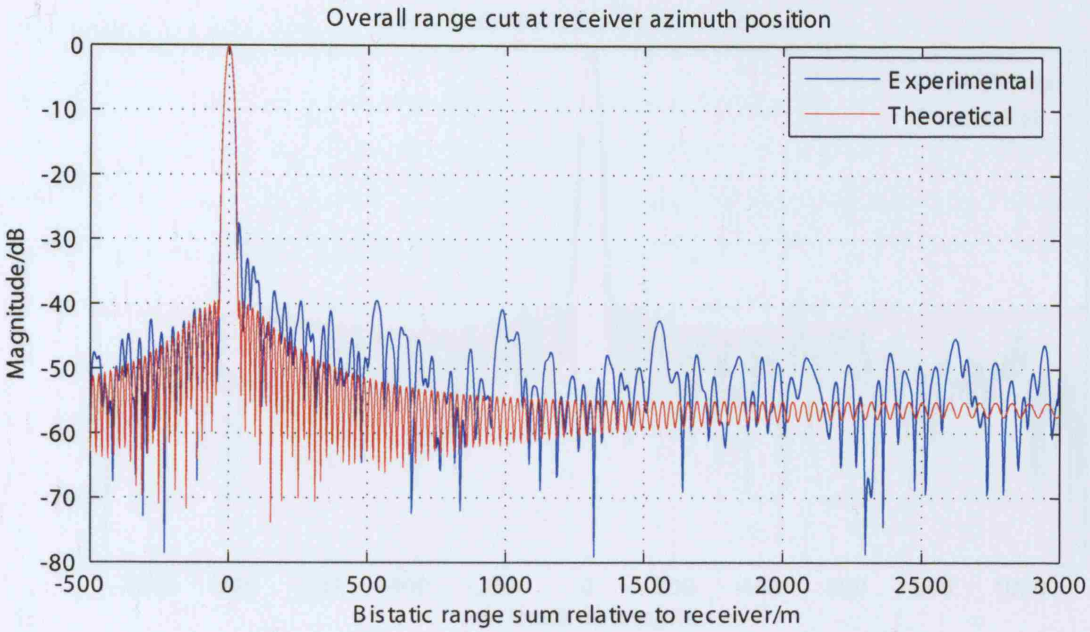

Figure 7-77: Overall range cut at the receiver azimuth position

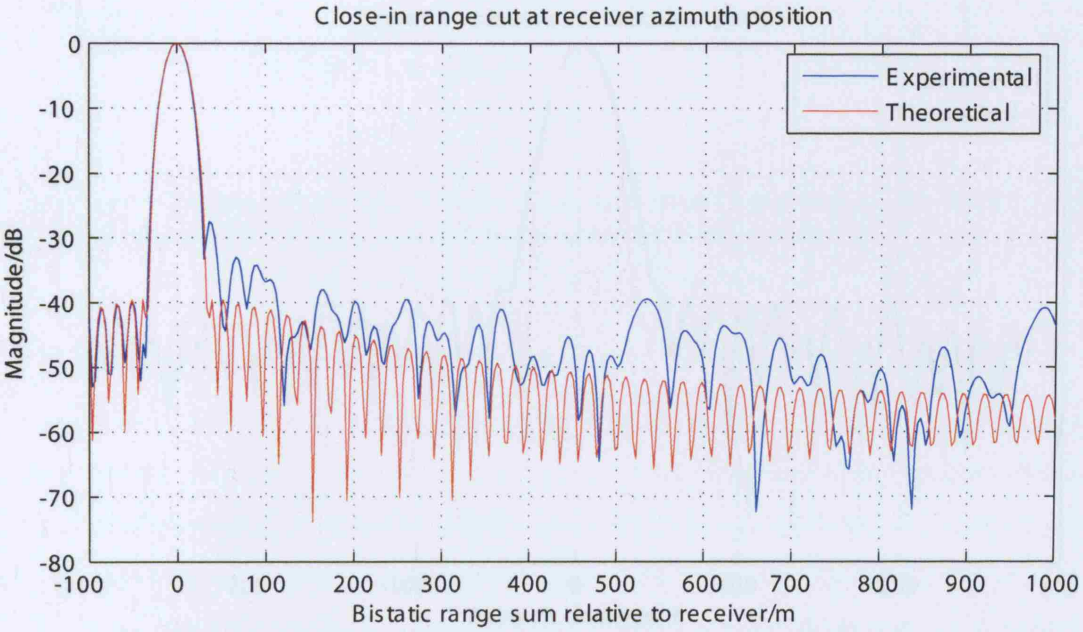

Figure 7-78: Close-in range cut at the receiver azimuth position

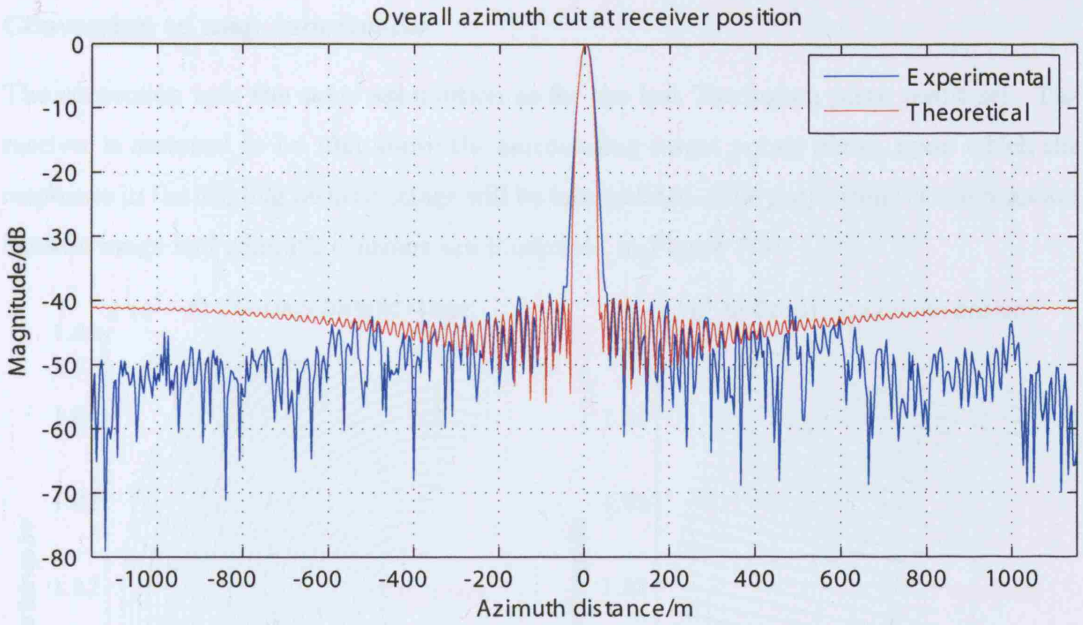

Figure 7-79: Overall azimuth cut at the receiver azimuth position

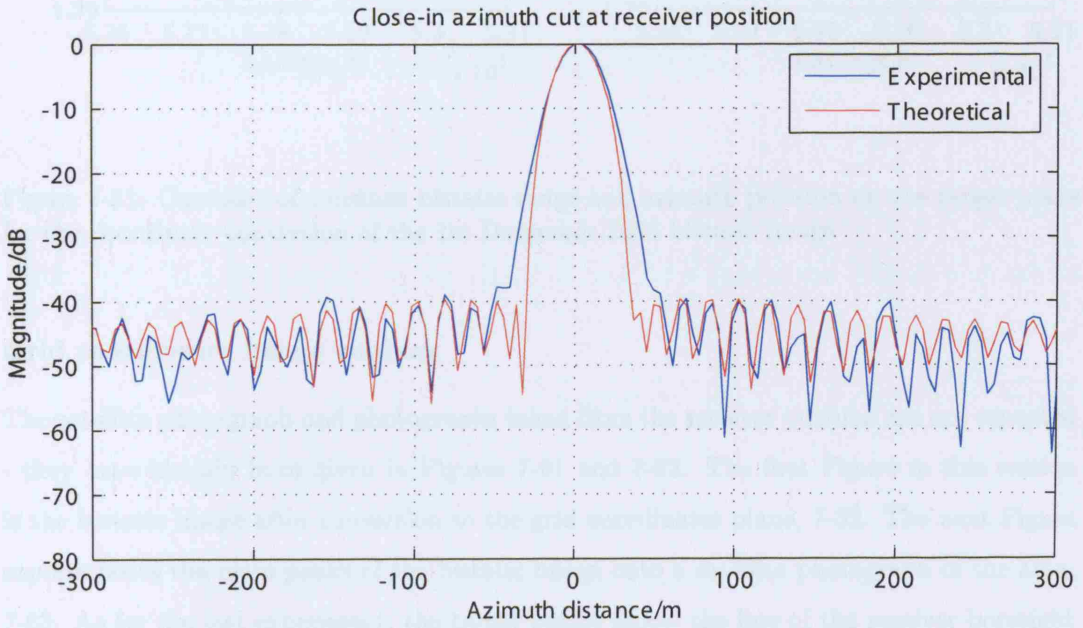

Figure 7-80: Close-in azimuth cut at the receiver azimuth position

Conversion to map coordinates

The conversion uses the same assumption as for the last Torrington place result set. The receiver is assumed to be 10m above the surrounding target points plane, upon which the responses in the original bistatic image will be interpolated. The projections of the constant bistatic range and azimuth contours are illustrated in Figure 7-81.

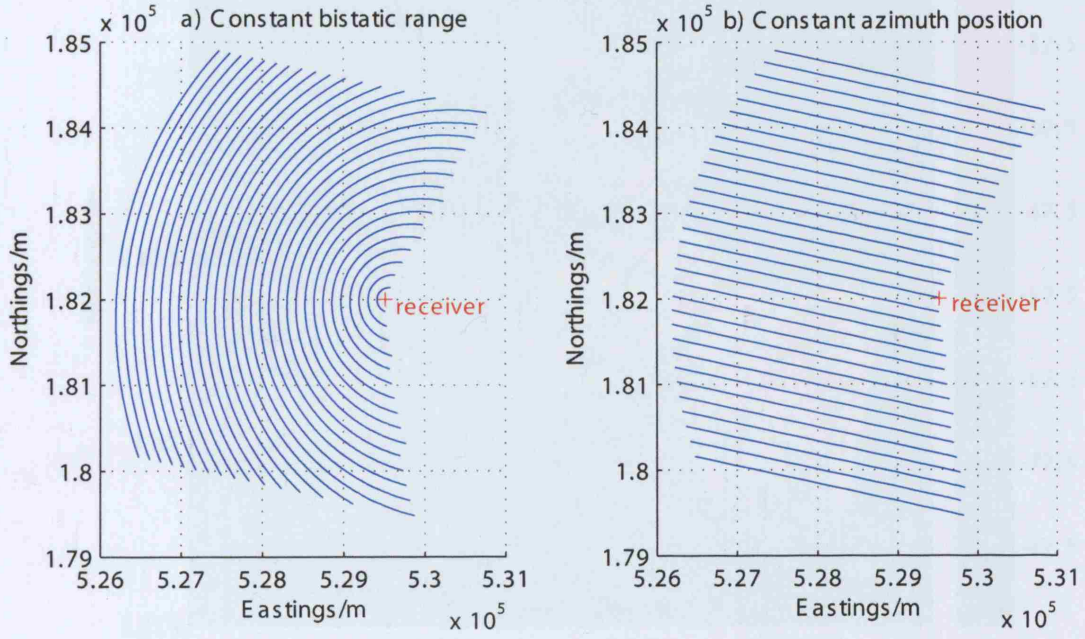

Figure 7-81: Contours of constant bistatic range and azimuth position on the target plane for the coordinate conversion of the 1st December 2004 bistatic image

Grid coordinates image analysis

The satellite photograph and photographs taken from the receiver position are not repeated - they have already been given in Figures 7-61 and 7-62. The first Figure in this section is the bistatic image after conversion to the grid coordinates plane, 7-82. The next Figure superimposes the main peaks of the bistatic image onto a satellite photograph of the area, 7-83. As for the last experiment, the target points follow the line of the receiver boresight along in the image. The higher power returns correspond to the two building edges and the Euston tower. Some of the scatterers present along the boresight direction appear to be common to both Torrington Place images, confirming them as actual features. The image

points analysed for the 12th November image are considered for this image as well, see Table 7.14.

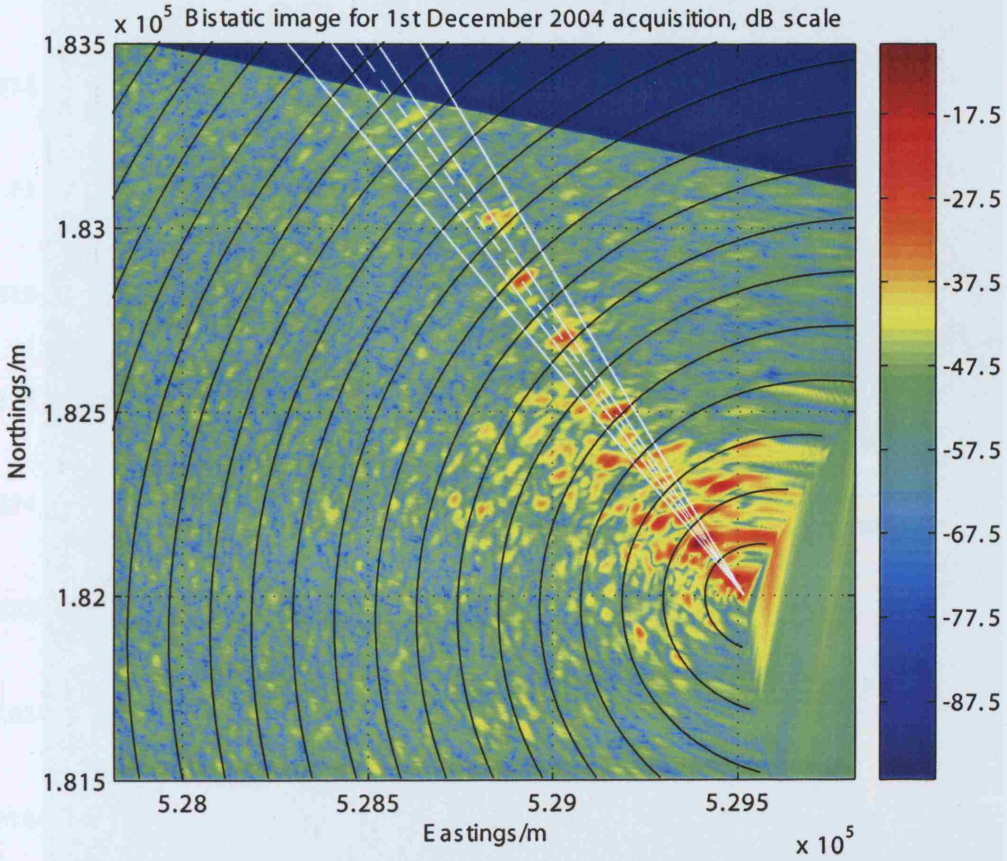

Figure 7-82: Bistatic image from the 1st December 2004 acquisition interpolated onto a grid coordinates plane

Feature	Position (Easting,Northing)/m	Magnitude relative to receiver/dB	Resolution (East)/m	Resolution (North)/m
Euston tower	(529155,182664)	-25.3	22.4	18.3
Scatterer 2	(528919,182860)	-28.3	26.8	18.1

Table 7.14: Selected features in 1st December 2004 image

The resolutions, bistatic angle and ground resolution cell size are reproduced in Figures 7-84 and 7-85. The maximum resolution along the East direction is larger than that for

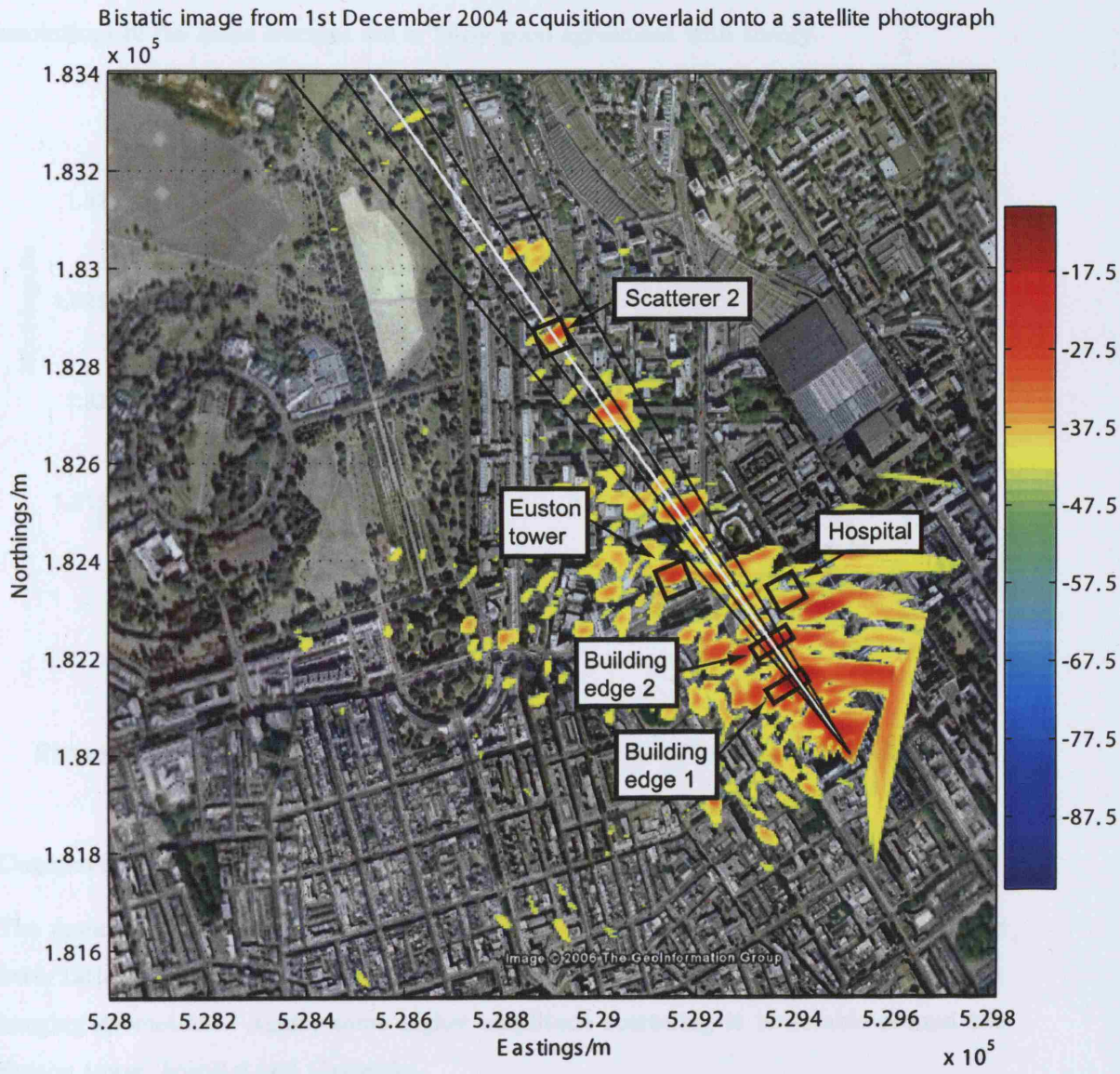

Figure 7-83: Bistatic image overlaid onto a satellite photograph of the area around Torrington Place, 1st December 2004

the previous acquisition, at 104m, and is similar to the results produced for the Portsdown acquisition. In the imaged area the resolutions are 28.3m and 15.4m along East and North, while the ground resolution cell is approximately $1200m^2$, all values are very similar to those

for the 12th November image. The bistatic angle is close to 90^0, as before. The measured resolutions of the scene features are in fairly good agreement with theory.

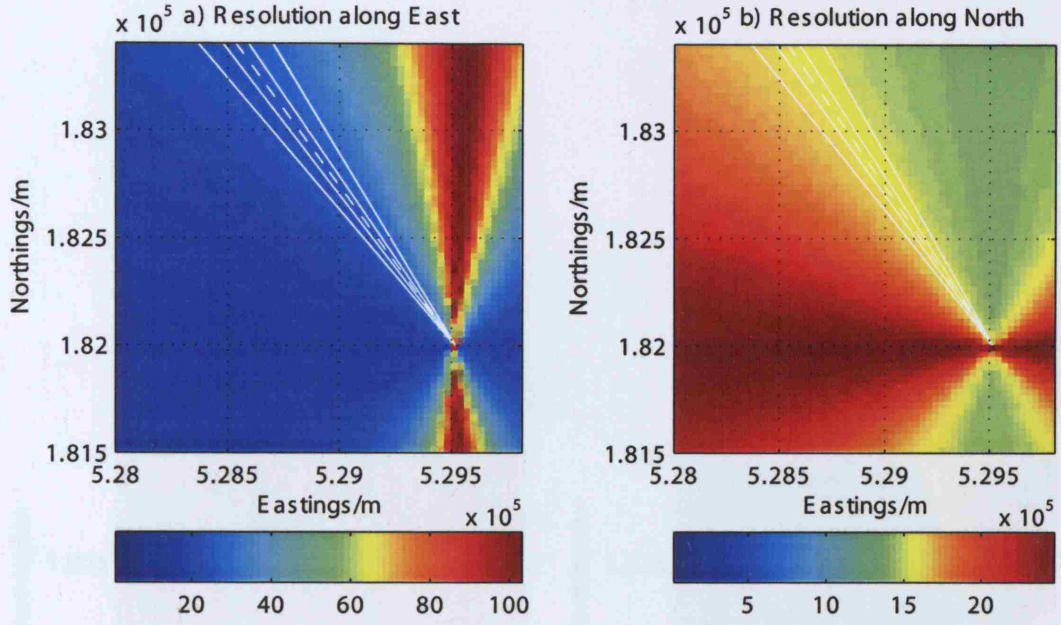

Figure 7-84: East and North directed resolutions for 1st December 2004 acquisition

Comparison with the monostatic image

The monostatic image is shown in Figure 7-86. Comparing this to the monostatic image from 12th November, there is a strong similarity, as would be expected for such similar imaging geometries. Again, some higher amplitude scattering is noticeable around the Euston tower, hospital and Gasworks.

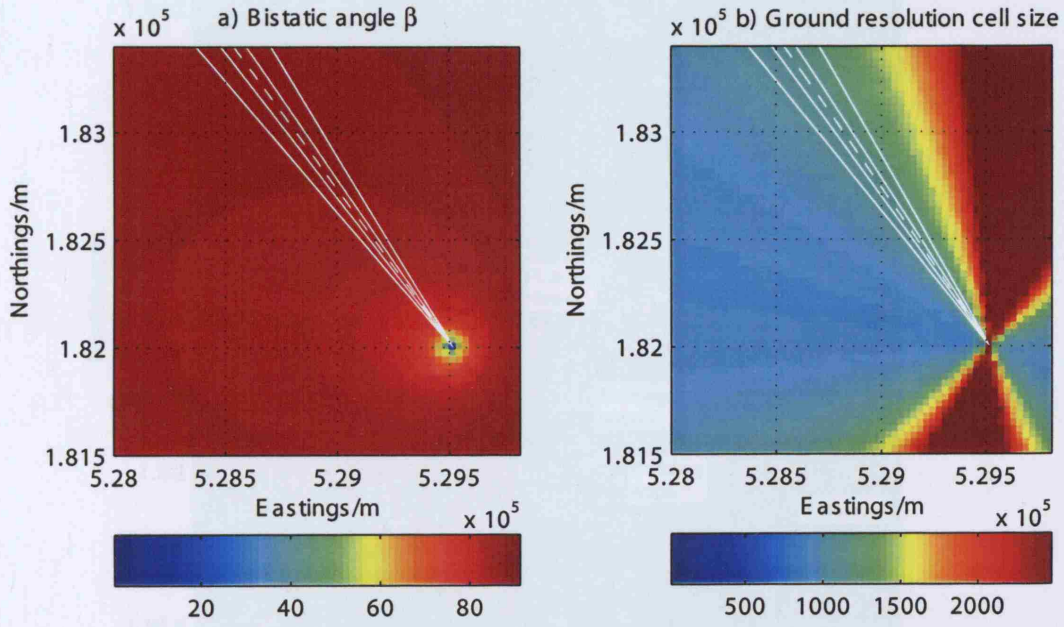

Figure 7-85: Bistatic angle and ground resolution cell size for 1st December 2004 acquisition

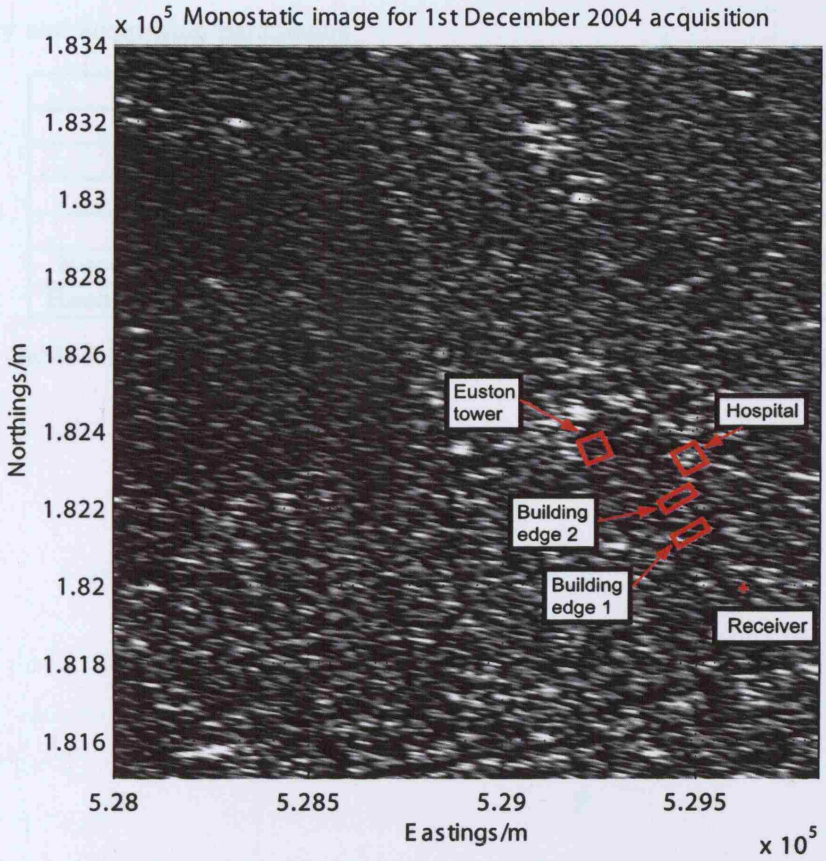

Figure 7-86: Monostatic image for 1st December 2004 acquisition

7.2.4 Torrington Place site, experiment 3

Overview and geometry

This is the third experiment performed at the Torrington place site. The same receiver location applies and satellite swath, although the receiver pointing direction and antenna used both differ. The antenna is parabolic antenna 2, while the pointing direction is towards the BT Tower, to the West of the receiver. The following table and figure summarise the geometry and acquisition parameters.

Swath	IS2
Satellite pass	Descending
Polarisation	VV
Pulse repetition frequency/Hz	1652.4156
Pulse length/s	27.1776×10^{-6}
Receiver position (Easting,Northing)/m	(529516,182000)
Receiver look direction (bearing)/degrees	281

Table 7.15: Acquisition details for the third Torrington Place experiment

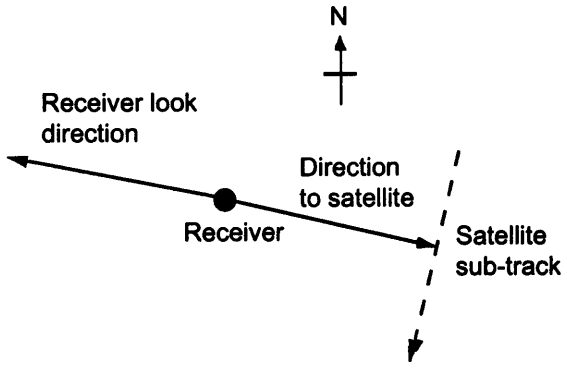

Figure 7-87: Imaging geometry for 19th August 2005 acquisition

Pre-processing

The measured direct signal phase of Figure 7-88 is fairly similar to those produced for the last two experiments at this site. The pulse compressed reflected signal magnitude plot of Figure 7-89 has the same form as before, with a large response at the receiver and several smaller amplitude responses within the imaged scene.

The next page shows the measured phase in the pulse compressed reflected signal array, and

the measured magnitude, both as functions of pulse number, Figures 7-88 and 7-91. The phase plot is quite linear and spans a range of 0.25rad. The magnitude plot is reasonably symmetrical, with a peak at pulse number 458.

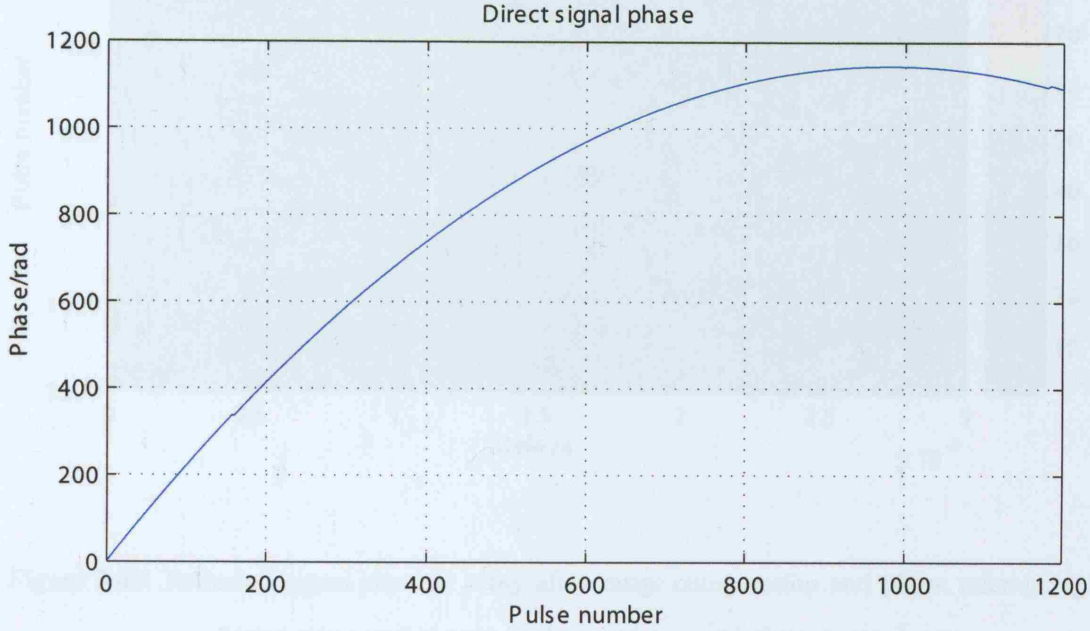

Figure 7-88: Measured phase of direct signal channel pulses

Next in this section of the results is the simulated direct signal path length in Figure 7-92 and the main processing parameters, reproduced in Table 7.2.4. The direct signal range or baseline has a minimum value of approximately 860km, as noted earlier in the direct signal amplitude analysis. The processing parameters are quite similar to those given for other acquisitions and again, confirming the beam centre crossing time through the use of Figures 7-88 and 7-91, produces a value of -0.316s, very close to theory.
The image signal-to-noise ratio is predicted to be,

$$SNR_{image} \approx 25.7 + 10\log_{10}(579) - 1.23 = 52.1dB$$

Azimuth compression here uses 579 pulses.

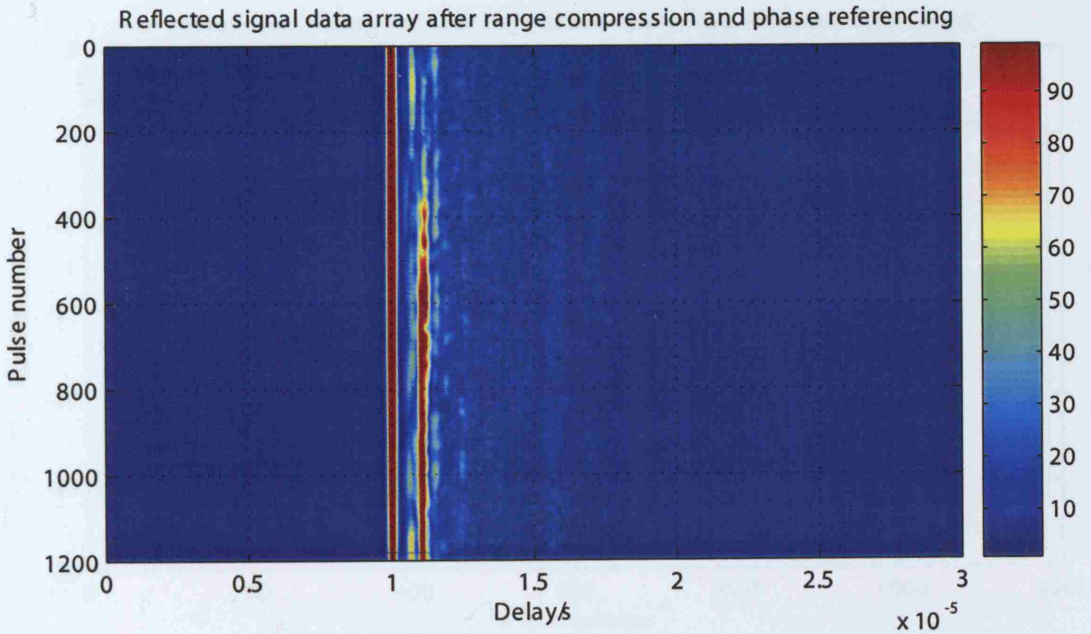

Figure 7-89: Reflected signal channel array after range compression and phase referencing

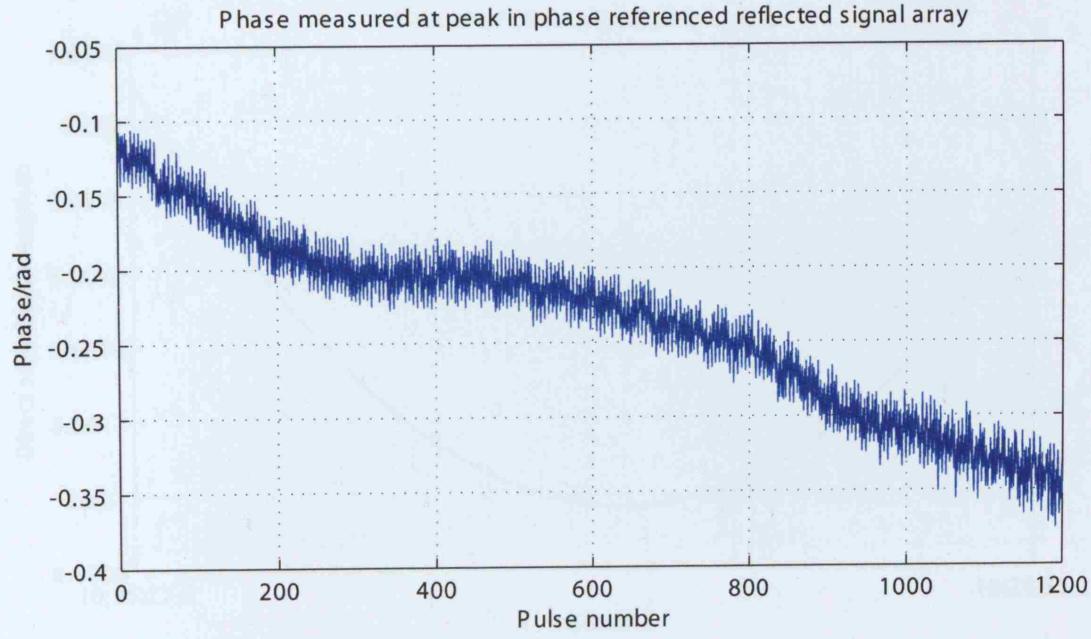

Figure 7-90: Phase measured at peak position in reflected signal channel array

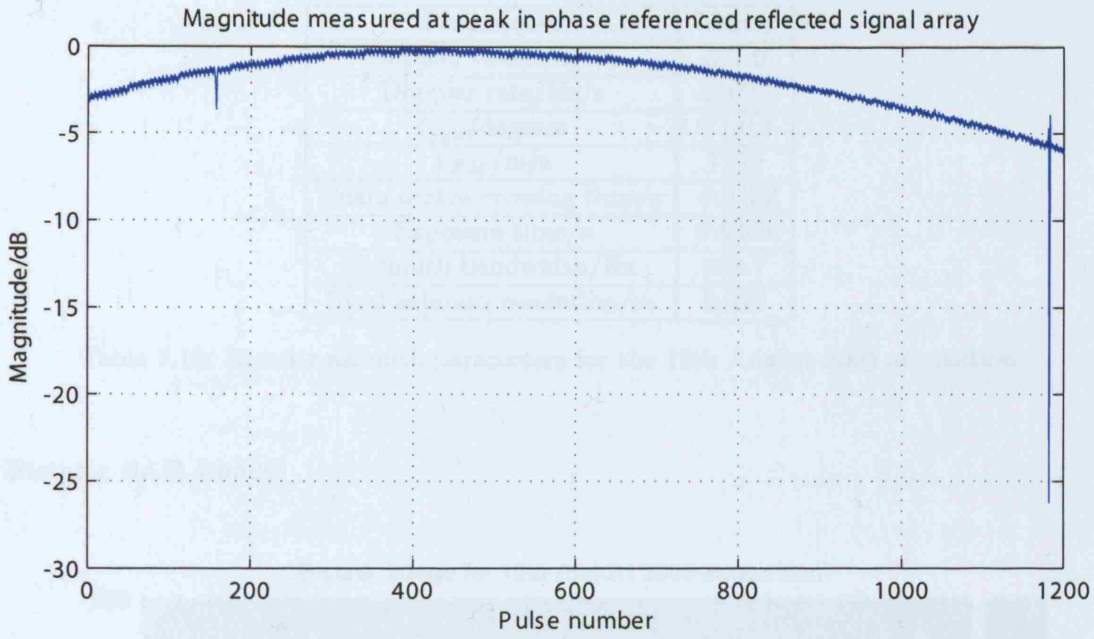

Figure 7-91: Magnitude measured at peak position in reflected signal channel array

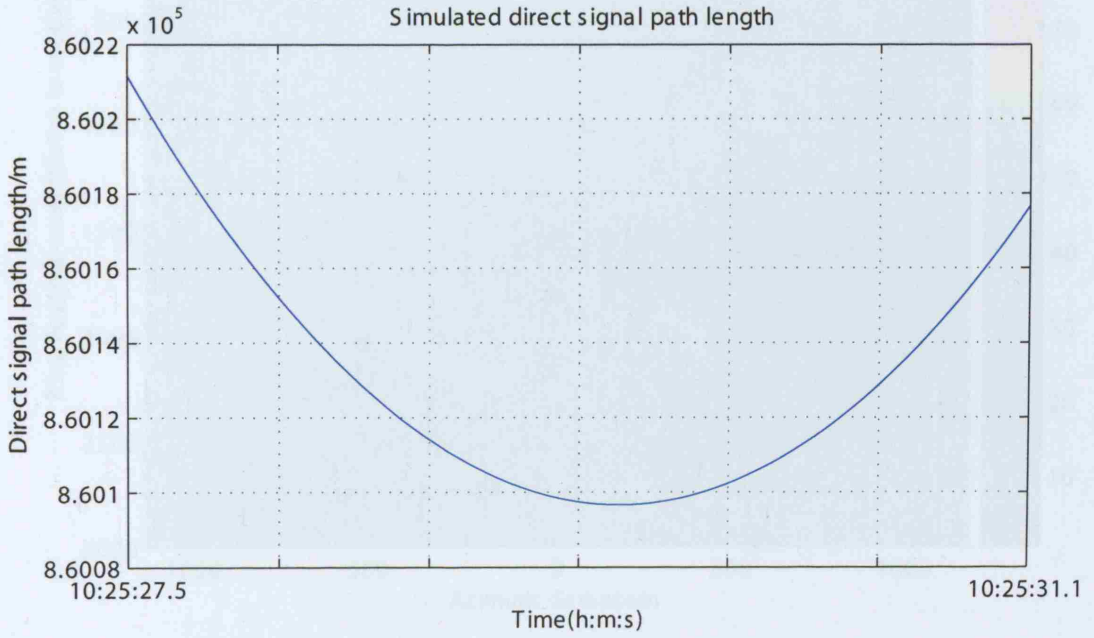

Figure 7-92: Simulated direct signal path length

Parameter	Value
Doppler centroid/Hz	331.0
Doppler rate/Hz/s	-2100.1
$\theta_{sq,c}$/degrees	0.1414
V_{FM}/m/s	7129
Beam centre crossing time/s	-0.3152
Exposure time/s	0.6368
Azimuth bandwidth/Hz	668.7
Ideal azimuth resolution/m	8.922

Table 7.16: Bistatic azimuth parameters for the 19th August 2005 acquisition

Bistatic SAR image

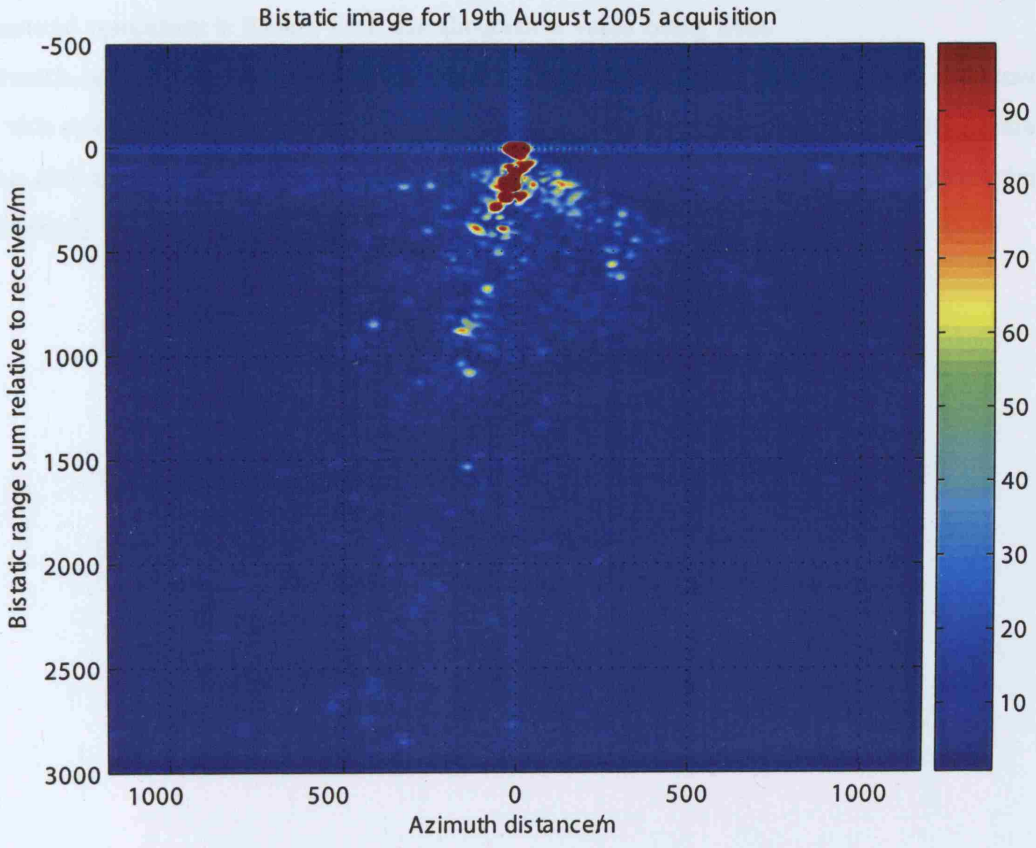

Figure 7-93: Bistatic image for 19th August 2005 acquisition, bistatic range sum versus azimuth

The bistatic image for bistatic range sum versus azimuth is plotted in Figure 7-93. Most of the scatterers may be found on a line at right angles to the azimuth axis. As the receiver antenna was pointing approximately at 90 degrees to the satellite path for this experiment, this is as expected.

The range cuts at the receiver position are shown in Figures 7-94 and 7-95. In addition to the reception of energy at a very small range sum difference relative to the receiver (less than 100m), there are four closely spaced scatterers at a relative range sum of less than 300m. The measured resolution of the main peak along this cut is 24.7m, compared to a theoretical value of 23.4m.

The azimuth cuts on the following page, Figures 7-96 and 7-97 illustrate the same mainlobe broadening and first sidelobe level increase produced in the other sets of results. The measured resolution is 23.6m, with the theoretical value being 24m.

Azimuth cuts of responses other than that produced at the receiver will not be examined for this or any of the other sets of results. It has already been demonstrated in the simulations and analysis of previous acquisitions that the SAR processing operation is producing adequately focused imagery.

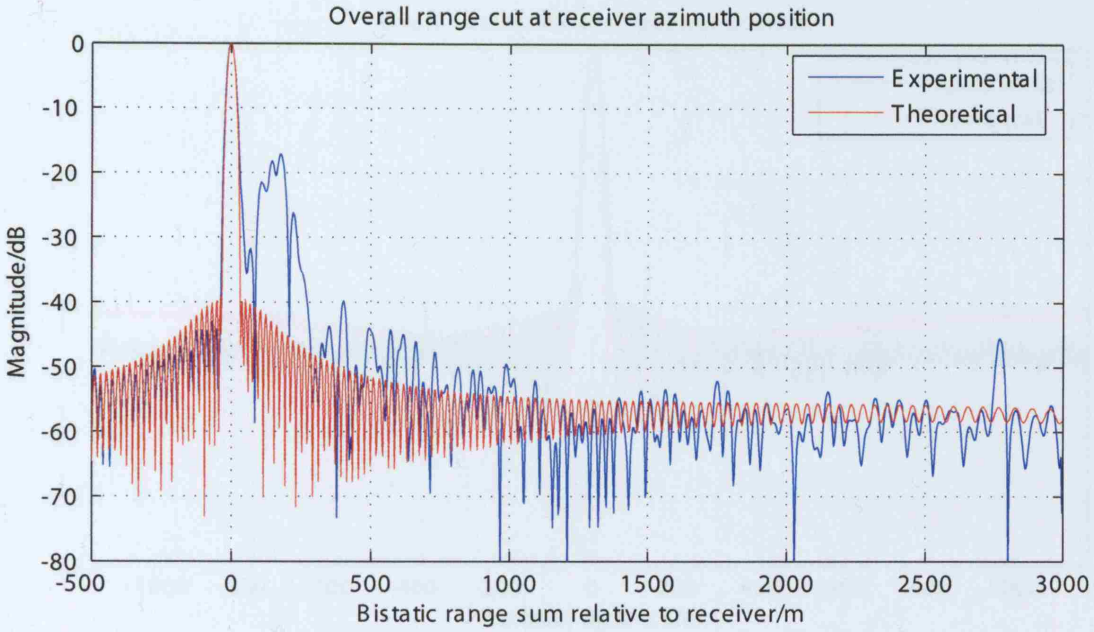

Figure 7-94: Overall range cut at the receiver azimuth position

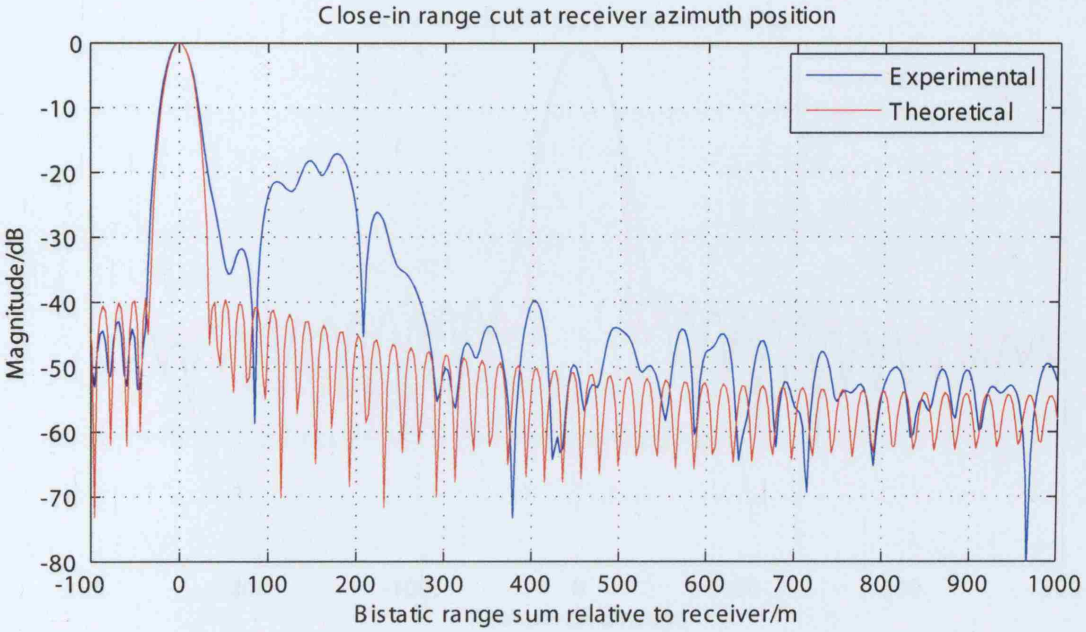

Figure 7-95: Close-in range cut at the receiver azimuth position

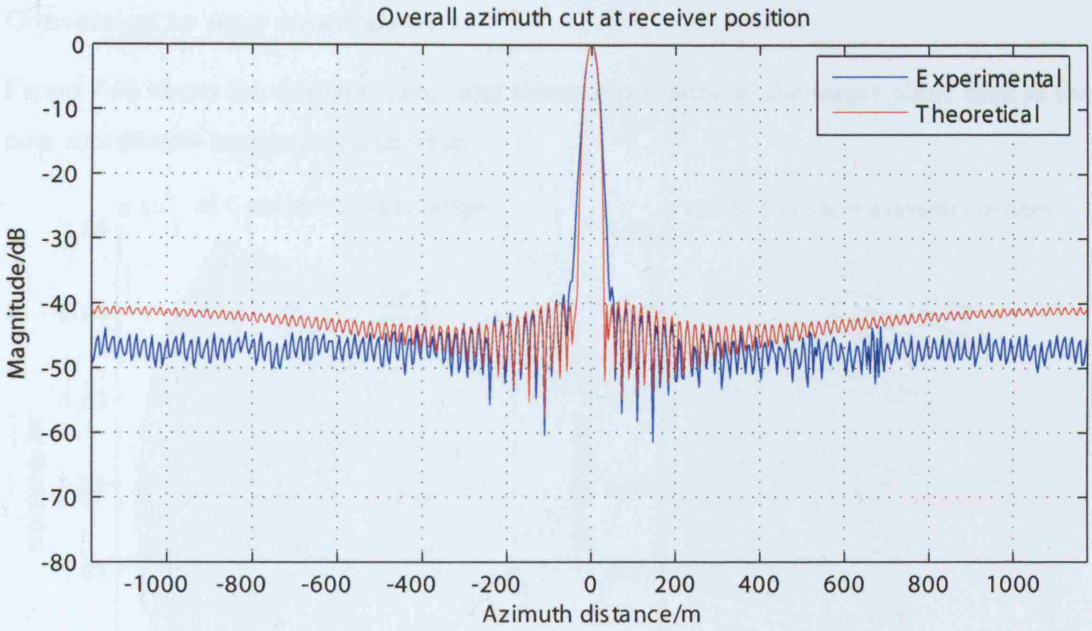

Figure 7-96: Overall azimuth cut at the receiver azimuth position

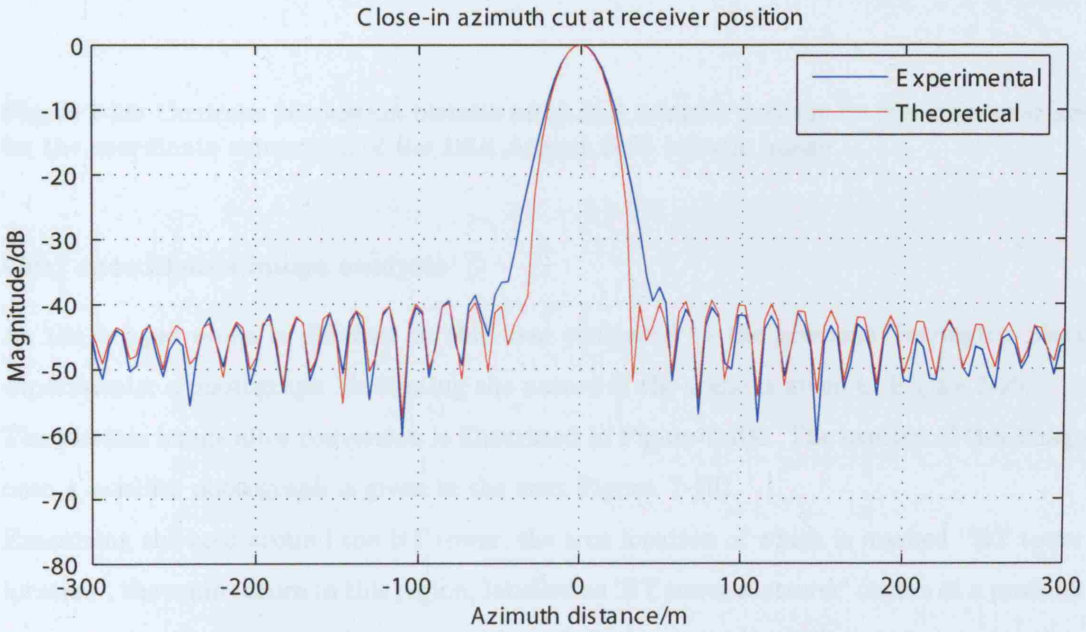

Figure 7-97: Close-in azimuth cut at the receiver azimuth position

Conversion to map coordinates

Figure 7-98 shows the constant range and azimuth contours on the target plane used in the map coordinates interpolation process.

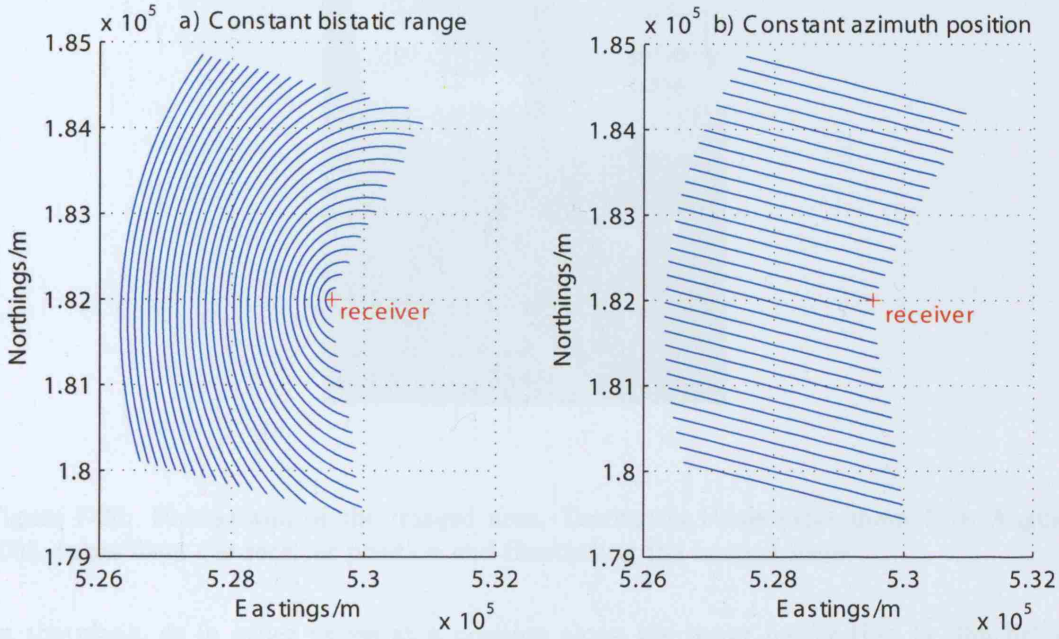

Figure 7-98: Contours of constant bistatic range and azimuth position on the earth's surface for the coordinate conversion of the 19th August 2005 bistatic image

Grid coordinates image analysis

As the imaged scene is different in this case compared to the previous Torrington place experiments, a photograph illustrating the nature of the scene is given in Figure 7-99.
The bistatic image after conversion is illustrated in Figure 7-100. The overlay of this image onto a satellite photograph is given in the next Figure, 7-101.
Examining the area around the BT tower, the true location of which is marked ''BT tower location', the main return in this region, labelled as 'BT tower scatterer' occurs at a position closer to the receiver than the true position of the tower itself. Although it appears that the BT tower scatterer has been received in the receiver antenna sidelobe, the potential error in antenna pointing direction means that this may not be the case. The separation of the two is 72m. The data conversion to this target plane assumes that the returns occur

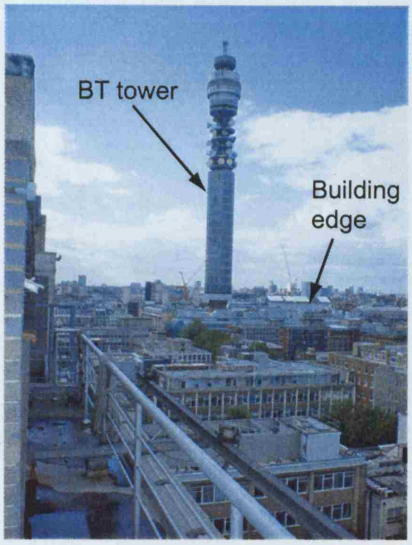

Figure 7-99: Photograph of the imaged area, Torrington Place experiment 19th August 2005, taken from the receiver position and illustrating the imaged scene

on the plane, or in other words at a position along the tower height that is 10m below the receiver. The return from the tower could conceivably be from near/at the top of the structure. The range R_T for the top of the tower will be less than the range R_T for the base, given the angle of incidence of the ASAR beam. If the range R_R does not vary by an equivalent amount for the base and top of the tower, then the range sum $R_T + R_R$ will be smaller for the top than for the base, resulting in the BT tower response being mapped to a closer position relative to the receiver in the image. This may be explained with a simple simulation. The tower has three potential scattering points, corresponding to the base (the intersection of the tower with the target plane), the top and the middle (half-way between base and top). The base of the tower as considered here is 10m below the receiver. The receiver is sited 65m above the ground and so the base of the tower is 55m above ground level. The tower is 175m high. Figure 7-102 illustrates the bistatic range sum for the three points along the tower height for an azimuth time variation of one second, and includes mean separation between each. The centre azimuth time of the simulation is the same as that of the data used for generation of the bistatic image. If the return from the tower originated from the mid-point, the range sum difference would be 40.8m, while if it

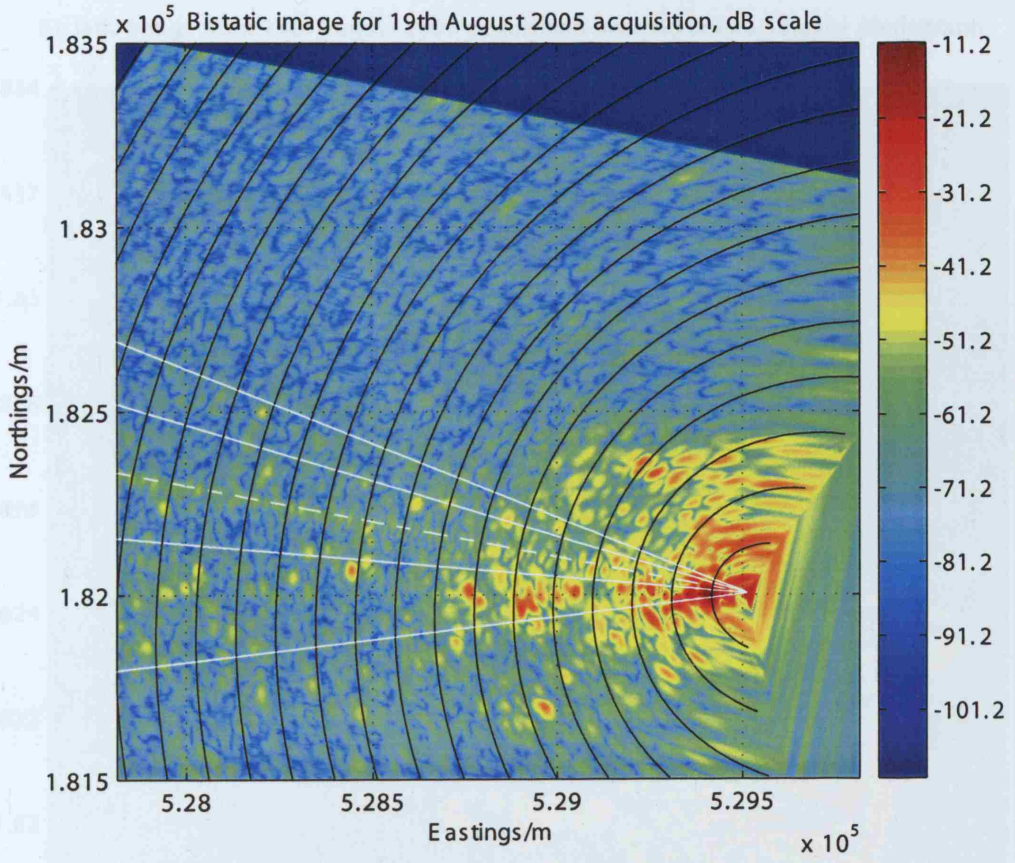

Figure 7-100: Bistatic image from the 19th August 2005 acquisition interpolated onto a grid coordinates plane

were from the top the difference between that and the base would be 91.9m. A range sum difference of 1m is equivalent to a ground range difference of 0.73m at the location of the tower. So the simulated ground range difference is 30m for the mid-point and 67m for the top. The latter value is close to that measured in the experimental image.

The bistatic ambiguity function plots are given in Figures 7-103 and 7-104. The East and North directed resolutions are 16.1m and 23.3m respectively. The ground resolution cell size for the imaged area is $848m^2$.

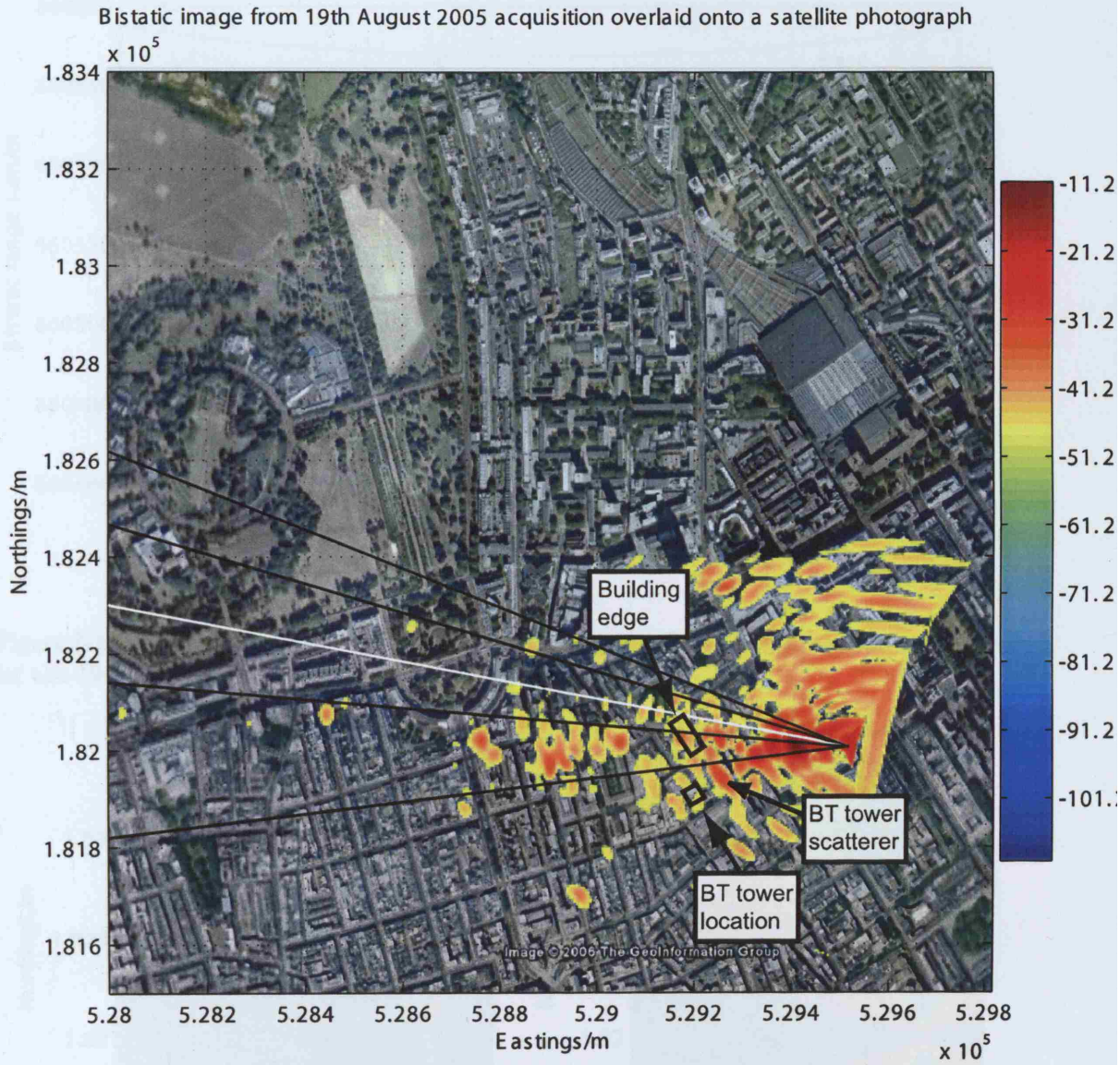

Figure 7-101: Bistatic image overlaid onto a satellite photograph of the area around Torrington Place, 19th August 2005

Comparison with the monostatic image

The monostatic image is shown in Figure 7-105. This IS2 image for central London is quite similar to the other examples, from 12th November 2004 and 1st December 2004. Examining

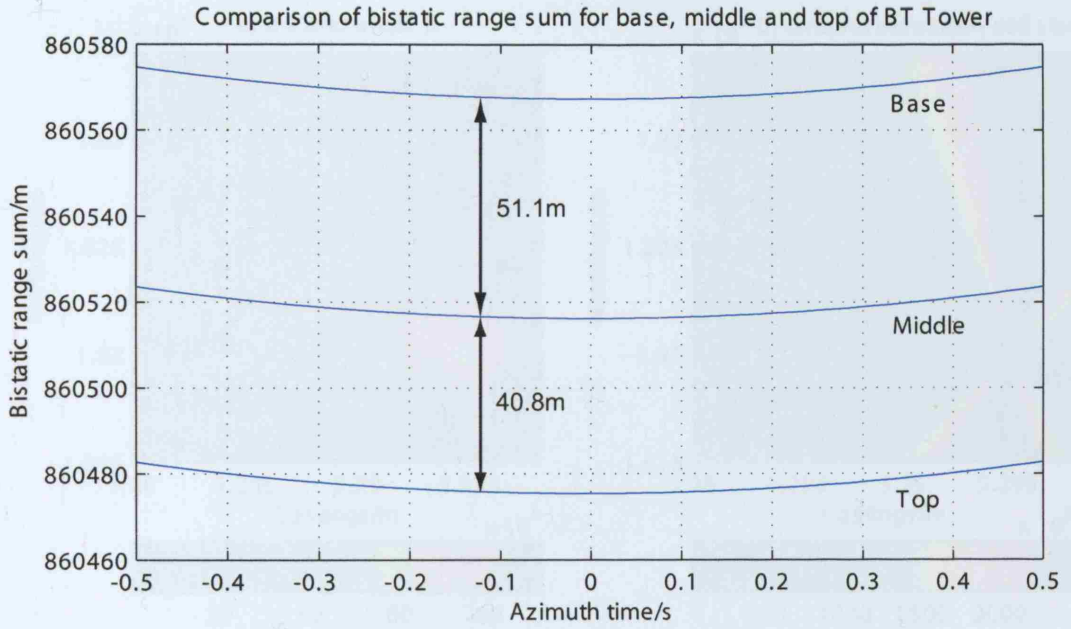

Figure 7-102: Simulation of the bistatic range sum of three points along the BT tower height for the 19th August 2005 acquisition

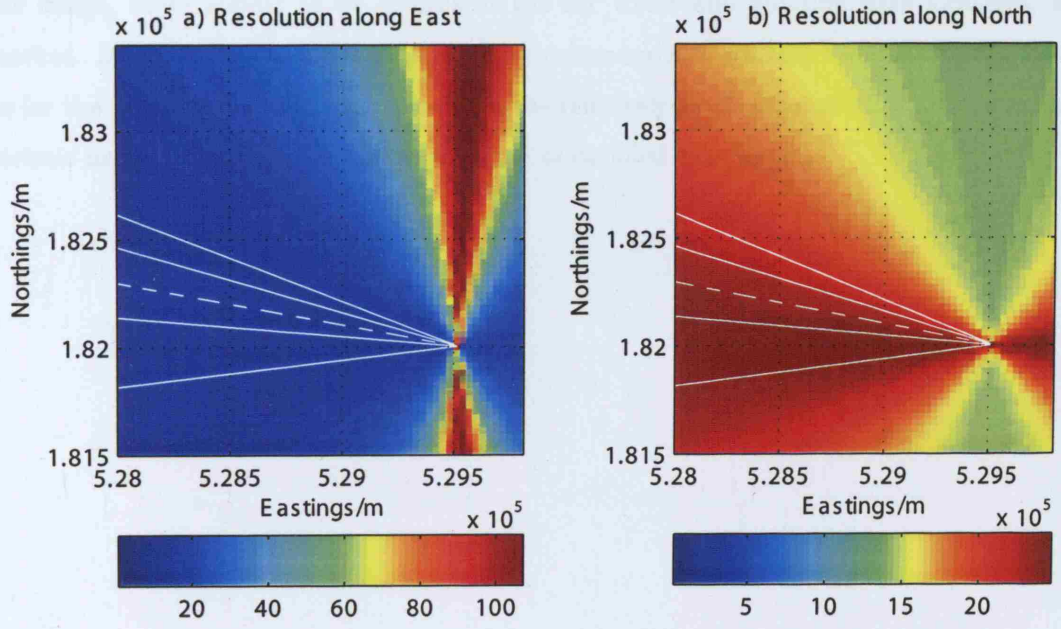

Figure 7-103: East and North directed resolutions for 19th August 2005 acquisition

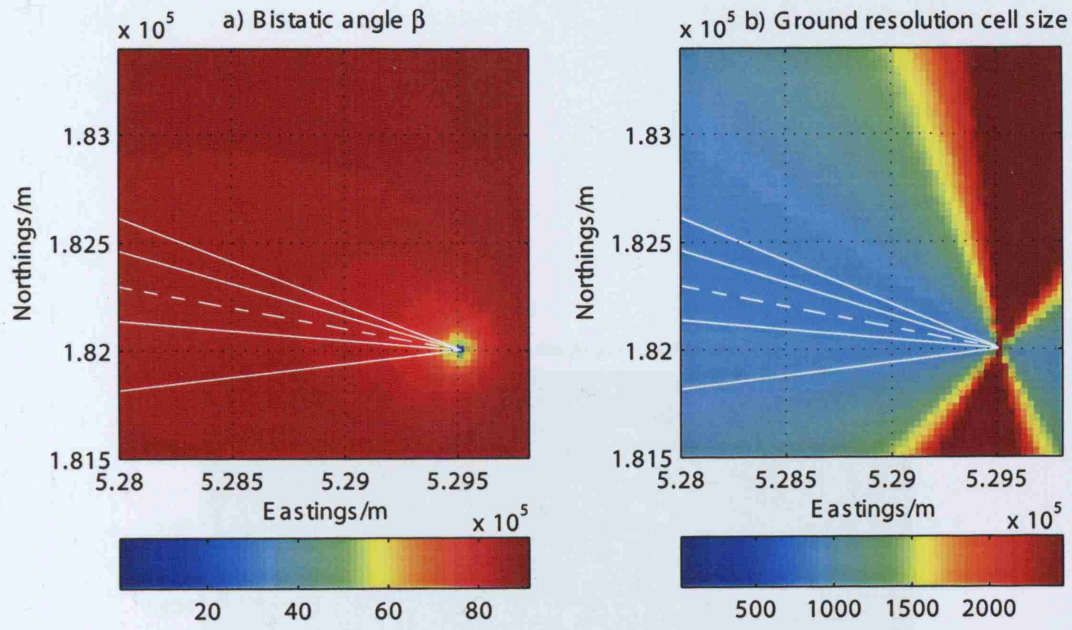

Figure 7-104: Bistatic angle and ground resolution cell size for 19th August 2005 acquisition

the image, there appear to be returns at the BT tower and building edge locations, as marked. Some of the buildings close to the receiver are also causing some scattering, but, as for the previous acquisitions, because of the relatively small amount of scatterers in the bistatic image it is difficult to make any kind of detailed comparison.

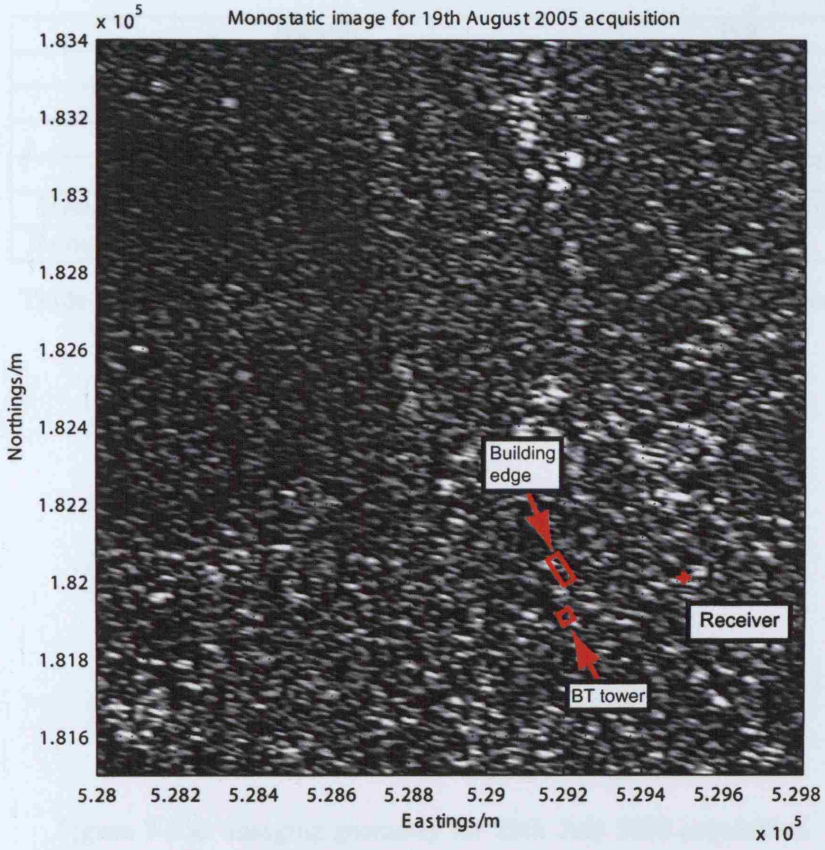

Figure 7-105: Monostatic image for 19th August 2005 acquisition

7.2.5 Gower Street site, experiment 1

Overview and geometry

This experiment was performed with the receiver sited on the roof of a University- owned building on Gower street in central London, on 25th July 2005. In contrast to the experiments already considered, the satellite pass was ascending, resulting in a night-time acquisition. Details are given in Table 7.2.5 and Figure 7-106.

Swath	IS2
Satellite pass	Ascending
Polarisation	VV
Pulse repetition frequency/Hz	1652.4156
Pulse length/s	27.1776×10^{-6}
Receiver position (Easting,Northing)/m	(529704,182003)
Receiver look direction (bearing)/degrees	328

Table 7.17: Acquisition details for the first Gower Street experiment

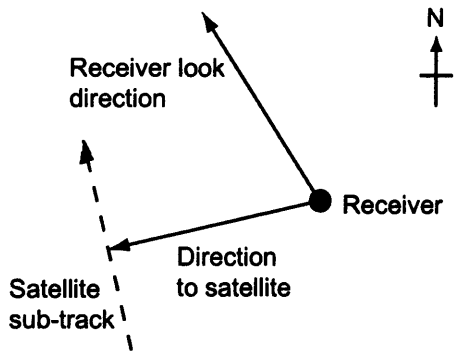

Figure 7-106: Imaging geometry for 25th July 2005 acquisition

Pre-processing

The measured direct signal phase may be found in Figure 7-107, which has a maximum value, corresponding to a minimum direct signal range, at pulse number 1659. The reflected signal data array is range compressed and phase referenced in the normal way to produce Figure 7-108. It is obvious from this that the amplitude of scatterers within the imaged scene is much less than that produced at the receiver. This may be explained by the receiver location and surroundings. On the roof of the Gower Street building, the receiver was sited

a few metres away from the roof edge, giving an increased roof area for close-in reflections. The reflected signal phase is linear, as before, although the gradient of the line is now positive, Figure 7-109. The dominant scatterer is displaced in azimuth from the receiver, but in the opposite direction to the other acquisitions. The linearity of this phase plot leads to the reasonably symmetrical nature of the magnitude plot of Figure 7-110. A decrease in pulse amplitude due to a loss of data may also be observed on the same graph.

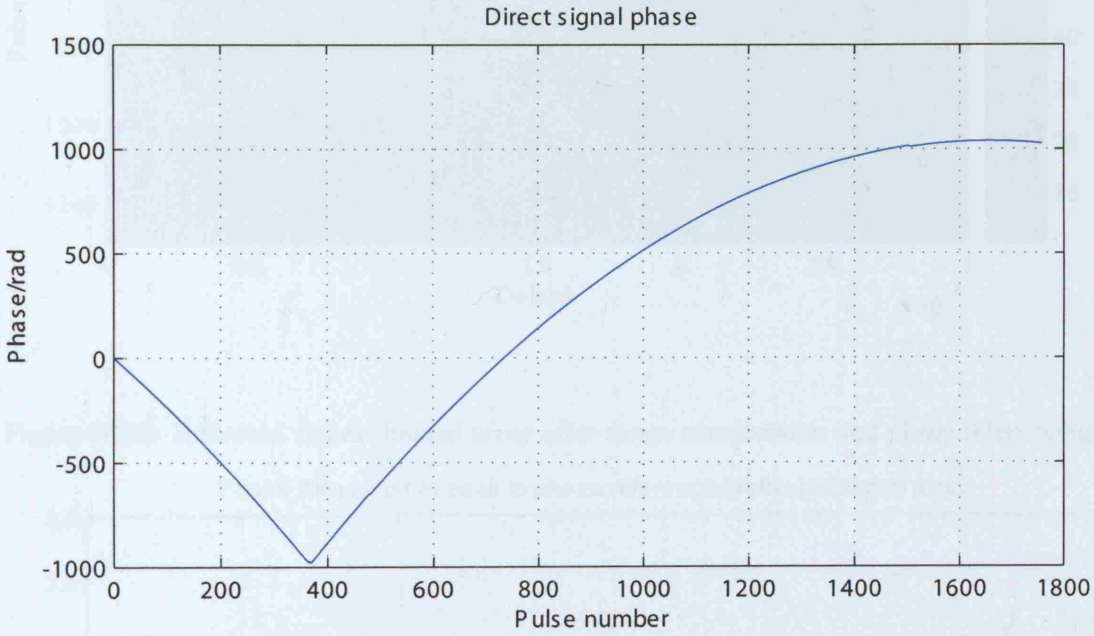

Figure 7-107: Measured phase of direct signal channel pulses

The simulated direct signal path length of Figure 7-111 gives a direct path range minimum of 845km, a reasonable result for an IS2 swath. The processing parameters of Table 7.2.5 are fairly similar to those of the previous images.

The image signal-to-noise ratio may be calculated,

$$SNR_{image} \approx 25.7 + 10\log_{10}(569) - 1.23 = 52.0dB$$

The maximum signal-to-noise ratio of the reflected signal pulses is 0dB before range compression. Azimuth compression uses 569 pulses.

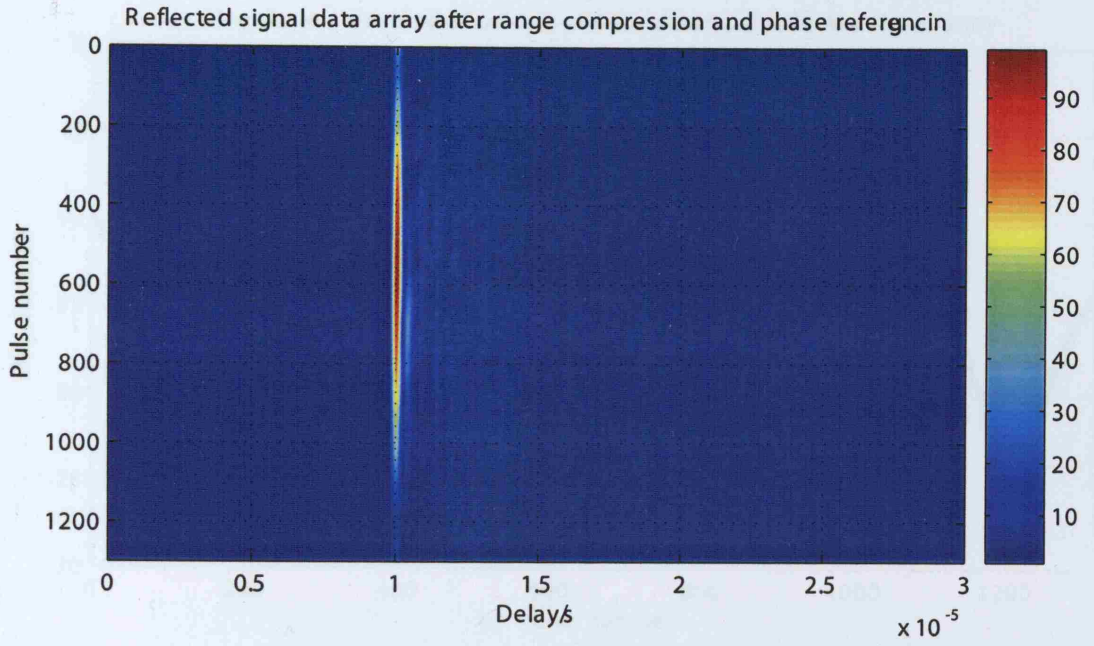

Figure 7-108: Reflected signal channel array after range compression and phase referencing

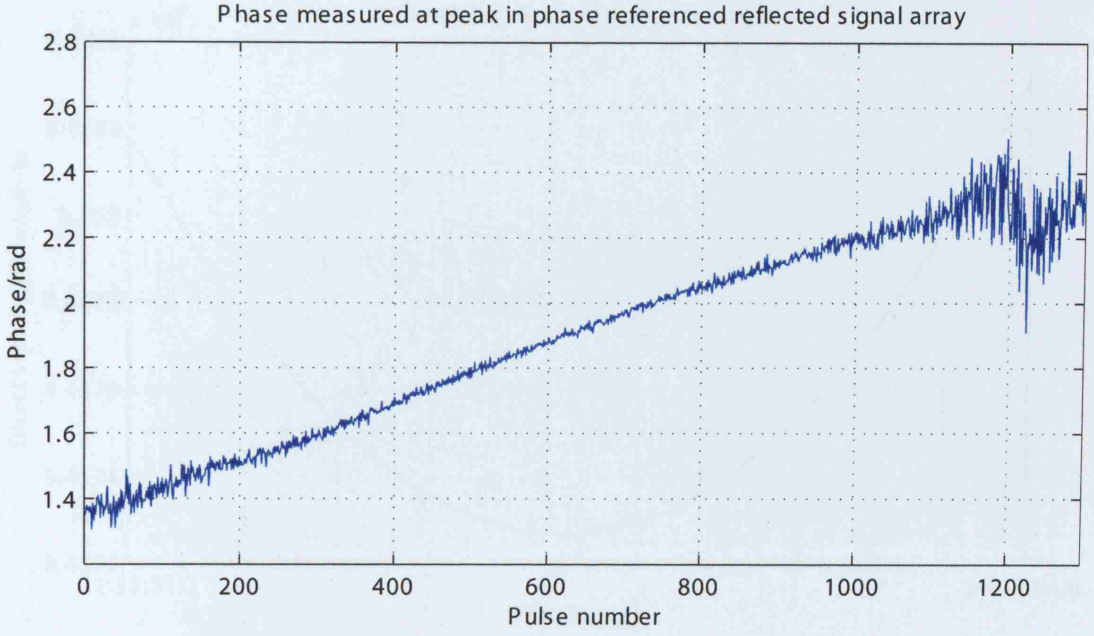

Figure 7-109: Phase measured at peak position in reflected signal channel array

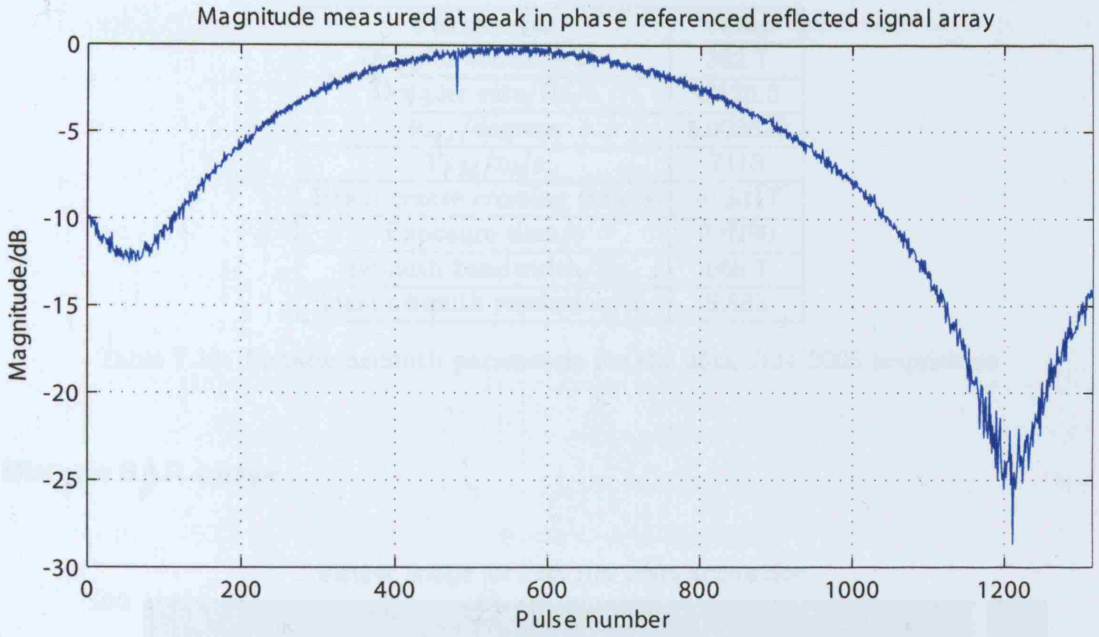

Figure 7-110: Magnitude measured at peak position in reflected signal channel array

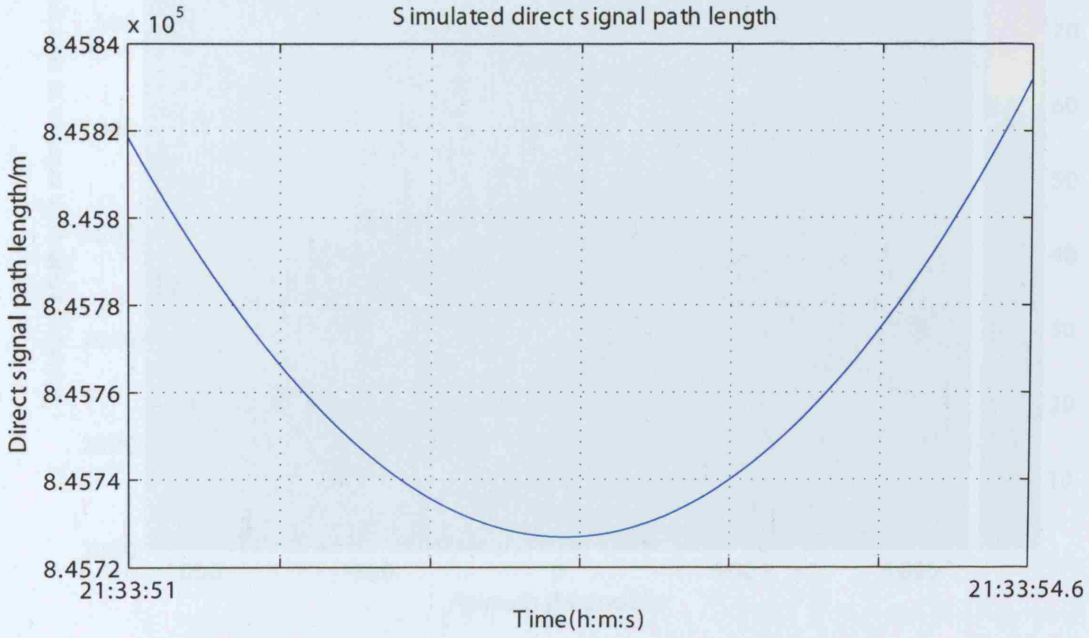

Figure 7-111: Simulated direct signal path length

Parameter	Value
Doppler centroid/Hz	352.7
Doppler rate/Hz/s	-2126.3
$\theta_{sq,c}$/degrees	0.002629
V_{FM}/m/s	7113
Beam centre crossing time/s	-0.3317
Exposure time/s	0.6290
Azimuth bandwidth/Hz	668.7
Ideal azimuth resolution/m	8.883

Table 7.18: Bistatic azimuth parameters for the 25th July 2005 acquisition

Bistatic SAR image

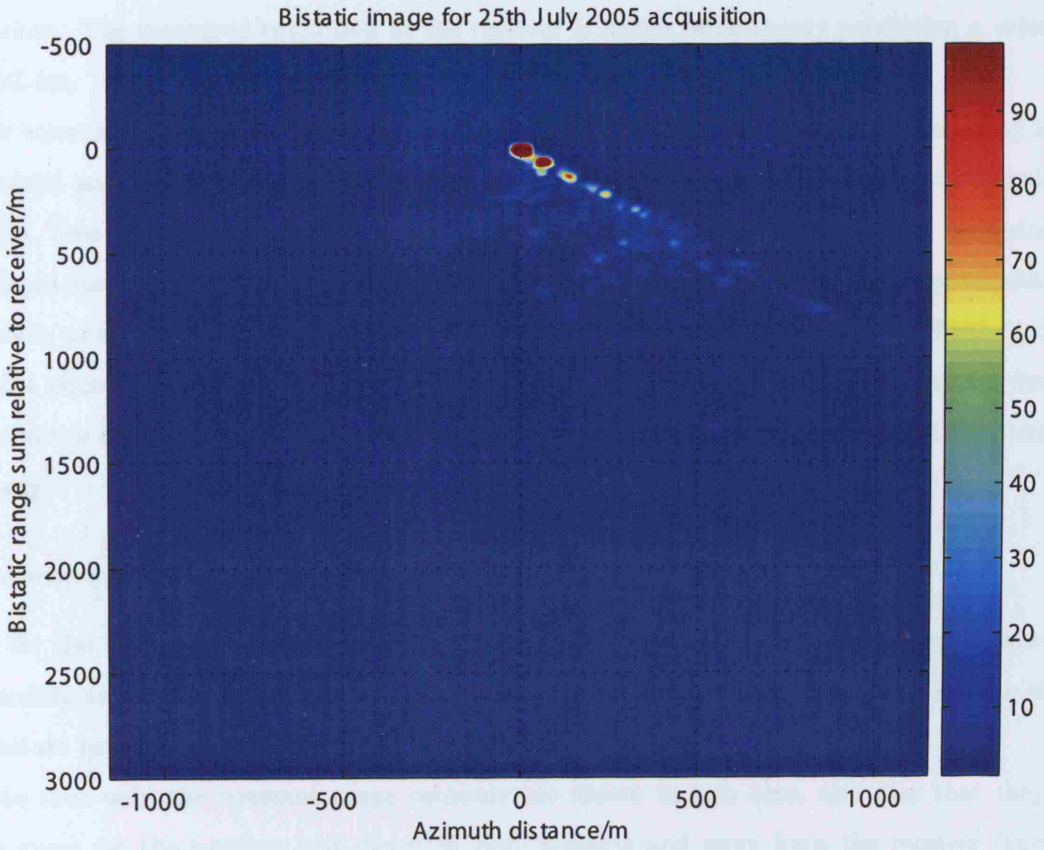

Figure 7-112: Bistatic image for 25th July 2005 acquisition, bistatic range sum versus azimuth

The bistatic image is plotted in Figure 7-112. Compared to the image plots for 12th November 2004 or 1st December 2004, the scatterers are displaced in the opposite direction, to the right of the main (receiver) response. This is as a result of the geometry, shown in Figure 7-106, where the satellite path is from South-South-East to North-North-West (approximately) and the receiver is pointing North-North-West. Only a few discrete target points may be observed in this image, compared to the large number for the other central London images.

This point is confirmed through examination of the range cuts of Figures 7-113 and 7-114. The increase in width of the mainlobe in the positive bistatic range sum direction compared to theory may be explained by the large roof area in front of the receiver described a few pages earlier. The main target response occurs at a range sum of 200m with respect to the receiver. The measured resolution at the receiver is 25.9m, with theory predicting a value of 23.4m.

The azimuth cuts may be found in Figures 7-115 and 7-116. The mainlobe broadening is minimal and so there is a closer correlation between the measured and theoretical magnitudes. Less mainlobe broadening in this set of data but with use of the same local oscillator and processor implies that the broadening shown in the azimuth cuts for the other acquisitions is as a result of the environment. This is partly confirmed by the measured reflected signal phase of 7-109, which is very linear - reflections from close to the receiver are due to a single dominant scatterer acting as a point target. Measured resolution is 23.8m (24m theory).

Conversion to map coordinates

As for the Torrington Place data sets, the receiver is assumed to be 10m above the surrounding target points. The conversion to a grid coordinates plane gives the contours of constant range sum as illustrated in Figure 7-117.

Note that only the constant range contours are shown in this case, and also that they are given for the receiver look direction both towards and away from the receiver (two solution sets). For the previous sets of results, the range (and azimuth) contours were shown for one direction only (away from the satellite) as the receiver antenna was pointing in that direction. Here the antenna is pointing in a North-North-West direction. The range contours plotted in Figure 7-117 do not have any values (or valid solutions to the

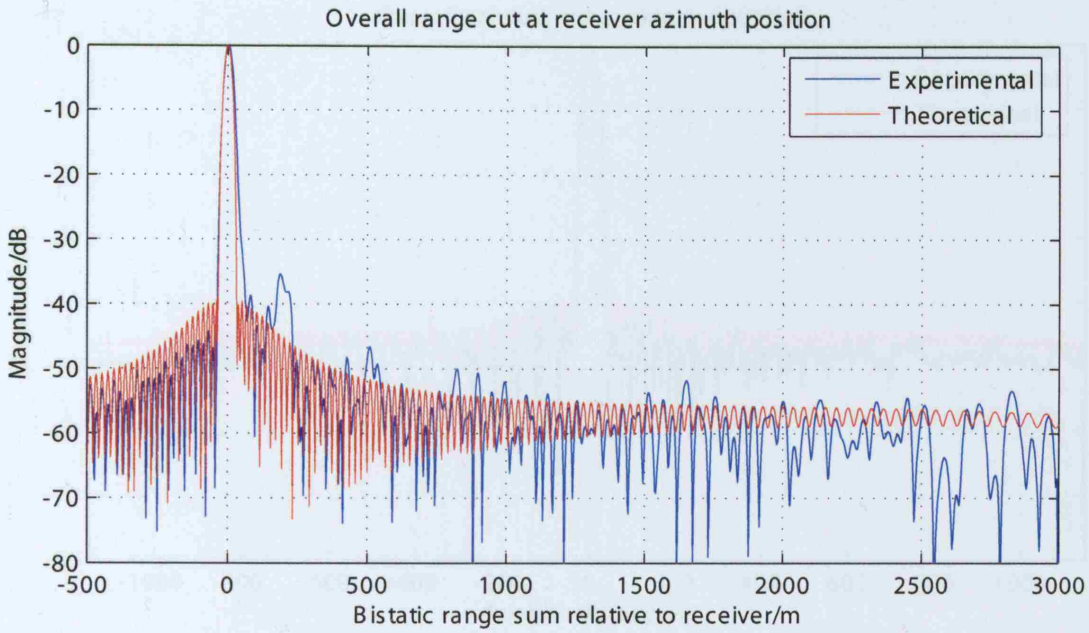

Figure 7-113: Overall range cut at the receiver azimuth position

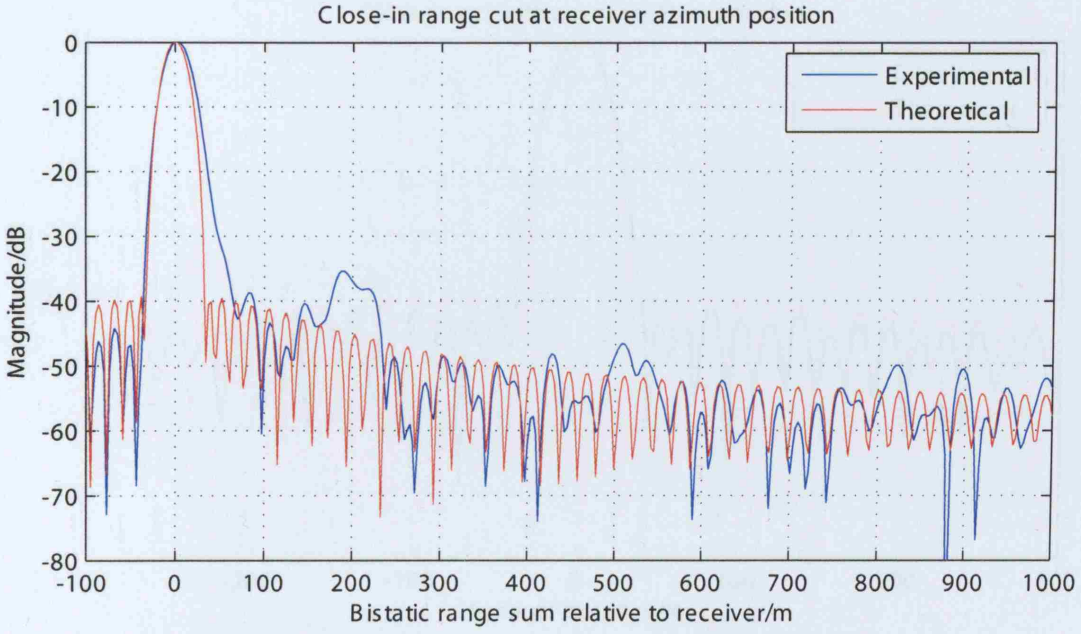

Figure 7-114: Close-in range cut at the receiver azimuth position

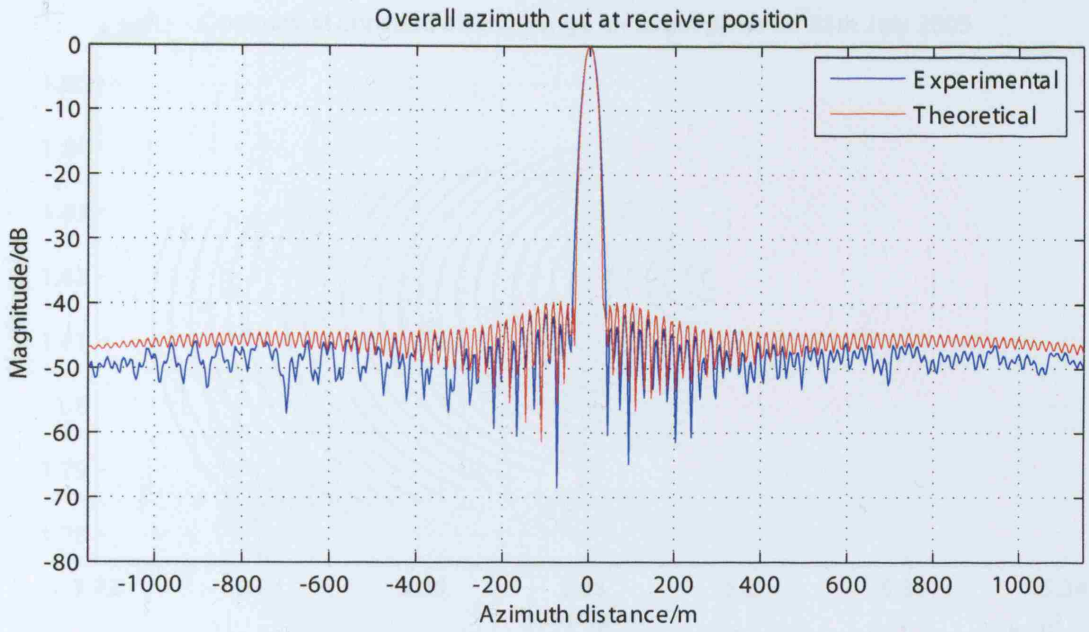

Figure 7-115: Overall azimuth cut at the receiver azimuth position

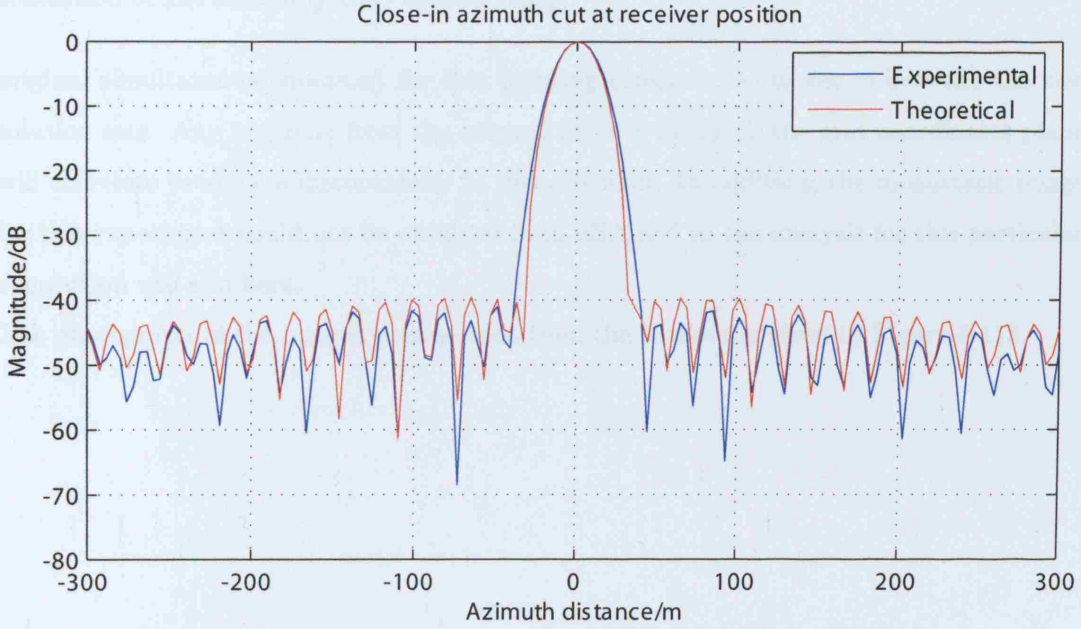

Figure 7-116: Close-in azimuth cut at the receiver azimuth position

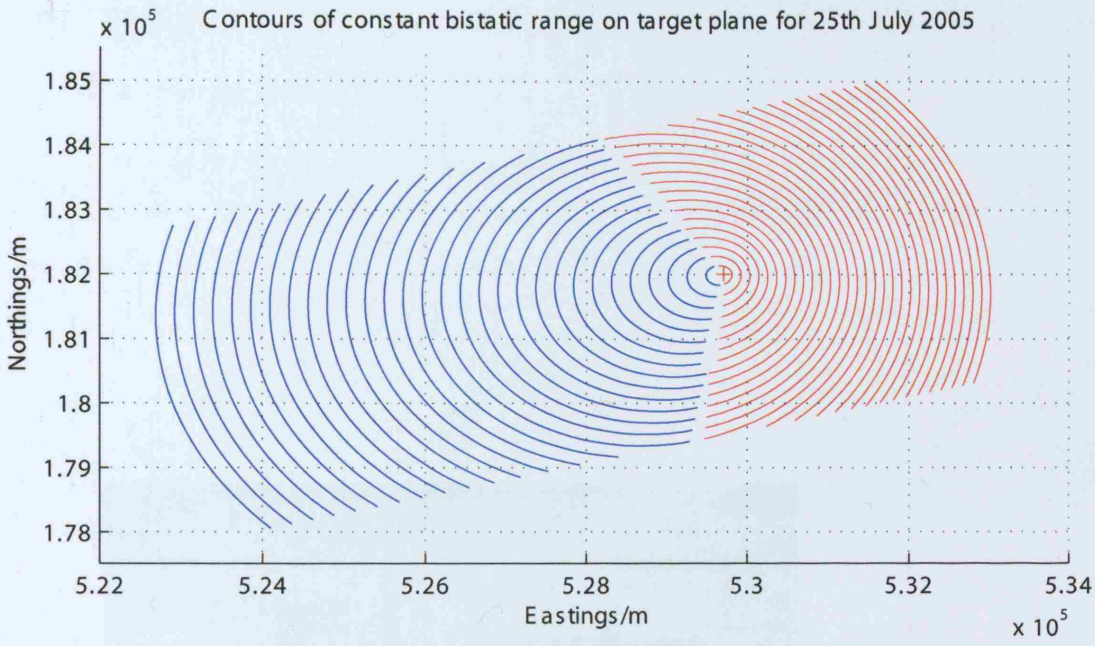

Figure 7-117: Contours of constant bistatic range only on the target plane for the coordinate conversion of the 25th July 2005 bistatic image

original simultaneous equation) for this pointing direction, as it lies in-between the two solution sets. Any mapping from the original bistatic image to the grid coordinates plane will therefore produce a discontinuity in this direction. In addition, the monostatic image for this experiment could not be obtained from ESA and so the analysis for this particular acquisition will end here.

The photograph of the imaged area as seen from the receiver is given in Figure 7-118.

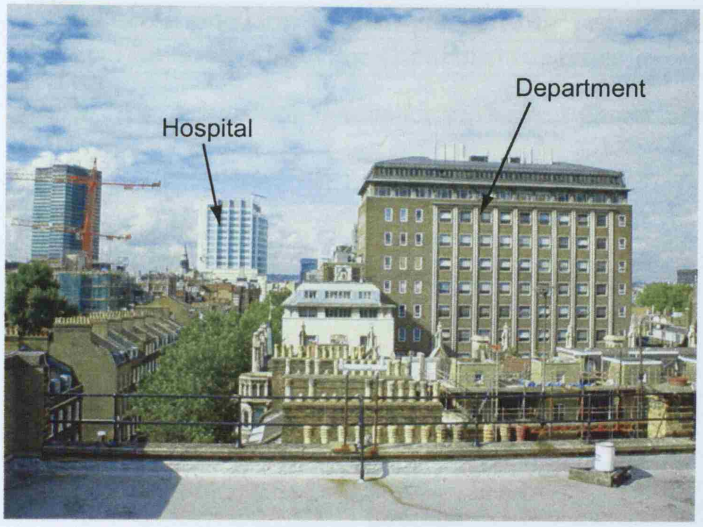

Figure 7-118: Photograph of the imaged area, Gower Street experiment 25th July 2005, taken from the receiver position and illustrating the imaged scene

7.2.6 Gower Street site, experiment 2

Overview and geometry

Again, the location was Gower Street (on 25th October 2005). An ascending pass satellite acquisition with ASAR in IS4 mode applies to this set of data. Acquisition and geometry details are given in Table 7.19 and Figure 7-119.

Swath	IS2
Satellite pass	Ascending
Polarisation	VV
Pulse repetition frequency/Hz	1694.99
Pulse length/s	27.1776×10^{-6}
Receiver position (Easting,Northing)/m	(529704,182003)
Receiver look direction (bearing)/degrees	5

Table 7.19: Acquisition details for the second Gower Street experiment

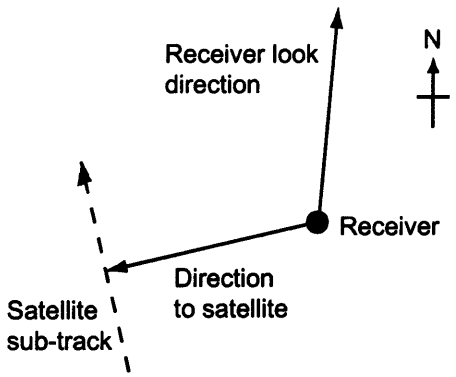

Figure 7-119: Imaging geometry for 25th October 2005 acquisition

Pre-processing

The range compressed reflected signal data as shown in the next Figure, 7-121 has more energy reflected from the scene than was observed for the first Gower Street experiment. The pointing direction of the receiver antenna differed for each of these acquisitions, which may explain this observation.

The reflected signal phase of Figure 7-122 is fairly linear over the range of 2000 pulses,

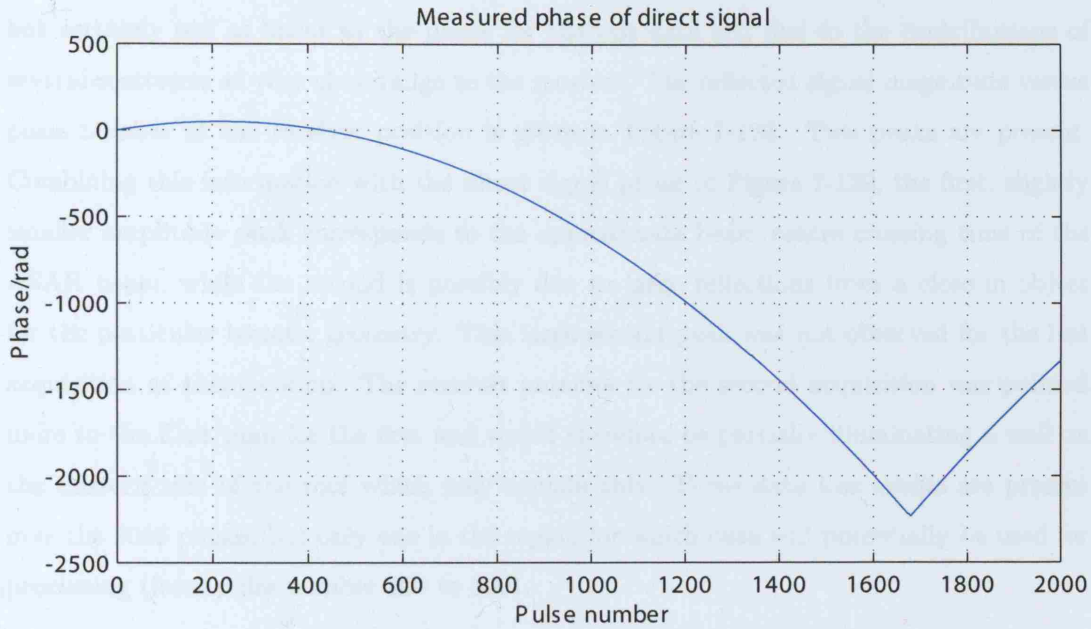

Figure 7-120: Measured phase of direct signal channel pulses

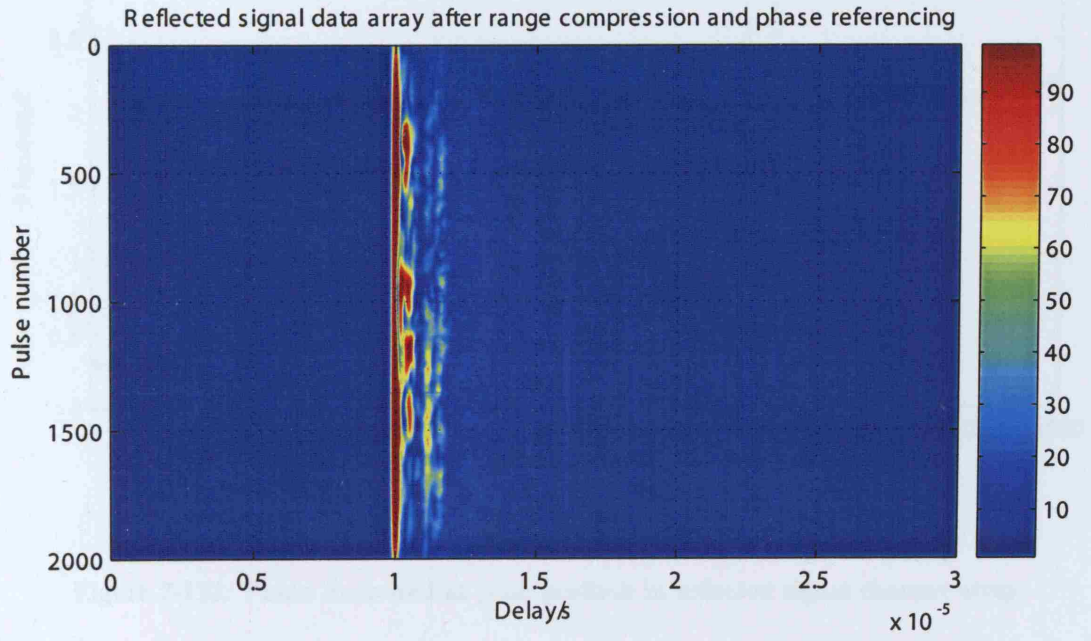

Figure 7-121: Reflected signal channel array after range compression and phase referencing

but certainly not as linear as the phase for the last data set, due to the contributions of several scatterers at very close range to the receiver. The reflected signal magnitude versus pulse number at the receiver position is given in Figure 7-123. Two peaks are present. Combining this information with the direct signal phase of Figure 7-120, the first, slightly smaller amplitude peak corresponds to the approximate beam centre crossing time of the ASAR beam, while the second is possibly due to large reflections from a close-in object for the particular bistatic geometry. This large second peak was not observed for the last acquisition at this location. The receiver antenna for the second acquisition was pointed more to the East than for the first and would therefore be partially illuminating a wall on the Eastern side of the roof which may explain this. Three data loss events are present over the 2000 pulses, but only one in the region for which data will potentially be used for processing (from pulse number 200 to 800).

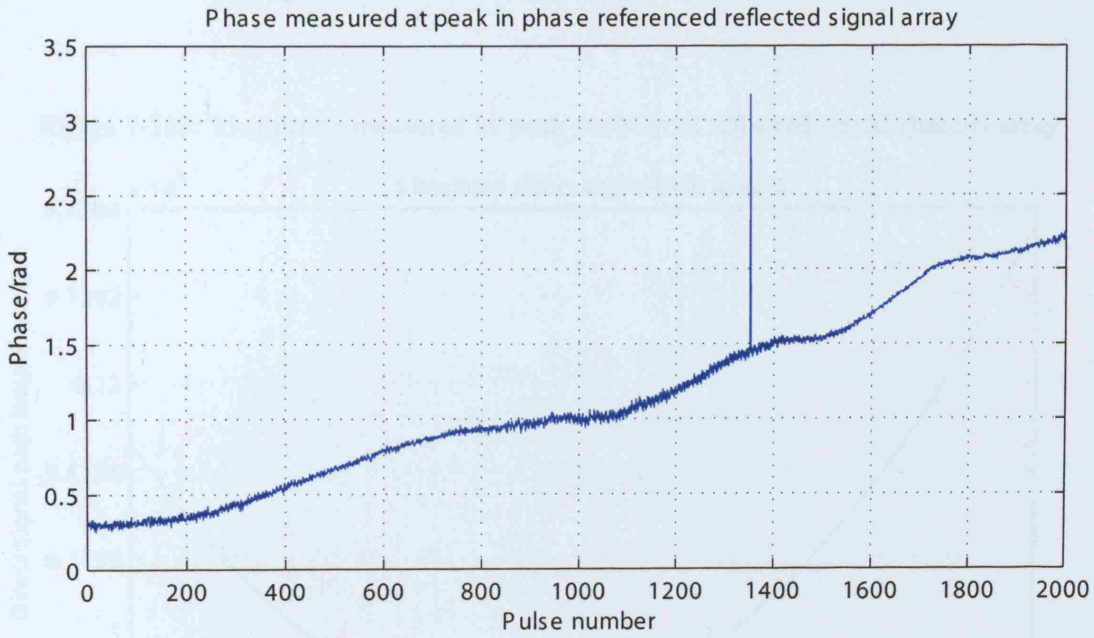

Figure 7-122: Phase measured at peak position in reflected signal channel array

The processing parameters are reproduced in Table 7.2.6. The Doppler rate has a smaller magnitude for this IS4 swath compared to the values presented for the IS2 swath experiments, as a result of the increased range between the satellite and the target area.

The image SNR is predicted to be,

$$SNR_{image} \approx 25.6 + 10\log_{10}(629) - 1.23 = 52.4dB$$

Azimuth compression has used 629 pulses.

Parameter	Value
Doppler centroid/Hz	-150.5
Doppler rate/Hz/s	-1968.5
$\theta_{sq,c}$/degrees	-0.06429
V_{FM}/m/s	7107
Beam centre crossing time/s	0.1529
Exposure time/s	0.6794
Azimuth bandwidth/Hz	668.7
Ideal azimuth resolution/m	8.867

Table 7.20: Bistatic azimuth parameters for the 25th October 2005 acquisition

Bistatic SAR image

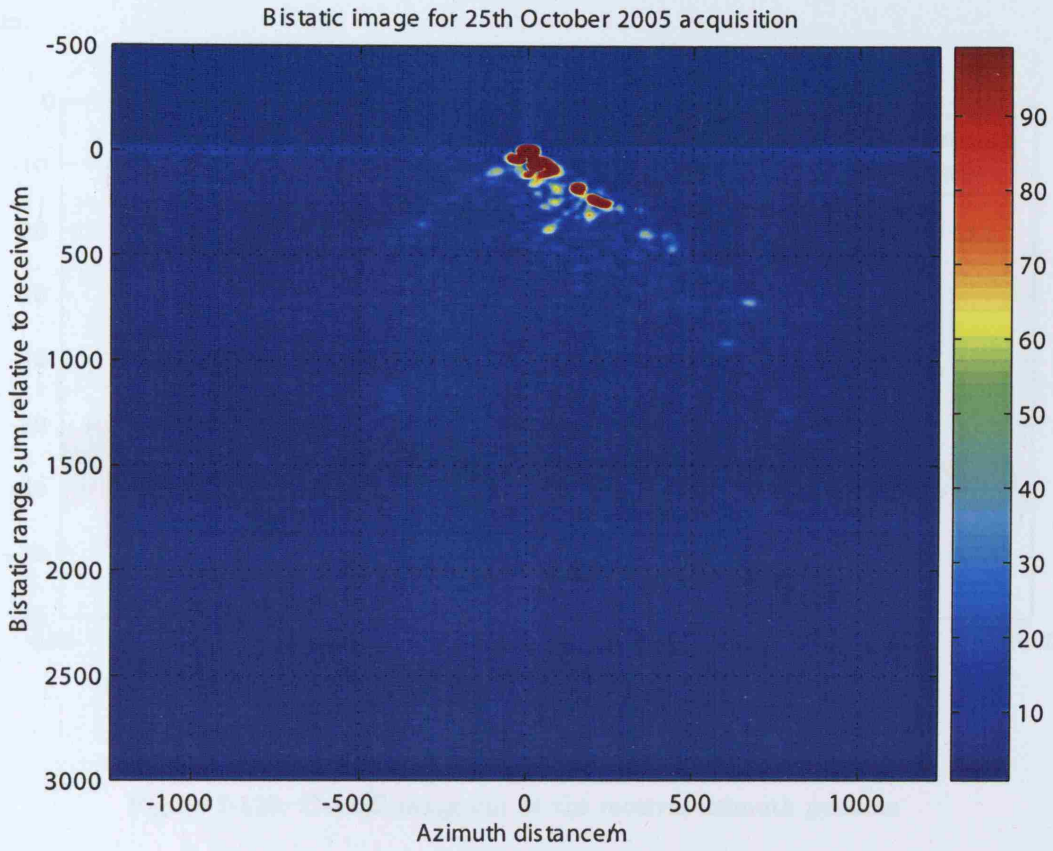

Figure 7-125: Bistatic image for 25th October 2005 acquisition, bistatic range sum versus azimuth

The scatterers in the bistatic image are aligned along approximately the same direction as for the previous acquisition, as can be seen in Figure 7-125, expected given the similar geometry (the difference in receiver look direction is small for the two experiments). More scatterers are present in this image compared to the previous image, particularly at close range and azimuth displacements relative to the receiver.

The range cuts are given in Figures 7-126 and 7-127, where the close-in scatterers noted in the main bistatic image may be noted. The measured resolution of the main peak is 24.7m (23.4m theory).

The azimuth cuts for this acquisition (Figures 7-128 and 7-129) are similar to those for the

7.2.7 Summary

This Chapter has presented the bistatic SAR imaging results acquired over the course of the PhD programme. Of all of the results, the imagery produced for the DSTL Portsdown West site is the most convincing of correct bistatic imaging operation, given the relatively uncluttered nature of the scene. The images produced for the Torrington Place site do contain some scatterers that may be matched to physical features in the scene, although the images are far more difficult to interpret as a result of the large number of potential targets. The two images produced for the Gower Street site are again, difficult to interpret, and the receiver location and imaged scene are perhaps even less ideal than for the Torrington Place site.

The correct focusing of point-like targets has been demonstrated for several bistatic images, both at the receiver position and at points some distance from the receiver. The targets analysed in this way are in reality not point scatterers and so their responses will exhibit some deviation from the ideal, as has been noted for the receiver responses in all of the images. Ideally, the image experiments would have made use of a man-made point target. For a monostatic image a corner reflector might be used, here a flat plate could have been used as in the experiments performed by Cazzani [10]. This would need to be carefully aligned to provide maximum energy reflected to the receiver. It would then be possible to calibrate the receiver in terms of RCS values of responses within the image. Because of difficulties experienced in obtaining acquisitions by ASAR over London and Portsmouth without conflicts from other users, and time constraints over the research programme this was unfortunately not possible, although it would have made a very useful addition to the results obtained.

The bistatic ambiguity function has been successfully applied to the imaging scenarios, with simulated data on ground resolution, bistatic angle and ground resolution cell size all being produced. This applies to a flat target plane, and the conversion from an azimuth, bistatic range image to a grid coordinates image relies on the same assumption. Whether the assumption is valid or not depends on the nature of the imaged scene, certainly it is more valid for the semi-rural Portsdown image than for the central London data, with a variety of buildings, all of different heights being imaged. The point is made with the third Torrington Place image, where the BT tower return appears to have been shifted in ground

range as a result of layover. Despite this flat target plane assumption, the measured and theoretical resolutions are all in fairly good agreement.

The bistatic images have also shown the signal energy that is received in the sidelobes of the receiver antenna, and must be discounted. A brief description of the potential azimuth ambiguities that may arise with the system has also been given, and it is noted that due to the combination of transmitter and receiver antenna patterns for the returns, (and the large difference between transmitter and receiver antenna azimuth beamwidths) the effect of these is likely to be small. It is however an important point to consider in the design of such a bistatic imaging system, particularly in the case where the receiver antenna azimuth beamwidth is close to in size or perhaps greater than that for the transmitter.

The comparison between monostatic and bistatic images has demonstrated some similarities in the areas of large amounts of scattering in both types of images. Given the small number of returns in the bistatic images, a detailed comparison is, however, difficult to perform.

Chapter 8

Conclusions and future work

8.1 Summary of findings

The main aim of this research programme has been the demonstration of a bistatic synthetic aperture radar system using a moving, space-based transmitter and a stationary ground-based receiver. This includes the associated signal processing algorithms, experimentation, and analysis of bistatic imagery, all of which have been achieved as outlined in this document. The data for the images was captured using a relatively simple and cheap receiver. The novelty of this work arises from the particular bistatic configuration as described above together with the choice of illuminator.

The principal contribution of the research has been the generation of bistatic SAR imagery with this system. In addition, the combination of signal processing techniques as outlined in Chapter 6, together with the analysis of the image results are all contributions to the field of bistatic radar research.

The imagery produced is focused (for the specific configuration investigated) and its generation and analysis have illustrated some of the particular considerations for such a system, including receiver sidelobe responses, azimuth ambiguities and space-variant resolution. It is apparent that a number of performance compromises must be made. Direct signal interference can reduce the dynamic range of the receiver and so must be suppressed. In this particular case the suppression technique imposed a constraint on the pointing direction of the receiver antenna. The final choice of pointing direction must be weighed against the resolution achievable as predicted by the bistatic ambiguity function. It was noted in the 25th October 2005 experiment that the resolution in the East direction was fairly poor for

the pointing direction of the antenna, for example. The receiver antenna beamwidth, if increased, will of course image a wider area given a transmit beamwidth of a similar or greater size. However, the depth of focus constraint on the processing algorithm may not be met for a larger imaged area, and depending on the combined transmit/receive antenna pattern, and amplitude of receiver antenna sidelobes, azimuth ambiguities may have an effect.

The system has been analysed in both co-operative and non-cooperative modes of operation through the first set of results for DSTL Portsdown West. The latter mode is demonstrated by the data for no phase synchronisation between receiver and transmitter. The ISLR increased as a result and there was a small shift in range of the output image. If the receiver data capture board had been switched on at the start of illumination of the local area by the ASAR beam, perhaps with a threshold detection in the direct signal channel, this would have reduced the overall data capture time and so improved the ISLR of the resultant image.

Such a bistatic imaging system would fulfil a local area SAR imaging role, perhaps as a complement to an existing monostatic imaging setup, for crop monitoring for example. It is certainly feasible that a bistatic system, although producing theoretically poorer resolution performance than its monostatic equivalent, would be able to provide additional information on a scene through bistatic scattering that would prove valuable. In addition, the processed images could potentially be made available in a much shorter time-frame than those from a monostatic system.

8.2 Future work

8.2.1 Bistatic SAR imaging

The imaging experiments as they stand have produced some useful results, but there is plenty of scope for extending the system to gain further understanding. Several bistatic SAR processors have been described in the open literature, with the approaches in Wong [61] (non-linear chirp scaling) and Sanz-Marcos [63] being of most interest. Successful application of such a processing scheme would enable imaging over a wider area and so potentially greater applicability of the system. In addition, Sanz-Marcos [63] describes using a digital elevation model (DEM) of the surrounding terrain to correctly focus target

points in the image. This is compared to the flat Earth model used in this investigation, which is fairly simplistic and only really applicable to a small number of imaging scenarios. The increased computational burden of the DEM approach as noted in the paper will have to be weighed against the advantages. The larger imaged area implies more scatterers and so data that is better suited to comparison with the monostatic imagery and also correspondingly more useful in determining bistatic clutter models.

The results produced have demonstrated imaging over different environments, but arguably not for widely differing bistatic geometries. This is illustrated by the theoretical bistatic angle for each acquisition lying within a few degrees of 90^0. The pointing direction of the receiver antenna, being away from the transmitter, will limit the potential variety of imaging geometries that may be investigated, and so an alternative direct signal suppression technique would be useful.

Mounting of the reflected channel antenna on the edge of the building/structure on which it is sited will reduce returns from very close to the antenna and so enable a wider dynamic range for the returns from the imaged area. This would mean that the weighting function applied in range and azimuth could be different, perhaps giving better resolution performance at the expense of higher sidelobes. One potential problem with this arrangement is the physical support necessary for the antenna given the potential wind strength at the edge of such a tall structure.

The phase noise of the receiver could be quantified more accurately. Although the system performed acceptably in terms of overall phase noise, as seen in the measured ISLR in the bistatic images, it would be useful to analyse the long-term phase stability of the local oscillators using the Allan variance from Allan [103].

Extension of the system to include multiple receivers could offer performance advantages in terms of resolution, for instance, although there would of course be added complexity introduced in the inter-receiver synchronisation and signal processing, as well as an increased cost.

A theoretical comparison of the ambiguity functions for a variety of illuminators and so imaging geometries would enable the performance achieved in this investigation to be put into a wider context, and could be combined with such information as transmit power and revisit time to give some idea as to the optimum choice of illuminator for a particular scenario.

Use of a man-made point target of known bistatic RCS would be necessary for system and image characterisation.

8.2.2 Bistatic displaced phase centre antenna technique

Physical DPCA uses an array of antennas aligned along the direction of travel of the moving platform. Pulses are transmitted from each antenna in turn. The velocity of the platform (and so the time taken for the array to travel the inter-element distance) is matched to the pulse repetition interval. This allows several 'looks' at the same target point from the same transmitter location, but at different times. Assuming a coherent system, the second pulse of each pair of transmitted pulses is subtracted from the first, which results in all returns from static scatterers canceling, leaving only those returns from moving targets.
Electronic DPCA uses a monopulse antenna with two displaced phase centres, from which sum and difference channels are formed. A cancellation rule may be derived, see Skolnik [90] for which returns from static scatterers are suppressed, this corresponds to an optimum phase centre separation W_{opt} of:

$$W = W_{opt} = 2VT$$

where V is the velocity of the platform and T is the pulse repetition interval. An additional weighting may be applied in the processor to the difference channel to account for the actual separation between the two phase centres being different to the optimum value for DPCA cancellation.
A fairly detailed theoretical analysis of bistatic DPCA was performed by a Masters level student in the early stages of this PhD programme, the results of which are presented in Müller [104], and also in Whitewood [60]. This related the specific bistatic geometry investigated (moving transmitter and stationary receiver) to the monostatic electronic DPCA theory covered in the last paragraph, and through the use of Matlab simulations presented estimates of expected system performance. The receiver would need two reflected signal channels, with a horizontal separation between them, and a single direct signal channel. The condition on the separation between the two reflected channel antennas is range dependent. As for the monostatic case, an additional weighting may be applied to the difference channel to account for any discrepancy between actual and ideal separation. This weighting will

also be range dependent, and so the DPCA processor will need to be highly adaptive, in contrast to the monostatic situation. For a fairly representative operating configuration, with a low flying air target 30km from the receiver, and the receiver look direction being in the same direction as the transmit beam, the overall signal-to-clutter-and-noise ratio achievable is typically 10dB. This is assuming a target velocity of at least 250km/h and coherent integration of 300 pulses. A target with a lower velocity would of course be more difficult to detect, while an aircraft travelling at 50km/h or less would not be detectable with the previous assumptions. In summary, given an adequate number of coherently integrated pulses and the ideal application of this bistatic DPCA processing scheme, sufficient clutter suppression should be achievable in order to detect air targets of interest. The application of this DPCA processor to an experimental bistatic system, in addition to a detailed analysis of the performance degradation with non-ideal processing, for example a mismatch between reflected signal channels, would make an interesting and valuable research investigation.

8.2.3 Bistatic interferometry

There is the possibility of using the system to perform bistatic interferometry experiments as described in Cherniakov [9]. As for bistatic DPCA, a three-channel receiver would be needed, for two reflected signal channels and one direct. As for the DPCA experiments, this would make a useful addition to the research and demonstrate the applicability of the system to another area, avalanche prediction.

Appendices

Appendix A

Calculation of effective satellite velocity

This is taken from Cumming [79]. The relevant equation relates the satellite velocity V_s, beam footprint velocity V_{gr} and effective velocity V_{FM},

$$V_{FM} \approx \sqrt{V_s V_{gr}}$$

This equation is accurate for zero Doppler pointing of the beam and a satellite orbit that may be approximated by a circular path over the target exposure time. The proof for the relationship is given in Cumming [79], Appendix 4A. This Appendix will describe the geometry and give the relevant equations used in calculating such parameters as V_{gr} and V_{FM}.

Starting with the diagram of Figure A-1. The coordinate system assumed is Earth Centred Rotating. θ_i is the angle of incidence of the radar beam with the ground, while θ_n is the angle of depression of the beam at the satellite. The Earth is locally spherical with radius R_e, while the satellite is at a height h above the Earth's surface. The target point considered, marked A, is at a range r from the satellite. G is an arc length, subtended by angle β_e, formed at the Earth's centre.

Assuming the incidence angle is known, the depression angle may be calculated,

$$\theta_n = \sin^{-1}\left(\frac{R_e}{(R_e + h)}\sin(180 - \theta_i)\right)$$

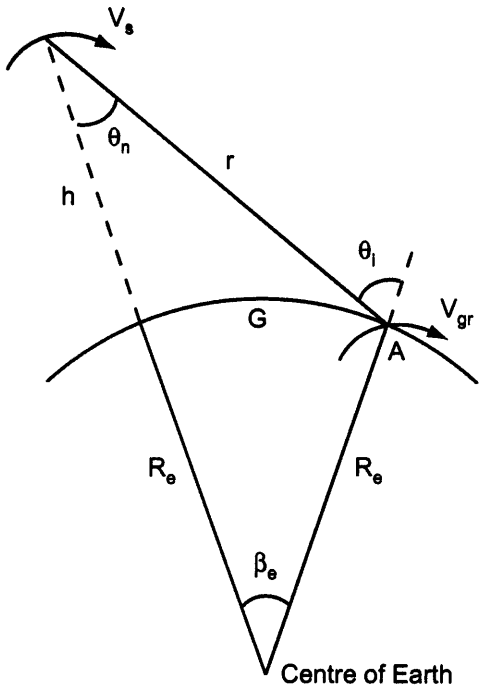

Figure A-1: Circular orbit, spherical Earth geometry for calculation of effective satellite velocity V_{FM}

The law of cosines gives the range r in terms of θ_n, R_e and h:

$$r = \frac{2(R_e + h)\cos(\theta_n) - \sqrt{4(R_e + h)^2 \cos(\theta_n)^2 - 4((R_e + h)^2 - R_e^2)}}{2}$$

The angle β_e is then,

$$\beta_e = \sin^{-1}\left(\frac{r}{(R_e + h)}\sin(180 - \theta_i)\right)$$

And the arc length,

$$G = R_e\beta_e$$

The locally circular orbit means that the satellite velocity is,

$$V_s = (R_e + h)\omega_s$$

The beam footprint velocity is in the same direction as V_s assuming that the Earth is locally

spherical, and given by,

$$V_{gr} = R_e \omega_s \cos(\beta_e)$$

Once the footprint velocity is known, the effective velocity V_{FM} is of course calculated with,

$$V_{FM} \approx \sqrt{V_s V_{gr}}$$

Appendix C

Range-Doppler transform of the bistatic baseband signal impulse response

This Appendix uses the Principle of Stationary Phase (PSOP), the relevant theory may be found in a number of texts, including Skolnik [90] and Cumming [79], and will not be repeated here.

In order to generate the azimuth Fourier transform of the bistatic signal baseband impulse response of Equation (6.2), it is necessary to start with the range Fourier transform, given by

$$Pp(f_{\tau,b}, t) = \int_{-\infty}^{\infty} pp(\tau_b, t) \exp\left(-j2\pi f_{\tau,b}\tau_b\right) d\tau_b$$

The phase of the integrand is

$$\theta_{rangeFT} = \frac{-2\pi(R(t;r_0) + R_R)}{\lambda} + \pi K_r \left(\tau_b - \frac{R(t;r_0) + R_R}{c}\right)^2 - 2\pi f_{\tau,b}\tau_b$$

This has a stationary point when $\frac{d\theta_{rangeFT}}{d\tau_b} = 0$, giving,

$$\tau_b = \frac{f_{\tau,b}}{K_r} + \frac{R(t;r_0) + R_R}{c}$$

Substituting into the integrand phase and using $f_0 = \frac{c}{\lambda}$ as the centre frequency of transmission of the signal,the phase becomes,

$$\theta_1 = \frac{2\pi(f_0 + f_{tau,b})(R(t;r_0) + R_R)}{c} - \frac{\pi f_{\tau,b}^2}{K_r}$$

the range Fourier transform is therefore,

$$Pp(f_{\tau,b}, t) = C_1 w_{a,b}(t - t_c) A_R W_r(f_{\tau,b}) \exp(j\theta_1)$$

C_1 is a constant introduced by the application of POSP. $W_r = w_r(f_{\tau,b}/K_r)$ is the transformed range signal envelope.

The azimuth Fourier transform is now applied. The signal in the range frequency, azimuth frequency domain is:

$$PP(f_{\tau,b}, f) = \int_{-\infty}^{\infty} Pp(f_{\tau,b}, t) \exp(-j2\pi ft) dt$$

The phase in the integrand is given by,

$$\theta_{azimuthFT} = \theta_1 - 2\pi ft$$

The stationary point is,

$$t = -\frac{r_0}{\frac{V_{FM}^2(f_0 + f_{\tau,b})}{cf}\sqrt{1 - \frac{c^2 f^2}{V_{FM}^2(f_0 + f_{\tau,b})}}}$$

This indicates the one-to-one correspondance between azimuth time and azimuth frequency, with a dependence upon $f_{\tau,b}$. The square root factor in the denominator is equal to the cosine of the squint angle at azimuth time t. The phase is, after substitution, and simplification becomes,

$$\theta_2 = -\frac{2\pi r_0 f_0}{c}\sqrt{D_b(f, V_{FM})^2 + \frac{2f_{\tau,b}}{f_0} + \frac{f_{\tau,b}^2}{f_0^2}} - \frac{\pi f_{\tau,b}^2}{K_r} - \frac{2\pi R_R(f_0 + f_{\tau,b})}{c}$$

Where $D_b(f, V_{FM}) = 1 - \frac{c^2 f^2}{V_{FM}^2 f_0^2}$. The azimuth Fourier transform result is,

$$PP(f_{\tau,b}, f) = C_2 W_{a,b}(f - f_{DC,b}) A_R W_r(f_{\tau,b}) \exp(j\theta_2)$$

The azimuth envelope has been transformed to $W_a(f - f_{DC,b})$, centred on the bistatic Doppler centroid.

The final step is to perform a range inverse Fourier transform:

$$pP(\tau_b, f) = \int_{-\infty}^{\infty} PP(f_{\tau,b}, f) \exp(j2\pi f_{\tau,b}\tau_b) df_{\tau,b}$$

In order to simplify the algebra, the square root term in θ_2, denoted $sqr(f_{\tau,b})$ is expanded as a power series in $f_{\tau,b}$ to give,

$$sqr(f_{\tau,b}) = -\frac{2\pi r_0 f_0}{c}\left[D_b(f, V_{FM}) + \frac{f_{\tau,b}}{D_b(f, V_{FM}) f_0} - \frac{f_{\tau,b}^2}{2f_0^2 D_b(f, V_{FM})^3}\frac{c^2 f^2}{V_{FM}^2 f_0^2}\right]$$

The terms higher in order than $f_{\tau,b}^2$ have been ignored, an approximation that is valid if:

$$D_b(f, V_{FM})^2 = 1 - \frac{c^2 f^2}{V_{FM}^2 f_0^2} >> \left|\frac{2f_{\tau,b}}{f_0} + \frac{f_{\tau,b}^2}{f_0^2}\right|$$

This is an acceptable approximation under the conditions of moderate aperture length and moderate squint. The phase in the integrand is now,

$$\theta_{rangeIFT} = \theta_{2,approx} + 2\pi f_{\tau,b}\tau_b$$

Where $\theta_{2,approx}$ is the phase θ_2 after substitution of the power series for the square root term. The stationary point is,

$$f_{\tau,b} = \frac{K_r}{1 - K_r Z_b}\left(\tau_b - \frac{r_0}{cD_b(f, V_{FM})} - \frac{R_R}{c}\right)$$

The term Z_b is,

$$Z_b = \frac{cr_0 f^2}{V_{FM}^2 f_0^3 D_b(f, V_{FM})^3}$$

The integrand phase, after substitution of this stationary point becomes,

$$\theta_3 = \pi K_{m,b}\left(\tau_b - \frac{r_0}{cD_b(f,V_{FM})} - \frac{R_R}{c}\right)^2 - \frac{2\pi f_0(r0D_b(f,V_{FM}) + R_R)}{c}$$

Where the modified range chirp FM rate is $K_{m,b} = \dfrac{K_r}{1 - K_r Z_b}$. The final result of the range-Doppler transform of the bistatic baseband signal impulse response is:

$$pP(\tau_b, f) = C_3 W_{a,b}(f - f_{DC,b}) A_R w_r\left(\frac{1}{1 - K_r Z_b}\left(\tau_b - \frac{r0}{cD_b(f,V_{FM})} - \frac{R_R}{c}\right)\right)\exp(j\theta_3)$$

Appendix D

Airborne trial processing

D.1 Introduction

As a test for the monostatic CSA algorithm, some experimental data from QinetiQ from an airborne SAR trial over Pershore airfield in Worcestershire was processed. The SAR system parameters given in the data set documentation are summarised in the diagram and table below.

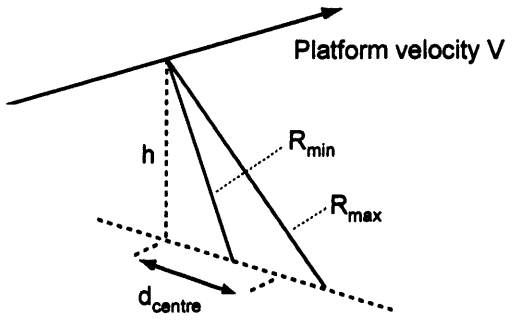

Figure D-1: Geometry for QinetiQ airborne SAR data acquisition

In addition to the above information, a reference chirp pulse is provided to indicate the form of the transmitted signal. Upon examination, it is noted that the LFM down-chirp has a length of 625 samples, or $5\mu s$, bandwidth of 100MHz, and therefore chirp rate of $2 \times 10^{13} Hz/s$. A Hanning window amplitude weighting is also present. The real and imaginary parts of the reference chirp are plotted below.

The bandwidth and weighting for the transmitted chirp signal result in a range resolution

D.2 Results and analysis

The images have been processed to have an azimuth resolution of 1m. The governing equation is,

$$\delta x = 0.886 \frac{V}{B_a}$$

The azimuth bandwidth is therefore $B_a = 0.886 \times 144.5 = 128Hz$ Figure D-3 illustrates a sample image supplied by QinetiQ and processed using the range-Doppler algorithm. Figure D-4 then shows the image processed using the monostatic chirp scaling algorithm programmed as part of this research programme.

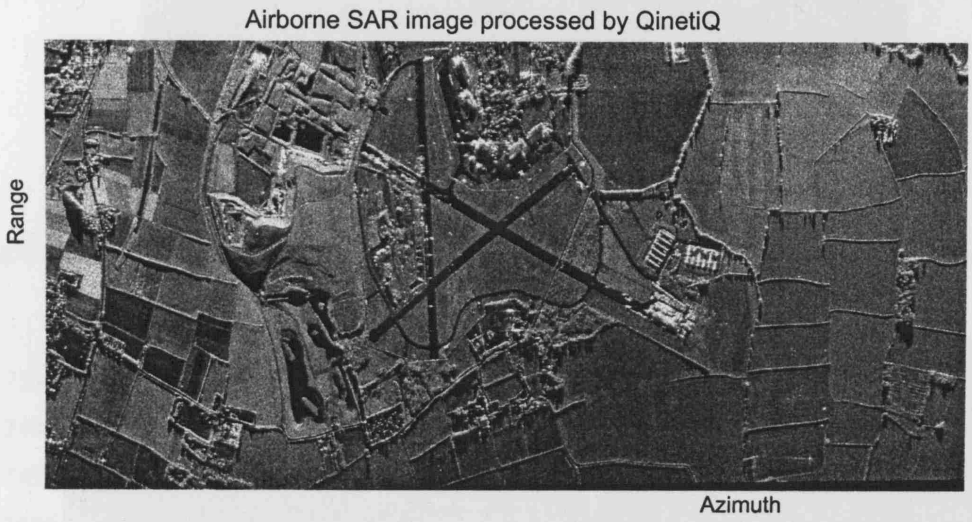

Figure D-3: Airborne SAR image processed by QinetiQ

A small section of the image in Figure D-4, covering part of the runway, is examined in more detail in Figures D-5.

Several point-like targets are present, one of which (marked) will be examined. Cuts along the azimuth and range dimensions are presented for the target in Figure D-6.

The azimuth cut has some asymmetry in the sidelobes, perhaps due to the antenna pattern variation in azimuth. The resolution measured is 1m in azimuth. The range resolution measured is 0.82m, although the -3dB width is formed from only three samples, and so any measurements are likely to be inaccurate. The apparent sidelobe level is higher than theory, although this may be due to adjacent targets.

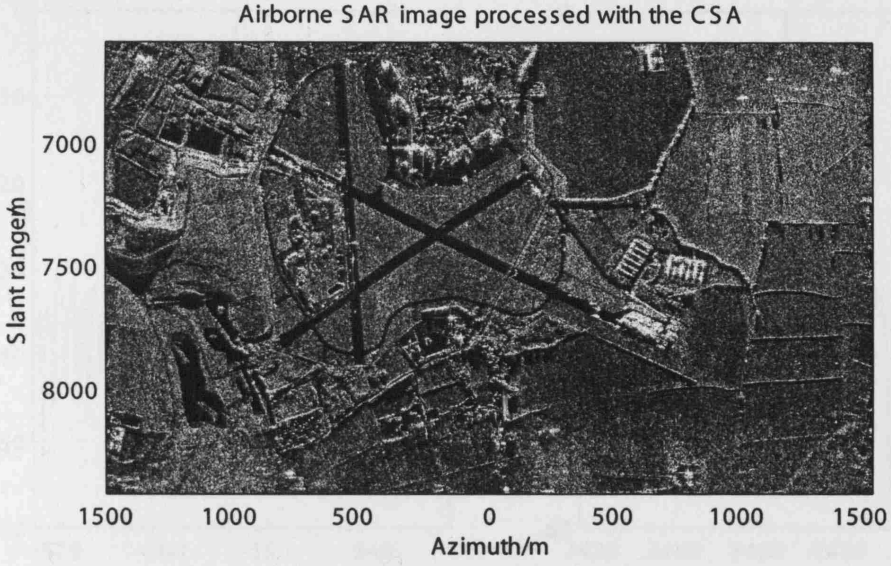

Figure D-4: Airborne SAR image processed using the monostatic chirp scaling algorithm

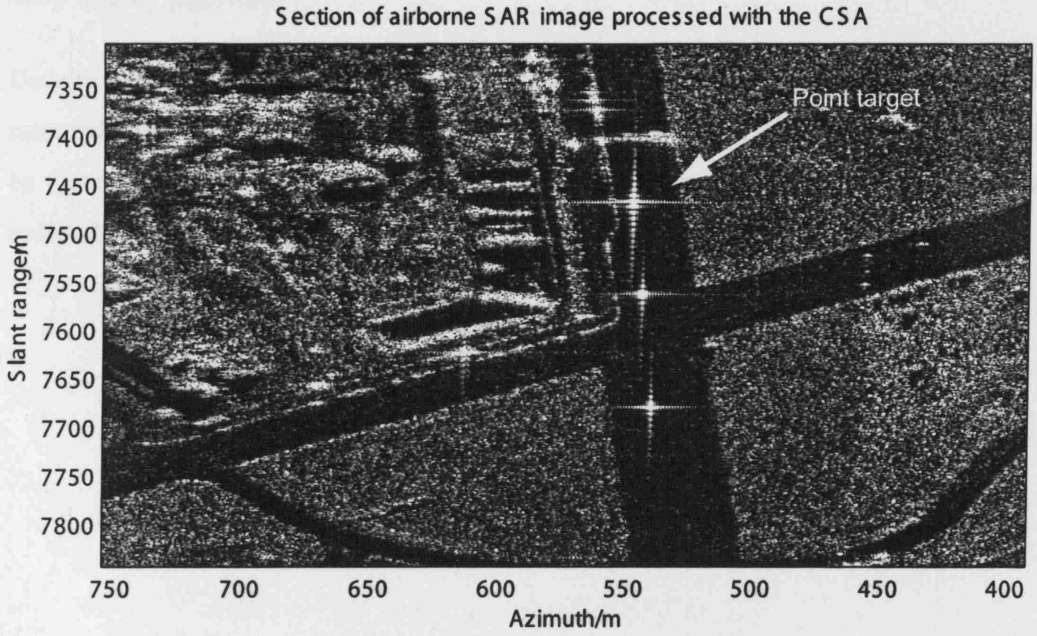

Figure D-5: Section of airborne SAR image processed using the monostatic chirp scaling algorithm

Bibliography

[1] H. D. Griffiths and N. R. W. Long, "Television-based bistatic radar," *IEE Proceedings F (Communications Radar and Signal Processing)*, vol. 133, no. 7, pp. 649–57, 1986.

[2] P. E. Howland, "Target tracking using television-based bistatic radar," *IEE Proceedings on Radar Sonar and Navigation*, vol. 146, no. 3, pp. 166–174, 1999.

[3] "Celldar," http://: www.roke.co.uk/sensors/stealth/celldar.asp.

[4] D. Martinsek and R. Goldstein, "Bistatic radar experiment," in *Proceedings of EUSAR 98*, 1998, pp. 561–564.

[5] M. Cherniakov, D. Nezlin, and K. Kubik, "Air target detection via bistatic radar based on leos communication signals," *IEE Proceedings on Radar Sonar and Navigation*, vol. 149, no. 1, pp. 33–38, 2002.

[6] H. D. Griffiths, A. J. Garnett, C. J. Baker, and S. Keaveney, "Bistatic radar using satellite-borne illuminators of opportunity," in *Proceedings of the IEE International Conference on Radar*, 1992, pp. 276–279.

[7] D. A. Whelan, "Discoverer ii program summary," *Proceedings of the IEEE International Radar Conference 2000*, pp. 7–8, 2000.

[8] M. E. Davis, "Technology challenges in affordable space-based radar," 1999, aIAA Space Technology Conference and Exposition, 18-23.

[9] M. Cherniakov, T. Zeng, and E. Plakidis, "Analysis of space-surface interferometric bistatic radar," *IEEE Geoscience and Remote Sensing Symposium 2003*, vol. 2, pp. 778–780, 2003.

[10] L. Cazzani, C. Colesanti, D. Leva, G. Nesti, C. Prati, F. Rocca, and D. Tarchi, "A ground based parasitic sar experiment," *IEEE Geoscience and Remote Sensing Symposium 2000*, vol. 38, no. 5, pp. 2132 – 2141, 2000.

[11] N. J. Willis, *Bistatic Radar*. Artech House Inc., 1991.

[12] E. Hanle, "Survey of bistatic and multistatic radar," *IEE Proceedings F*, vol. 133, no. 7, pp. 587–595, 1986.

[13] J. I. Glaser, "Fifty years of bistatic and multistatic radar," *IEE Proceedings F*, vol. 133, no. 7, pp. 596–602, 1986.

[14] G. L. Tyler, V. R. Eshleman, G. Fjeldbo, H. T. Howard, and A. M. Peterson, "Bistatic radar detection of lunar scattering centres with lunar orbiter 1," *Science*, no. 157, pp. 193–195, 1967.

[15] A. M. Peterson, C. C. Teague, and G. L. Tyler, "Bistatic radar observation of long-period directional ocean-wave spectra with loran-a," *Science*, no. 170, pp. 158–161, 1970.

[16] Y. S. Hsu and D. C. Lorti, "Spaceborne bistatic radar an overview," *IEE Proceedings F*, vol. 133, no. 7, pp. 642–647, 1986.

[17] H. D. Griffiths, "From a different perspective: principles, practice and potential of bistatic radar," in *Proceedings of the International Radar Conference*, 2003, pp. 1–7.

[18] J. G. Schoenenberger and J. R. Forrest, "Principles of independent receivers for use with co-operative radar transmitters," *Radio and Electronic Engineer*, vol. 52, no. 2, pp. 93–101, 1982.

[19] Z. Q. Yang, W. H. Guo, and D. J. Pan, "Principle and test of a bistatic radar," in *Proceedings of the CIE International Conference on Radar*, 1991, pp. 130–134.

[20] A. Munich and E. Schecker, "Bistatic system passively tracks radar targets," *Microwaves and RF*, vol. 30, no. 9, pp. 78–83, 1991.

[21] B. Wardrop and M. Molyneux-Berry, "Active-passive bistatic surveillance for long range air defense," *Microwave Journal*, vol. 35, no. 6, pp. 98, 101–4, 108, 110–11, 1992.

[22] R. de Porrata-Doria i Yague, A. Elias Fuste, and J. Fernandez de Muniain, "Rf receiver for a bistatic radar," *R.F. Design*, vol. 17, no. 3, pp. 106, 109–13, 1994.

[23] B. D. Nordwall, "Bistatic radar facility provides tool for gauging rcs stealthiness," *Aviation Week and Space Technology*, pp. 68–69, 1999.

[24] D. T. Gjessing and J. Saebboe, "Bistatic matched illumination radar involving synthetic aperture and synthetic pulse for signal to clutter enhancement and target characterization," 2001, triad AS Norway, 20-4.

[25] T. Johnsen, K. E. Olsen, and R. Gundersen, "Hovering helicopter measured by bi-/multistatic cw radar - detection and classification issues," in *Proceedings of the IEEE Radar Conference*, 2003, pp. 165–170.

[26] R. Burkholder, L. Gupta, and J. Johnson, "Comparison of monostatic and bistatic radar images," *IEEE Antennas and Propagation Magazine*, vol. 45, no. 3, pp. 41–50, 2003.

[27] M. Weiss, "Ebira: Experimental bistatic radar for air surveillance," *IGARSS '03 IEEE International Geoscience and Remote Sensing Symposium*, vol. 7, no. 2, pp. 4335–4337, 2003.

[28] M. Weib, "Synchronisation of bistatic radar systems," *IGARSS '04 IEEE International Geoscience and Remote Sensing Symposium*, vol. 3, pp. 1750 – 1753, 2004.

[29] A. Horne and G. Yates, "Bistatic synthetic aperture radar," in *Proceedings of IEE International Conference on Radar*, 2002, pp. 6–10.

[30] G. Yates and A. M. H. et. al., "Bistatic sar image formation," *Proceedings of EUSAR 2004*, pp. 581–584, 2004.

[31] J. Ender, I. Walterscheid, and A. Brenner, "New aspects of bistatic sar: processing and experiments," *IGARSS '04 IEEE International Geoscience and Remote Sensing Symposium*, vol. 3, pp. 1758 – 1762, 2004.

[32] B. D. Rigling and R. L. Moses, "Polar format algorithm for bistatic sar," *IEEE Transactions on Aerospace and Electronic Systems*, vol. 40, no. 4, pp. 1147–1159, 2004.

[33] D. D'Aria, A. M. Guarnieri, and F. Rocca, "Bistatic sar processing using a standard monostatic processor," *Proceedings of EUSAR 2004*, pp. 385–388, 2004.

[34] O. Loffeld, H. Nies, U. Gebhardt, V. Peters, and S. Knedlik, "Bistatic sar - some reflections on rocca's smile," *Proceedings of EUSAR 2004*, pp. 379–384, 2004.

[35] R. C. G. Robertshaw and J. SantaPietro, "Range-doppler and clutter considerations in designing a bistatic space based gmti radar system," in *IEEE International Radar Conference*, 2005, pp. 310 – 315.

[36] S. Gleason, S. Hodgart, S. Yiping, C. Gommenginger, S. Mackin, M. Adjrad, and M. Unwin, "Detection and processing of bistatically reflected gps signals from low earth orbit for the purpose of ocean remote sensing," *IEEE Transactions on Geoscience and Remote Sensing*, vol. 43, no. 6, pp. 1229 – 1241, 2005.

[37] J. M. Hawkins, "An opportunistic bistatic radar," in *Proceedings of the International Radar Conference*, 1997, pp. 318–22.

[38] J. Fawcette, "Vulnerable radars seek a safe sanctuary," *MSN Microwave Systems News*, vol. 10, no. 4, pp. 45, 47–8, 50, 1980.

[39] G. Retzer, "A passive detection system for a wide class of illuminator signals," 1979, (FGAN-Forschungsinst. fur Hochfrequenzphys. Wachtberg-Werthhoven West Germany) 620-3.

[40] E. C. Thompson, "Bistatic radar noncooperative illumination synchronization techniques," in *Proceedings of the IEEE National Radar Conference 1989*, 1989, pp. 29–34.

[41] R. F. Ogrodnik, "Bistatic laptop radar: an affordable silent radar alternative," 1996, (Rome Lab. NY USA) 369-73.

[42] C. L. Zoeller, M. C. B. Jr., and M. J. T. Moody, "Passive coherent location radar demonstration," *Proceedings of the Thirty-Fourth Southeastern Symposium on System Theory*, pp. 358–362, 2002.

[43] J. E. Hershey and J. E. Schroeder, "Bistatic radar without transmitted signal - covert altimetry concept," *IEEE Transactions Aero Elec Sys*, vol. 26 PART 5, pp. 732–736, 1990.

[44] *IEE Proceedings on Radar, Sonar and Navigation: Special Issue on Passive Radar Systems*, vol. 152 (3), 2005.

[45] D. Howland, P.E.; Maksimiuk and G. Reitsma, "Fm radio based bistatic radar," *IEE Proceedings on Radar Sonar and Navigation*, vol. 152, no. 3, pp. 107 – 115, 2005.

[46] R. Saini and M. Cherniakov, "Dtv signal ambiguity function analysis for radar application," *IEE Proceedings on Radar, Sonar and Navigation*, vol. 152, no. 3, pp. 133 – 142, 2005.

[47] H. Griffiths and C. Baker, "Passive coherent location radar systems. part 1: performance prediction," *IEE Proceedings on Radar, Sonar and Navigation*, vol. 152, no. 3, pp. 153 – 159, 2005.

[48] C. Baker, H. Griffiths, and I. Papoutsis, "Passive coherent location radar systems. part 2: waveform properties," *IEE Proceedings on Radar, Sonar and Navigation*, vol. 152, no. 3, pp. 160 – 168, 2005.

[49] H. M. Braun and P. Hartl, "Bistatic radar in space a new dimension in imaging radar," *IGARS 89 International Geoscience and Remote Sensing Symposium*, vol. 4, pp. 2261–2264, 1989.

[50] M. Soumekh, "Bistatic synthetic aperture radar imaging using wide-bandwidth continuous-wave source," *Proceedings of the Society of Photo-Optical Instrumentation Engineers (SPIE)*, pp. 99–109, 1998.

[51] A. Moccia, G. Rufino, M. D'Errico, G. Alberti, and G. Salzillo, "Bissat: a bistatic sar for earth observation," *IGARSS '02 IEEE International Geoscience and Remote Sensing Symposium*, vol. 5, pp. 2628 – 2630, 2002.

[52] G. Rufino and A. Moccia, "Scientific applications of a bistatic radar mission based on a small satellite," *Proceedings of the Society of Photo-Optical Instrumentation Engineers (SPIE)*, pp. 1–12, 2002.

[53] H. Huang and D. Liang, "The comparison of attitude and antenna pointing design strategies of noncooperative spaceborne bistatic radar," in *IEEE International Radar Conference*, 2005, pp. 568 – 571.

[54] J. C. McIntosh, C. E. Clary, and L. Ray, "An adaptive algorithm for enhanced target detection for bistatic space-based radar," in *Proceedings of the IEEE Radar Conference 2001*, 2001, pp. 70–74.

[55] M. Cherniakov, K. Kurt, and D. Nezlin, "Bistatic synthetic aperture radar with non-cooperative leos based transmitter," *IEEE Geoscience and Remote Sensing Symposium 2000*, vol. 2, pp. 861–862, 2000.

[56] J. Homer, K. Kubik, I. D. Mojarrabi, Longstaff, E. Donskoi, and M. Cherniakov, "Passive bistatic radar sensing with leos based transmitters," *IGARSS '02 IEEE International Geoscience and Remote Sensing Symposium*, vol. 1, pp. 438–440, 2002.

[57] B. Mojarrabi, J. Homer, K. Kubik, and I. D. Longstaff, "Power budget study for passive target detection and imaging using secondary applications of gps signals in bistatic radar systems," *IGARSS '02 IEEE International Geoscience and Remote Sensing Symposium*, vol. 1, pp. 449–451, 2002.

[58] H. D. Griffiths, C. J. Baker, J. Baubert, N. Kitchen, and M. Treagust, "Bistatic radar using satellite-borne illuminators," in *IEE International Radar Conference*, 2002, pp. 1–5.

[59] M. Cherniakov, "Space-surface bistatic synthetic aperture radar: Prospective and problems," in *IEE International Radar Conference*, 2002, pp. 22 – 25.

[60] A. P. Whitewood, B. R. Müller, H. D. Griffiths, and C. J. Baker, "Bistatic synthetic aperture radar with application to moving target detection," in *Proceedings of the International Radar Conference.*

[61] F. H. Wong and T. S. Yeo, "New applications of non-linear chirp scaling in sar data processing," *IEEE Transactions on Geoscience and Remote Sensing*, vol. 39, no. 5, pp. 946 – 953, 2001.

[62] J. Sanz-Marcos, J. Mallorqui, and A. Broquetas, "Bistatic parasitic sar processor evaluation," *IGARSS '04 IEEE International Geoscience and Remote Sensing Symposium*, vol. 6, pp. 3666 – 3669, 2004.

[63] J. Sanz-Marcos, P. Prats, and A. Broquetas, "Bistatic fixed-receiver parasitic sar processor based on the back-propagation algorithm," *IGARSS '05 IEEE International Geoscience and Remote Sensing Symposium*, vol. 2, pp. 1056 – 1059, 2005.

[64] X. He, M. Cherniakov, and T. Zeng, "Signal detectability in ss-bsar with gnss non-cooperative transmitter," *IEE Proceedings on Radar, Sonar and Navigation*, vol. 152, no. 3, pp. 124–132, 2005.

[65] D. J. Coe and R. G. White, "Moving target detection in sar imagery: Experimental results," in *Proceedings of the IEEE International Radar Conference*, 1995, pp. 644–649.

[66] T. J. Nohara, "Comparison of dpca and stap for space-based radar," in *Proceedings of the IEEE International Radar Conference.*

[67] R. Klemm, "Comparison between monostatic and bistatic antenna configurations for stap," *IEEE Transactions on Aerospace and Electronic Systems*, vol. 36, no. 2, pp. 596 – 608, 2000.

[68] W. L. Melvin, M. J. Callahan, and M. C. Wicks, "Bistatic stap: application to airborne radar," in *Proceedings of the IEEE Radar Conference 2002*, 2002, pp. 1–7.

[69] "Envisat website," http://envisat.esa.int.

[70] B. Rosich, M. Zink, and R. T. et al., "Asar instrument performance and product quality status," *Proceedings of the IEEE International Geoscience and Remote Sensing Symposium*, pp. 1109–1111, 2003.

[71] A. Moccia, N. Chiacchio, and A. Capone, "Spaceborne bistatic synthetic aperture radar for remote sensing applications," *International Journal of Remote Sensing*, vol. 21, no. 18, pp. 3395–3414, 2000.

[72] A. Moccia, S. Vetrella, and R. Bertoni, "Mission analysis and design of a bistatic synthetic aperture radar on board a small satellite," *Acta Astronautica*, vol. 47, no. 11, pp. 819–829, 2000.

[73] G. Krieger, H. Fiedler, J. Mittermayer, K. Papathanassiou, and A. Moreira, "Analysis of multistatic configurations for spaceborne sar interferometry," *IEE Proceedings on Radar, Sonar and Navigation*, vol. 150, no. 3, pp. 87–96, 2003.

[74] R. B. Olsen and T. Wahl, "The ship detection capability of envisat's asar," *IEEE International Geoscience and Remote Sensing Symposium*, pp. 3108–3110, 2003.

[75] P. Antonik, R. Bonneau, R. Brown, S. Ertan, V. Vannicola, D. Weiner, and M. Wicks, "Bistatic radar denial/embedded communications via waveform diversity," in *IEEE International Radar Conference*, 2001, pp. 41 – 45.

[76] S. Ertan, H. D. Griffiths, and M. W. et. al., "Bistatic radar denial by spatial waveform diversity," in *Proceedings of the IEE International Radar Conference*, 2002, pp. 17–21.

[77] H. Griffiths, M. Wicks, D. Weiner, R. Adve, P. Antonik, and I. Fotinopoulos, "Denial of bistatic hosting by spatial-temporal aveform design," *IEE Proceedings on Radar, Sonar and Navigation*, vol. 152, no. 2, pp. 81 – 88, 2005.

[78] G. Schreier, *SAR geocoding data and systems.* Wichmann, 1993.

[79] I. G. Cumming and F. H. Wong, *Digital Processing of Synthetic Aperture Radar Data: Algorithms and Implementation.* Artech House, Inc., 2005.

[80] C. Wu, "A digital system to produce imagery from sar data," *AIAA Conference: System Design Driven by Sensors*, 1976.

[81] R. Bamler, "A comparison of range-doppler and wavenumber domain sar focusing algorithms," *IEEE Transactions on Geoscience and Remote Sensing*, vol. 30, no. 4, pp. 706–713, 1992.

[82] C. Cafforio, C. Prati, and F. Rocca, "Sar data focusing using seismic migration techniques," *IEEE Transactions on Aerospace and Electronic Systems*, vol. 27, no. 2, pp. 194–207, 1991.

[83] R. K. Raney, H. Runge, R. Bamler, I. G. Cumming, and F. H. Wong, "Precision sar processing using chirp scaling," *IEEE Transactions on Geoscience and Remote Sensing*, vol. 32, no. 4, pp. 786–799, 1994.

[84] J. Ender, "Signal theoretical aspects of bistatic sar," *IGARSS '03 IEEE International Geoscience and Remote Sensing Symposium*, vol. 3, pp. 1438–1441, 2003.

[85] T. Zeng, M. Cherniakov, and T. Long, "Generalized approach to resolution analysis in bsar," *IEEE Transactions on Aerospace and Electronic Systems*, vol. 41, no. 2, pp. 461–474, 2005.

[86] "National gps network website," http://www.ordnancesurvey.co.uk/oswebsite/gps/.

[87] J. D. Kraus, *Antennas.* McGraw-Hill Book Company, 1988.

[88] R. J. Mailloux, *Phased array antenna handbook.* Artech House, 1994.

[89] "Parsec ltd," http://www.parsec.co.za/.

[90] M. I. Skolnik, *Radar Handbook.* McGraw-Hill, 1990.

[91] E. N. Fred, J. P. Reilly, and M. N. Cohen, *Radar Design Principles.* McGraw-Hill Book Co., 1991.

[92] C. A. Balanis, *Antenna Theory: Analysis and Design.* Wiley-Interscience, 2005.

[93] A. D. Olver, P. J. B. Clarricoats, A. A. Kishk, and L. Shafai, *Microwave Horns and Feeds.* IEE and IEEE, 1991.

[94] "Details on hdl_ant.exe," www.w1ghz.org/antbook/chap5.pdf.

[95] A. Rudge, K. Milne, A. Olver, and P. Knight, *The Handbook of Antenna Design.* IET, 1982.

[96] R. G. Vaughan, N. L. Scott, and D. R. White, "The theory of bandpass sampling," *IEEE Transactions on Signal Processing*, vol. 39, no. 9, pp. 1973 – 1984, 1991.

[97] D. M. Akos, M. Stockmaster, J. B. Y. Tsui, and J. Caschera, "Direct bandpass sampling of multiple distinct rf signals," *IEEE Transactions on Communications*, vol. 47, no. 7, pp. 983–988, 1999.

[98] C. E. Cook and M. Bernfeld, *Radar Signals.* Academic Press, 1965.

[99] W. P. Robins, *Phase Noise in Signal Sources.* Peter Peregrinus Ltd., 1982.

[100] L. V. Blake, *Radar Range Performance Analysis.* Munro Publishing, 1991.

[101] J. C. Curlander and R. N. McDonough, *Synthetic Aperture Radar Systems and Signal Processing.* John Wiley and Sons Inc., 1991.

[102] W. G. Carrara, R. M. Majewski, and R. S. Goodman, *Spotlight Synthetic Aperture Radar: Signal Processing Algorithms.* Artech House, 1995.

[103] D. W. Allan, N. Ashby, and C. C. Hodge, "The science of timekeeping," hP Application note 1289.

[104] B. Müller, "Bistatic moving target detection using envisat satellite as illuminator," masters thesis, UCL Department of Electronic and Electrical Engineering.